N° d'ordre NNT : 2025ENTP0011

THÈSE DE DOCTORAT DE L'ENTPE

Membre de l'Université de Lyon

École Doctorale N° 162
Mécanique, Énergétique, Génie Civil et Acoustique

Spécialité : Acoustique

Maxime Morell

Synthesis and implementation of nonlinear boundary operators for acoustical applications

Synthèse et implémentation d'opérateurs non-linéaires de frontière pour applications acoustiques

---

Devant le jury composé de :

MARYAM GHANDCHITEHRANI	Professeure University of Groningen	-	Rapporteure
HERVÉ LISSEK	Maître d'enseignement et de recherche EPFL	-	Rapporteur
STEFANIA LO FEUDO	Maîtresse de Conférence ISAE-Supmeca	-	Examinatrice
GHISLAIN RAZE	Chargé de Recherche FNRS University of Liège	-	Examinateur
OLIVIER THOMAS	Professeur des Universités ENSAM	-	Président du jury
EMMANUEL GOURDON	ICTPE ENTPE	-	Co-directeur de thèse
MANUEL COLLET	Directeur de Recherche CNRS, Ecole Centrale Lyon	-	Co-directeur de thèse
EMANUELE DE BONO	Docteur Ecole Centrale Lyon	-	Co-encadrant de thèse

Remerciements

Cette thèse a été réalisée au sein du Laboratoire de Tribologie et Dynamique des Systèmes (LTDS), sur les sites de l'Ecole Centrale Lyon et de l'ENTPE. J'ai ainsi eu la chance de côtoyer de nombreuses personnes, et je tiens à exprimer ici ma gratitude pour leur soutien et contribution tout au long de cette expérience.

I would like to express my sincere thanks to Prof. M. Ghandchi Tehrani and Prof. H. Lissek for accepting the long and demanding task of evaluating my work.
I also extend my gratitude to Prof. G. Raze, Prof. S. Lo Feudo and Prof. O. Thomas for the interest they showed in my work, and for agreeing to serve as members of the jury.
The depth of the scientific discussion during the defense were highly stimulating in many aspects, and I thank all the members of the jury for that.

Tout d'abord, je tiens à exprimer ma plus profonde reconnaissance à Monsieur M. Collet et Monsieur E. Gourdon, qui m'ont fait confiance pour conduire ces travaux sous leur supervision, d'abord lors de deux stages, puis au cours d'une thèse de doctorat. Leurs encouragements, leur disponibilité, leur implication et leur extrême créativité ont été d'une aide précieuse pour mener à bien ce projet. Leur enthousiasme communicatif pour la recherche et tout particulièrement ce sujet m'a constamment poussé à faire mieux.

J'adresse une reconnaissance particulière pour Monsieur E. De Bono pour la justesse, limplication et la bienveillance avec lesquelles il ma conseillé et encadré. Sa passion pour le sujet en fait un expert, et je le remercie sincèrement pour m'avoir apporté toute son experience tant lors de ce premier stage que durant ces trois années de doctorat. La qualité scientifique de ma supervision, avec Manuel, Emmanuel et Emanuele, a fortement participé à l'aboutissement de ces travaux.

Les expériences menées au cours de cette thèse ont été possibles grâce à la grande compétence des ingénieurs et techniciens qui ont participé, de près ou de loin, à leur conception. Je remercie sincèrement Messieurs A. Ezzerouki, S. Lemahieu pour leur disponibilité et la précision avec laquelle ils ont réalisé leur travail, sans lesquels ces expériences n'auraient pu avoir lieu. Je remercie également Messieurs S. Léone, M. Vanwolleghem et J. Blanc Gonnet pour leur aide précieuse.

J'exprime ma gratitude à mes nombreux collègues avec qui j'ai partagé des pauses, des cafés, des discussion scientifiques, des week-ends, des tarots, des afterworks, des conférences et des séminaires. Travailler à vos côtés, que ce soit à l'ENTPE ou à Centrale, ont rendu ces années infiniment plus agréables.

D'un point de vue plus personnel, je remercie chaleureusement mes amis pour leur soutien, les nombreux week-ends d'évasion, leur aide et les échanges de tous les jours. La Bricoloc a été d'un soutien indéfectible, ce

depuis plusieurs années, merci à vous: Thomas, Guillaume, Nicolas, Maxence, Corentin, Yohan, Thibault, Dylan, Romain, Lounès et Grégoire. Merci Paul pour ta présence et ta gentillesse.

Je remercie ma belle-famille, Bruno, Anne et Laurie, pour les week-ends partagés et les sorties vélo.

Je remercie très sincèrement mes grands-parents, Robert, Claude, Monique et Jean-Marie pour avoir grandement participé à faire de moi ce que je suis aujourd'hui.

Mes parents et ma soeur ont fait preuve d'un soutien et d'une confiance sans égal, me permettant d'arriver à cet objectif grâce à leur conseils. Ils ont été des acteurs essentiels de mon developpement personnel, intellectuel et professionnel, et je ne les remercierai jamais assez pour ça.

Enfin, j'adresse mes remerciements les plus chaleureux à Clara, pour son soutien inestimable au cours de ces trois années. Cette thèse n'aurait pu aboutir sans sa patience et son écoute.

Résumé

Si la réduction du bruit est aujourd'hui un enjeu majeur pour la santé et le confort, les dispositifs capables d'assurer une atténuation large bande aux basses fréquences et pour de faibles amplitudes d'excitation demeurent rares. Les résonateurs acoustiques non linéaires ont montré un fort potentiel, mais uniquement à très fortes amplitudes, ce qui limite leur utilisation dans des applications courantes, telles que l'acoustique du bâtiment. Les travaux présentés dans cette thèse visent à lever ce verrou technologique en développant un résonateur acoustique non linéaire fonctionnant à faibles amplitudes d'excitation grâce à une stratégie de contrôle d'impédance. Cela consiste à modifier les conditions de réflexion et d'absorption de frontières en agissant sur l'impédance de la surface considérée. Ce travail de doctorat développe un résonateur électroacoustique non linéaire programmable et fonctionnant à faible amplitude, constitué d'un haut-parleur collocalisé avec des microphones, le tout relié à un processeur calculant la variable de commande pour imposer un comportement non linéaire. La stratégie de contrôle permettant ce développement est formalisée, présentée et validée par des simulations numériques ainsi que par des expériences en champ libre dans la première partie de la thèse. Une extension de la méthode est proposée afin d'améliorer les performances des résonateurs non linéaires synthétisés, indépendamment des conditions initiales. Pour évaluer les capacités d'absorption du résonateur électroacoustique, un banc expérimental dédié ainsi que le modèle associé ont été développés et étudiés à l'aide d'outils numériques et analytiques. L'expérience consiste à coupler le résonateur créé à un mode acoustique de tube afin de mettre en évidence une absorption efficace de l'énergie acoustique pour divers comportements non linéaires programmés. Ensuite, un réseau de résonateurs électroacoustiques non linéaires (un liner) est implémenté expérimentalement et modélisé par l'utilisation d'éléments finis. Ce dernier présente des capacités d'absorption large bande tout en montrant un comportement stable. De plus, l'existence de solitons au sein du réseau non linéaire est étudiée à travers un modèle et une étude analytique, permettant d'établir des conditions d'existence de celui-ci. L'amélioration de la méthode, l'investigation et la conception de phénomènes non linéaires dans des réseaux de résonateurs constituent les principales perspectives de ce travail, afin de proposer des solutions efficaces pour le contrôle du bruit.

Abstract

As the need to reduce acoustic levels for health and comfort continues to grow, solutions for achieving broadband noise mitigation at low frequencies and low excitation amplitudes remain few. Acoustic nonlinear resonators have shown strong potential, but only at very high excitation amplitudes, limiting their use in typical real-life applications such as building acoustics. The work presented in this thesis addresses this limitation by developing an acoustic nonlinear resonator operating at low excitation amplitudes through an Impedance control strategy. Impedance control consists in modifying the reflection and absorption conditions of boundaries by the modification of the impedance of the considered surface. This work develops a digitally programmable nonlinear electroacoustic resonator at low excitation amplitude that consists in a loudspeaker collocated with microphones and connected to a processor estimating the command variable for implementing a nonlinear behavior at low amplitudes. The control strategy enabling this development is formalized, presented and validated through numerical simulations and open-field experiments in the first part of the thesis. An extension of the method is proposed to enhance the performances of the synthesized nonlinear resonators regardless of the initial conditions To evaluate the absorption capabilities of the electroacoustic resonator, a dedicated experimental bench and its associated model studied with both numerical and analytical tools – is developed. The experiment couples the synthesized resonator to an acoustic mode of a tube, and shows effective absorption of the acoustic energy for various programmed nonlinear behaviors. Building on these results, a network of nonlinear synthesized resonators (a liner) is experimentally implemented and modeled using finite element analysis. The nonlinear liner exhibits broadband absorption capabilities with stable behavior. Additionally, the existence of solitons inside the nonlinear network is investigated through a model and its analytical study, and conditions of existence are established. The further improvement of the method, investigations and design of nonlinear phenomena in the network of nonlinear resonators consist in the main perspectives of the present work to propose efficient solutions to noise control.

Résumé Long en Français

Introduction

Cette thèse de doctorat a été financée par le Ministère de la Transition Écologique et réalisée au Laboratoire de Tribologie et Dynamique des Systèmes (LTDS), sur les sites de l'École Centrale de Lyon (ECL) et de l'École Nationale des Travaux Publics de l'État (ENTPE), d'octobre 2022 à décembre 2025. Elle s'inscrit dans la continuité d'une idée originale de Manuel Collet et Emanuele De Bono formulée en 2020, et d'un premier stage réalisé en avril 2021 à l'ECL sous leur supervision, qui avait permis d'explorer la faisabilité expérimentale du concept. J'ai ainsi eu l'opportunité de travailler pendant plus de trois ans sous la direction de Manuel Collet, d'Emmanuel Gourdon et d'Emanuele De Bono sur le contrôle des frontières acoustiques et la création de résonateurs non linéaires fonctionnant à faibles amplitudes d'excitation.

Si la réduction du bruit est aujourd'hui un enjeu majeur pour la santé et le confort, les dispositifs capables d'assurer une atténuation large bande aux basses fréquences et pour de faibles amplitudes d'excitation demeurent rares. Les résonateurs acoustiques non linéaires ont montré un fort potentiel, mais uniquement à très fortes amplitudes, ce qui limite leur utilisation dans des applications courantes, telles que l'acoustique du bâtiment. L'objectif principal de cette thèse est donc de développer des résonateurs acoustiques non linéaires pour l'atténuation du bruit à faibles amplitudes, en s'appuyant sur des techniques de contrôle actif. Le couplage multi-physique (vibrations, acoustique et électricité via le contrôle) associé à l'étude des dynamiques non linéaires offre un cadre scientifique particulièrement stimulant.

La méthode développée permet la programmation numérique de comportements non linéaires dans le régime linéaire des actionneurs, et son extension rend possible une meilleure maîtrise des dynamiques non linéaires étudiées. Son application aux résonateurs électroacoustiques est démontrée au travers de trois expériences et de leurs modèles associés :

- le résonateur synthétisé est étudié en champ ouvert;
- le résonateur synthétisé est étudié à travers son couplage avec un mode acoustique de tube;
- un réseau de résonateurs électroacoustiques est étudié pour former un métamateriau non-linéaire.

Des outils analytiques et numériques ont été mobilisés pour la prédiction, la compréhension et la conception des résonateurs dans ces différents contextes.

Chapitre 2 : Contrôle du bruit et des vibrations

Le Chapitre 2 situe ce travail de doctorat dans un cadre scientifique plus large et en expose les principes fondamentaux. Il se place à l'intersection de trois domaines principaux : le contrôle non linéaire des vibrations

mécaniques, le contrôle acoustique passif et le contrôle actif par impédance. La revue de littérature proposée présente les bases théoriques mobilisées dans ce manuscrit, tout en retraçant les raisons scientifiques et historiques qui ont conduit à cette thèse.

Les études de la littérature soulignent l'importance du contrôle du bruit et la nécessité de s'inspirer des méthodes développées en mécanique vibratoire. Dans ce domaine, les dispositifs linéaires se révèlent insuffisants face aux fortes variations de paramètres rencontrées en pratique. Les résonateurs non linéaires ont donc été développés, permettant de tirer parti de phénomènes spécifiques bifurcations, auto-accordage, élargissement de bande, dissipation rapide de l'énergie mais au prix de comportements parfois indésirables tels que des courbes de résonance détachées (isolas), des régimes chaotiques ou une dépendance aux conditions initiales.

En acoustique, certains constats sont similaires, et d'autres s'imposent :

- Les dispositifs passifs restent limités aux basses fréquences (faible efficacité, encombrement, bande étroite) et ne sont pas adaptatifs;
- Les résonateurs non linéaires passifs offrent un potentiel d'adaptabilité et de large bande, mais nécessitent des amplitudes d'excitation trop élevées pour des applications usuelles;;
- Le contrôle de bruit actif création d'ondes en opposition de phase (ANC) apporte une grande adaptabilité, mais son efficacité spatiale est restreinte et son coût énergétique élevé;
- Le contrôle d'impédance (IC) constitue une alternative prometteuse, capable d'améliorer l'absorption acoustique avec une consommation énergétique réduite. Toutefois, les approches actuelles restent limitées à des comportements linéaires, ce qui empêche d'exploiter les bénéfices des phénomènes non linéaires.

C'est dans ce contexte que s'inscrit ce travail doctoral, dont l'objectif est de permettre la synthèse de comportements non linéaires au sein du contrôle d'impédance, et ce à faibles amplitudes d'excitation (inférieures à 110 dB), afin d'ouvrir la voie à de nouvelles stratégies de mitigation acoustique.

Chapitre 3 : Programmer les non-linéarités

Le Chapitre 3 présente une méthode permettant d'implémenter des comportements non linéaires dans des actionneurs à faibles amplitudes d'excitation. L'objectif de ce chapitre est donc de poser le cadre mathématique du contrôle, d'en préciser les hypothèses et les conditions d'application, et d'en explorer les possibilités ainsi que les limites.

La stratégie de contrôle est d'abord formulée pour un système à n degrés de liberté, puis appliquée au cas d'un résonateur électroacoustique. La validation est effectuée par des simulations numériques et des essais expérimentaux, confirmant la faisabilité et la robustesse de l'approche.

Les principales contributions de ce chapitre sont :

- la formalisation mathématique du contrôle par inversion de modèle avec consigne définie par un exosystème;
- la démonstration analytique de la convergence asymptotique, établissant la stabilité inconditionnelle de la stratégie;

- la création de résonateurs électroacoustiques non linéaires programmables numériquement, opérant à faibles amplitudes d'excitation (inférieures à 110 dB).

Enfin, plusieurs perspectives sont ouvertes :

- étendre la preuve de convergence asymptotique au cas général;
- appliquer la stratégie à d'autres transducteurs (création de capteurs non linéaires adaptatifs, de transducteurs plasmacoustiques non-linéaires [140], matériaux piézoélectriques);
- améliorer la méthode pour réduire la résonance résiduelle liée au schéma numérique, soit en dissociant calcul et mesure, soit en augmentant la fréquence d'échantillonnage, soit en ajoutant une boucle de rétroaction avec capteur supplémentaire [159].

Chapitre 4 : Un système acoustique couplé à deux degrés de liberté

Le chapitre 4 présente le couplage du résonateur électroacoustique non linéaire (NER) avec un mode acoustique de tube. Deux principaux objectifs sont identifiés :

- évaluer la capacité de la stratégie de contrôle à imposer une large variété de comportements non linéaires;
- analyser l'efficacité du NER pour absorber l'énergie et contrôler un mode acoustique, en comparaison avec un Résonateur à Masse Accordée (Tuned Mass Damper) optimisé.

Pour atteindre ces objectifs, un banc expérimental a été développé et adapté du modèle de Bellet [16]. Celui-ci a été validé numériquement et expérimentalement, puis étudié analytiquement. Si les simulations numériques reproduisent fidèlement le comportement observé, les calculs analytiques, bien que moins précis, fournissent une compréhension qualitative des phénomènes.

Plusieurs comportements non linéaires sont étudiés expérimentalement : raideur cubique (durcissante et molissante), potentiel logarithmique, et lois linéaires par morceaux (continues ou discontinues). Les résultats expérimentaux sont confrontés à des simulations numériques et à des études analytiques du modèle de l'expérience. Une partie de ces travaux a donné lieu à deux publications [114, 112].

Les expériences démontrent que le résonateur électroacoustique non-linéaire peut contrôler efficacement un mode acoustique de tube et absorber l'énergie, avec de meilleures performances qu'un absorbeur linéaire de type Résonateur à Masse Accordée. Cependant, les performances du résonateur non-linéaires sont fortement dépendantes du points d'équilibre atteint, lui-même défini par les conditions initiales.

Cette analyse confirme la robustesse de la stratégie de contrôle et ouvre la voie à son utilisation pour l'absorption acoustique, ou bien à l'utilisation du dispositif comme banc de test pour explorer des comportements non linéaires atypiques avant des expérimentations plus coûteuses.

Chapitre 5 : Cibler des points d'équilibres spécifiques

Il a été montré lors du Chapitre 5 que le résonateur électroacoustique absorbe davantage d'énergie lorsqu'il fonctionne autour d'un point d'équilibre de forte énergie. Or, les systèmes mécaniques non linéaires présentent

des bassins d'attraction complexes dépendant des conditions initiales [155]. Ainsi, un système forcé peut être attiré vers différents équilibres stables, ce qui influence fortement ses performances.

L'objectif de ce chapitre est donc de:

- développer une stratégie de contrôle permettant de sélectionner un point d'équilibre stable parmi plusieurs coexistants à une même fréquence;
- démontrer la capacité de cette stratégie à assurer l'absorption d'énergie par l'ER en ciblant l'équilibre désiré.

Imposer mécaniquement des conditions initiales à un résonateur électroacoustique est une tâche difficile, et les stratégies classiques de contrôle ne prennent pas en compte la sélection synthétique d'un équilibre lorsque plusieurs solutions stables coexistent, laissant les conditions initiales et le chemin parcouru décider du point d'équilibre. Pour surmonter cette limite, une extension de la stratégie de contrôle par l'apport d'énergie à l'Exosystème (présenté au Chapitre 3) est proposée. Elle consiste à intégrer en temps réel la dynamique de l'Exosystème non linéaire enrichie d'une variable artificielle transitoire qui fournit l'énergie nécessaire pour atteindre le point d'équilibre désiré. Une fois ce point atteint, le système conserve la trajectoire programmée, même après l'extinction de la variable synthétique ajoutée.

Cette contribution représente une avancée majeure dans le domaine du contrôle d'impédance non linéaire généralisé [78, 43, 114, 112], jusque-là limité à des excitations artificielles de type balayage sinusoïdal.

La stratégie est validée numériquement puis expérimentalement :

- un premier essai en champ quasi-ouvert démontre la possibilité d'atteindre le point d'équilibre d'une dynamique de type Duffing;
- un second essai où le résonateur électroacoustique est couplé à un mode de tube acoustique, confirme l'efficacité du contrôle pour absorber de l'énergie, même en présence de forts couplages pouvant menacer la stabilité du système [42].

Dans les deux cas, le resonateur électroacoustique atteint le point d'équilibre programmé sous excitation mono-harmonique.

Ce chapitre ouvre de nombreuses perspéctives comme l'optimisation de la forme, de l'amplitude et de la durée du transitoire artificiel, l'étude des excitations multiharmoniques ou d'autres types de non-linéarités, ainsi que le développement d'architectures hybrides intégrant du feedback.

Ce travail constitue une étape essentielle vers la maîtrise complète des impédances non linéaires programmables, ouvrant la voie à la conception d'impédances optimales pour l'atténuation du bruit dans des scénarios réalistes, par exemple pour réduire les bruits tonals en acoustique des salles.

Chapitre 6 : Un métamateriau acoustique non-linéaire

L'objectif du Chapitre 6 est de concevoir et d'étudier un liner acoustique constitué de résonateurs électroacoustiques non linéaires, comme solution innovante pour l'atténuation du bruit à faibles amplitudes d'excitation. Ce travail constitue une première étape vers le développement de liners non linéaires fonctionnant dans ce régime. Les objectifs principaux sont :

- développer un banc expérimental et évaluer les performances du liner non-linéaire en termes de réduction sonore;
- analyser les phénomènes non linéaires apparaissant dans ces métamatériaux, par l'observation expérimentale et via des prédictions analytiques et numériques;
- modéliser le banc expérimental afin de prédire et mieux comprendre le comportement du métamatériau non-linéaire.

Ce chapitre propose ainsi la réalisation expérimentale d'un métamatériau non linéaire à faibles amplitudes, met en évidence l'élargissement de la bande de fréquences efficace par rapport à un liner linéaire. De plus, une étude analytique des conditions d'apparition éventuelle de solitons dans ces dispositifs est réalisée.

Ces résultats constituent une étape préliminaire vers le développement de métamatériaux programmables et l'étude approfondie des dynamiques non linéaires appliquées à l'atténuation acoustique. Ce chapitre ouvre de nombreuses perspectives, dont les principales sont :

- l'optimisation des paramètres des liners afin de réduire la transmission des ondes incidentes à travers le liner;
- l'exploration d'autres comportements non linéaires, par exemple des raideurs molissantes pour cibler les basses fréquences;
- l'étude du couplage fort entre un liner non linéaire et un mode acoustique de tube, susceptible de révéler des phénomènes non-linéaires intéressants pour la compréhension des métamatériaux non-linéaires et pour le contrôle acoustique et vibratoire;
- l'analyse des comportements complexes tels que bandes chaotiques et régimes quasi-périodiques, pouvant améliorer les performances et enrichir la compréhension des métamatériaux non linéaires et des phénomènes physiques et biologiques comme celui de la cochlée [124]);
- le développement des métamatériaux capables de supporter la propagation de solitons, afin de gérer la localisation d'énergie pour l'atténuation acoustique, voire la récupération d'énergie.

Ce chapitre ouvre la voie à de futures recherches sur les liners acoustiques non linéaires, qui présentent un fort potentiel pour le contrôle du bruit lorsqu'ils sont optimisés.

Conclusion

Ce manuscrit présente le développement d'une stratégie de contrôle innovante permettant la programmation numérique de comportements non linéaires dans des résonateurs électroacoustiques à faibles amplitudes d'excitation. L'objectif est de répondre à un enjeu majeur du contrôle acoustique : l'atténuation large bande des basses fréquences, encore difficile à atteindre avec les dispositifs classique.

Cette thèse de doctorat constitue une avancée significative dans le domaine du contrôle actif non linéaire appliqué à l'acoustique. Elle montre qu'il est possible de tirer parti des phénomènes non linéaires à faibles amplitudes grâce à des stratégies de contrôle adaptées, et ouvre des perspectives prometteuses tant pour l'atténuation du bruit dans des scénarios réalistes (par exemple en acoustique du bâtiment) que pour l'étude fondamentale des métamatériaux non linéaires.

Table of contents

List of figures xvii

List of tables xxv

1 Introduction 1

2 Vibration and Noise Control 5

2.1 Context . . . 5
2.2 Vibration control . . . 6
2.2.1 The Tuned Mass Damper (TMD) . . . 6
2.2.2 Nonlinear resonators . . . 9
2.2.3 Nonlinear resonators for vibration control . . . 12
2.3 Noise control . . . 13
2.3.1 Classical systems for noise mitigation . . . 13
2.3.2 Electro-active systems for noise control . . . 17
2.4 Problem . . . 31
2.5 Manuscript outline . . . 31

3 Programming nonlinearity 33

3.1 Principle and formulation of the problem . . . 33
3.1.1 The set-point . . . 34
3.1.2 A model-inversion based feed-forward controller . . . 34
3.1.3 General formulation . . . 35
3.1.4 Algorithm . . . 35
3.2 Application to the case of the electroacoustic resonator . . . 37
3.2.1 The plant and the controller . . . 37
3.2.2 Asymptotic Convergence . . . 38
3.2.3 Design of the desired dynamic behavior . . . 38
3.3 Numerical simulations . . . 39
3.3.1 Method . . . 39
3.3.2 The synthesis of linear resonators . . . 39
3.3.3 The effect of time delay . . . 42
3.3.4 Validation of the synthesis of nonlinear resonators by a comparison to an analytical solution 43
3.4 Experimental validation . . . 45
3.4.1 Experimental set-up . . . 45
3.4.2 Experimental validation of the control strategy . . . 46

3.4.3 Study of the classical nonlinear behaviors . . . 50

4 An acoustic two degree of freedom system 55
4.1 Considered system . . . 56
4.1.1 Principle and experimental set-up . . . 56
4.1.2 Model General Hypotheses . . . 56
4.1.3 The acoustic source model . . . 57
4.1.4 The reduced section tube model . . . 58
4.1.5 The coupling box model . . . 60
4.1.6 Coupled equations of the two-degree-of-freedom model . . . 61
4.2 Numerical Simulations . . . 61
4.3 Analytical study . . . 63
4.4 Experimental set-up and methods . . . 65
4.4.1 Experimental set-up . . . 65
4.4.2 Parameters of the experimental bench . . . 66
4.5 Targeting a cubic restoring force function . . . 67
4.5.1 Design . . . 67
4.5.2 Analytical predictions . . . 70
4.5.3 Experimental results . . . 75
4.6 Targeting a non polynomial restoring force function . . . 83
4.6.1 Design . . . 83
4.6.2 Analytical predictions . . . 85
4.6.3 Experimental results . . . 88
4.7 Targeting a nonsmooth restoring force function . . . 90
4.7.1 Design . . . 90
4.7.2 Analytical predictions . . . 92
4.7.3 Experimental results . . . 95
4.8 Conclusion of the chapter . . . 98

5 Targeting specific equilibrium points 101
5.1 Theoretical developments . . . 101
5.1.1 By adding synthetic external forces . . . 102
5.1.2 By adding synthetic external displacement or speed . . . 103
5.2 Numerical simulations . . . 103
5.2.1 By adding synthetic external forces . . . 103
5.2.2 By adding synthetic external displacement or speed . . . 105
5.3 The quasi-open field experiment . . . 105
5.3.1 Results for a added synthetic external forces . . . 106
5.3.2 Results for a synthetic external displacement or speed . . . 108
5.4 The coupled-tube experiment . . . 110
5.5 The coupled-tube experiment . . . 110
5.5.1 Experimental set-up . . . 110
5.5.2 Results for a fictive pressure . . . 110
5.5.3 Results for a synthetic external displacement or speed . . . 114

5.6 Conclusion . . . 115

6 A Nonlinear Acoustic Metasurface 117
6.1 Introduction . . . 117
6.2 Considered system . . . 118
6.3 A finite element model approach . . . 119
6.4 The experiment . . . 121
6.4.1 Experimental set-up . . . 121
6.4.2 Experimental tests and post-processing methods . . . 123
6.5 The linear metasurface . . . 125
6.5.1 The single resonator problem . . . 125
6.5.2 The distributed network of resonators . . . 127
6.6 The nonlinear metasurface . . . 129
6.6.1 A single nonlinear resonator . . . 129
6.6.2 The distributed network of nonlinear resonators . . . 133
6.7 Perspective: study of solitons inside the metasurface . . . 135
6.7.1 Behavior of the liner . . . 136
6.7.2 Search for localized solitons . . . 139
6.8 Conclusion of the chapter . . . 140

7 Conclusion and Perspectives 141

References 145

Appendix A ER's parameters estimation 155
A.1 The Thiele-Small parameters . . . 155
A.2 The sensitivity of microphones . . . 157
A.3 Data for the cells used in Chapter 5 (metamaterial) . . . 158
A.3.1 Thiele-Small parameters . . . 158
A.3.2 Microphones . . . 160

Appendix B Estimation of parameters of the acoustic mode of the tube's cavity 163
B.1 Method . . . 163
B.2 Influence of the anti-resonance . . . 164
B.3 Sensitivity analysis of the damping parameter . . . 165

Appendix C Analytical study 167
C.1 General study . . . 167
C.1.1 The standard form system . . . 167
C.1.2 Fast system dynamics . . . 170
C.1.3 Unstable zones of the SIM . . . 171
C.1.4 Slow system dynamics . . . 174
C.2 The cubic restoring force function . . . 176
C.3 The non polynomial restoring force function . . . 179
C.4 The Piecewise linear restoring force function . . . 181

Appendix D The cubic restoring force with a periodic time-dependent coefficient **183**

Appendix E The Metasurface experiment **195**

E.1 The acoustic sources calibration 195

E.2 The rigid liner configuration 196

List of figures

2.1 Decibel scale and associated pressure and potential causes. Author: Izaak Neutelings. 5
2.2 Scheme of a primary oscillator attached to the Tuned Mass Damper. 7
2.3 Frequency Response Function of (a) an optimized TMD with [7]; (b) a weakly coupled TMD. . 8
2.4 Scheme of a primary oscillator weakly coupled with a grounded Tuned Mass Damper. 8
2.5 Time histories of a primary oscillator weakly coupled with a grounded Tuned Mass Damper with $M = 1$, $c_1 = 0.1$, $k_1 = 1$, $m_2 = 1$, $k_2 \approx 0.96$, $c_2 \approx 0.09$, $\gamma = 0.1$, $A = 0$ and with initial conditions $x_1(0) = 1$ and $\dot{x}_1(0) = x_2(0) = \dot{x}_2(0) = 0$ 9
2.6 Frequency Response Curves of the Duffing oscillator obtained by HBM. 10
2.7 Scheme of a primary oscillator coupled with a NES. 10
2.8 Time histories with initial conditions $x_1(0) = 1$ and $\dot{x}_1(0) = x_2(0) = \dot{x}_2(0) = 0$ of a primary oscillator weakly coupled with a grounded (a) NES with $M = 1$, $c_1 = 0.1$, $k_1 = 1$, $m_2 = 1$, $k_2 = 0$, $c_2 \approx 0.09$, $\beta_2 = 30$, $\gamma = 0.1$, $A = 0$; (b) NDVA with $M = 1$, $c_1 = 0.1$, $k_1 = 1$, $m_2 = 1$, $k_2 = 0.7$, $c_2 \approx 0.09$, $\beta_2 = 30$, $\gamma = 0.1$, $A = 0$. 10
2.9 Backbone curves of NES, NLTVA and linear oscillators. 11
2.10 Frequency Response Curves of the Primary oscillator linked to a NES, obtained by a perturbation method [92], where σ is the detuning parameter corresponding to $\omega/\omega_1 = 1 + \sigma\varepsilon$ with $\varepsilon << 1$. 12
2.11 (a) Absorption coefficient of a fibrous absorbent material with a flow-resistance of 20 CGS units depending of the layer thickness in cm, from [45]; (b) Absorption coefficient of a porous material computed with the JCA model using classical parameters for acoustic foams; (c) Micro-structures of three different materials: acoustic foam (c.a), glass fiber (c.b) and mineral wool (c.c), from [166]. 14
2.12 Schematic of a (a) QR with the two firsts shape modes in terms of pressure; (b) HR. 15
2.13 Schematic of (a) a perforate-over-honeycomb-core acoustic liner, from [14], (b) dual-resonance liner design, from [14]. (c) Picture of resonant inclusions in a material, from [73]. 16
2.14 (a) Picture of the visco-elastic membrane from [16]; (b) Response of nonlinear HR obtained by numerical schemes, from [3]. 17
2.15 Schematic of the ANC principle with the description of the displacement of air particles. 18
2.16 Patents of (a) Lueg [103] ; (b) Olson [121]. 19
2.17 (a) Scheme of the experimental arrangement of active porous-plate absorbers, from [77] ; (b) Scheme of one cell hybrid absorber, from [61]. 20
2.18 Scheme of (a) normal incidence conditions ; (b) grazing incidence conditions. 21
2.19 Scheme of a loudspeaker with a back-cavity, from [41]. 24

2.20 (a) Scheme of the experimental set-up featuring an accelerometer for velocity sensing, from [153]; (b) Scheme of the experimental set-up featuring amicrophone in the loudspeaker's back-cavity for velocity sensing, from [159]; (c) Scheme of the experimental set-up featuring a vibrometer for velocity sensing, from [100]; (d) Model of the dual coil electrodynamic loudspeaker, from [133]. 26
2.21 Scheme of the experimental setup with the Howland current pump enabling a electrical current driven control, from [134]. 27
2.22 Scheme of the waveguide, and Insertion Loss (I_L) measurements relative to incident waves directions, from [87]. 29
2.23 Illustration of the state of the art of Active Noise Control 30

3.1 Block diagram of the open-loop control 36
3.2 (a) Envelopes of the actual displacement $\hat{x}$ and the ES displacement $\hat{x}_d$; (b) Electrical current computed during the simulation with $\eta_M = \eta_K = \eta_R = 1$. 40
3.3 Envelopes of the actual displacement $\hat{x}$ and the ES displacement $\hat{x}_d$ with $\eta_M = 1$ 40
3.4 Envelopes of the actual displacement $\hat{x}$ and the ES displacement $\hat{x}_d$ with $\eta_M = \eta_R = 1$ and $\eta_K = 4$ for a RK4 scheme that takes into account the evolution of the pressure at the intermediate stages. The sampling frequency is 50 kHz. 41
3.5 Envelopes of the actual displacement $\hat{x}$ and the ES displacement $\hat{x}_d$ with $\eta_M = \eta_R = 1$ and $\eta_K = 4$ for a Euler scheme at different sampling frequencies. 42
3.6 Envelopes of the actual displacement $\hat{x}$ with $\eta_M = 1$ with and without the time delay $\tau = 2 \times 10^{-5}$ s 43
3.7 Amplitude response of the Duffing equation featuring a hardening behavior with linear and cubic stiffness. 44
3.8 Comparison between the analytical solution of Eq. (3.7b) obtained by Harmonic Balance Method (HBM), and the envelopes $\hat{x}_d$ and $\hat{x}$ of the simulated ES targeted displacement x_d and of the ER response x respectively, in case of (a) increasing or (b) decreasing frequency sweep excitation. . 44
3.9 Basins of attraction of the ES Eq. 5.1b. The black (respectively, white) color zone indicates that the system tends towards the high (respectively, low) energy equilibrium point. 45
3.10 (a) Picture and (b) scheme of the open-field experimental set-up. 46
3.11 Amplitude, phase and coherence of the mobility $Y(s) = v(s)/p(s)$ for different cases. 47
3.12 Comparison of the ER responses in pressure and velocity, controlled by either RTI or IIR algorithms in case of (a) stationary regime, and (b) transient regime. 48
3.13 Envelopes of the velocity of the membrane, pressure close to it, and electrical current computed during the experiment under a sine sweep excitation with $\eta_M = 1$ and $\eta_R = 1/8$. 49
3.14 Time signal, Spectrogram and FFT of the measured pressure close to the loudspeaker's membrane with $\eta_R = 1/8$, $\eta_K = \eta_M = 1$ and $\beta_{\text{NL}} = 10^{10}$ m^{-2}. 50
3.15 Parametric study of the nonlinear parameter: ER's membrane velocity envelopes and bifurcation frequencies with the parameters $\eta_M = 1$, $\eta_K = 1$, $\eta_R = 1/8$. 51
3.16 Parametric study of the excitation amplitudes: envelopes of the ER's membrane measured velocity with the desired parameters $\eta_M = 1$, $\eta_K = 1$, $\eta_R = 1/8$. 51
3.17 Parametric study of the damping parameter: envelopes of the pressure and velocity of the ER's membrane with $\eta_K = 1$, $\eta_M = 1$ and $\beta_{\text{NL}} = 10^{10}$ m^{-2} 53
3.18 Envelopes of the ER's membrane velocity and pressure close to it and electrical current computed during the experiment with $\eta_M = \eta_K = 1$, $\eta_R = 2.068$, and $\beta_{\text{NL}} = 5 \times 10^{13}$ m^{-2}. 53

4.1 Experimental scheme 56

4.2 Experimental setup . . . 66
4.3 Design of Cubic behavior . . . 68
4.4 Design of Cubic behavior . . . 69
4.5 Figures of the SIM of the two degree of freedom system defined by equations (C.25,4.36), with $P = 0.5$ Pa. Predictions made with parameters from Configuration B. . . . 71
4.6 Figures of the equilibrium points of the two degree of freedom system defined by equation (C.53), with $P = 0.8468$ Pa. Predictions made with parameters from Configuration B. . . . 72
4.7 Figures of the equilibrium points of the two degree of freedom system defined by equation (C.53), with $P = 0.8468$ Pa for both hardening (a,b) and softening (c,d) behaviors. Predictions made with parameters from Configuration B. . . . 73
4.8 Figures of the equilibrium points of the two degree of freedom system defined by equation (C.53), with $P = 0.4418$ Pa. (a) The SIM and the numerical integration; (b) The equilibrium points in the (σ, N_m, N_a) plane; (c,d) Projections of the equilibrium points in the (σ, N_a) (c) and (σ, N_m) (d) planes. Predictions made with parameters from Configuration A, with $\beta_{\mathrm{NL}} = 2 \times 10^{11}$ m^{-2}, $\eta_K = 1$. 74
4.9 Experimental results for the cubic restoring force. Variation of the pressure amplitude inside the reduced section tube (top), and variation of the electrical current amplitude sent to the ER (bottom). Results obtained from Configuration A. . . . 75
4.10 Experimental time histories for the cubic restoring force: pressure inside the reduced-section tube. Results obtained from Configuration A. . . . 76
4.11 Experimental and corresponding numerical results obtained from direct numerical integration of Eq. (4.23): variation of the pressure amplitude. Results obtained from Configuration A. . . . 77
4.12 Experimental and corresponding numerical results obtained from direct numerical integration of Eq. (4.23): variation of the pressure amplitude. Results obtained from Configuration B. . . . 78
4.13 Variations of pressure inside the reduced-section tube and electrical current injected in the ER under frequency sweeps excitation for different values of damping η_R. Results obtained from Configuration B. . . . 80
4.14 Experimental results: variations of pressure inside the reduced-section tube and electrical current injected in the ER under frequency sweeps excitation. Results obtained from Configuration B. . 81
4.15 Analytical predictions: figures of the equilibrium points of the two degree of freedom system defined by equation (C.53), with $P = 0.8468$ Pa. Equilibrium points in the (a) (σ, N_m, N_a) plane; (b) (σ, N_a) plane; (c) (σ, N_m) plane. Results obtained from Configuration B. . . . 82
4.16 Experimental results: pressure inside the reduced-section tube at 580 Hz. Results obtained from Configuration B. . . . 83
4.17 Design of the logarithmic potential behavior. . . . 84
4.18 Restoring forces of the Logarithmic potential and Cubic Softening nonlinearities with different parameters. . . . 85
4.19 Figures of the SIM of the two degree of freedom system defined by equation (C.85), with $P = 0.4418$ Pa. Predictions made with parameters from Configuration A. . . . 86
4.20 Figures of the equilibrium points of the two degree of freedom system defined by equation (C.53), with $P = 0.4418$ Pa. (a) The SIM ; (b) The equilibrium points in the (σ, N_m, N_a) plane; (c,d) Projections of the equilibrium points in the (σ, N_a) (c) and (σ, N_m) (d) planes. Predictions made with parameters from Configuration A ($\eta_K = 1.5496$). . . . 87

4.21 Figures of the equilibrium points of the two degree of freedom system defined by equation (C.53), with $P = 0.4418$ Pa. (a) The SIM; (b) The equilibrium points in the (σ, N_m, N_a) plane; (c,d) Projections of the equilibrium points in the (σ, N_a) (c) and (σ, N_m) (d) planes. Predictions made with parameters from Configuration A (excepted for $\eta_K = 1.3496$). 88
4.22 Experimental and numerical results of the logarithmic potential restoring force at low excitation amplitudes. Results obtained from Configuration A. 89
4.23 Experimental results for the logarithmic potential restoring force at high excitation amplitude with $\beta_{\mathrm{NL}} = 3 \times 10^9$ m^{-2}. Results obtained from Configuration A. 89
4.24 Design of Piecewise linear 90
4.25 Design of Piecewise linear discontinous 92
4.26 Predictions made with parameters from Configuration A. 92
4.27 Figures of the equilibrium points (a) in the (σ, N_m, N_a) plane; (b) in the (σ, N_a) plane of the two degree of freedom system defined by equation (C.53), with $P = 0.4418$ Pa. Predictions made with parameters from Configuration A (excepted for $\eta_K = 1$). 93
4.28 Figures of the equilibrium points of the two degree of freedom system defined by equation (C.53), with $P = 0.4418$ Pa. Predictions made with parameters from Configuration A (excepted for $\eta_K = 1.1$). 94
4.29 Experimental results for the piece-wise linear restoring force. Results obtained from Configuration A. 95
4.30 Experimental results for the discontinuous piece-wise linear restoring force. Results obtained from Configuration C. 96
4.31 Experimental time histories for the discontinuous piecewise linear restoring force for sinusoidal excitation at 537 Hz and 580 Hz (a) and its Henon map (b). 97
4.32 Experimental time histories for the discontinuous piecewise linear restoring force of the computed variables during the experiment. Results obtained from Configuration **C**. 98

5.1 Plot of the additional synthetic transient f_{ext}^a. 104
5.2 Basins of attraction of the ES with the additional synthetic transient f_{ext}^a given by Eq. (5.6), for different amplitudes a. The black (respectively white) color zone indicates that the system tends to the high (respectively low) energy equilibrium point. 104
5.3 Envelopes of the measured velocity and sound pressure on the ER's membrane, under increasing and decreasing frequency sweep excitations, or under mono-harmonic sine excitations, without employing additional synthetic transients in f_{ext}^{ES}. 106
5.4 Experimental procedure consisting of a sequence of 6 phases over a 14 seconds measurement. . 107
5.5 Measured sound pressure (a) and velocity (b) on the ER's membrane during the different phases along the timeline of Fig. 5.4, with $f_{ext} = f_{ext}^m + f_{ext}^a$ under a 590 Hz sinusoidal excitation. 107
5.6 Envelopes of sound pressure and velocity amplitudes on the ER's membrane under increasing (solid-line) and decreasing (dashed-line) frequency sweep external excitation, in case of $f_{ext}^a = 0$. On the same graphs, pressure and velocity amplitudes of the ER response with $f_{ext} \neq 0$, under sinusoidal excitations at 580 Hz, 590 Hz, 600 Hz, and 610 Hz are displayed as dots. 108

5.7 Envelopes of sound pressure and velocity amplitudes on the ER's membrane under increasing (solid-line) and decreasing (dashed-line) frequency sweep external excitation, in case of $x_d^a = 0$ and $\dot{x}_d^a = 0$. On the same graphs, pressure and velocity amplitude of the ER response under sinusoidal excitation (at 580 Hz, 590 Hz, 600 Hz, and 610 Hz) during phases B and C with adding an external synthetic (a) displacement $x_d^{ES} = x_d + x_d^a$ with $\dot{x}_d^a = 0$, (b) velocity $\dot{x}_d^{ES} = \dot{x}_d + \dot{x}_d^a$ with $x_d^a = 0$. 109

5.8 Measured sound pressure (a) and velocity (b) on the ER's membrane during the different phases along the timeline of Fig. 5.4, with $x_d^{ES} = x_d + x_d^a$, and $\dot{x}_d^a = 0$ under a 580 Hz sinusoidal excitation. The amplitude of the added variable synthetic displacement is fixed to $a = 2 \times 10^{-5}$ m. 109

5.9 Measured sound pressure (a) and velocity (b) on the ER's membrane during the different phases along the timeline of Fig. 5.4, with $\dot{x}_d^{ES} = \dot{x}_d + \dot{x}_d^a$, and $x_d^a = 0$ under a 600 Hz sinusoidal excitation. The amplitude of the added variable synthetic velocity is fixed to $a = 0.25$ m.s^{-1}. 109

5.10 Envelopes of the measured pressure inside the S_t-tube, and ES displacement under increasing and decreasing frequency sweep excitations in case of $f_{ext}^{ES} = f_{ext}^m$, along with the values obtained under mono-harmonic sine excitations (a) with $f_{ext}^{ES} = f_{ext}^m$; (b) with $f_{ext}^{ES} = f_{ext}^m + f_{ext}^a$ during phase C, after the extinguishment of f_{ext}^a. 111

5.11 Measured pressures (a) inside the tube with a reduced section and (b) inside the coupling box at the ER's membrane surface for a 580 Hz mono-harmonic signal ; (c) Estimated displacement of the ER's membrane computed in the control loop for a 580 Hz sine excitation signal. 112

5.12 Phases A and B of the measured pressure inside the reduced section tube (a,c,e), and estimated displacement of the ER's membrane computed in the control loop (b,d,f) for a 575 Hz sine excitation signal. 113

5.13 Envelopes of sound pressure and velocity amplitudes on the ER's membrane under increasing (solid-line) and decreasing (dashed-line) frequency sweep external excitation, in case of $x_d^a = 0$ and $\dot{x}_d^a = 0$. On the same graphs, pressure and velocity amplitude of the ER response under sinusoidal excitation (at 580 Hz, 590 Hz, 600 Hz, and 610 Hz) during phases B and C with adding an external synthetic (a) displacement $x_d^{ES} = x_d + x_d^a$ with $\dot{x}_d^a = 0$, (b) velocity $\dot{x}_d^{ES} = \dot{x}_d + \dot{x}_d^a$ with $x_d^a = 0$. 114

5.14 Measured pressures (a,c) inside the tube with a reduced section for a 575 Hz mono-harmonic signal ; (c,d) Estimated displacement of the ER's membrane computed in the control loop for a 575 Hz sine excitation signal for both cases: (a,b) $x_d^{ES} = x_d + x_d^a, \quad \dot{x}_d^a = 0$; (c,d) $\dot{x}_d^{ES} = \dot{x}_d + \dot{x}_d^a$, $x_d^a = 0$. 115

6.1 Schematic of an asymmetric acoustic liner. 118

6.2 Experimental setup, with M1,M2,M3 and M4 being the 4 microphones used in the 4 Microphone Method (4MM), and LS A and LS B the loudspeakers of each side. 122

6.3 Picture of the ER. 123

6.4 Experimental and FE results obtained with 1 ER (OC configuration): (a) Transmission Loss, (b) Power Reflection coefficient, (c) Power Absorption coefficient. 126

6.5 Experimental results obtained with 1 ER with $\eta_R = 1/2$: (a) Transmission Loss, (b) Power Reflection coefficient, (c) Power Absorption coefficient. 127

6.6 Experimental results obtained with 1 ER with $\eta_K = 3$: (a) Transmission Loss, (b) Power Reflection coefficient, (c) Power Absorption coefficient. 127

6.7 Experimental and FE results obtained with 7 ERs (OC configuration): (a) Transmission Loss, (b) Power Reflection coefficient, (c) Power Absorption coefficient. 128
6.8 Experimental results obtained with 7 ERs with $\forall j \in [\![1,7]\!]$, $f_d^{[j]} = 1100$ Hz: (a) Transmission Loss, (b) Power Reflection coefficient, (c) Power Absorption coefficient. 129
6.9 Experimental results obtained with 7 ERs with $\forall j \in [\![1,7]\!]$, $\eta_R^{[j]} = 1/2$: (a) Transmission Loss, (b) Power Reflection coefficient, (c) Power Absorption coefficient. 129
6.10 Experimentally obtained ES Displacement with increasing and decreasing frequency sweeps and single frequency excitation signals with both $f_{ext}^{ES} = f_{ext}^{m}$ and $f_{ext}^{ES} = f_{ext}^{m} + f_{ext}^{a}$ with $a = 40$ Pa. The experimental results are compared with an HBM solution of the ES equation with one harmonic (with the value of the excitation assumed of constant amplitude equal to the mean pressure (≈ 1.70 Pa) measured during the experiment). 130
6.11 Experimental (a,b,c) and FE (d,e,f) results obtained with 1 ER with the classical control strategy ($f_{ext}^{ES} = f_{ext}^{m}$): (a,d) Transmission Loss, (b,e) Power Reflection coefficient, (c,f) Power Absorption coefficient. 131
6.12 Experimental results obtained with 1 ER with the modified control strategy ($f_{ext}^{ES} = f_{ext}^{m} + f_{ext}^{a}$): (a) Transmission Loss, (b) Power Reflection coefficient, (c) Power Absorption coefficient. 132
6.13 Time plots and corresponding spectrogram with 1 ER in the case of classical ($f_{ext}^{ES} = f_{ext}^{m}$) and modified control strategy ($f_{ext}^{ES} = f_{ext}^{m} + f_{ext}^{a}$) for a 1020 Hz sine excitation: (a) Transmission Loss, (b) Power Reflection coefficient, (c) Power Absorption coefficient. 133
6.14 Experimental results obtained with 7 ERs with the classical control strategy ($f_{ext}^{ES} = f_{ext}^{m}$): (a) Transmission Loss, (b) Power Reflection coefficient, (c) Power Absorption coefficient. 134
6.15 Experimental and FE results obtained with 7 ERs with the modified control strategy ($f_{ext}^{ES} = f_{ext}^{m} + f_{ext}^{a}$): (a) Transmission Loss, (b) Power Reflection coefficient, (c) Power Absorption coefficient. 134
6.16 ES Displacement obtained with Cell 1 for 7 ERs. 135
6.17 Experimental TL obtained with 7 ERs with the classical control strategy ($f_{ext}^{ES} = f_{ext}^{m}$), with the excitation gain being: (a) 2, (b) 3, (c) 4. 135
6.18 The $n-$th cell modeled by an analogous electrical circuit (TLA). 136
6.19 Effective potentials V_{eff} for different restoring forces of the resonator. 140

A.1 Experimental setup 155
A.2 Experimental setup and results for the estimation of the parameters of the loudspeaker's first mode, for the cell used in Chapters 3, 4 and 5. 156
A.3 Experimental setup for estimating the built-in microphones sensitivity of the cell used in Chapter 6.157
A.4 Experimental setup for estimating the Thiele-Small parameters of the loudspeaker used in the Chapter 6. 158
A.5 First set of Open Current (OC) and Proportional Current (PC) measurements for the ERs. 160
A.6 Figures of the sensitivity of the 4 microphones for the 7 ERs with respect to the frequency. . . . 162

B.1 Picture (a) and Scheme (b) of the model for the rigid termination set-up. 163
B.2 Envelop of the pressure inside the tube with a reduced section with a rigid termination. 164
B.3 Variation of the pressure amplitude inside the reduced-section tube with a rigid termination . . . 165
B.4 Variation of the pressure amplitude inside the reduced-section tube as a function of frequency for multiple values of damping c_a with (a) increasing frequency sweep (b) decreasing frequency sweep. 166
B.5 Least mean square indicator of the difference of simulations done with multiple values of c_a . . 166

E.1 Mean value of the envelope of the pressure measured by the nearest microphone of the loudspeaker. 196
E.2 Experimental results obtained with the fully rigid configuration: (a) Transmission Loss, (b) Power Reflection coefficient, (c) Power Absorption coefficient. 196

List of tables

3.1 Thiele-Small parameters of the ER. 39

4.1 Dimensions of the experiment. 65
4.2 The calculated parameters of the model under standard conditions: the static air pressure 1013.25hPa and temperature 20°C. 67
4.3 The measured parameters of the model (mean value of the estimated parameters of the set of measurements) ± the standard deviation of the estimated values of the set of measurements. . . 67
4.4 Parameter values for the cubic hardening restoring force results (f_d being the desired resonance frequency). 69
4.5 Parameter values for the cubic softening restoring force results. 70
4.6 Parameter values for the logarithmic potential restoring force results. 85
4.7 Parameter values of the piece-wise linear restoring force experiment. 91
4.8 Parameter values of the piece-wise linear restoring force experiment. 92

5.1 The measured parameters of the model (mean value of the estimated parameters of the set of measurements) ± the standard deviation of the estimated values of the set of measurements. . . 110

6.1 Dimensions of the experiment 121

A.1 Mean value and standard deviation of the estimated Thiele-Small parameters for each cell. . . . 158
A.2 Estimation of the Thiele-Small parameters for each measurement 159
A.3 Sensitivity parameters of the microphones of the Cells. 161
A.4 Offset parameters of the microphones of the Cells. 161

Chapter 1

Introduction

Context

This Ph.D. thesis has been financed by the French ministry "Ministère de la Transition Ecologique". The thesis has been realized in the Laboratoire de Tribologie et Dynamique des Systèmes (LTDS), on the sites of Ecole Centrale Lyon (ECL) and of Ecole Nationale des Travaux Publics de l'Etat (ENTPE), from October 2022 to December 2025. This granted me the opportunity to work for more than three years under the supervision of Manuel COLLET, Emmanuel GOURDON and Emanuele DE BONO on the exciting topic of acoustic boundary control with the creation of acoustic nonlinear resonators at low excitation amplitudes. The fundamental idea, from Manuel COLLET and Emanuele DE BONO, dates back from 2020, and was first experimentally investigated during my internship in April 2021 at Ecole Centrale de Lyon under the supervision of Manuel COLLET and Emanuele DE BONO.

General Objectives

This thesis aims at developing acoustic nonlinear resonators for noise mitigation at low excitation amplitudes by the means of active control. The multi-physical coupling (vibrations, acoustic and electric via active control), with the investigation of nonlinear dynamics provide a challenging topic. A method for achieving the digital programming of nonlinear behaviors in the linear regime of actuators is here developed. Then, it is extended to enable better controllability of the nonlinear dynamics at stake. The use of the method for synthesizing nonlinear electroacoustic resonators is studied through three experiments and models: one where the electroacoustic resonator is placed in a quasi-open-field environment, another where the electroacoustic resonator is coupled to an acoustic mode of a tube, and finally where a network of electroacoustic resonators is developed. Analytical and numerical tools are used for the prediction, understanding and design of the resonators in different contexts.

Scientific productions

This thesis led to the following scientific productions:

- Journal publications:
  - E. De Bono, M. Morell, M. Collet, E. Gourdon, A. Ture Savadkoohi, M. Ouisse, C.H. Lamarque (2024). **Model-inversion control to enforce tunable duffing-like acoustical response on an**

electroacoustic resonator at low excitation levels. *Journal of Sound and Vibration*, Vol. 570, 118070. DOI: 10.1016/j.jsv.2023.118070

- M. Morell, E.Gourdon, M. Collet, A. Ture Savadkoohi, E. De Bono, C.H. Lamarque (2024). **Towards digitally programmed nonlinear electroacoustic resonators for low amplitude sound pressure levels: modeling and experiments**. *Journal of Sound and Vibration*, Vol. 584, 118437. DOI: 10.1016/j.jsv.2024.118437
- M. Morell, M. Collet, E. Gourdon, A. Ture Savadkoohi, E. De Bono (2025). **Experimental validation of the analytical modelling of a digitally created duffing acoustic nonlinear oscillator at low amplitudes**. *Mechanics&Industry*, **26**,2. DOI: 10.1051/meca/2024036
- M. Morell, A. Labetoulle, E. Gourdon, E. De Bono, M. Collet, A. Ture Savadkoohi (2025). **On the programming of cubic acoustic resonator with periodic time-dependent coefficient**. *Communications in Nonlinear Science and Numerical Simulation*, Vol. 150, 108972. DOI: 10.1016/j.cnsns.2025.108972
- M. Morell, E. De Bono, E. Gourdon, M. Collet, A. Ture Savadkoohi, C.H. Lamarque (2025). **A model-inversion control strategy to attain desired equilibrium points when synthesizing nonlinear resonators**. *In Review*.

- Communications in International Conferences:
  - M. Morell, M. Collet, E. Gourdon, A. Ture Savadkoohi, E. De Bono. **Control of an acoustic mode by a digitally created Nonlinear Electroacoustic Absorbeur at low excitation levels: Analytical and Experimental results**. ID:533. *NODYCON2023, 18 - 22 June 2023, Rome, Italy*.
  - M. Morell, E.Gourdon, M. Collet, A. Ture Savadkoohi, E. De Bono. **Nonlinear Digitally created Electroacoustic Absorber Designed for Acoustic Energy Pumping.** *Forum Acusticum 2023, 11-15 September 2023, Turin, Italy.*
  - M. Morell, M. Collet, E. Gourdon, A. Ture Savadkoohi, E. De Bono. **On the Noise Reduction via a Weakly-Coupled Digitally Programmed Nonlinear Electroacoustic Absorber.** 109669. *SMASIS 2023, 11-13 September 2023, Austin, Texas, United States.*
  - M. Morell, E. Gourdon, M. Collet, A. Ture Savadkoohi. **Control of an acoustic mode by a digitally created Nonlinear Electroacoustic Absorber at low excitation levels: Experimental results.** hal-04165859. *SURVISHNO 2023, 10-13 July 2023, Toulouse, France.*
  - E. Gourdon, M. Morell, E. De Bono, M. Collet, A. Ture Savadkoohi, C.-H. Lamarque. **Digitally programmed nonlinear electroacoustic resonators.** *EUROMECH Colloquium 633, 27-29 May 2024, Lyon, France.*
  - E. De Bono, M. Morell, M. Collet, E. Gourdon, A. Ture Savadkoohi, C.-H. Lamarque. **Toward digitally programmed meta-systems with enforced nonlinear responses: an example in electroacoustics.** *EUROMECH Colloquium 633, 27-29 May 2024, Lyon, France.*
  - M. Morell, M. Collet, E. Gourdon, A. Ture Savadkoohi, E. De Bono. **Towards acoustic piece-wise linear resonators.** ID:236 *ENOC 2024, 22-26 July 2024, Delft, Netherlands.*
  - M. Morell, M. Collet, E. Gourdon, E. De Bono, A. Ture Savadkoohi. **Towards the Programming of Nonlinear Actuators: The Example of the Nonlinear Electroacoustic Resonator.** *SMASIS 2024, 9-11 September 2024, Atlanta, Georgia, United States.*

- M. Morell, E. De Bono, E. Gourdon, M. Collet, A. Ture Savadkoohi, C.H. Lamarque. **Control of a nonlinear electroacoustic resonator: real-time selection of the equilibrium point.** *Forum Acusticum Euronoise 2025, 23-26 June 2025, Málaga, Spain.*
- M. Morell, M. Collet, E. Gourdon, E. De Bono, A. Ture Savadkoohi. **Towards Nonlinear Acoustic Metamaterials for Energy Absorption andEnergy Localization.** *SMASIS 2025, 08-10 September 2025, St. Louis, Missouri, United States.*

Outline of the manuscript

This Ph.D. work starts with a state of the art of methods and devices for acoustic mitigation, along with existing methods for creating nonlinear behaviors in Chapter 2. To develop nonlinear resonators at low excitation amplitudes, the developed method, its mathematical formalization, and its application to an electroacoustic resonator in an quasi-open-field environment are presented in Chapter 3. Chapter 4 features the coupling of the electroacoustic resonator to an acoustic mode of a tube, with the study of the model via analytical and numerical tools. Multiple nonlinear restoring forces are studied to demonstrate the variety of programmable behaviors, and to assess the absorption capabilities of the ER. Chapter 5 extends the control strategy to enable the best possible performances of the nonlinear resonator regardless of initial conditions, validated through numerical studies and the two previous experiments. Finally, Chapter 6 consists in the creation of an array of nonlinear resonators to develop an acoustic metasurface with nonlinear behavior at low excitation amplitudes. Particular behaviors of the metasurface, such as solitary waves, are investigated for future perspectives.

Chapter 2

Vibration and Noise Control

This chapter sets the present work within the broader research context and outlines the fundamental principles underlying the proposed studies. It lies at the intersection of three main domains: nonlinear mechanical vibration control, passive acoustic control, and active impedance control. The proposed literature review tries to present the fundamentals used throughout the manuscript, while representing the scientific and historical reasons that led to this doctoral thesis.

2.1 Context

The environmental noise is defined as "noise emitted from all sources, except industrial workplaces. The EU Directive on the management of environmental noise adds industrial sites as sources of environmental noise" [164]. As the definition of the sources is large, the main ones can be identified as created by road traffic, aircrafts, railroads, constructions, industries, and buildings such as transmitted noise from neighbors or generated from consumer products. For example, busy traffic in a urban environment produces noise from 80 to 90 dB Sound Pressure Level (dB SPL), while an aircraft generates sounds that can grow to above 130 dB SPL near the source.

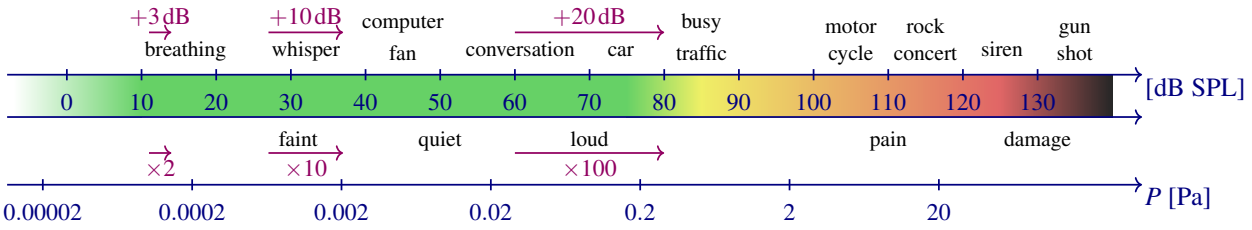

Fig. 2.1 Decibel scale and associated pressure and potential causes. Author: Izaak Neutelings.

The World Health Organization (WHO) aims at quantifying the disability-adjusted life years (DALYs) being the "sum of the potential years of life lost due to premature death and the equivalent years of 'healthy' life lost" [164]. Indeed, the burden caused by the noise can have short and long term implications such as:

- Cardiovascular diseases such as hypertension and ischaemic heart disease [9];
- Sleep disturbance [11];
- Tinnitus [164];
- Hearing and Cognitive impairments [148];

- Annoyance [164].

The WHO identified in its 2011 report that the DALYs lost in the western European countries each year range from 1.0 to 1.6 million. As a result, noise pollution is recognized as a serious public health hazard, leading to the creation of regulations and guidelines [165]. The constraints set by regulations require better sound absorption, specifically at low frequencies where the classical materials are not suitable options.

The propagation of waves through a medium is an issue tackled across many fields of physics and engineering. Noise and vibration are linked, as noise can be emitted by vibrations of a surface, and conversely. As a result, many absorption techniques are inspired from mechanics in the acoustic field, leading to the need to study vibration control in parallel with noise control.

2.2 Vibration control

The field of vibration control has quickly developed since the 1950's, driving numerous innovations. The technological progress is bound by its progress, as in Aeronautics and Aerospace. In this area, two main topics emerge:

- At the material scale: advances often focus on composite structures designed to reduce weight and volume while maintaining reliable performance under extreme conditions. This leads to a strong need to reduce the vibrations of such materials, therefore supporting the development of the vibration control field, from the characterization of the material behaviors to the damping of unwanted oscillations.
- At the structure scale: aircraft and rockets in aeronautics and aerospace lose weight as fuel is consumed and are submitted to large variations of the parameters values such as pressure, temperature or humidity. This causes significant changes in their structural properties, such as resonance frequency or fluid structure interactions. It results in the need for the ability to control the structure vibrations over the entire journey, which requires either wide-bandwidth control strategies or adaptive vibration controllers.

Many techniques exist to dissipate energy from vibrations: by friction, or using visco-elastic materials, or with viscous materials, each offering moderate efficiency at all frequencies. The necessity for high vibration damping of a primary structure can also be realized by creating an anti-resonance at the system's resonance by coupling it with a secondary oscillator. This approach, known as the Tuned Mass Damper (TMD), requires tuning the secondary oscillator to the targeted frequency to achieve effective damping that need the identification of specific modes that can change during the system life.

2.2.1 The Tuned Mass Damper (TMD)

The TMD principle was first introduced by Frahm in [59] and later formalized by Den Hartog [47]. Consider a primary oscillator of mass M connected to the ground by a spring with stiffness k_1, and coupled to a TMD being a secondary oscillator of mass m linearly attached with a spring of stiffness k_2 to the primary oscillator.

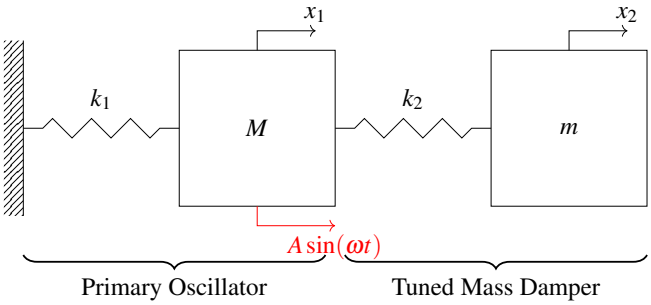

Fig. 2.2 Scheme of a primary oscillator attached to the Tuned Mass Damper.

The equation of motion writes for $t \in [0,T]$, $T > 0$:

$$M\ddot{x}_1(t) + k_1 x_1(t) + k_2(x_1(t) - x_2(t)) = A\sin(\omega t) \tag{2.1a}$$

$$m\ddot{x}_2(t) + k_2(x_2(t) - x_1(t)) = 0 \tag{2.1b}$$

where x_1 and x_2 are the displacements of the masses M and m, A stands for the amplitude of the sinusoidal excitation of the primary oscillator at angular frequency ω. By considering the form of the solutions with $j^2 = -1$ as:

$$x_1(t) = \Im(a_1 \, \mathrm{e}^{j\omega t}), \tag{2.2a}$$

$$x_2(t) = \Im(a_2 \, \mathrm{e}^{j\omega t}), \tag{2.2b}$$

where $\Im$ denotes the imaginary part of a complex number. The substitution into Eqs. 2.1 yields a linear system of a_1 and a_2 that can be solved. It gives the solutions:

$$a_1(\omega) = \frac{A}{M} \frac{1 - \dfrac{\omega^2}{\omega_2^2}}{\left(1 - \dfrac{\omega^2}{\omega_2^2}\right)\left(\omega_1^2 - \omega^2 + \omega_2^2\mu\right) - \omega_2^2\mu} \tag{2.3a}$$

$$a_2(\omega) = \frac{A}{M} \frac{1}{\left(1 - \dfrac{\omega^2}{\omega_2^2}\right)\left(\omega_1^2 - \omega^2 + \omega_2^2\mu\right) - \omega_2^2\mu} \tag{2.3b}$$

with the natural frequencies of both masses $\omega_1^2 = k_1/M$ and $\omega_2^2 = k_2/m$, and where $\mu = m/M$ stands for the mass ratio. Den Hartog noticed that the amplitude of a_1 becomes zero when $1 - \omega^2/\omega_2^2 = 0$. Taking $\omega = \omega_2$ nullifies the amplitude of the primary oscillator, meaning that the secondary oscillator must be excited at resonance to obtain this result. The secondary oscillator response becomes $a_2 = -\dfrac{A}{k_2}$.
When the primary system is excited at its natural frequency ω_1, Den Hartog demonstrated that tuning the resonance frequency of the TMD to the one of the primary oscillator is not optimal. He studied the case of a damped secondary oscillator and proposed approximate formulas for optimal damping and frequency tuning for minimizing the primary oscillator's response while keeping the induced resonances as small as possible. Later, Asami *et al.* derived the exact solution for the equal-peak design [7], pictured in Fig. 2.3a where the primary oscillator's response is compared to the one coupled to a TMD. The two distinct peaks in the TMD case are clearly visible.

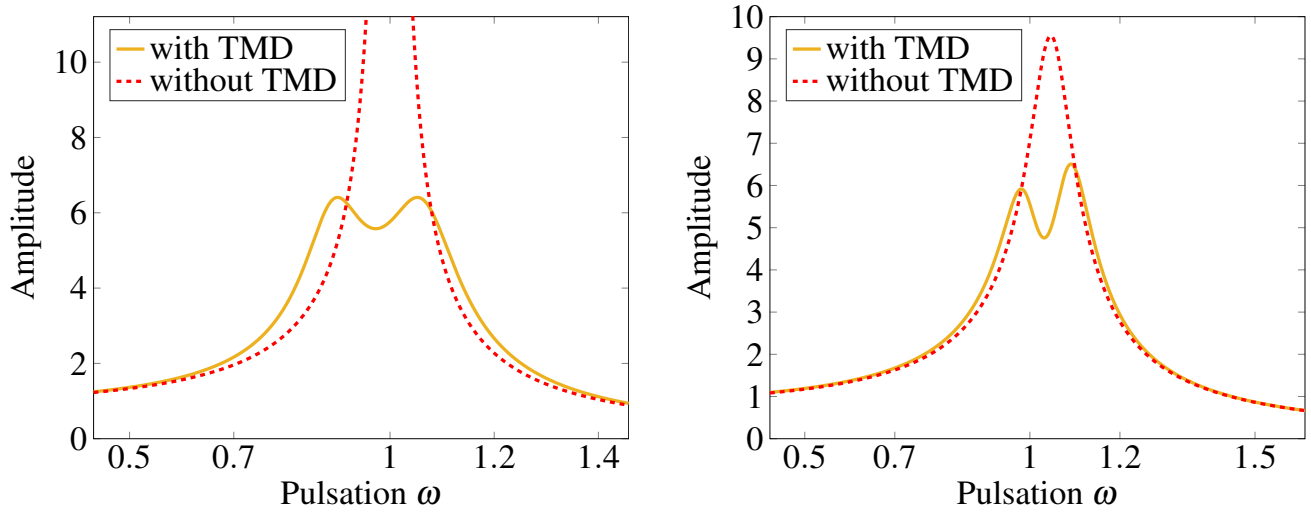

(a) $M = 1$, $k_1 = 1$, $m_2 = 0.05$, $k_2 \approx 0.045$, $c_2 \approx 0.13$

(b) $M = 1$, $c_1 = 0.1$, $k_1 = 1$, $m_2 = 1$, $k_2 \approx 0.96$, $c_2 \approx 0.09$, $\gamma = 0.1$

Fig. 2.3 Frequency Response Function of (a) an optimized TMD with [7]; (b) a weakly coupled TMD.

In case of damped primary oscillator, or more complex structures, a closed-form formula for determining optimal damping and frequency can not be found. In such situations, numerical optimization must be employed [95], such as in the more complex case:

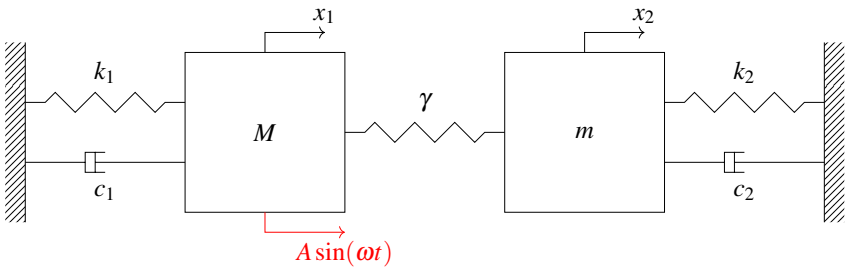

Fig. 2.4 Scheme of a primary oscillator weakly coupled with a grounded Tuned Mass Damper.

where γ is the stiffness of the spring coupling the primary oscillator to the TMD, and c_1, c_2 the damping coefficients of viscous dampers linked to the two masses. Equations of motion writes:

$$M\ddot{x}_1(t) + c_1\dot{x}_1(t) + k_1x_1(t) + \gamma(x_1(t) - x_2(t)) = A\sin(\omega t) \tag{2.4a}$$

$$m\ddot{x}_2(t) + c_2\dot{x}_2(t) + k_2x_2(t) + \gamma(x_2(t) - x_1(t)) = 0 \tag{2.4b}$$

The amplitude can be found easily by solving the linear system:

$$a_1(\omega) = \frac{A\gamma(-m\omega^2 + jc_2\omega + k_2 + \gamma)}{(-m\omega^2 + jc_2\omega + k_2 + \gamma)(-M\omega^2 + jc_1\omega + k_1 + \gamma) - \gamma^2} \tag{2.5a}$$

$$a_2(\omega) = \frac{A\gamma}{(-m\omega^2 + jc_2\omega + k_2 + \gamma)(-M\omega^2 + jc_1\omega + k_1 + \gamma) - \gamma^2} \tag{2.5b}$$

The response of the grounded TMD coupled to the primary oscillator is plotted in Fig. 2.3b. In this configuration, achieving an equal-peak design is more challenging, as no exact closed-form solution exists. Parameters must be numerically optimized regarding the amplitude of the primary mass [95]. However, when the primary oscillator's

properties vary (e.g. aging), the maximum amplitude of the induced resonances can increase, leading to hazardous situations if the excitation frequency approaches those peaks. As a result, TMDs are used in various and numerous contexts, but continuously monitoring the properties of the main system remains important to prevent dangerous situations.

Additionally, the numerical simulation pictured in Fig. 2.5 performed in free regime for a weakly grounded TMD shows that the energy exchange occurs in both directions. This bidirectional energy transfer is due to the tuning of the TMD, whose resonance frequency is close to one of the primary system.

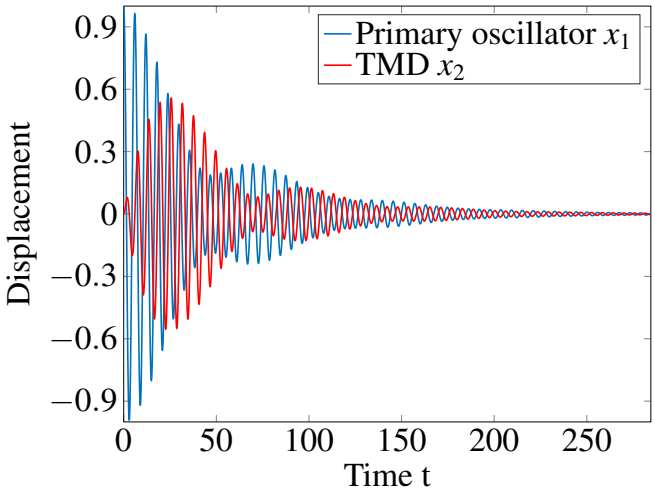

Fig. 2.5 Time histories of a primary oscillator weakly coupled with a grounded Tuned Mass Damper with $M = 1$, $c_1 = 0.1$, $k_1 = 1$, $m_2 = 1$, $k_2 \approx 0.96$, $c_2 \approx 0.09$, $\gamma = 0.1$, $A = 0$ and with initial conditions $x_1(0) = 1$ and $\dot{x}_1(0) = x_2(0) = \dot{x}_2(0) = 0$

2.2.2 Nonlinear resonators

Nonlinearities enable to broaden the efficiency bandwidth without introducing additional resonances at lower and higher frequencies. Moreover, several nonlinear phenomena contribute to a faster transient reduction of energy through a mechanism known as Targeted Energy Transfer (TET) when a pure nonlinearity is considered. These effects come from the energy-frequency dependence inherent to nonlinear systems. As an illustration, consider the classical Duffing equation [89]:

$$m\ddot{x}_2(t) + c_2\dot{x}_2(t) + \beta_2 x_2(t)^3 = 0 \tag{2.6}$$

By solving this equation using the Harmonic Balance Method (HBM), the Frequency Response Curve (FRC) of the Duffing oscillator [118] is plotted in Fig. 2.6 for three values of the parameter β. One can observe that, depending on the value of the parameter β, the FRC exhibits distinct shapes and bends in different directions: 3 stable equilibrium points co-exist for a single frequency. This phenomena is known as folding.

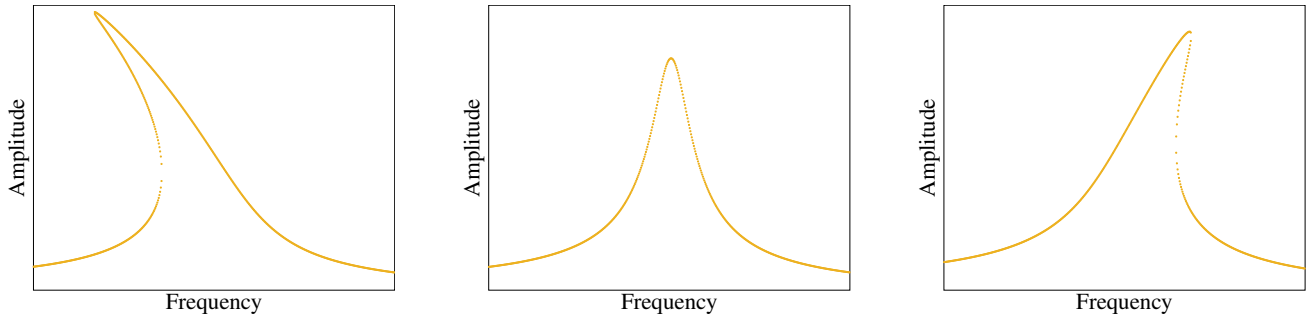

(a) $\beta < 0$ (b) $\beta = 0$ (c) $\beta > 0$

Fig. 2.6 Frequency Response Curves of the Duffing oscillator obtained by HBM.

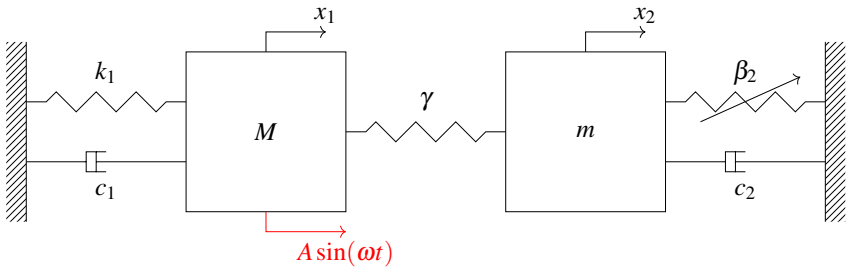

Fig. 2.7 Scheme of a primary oscillator coupled with a NES.

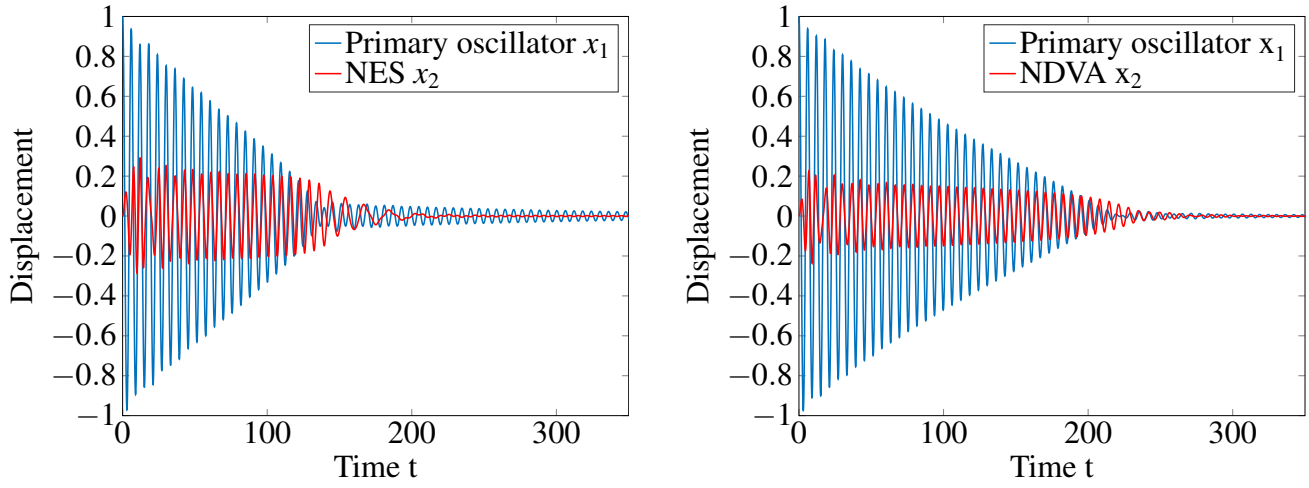

(a) NES (does not feature a linear stiffness: $k_2 = 0$)

(b) Nonlinear Dynamic Vibration Absorber (NDVA) (features a linear stiffness: $k_2 = 0.7$)

Fig. 2.8 Time histories with initial conditions $x_1(0) = 1$ and $\dot{x}_1(0) = x_2(0) = \dot{x}_2(0) = 0$ of a primary oscillator weakly coupled with a grounded (a) NES with $M = 1$, $c_1 = 0.1$, $k_1 = 1$, $m_2 = 1$, $k_2 = 0$, $c_2 \approx 0.09$, $\beta_2 = 30$, $\gamma = 0.1$, $A = 0$; (b) NDVA with $M = 1$, $c_1 = 0.1$, $k_1 = 1$, $m_2 = 1$, $k_2 = 0.7$, $c_2 \approx 0.09$, $\beta_2 = 30$, $\gamma = 0.1$, $A = 0$.

In a coupled configuration, as represented in Fig. 2.7, this nonlinear behavior leads to a modification of the frequency at which the amplitude decreases, significantly reducing the energy transferred back to the primary oscillator, as it can be observed in Fig. 2.8a. For a purely nonlinear added resonator (referred to as Nonlinear Energy Sink (NES) [157]), the energy of the primary oscillator decreases without gaining energy back from the NES, a phenomenon called Targeted Energy Transfer. This mechanism was first explained by Gendelman and Vakakis *et al.* [65, 156]. A few phenomena arising from NESs for vibration control specific to nonlinear dynamics are presented here:

- *Bifurcations* describe qualitative changes in the topology of a dynamical system's behavior as a system parameter crosses a critical threshold. In practice, varying a parameter (the most common are the excitation frequency and amplitude parameters, but it can be any parameter of the system) leads to following a solution branch that cannot be continued analytically. A formal definition, given by [90], can be quoted here: *"The appearance of a topologically nonequivalent phase portrait under variation of parameters is called a bifurcation"*. Bifurcations enable many basic phenomena that can not happen in linear dynamics, such as multiple co-existing stable equilibrium points, sudden transitions from one equilibrium point to another (leading to possible nonlinear hysteresis loops), and chaotic dynamics. These phenomena are often visualized using bifurcation diagrams, which plot the system's fixed points as functions of the varying parameter.

- Nonlinear resonators generally do not require tuning to have a working point for energy mitigation. This advantage comes from the amplitude-frequency dependence of nonlinear systems. While the NESs only feature a pure nonlinear stiffness, Nonlinear Tuned Vibration Absorbers (NLTVA) also contain a linear stiffness. Indeed, as NESs and Nonlinear Tuned Vibration Absorbers (NLTVA) [132] contain a nonlinear stiffness part, the resonator can resonate with a primary oscillator at all frequencies (theoretically), provided that the excitation amplitude is appropriate. The backbone curves of Duffing oscillators in case of a NLTVA, a NES and a Linear oscillator are pictured in Fig.2.9. Notably, while the backbone curve of a NES guarantees an intersection with the linear oscillator's resonance frequency ω_1, the NLTVA curve does not necessarily intersect at this point. However, the NLTVA enables to lower the activation threshold amplitude required to engage the nonlinear resonance.

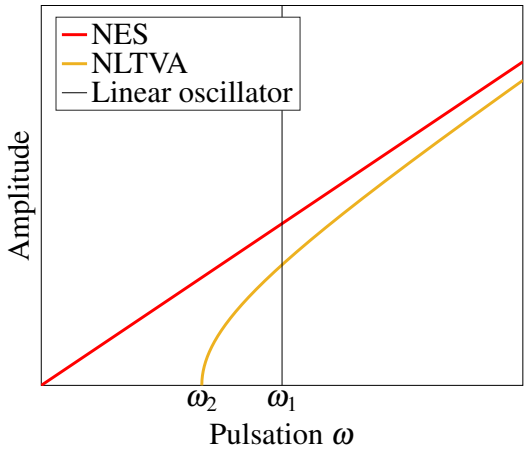

Fig. 2.9 Backbone curves of NES, NLTVA and linear oscillators.

- *Isolated responses branches*, also known as detached resonance curves or isolas, can appear in nonlinear systems, particularly affecting the primary oscillator in coupled setups. These isolated branches represent unwanted responses, as they are disjoint from the main FRC and can lead to unexpected large amplitude oscillations. The isolas can attach to the main branch with growing excitation amplitudes. However, nonlinear damping make possible to prevent the appearance of the detached resonance curve [70]. Figure 2.10 illustrates the amplitude of the primary system N_1 (magnitude of the corresponding complex variable) obtained by solving the 2 degree-of-freedom system using the Multiple Scale Method with the Complex variables of Manevitch (Complexification Averaging), which is a method detailed in Appendix C. It shows the appearance of the isolated response: in Fig. 2.10a for a low excitation amplitude $A = 0.5$ the detached resonance curve does not exist. In Fig. 2.10b with higher excitation amplitude $A = 1$ the detached resonance

curve appears, although it has not yet attached to the main branch. In Fig. 2.10c the excitation amplitude is increased to $A = 1.5$, showing that the isolated response has merged with the main response branch. It can be an issue as the oscillation amplitudes of the primary oscillator usually significantly increase with this phenomenon.

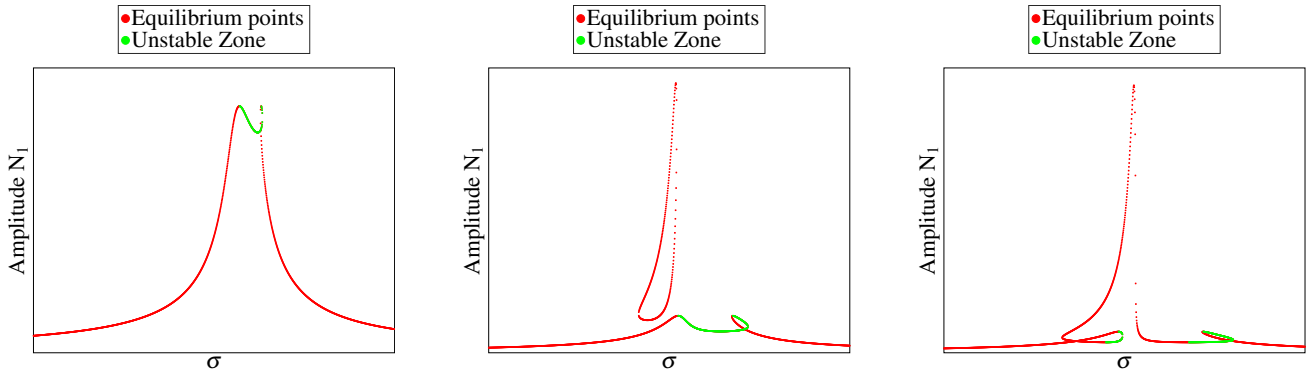

(a) $A = 0.5$ (b) $A = 1$ (c) $A = 1.5$

Fig. 2.10 Frequency Response Curves of the Primary oscillator linked to a NES, obtained by a perturbation method [92], where σ is the detuning parameter corresponding to $\omega/\omega_1 = 1 + \sigma\varepsilon$ with $\varepsilon << 1$.

- *Chaotic behavior* can appear at high amplitudes. Chaotic behavior corresponds to deterministic oscillations that can be significantly modified by extremely small perturbations of the initial conditions. As a result, such systems are difficult to forecast, such as the weather.

2.2.3 Nonlinear resonators for vibration control

The control of vibrations in linear resonators using nonlinear ones was first proposed by Roberson in [136]. This concept involves employing resonators with both linear and nonlinear restoring force components (a linear stiffness part and a nonlinear stiffness part), called the Nonlinear Dynamic Vibration Absorber (NDVA). Figure 2.8b offers a brief comparison with the efficiency of the NES: while the NDVA features a TET phenomenon, it shows a longer transient decrease than the NES (here for non-optimized parameters). The NDVA concept has been extended in numerous contributions (ans is now often referred to as NLTVA), which remains an active area of research [49, 79, 104, 146, 132]. Note that the NES does not contain a linear stiffness, contrary to the NDVA and the NLTVA. The difference between a NDVA and a NLTVA is that the NDVA aims at reducing energy in a linear primary oscillator while the NLTVA aims at reducing energy in a nonlinear one.

These resonators mainly feature cubic nonlinearities, which were the first resonators to have experimentally validated the TET phenomenon [109, 88, 72, 106]. However, other forms of nonlinearities can feature TET, and show excellent potential for mitigating vibrations, such as vibro-impact resonators [157, 71, 64, 119, 120], piece-wise resonators [67, 66, 94, 82, 83, 38], and with non-polynomial nonlinearities [66, 114]. Nonlinear stiffness [62] is the first choice for vibration mitigation, but nonlinear damping gained interest recently [63, 145, 150, 51] due to its benefits in managing isolated branches and extending the dynamic range of NESs [70].

The NES principle has been applied to various vibration sources, ranging from the mitigation of the vibrations induced by aeroelastic coupling of airplane wings [96, 97, 104, 129] and of vibration of cables [162, 163, 98], to reducing structural damages from earthquakes [120, 119, 72]. However, these mechanical devices often increase the overall mass of the system, while being bulky as they require space to oscillate. As a result, an extensive amount of studies emerges on the coupling of piezoelectric patches to the main structures. To enhance

their efficiency, nonlinear electrical shunts are employed for vibration mitigation [5, 4, 44, 142, 141, 143, 132]. Moreover, energy harvesting applications started exploiting TET with piezoelectric nonlinear shunts [55].

2.3 Noise control

Noise mitigation strategies rely upon the absorption or ad-hoc reflection of sound waves. The most traditional approach is the use of absorbing materials. However, their limitations – such as low efficiency at low frequencies or the need for bulky configurations – have motivated a range of innovative research solutions. In this context, various devices have been developed, and a first classification of these noise control devices can be made based upon the need, or not, to provide external (electrical usually) power for their functioning. Hence, we define electro-active noise control systems those who require external electrical power for their functioning. A subset of electro-active noise control systems are the "acoustically active" devices, which radiates acoustical energy in the domain (an acoustic cavity for example) where noise must be mitigated. Classical Active-Noise-Cancellation strategies [103, 75] are conceived as acoustically active systems, as they behave as (secondary) acoustic sources which radiate the so-called anti-noise to destructively interfere with the primary noise. Instead, notice that electro-active noise control strategies include the active control of acoustic impedance [122, 105], where electrical energy is provided to tune the impedance parameters and achieve larger noise absorption performances. Hence, the impedance control strategy is conceived to be acoustically passive. This section presents the main and common approaches in passive and active systems, and does not aim at presenting an exhaustive list of all engineered devices. Particular emphasis is placed on the Impedance Control (IC) principle, which represents a cornerstone of the present work.

2.3.1 Classical systems for noise mitigation

Mechanisms for reducing acoustic levels are various, ranging from destructive interference to energy dissipation through viscous and thermal losses. A classical problem in acoustics is the treatment of a room with uniform walls, first addressed by Morse in [116] through the definition of acoustic impedance. The variety of passive systems for wall treatment is extensive, encompassing materials such as acoustic foams or different kinds of resonators.

The acoustic foam

Acoustic foams are among the most widely used passive noise control materials due to their relatively low cost, ease of integration, and effectiveness at mid-to-high frequencies. They are porous structures that dissipate acoustic energy primarily as heat through viscous friction between the oscillating air particles and the solid skeleton of the foam [86]. Additional attenuation arises from the natural viscous losses of the fluid carrying the wave, combined with the thermal losses due to compression and expansion of the fluid within the pores [33]. The study of these dissipative effects in the 1990's led to the creation of the Johnson-Champoux-Allard (JCA) model from studies made by Johnson *et al.* and Champoux *et al.* [86, 33] which is extremely used but presents limitations at low frequencies. However, it has been demonstrated that the performance of acoustic foams significantly drops below 1 kHz unless excessive thickness is used [45] as shown in Figs. 2.11a and 2.11b. These figures show the absorption coefficient computed under normal incidence for different material thicknesses, for fibrous material in Fig. 2.11a and foam in Fig. 2.11b. Both figures present a better energy absorption at high frequencies, while frequencies under 1 kHz demonstrates the need for high thickness to improve sound absorption. One can observe that even the "infinite" thickness prediction in Fig. 2.11a does not reach an absorption coefficient of 1.

Generally, acoustic foams exhibit high absorption capabilities above 1000 kHz where the incident wavelengths are small enough to enable the interactions in the matrix and pores of the foam. Conversely, lower frequencies corresponding to higher wavelengths do not allow the waves to penetrate inside the acoustic foam matrix, limiting sound absorption. To overcome this, acoustic foams are often combined with resonant inclusions or perforated panels to enhance low-frequency performance.
As a result, a significant amount of research studies the enhancement of the acoustic absorption capabilities of an acoustic material, and preferably bio-based such as vegetal wools (e.g. hemp wool, flax wool) [6, 68, 127, 166], whose micro-structure is depicted in Fig.2.11c.

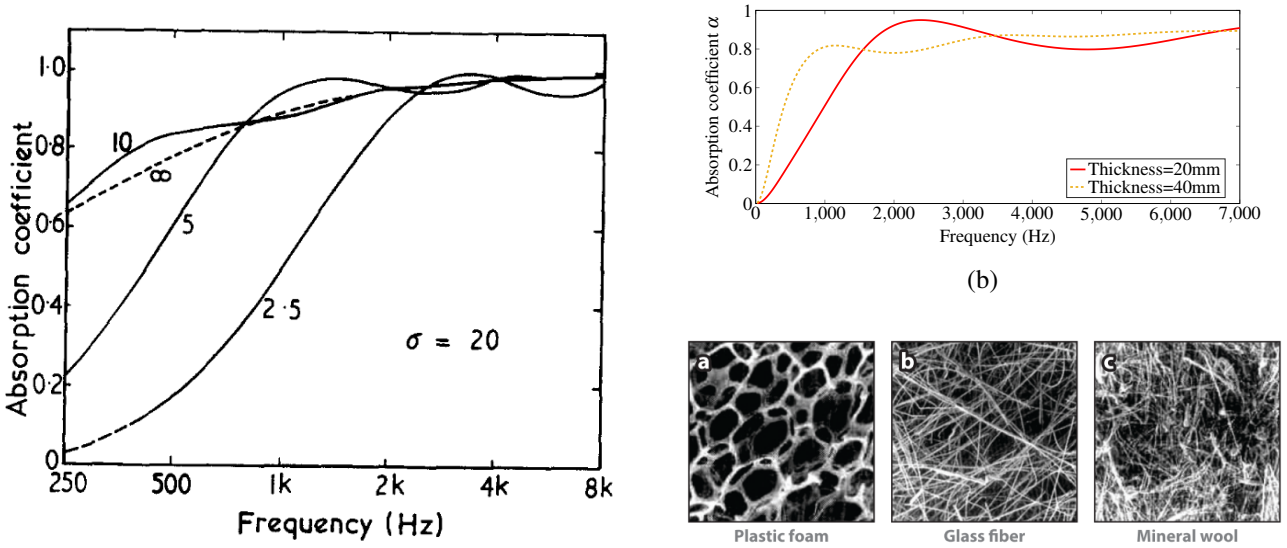

(a) (b) (c)

Fig. 2.11 (a) Absorption coefficient of a fibrous absorbent material with a flow-resistance of 20 CGS units depending of the layer thickness in cm, from [45]; (b) Absorption coefficient of a porous material computed with the JCA model using classical parameters for acoustic foams; (c) Micro-structures of three different materials: acoustic foam (c.a), glass fiber (c.b) and mineral wool (c.c), from [166].

Another approach for dissipating acoustic energy lies on resonators such as the Helmholtz resonator and the quarter-wavelength one. Resonators consist of inclusions of various shapes that primarily use their first resonance for noise mitigation.

The quarter-wavelength resonator

A well-known example is the quarter-wavelength resonator, which consists of a cavity closed at one end and open at the other, with a length equal to one-quarter of the wavelength of the targeted frequency. When an incident wave enters the resonator, it is reflected at the closed end and creates a reflected wave in the resonator that gets out with a 180 degrees phase shift. As a result, the reflected and incident waves are out of phase, creating destructive interference. The eigenfrequencies $f_{QR,k}$ and the corresponding length L_{QR} for the quarter wavelength resonator are easily linked by the following equation [56]:

$$f_{QR,k} = \frac{(2k-1)c}{4L_{QR}}, \tag{2.7}$$

where c is the sound velocity and where $k \in \mathbb{N}^*$ indicates the resonator's eigenmode index. The length of the resonator is selected to target the cancellation of a specific frequency, estimated from Eq. (2.7) with $k = 1$, as maximum efficiency is achieved at the first mode. While the resonator does dissipate a small part of acoustic energy through friction, its primary mechanism is the cancellation of sound by generating an out-of-phase wave. However, targeting low frequency noise mitigation necessitates bulky resonators, which is unreasonable for practical implementations.

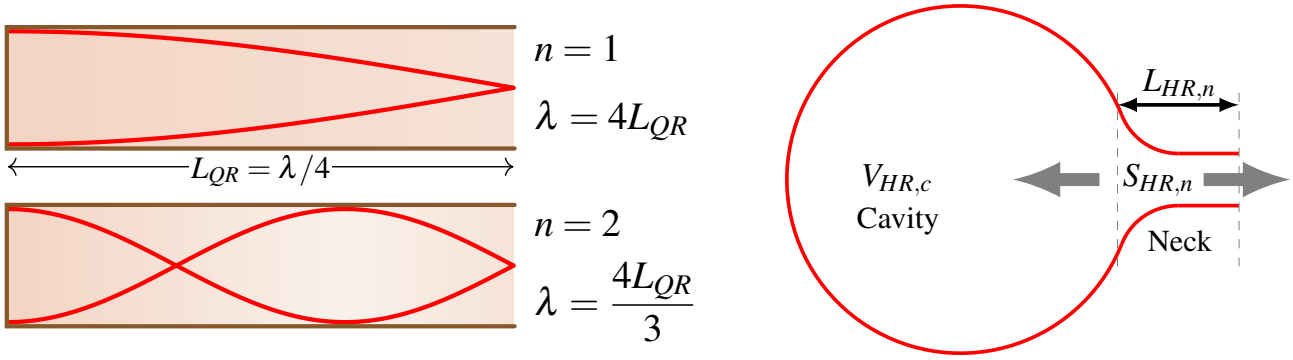

(a) (b)

Fig. 2.12 Schematic of a (a) QR with the two firsts shape modes in terms of pressure; (b) HR.

The Helmholtz resonator

The Helmholtz Resonator (HR) appears to be the most widely used, and extensively studied acoustic resonator. Unlike the quarter-wavelength resonator, its noise-mitigation mechanism relies primarily on viscous and thermal losses. The HR is composed of a cavity and a neck connecting the cavity to the outside. Assuming the operating wavelengths long compared to the dimensions of the HR, and excitation amplitudes low enough to keep the acoustic medium in its linear regime, the HR can be modeled as a single degree-of-freedom system:

- the air in the neck is modeled by a moving mass;
- the air in the cavity is modeled by a spring.

These are standard acoustic modeling approaches, as detailed in [102, 137, 3, 74]. First derived by Hermann von Helmholtz, the frequency of the HR first eigenmode is:

$$f_{HR} = \frac{c}{2\pi}\sqrt{\frac{S_{HR,n}}{V_{HR,c}L_{HR,n}}}, \tag{2.8}$$

where $S_{HR,n}$ and $L_{HR,n}$ stand for the cross section area and length of the neck, respectively. The parameter $V_{HR,c}$ corresponds to the volume of the cavity. The resonator dissipates acoustic energy by converting it into heat through two main mechanisms: viscous friction between the moving air and the HR walls, and heat conduction coming from the heat generated during the compression-expansion cycles of the cavity air. These effects are further enhanced by the resonance that increases both the particle velocity gradients and the particle velocity amplitudes in the cavity and neck. As a result, the HR efficiency is highly efficient, but only a narrow frequency bandwidth centered around its resonance frequency.

Mixed systems for passive sound absorption

Each of the previously presented passive devices offer distinct advantages and limitations. Mixed solutions that embed various passive devices enable the design of efficient solutions for absorbing sound energy over a wide frequency range. While many arrangements of these solutions exist [149, 166], a notable example consists in the creation of an acoustic liner containing a perforated facesheet over Helmholtz and quarter wavelength resonators by Beck *et al.* [14], whose schematic is showed in Fig. 2.13b. This approach resembles the perforated facesheet honeycomb core (represented in Fig. 2.13a) that contains quarter wavelength resonators, therefore with the depth of the device limiting the frequencies of efficiency [139, 138]. Beck's approach [14] enables to couple the cancellation effects of the quarter-wavelength resonator with the dissipating effects of the Helmholtz resonator, while allowing to target lower frequencies with Helmholtz resonators for a given material depth without affecting the efficiency at high frequency.
Furthermore, an extremely common approach consists in creating inclusion in porous materials to increase their low-frequency sound absorption [93, 73], as the panel with inclusions showed in Fig. 2.13c.

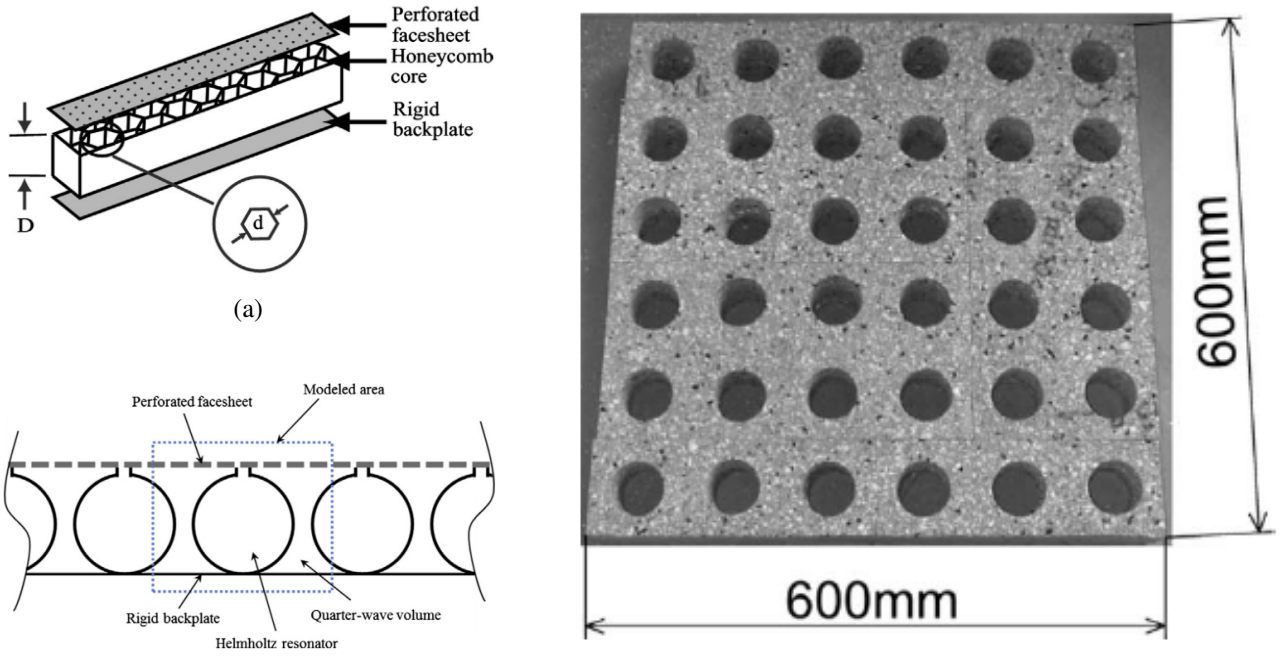

Fig. 2.13 Schematic of (a) a perforate-over-honeycomb-core acoustic liner, from [14], (b) dual-resonance liner design, from [14]. (c) Picture of resonant inclusions in a material, from [73].

Nonlinear regimes for noise mitigation

As discussed in the Vibration Control Section 2.2, nonlinear oscillators enable the exploitation of nonlinear phenomena for enhanced energy dissipation. While nonlinear dynamics have been extensively studied in mechanics, the use of nonlinearity for acoustic absorption started with the pioneering work of Bellet *et al.* in [16, 15]. In [16], a visco-elastic membrane, pictured in Fig. 2.14a, is driven in its nonlinear regime, leading to effective nonlinear behaviors for acoustic energy pumping. The membrane was coupled to an acoustic mode of a tube through a coupling box, featuring phenomena such as TET, quasi-periodic regime and excellent dissipation of the acoustic energy. However, the amplitude threshold to activate nonlinear effects remains extremely high

(above 400 Pa), preventing its use in common applications.

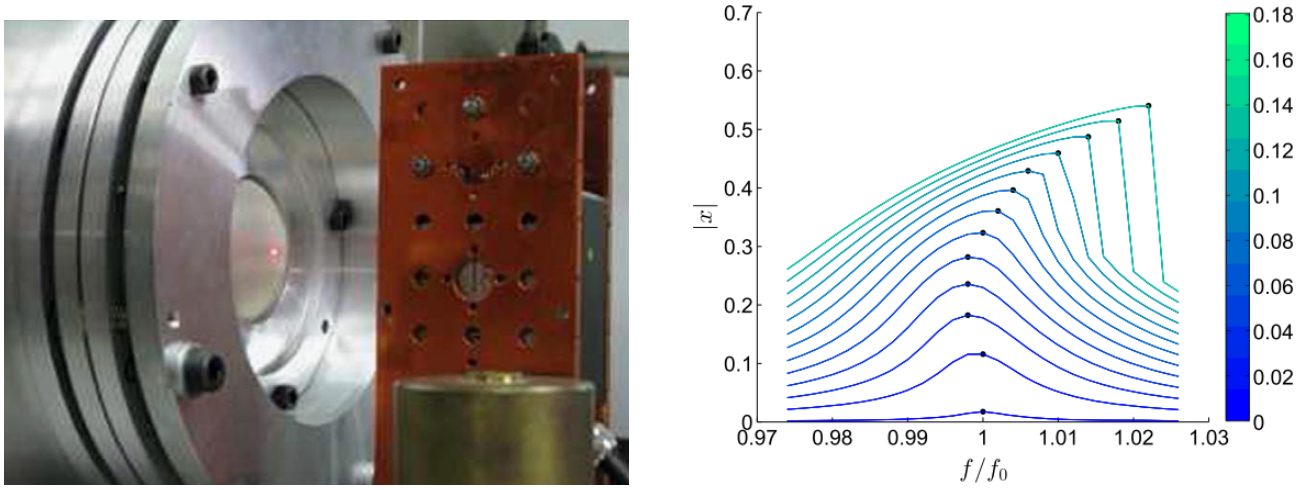

(a) (b)

Fig. 2.14 (a) Picture of the visco-elastic membrane from [16]; (b) Response of nonlinear HR obtained by numerical schemes, from [3].

Building upon this work, Alamo Vargas *et al.* in [3, 158] and Gourdon *et al.* in [74] excited Helmholtz Resonators in their nonlinear regime, effectively creating acoustic nonlinear resonators. The backbone curve obtained by numerical continuation in Fig. 2.14b reveals a hardening behavior of the HR. While the amplitude levels are lowered compared to the ones reported in [16], the acoustic excitation thresholds for nonlinear regimes remains high compared to the acoustic levels of common applications (300 Pa). These devices would be adapted for aeroacoustic applications (e.g. aircraft engines), but are not suited for common applications (e.g. buildings).

To reduce the acoustic excitation level required to trigger nonlinear phenomena, the use of electrically active resonators is presented in the next Section.

2.3.2 Electro-active systems for noise control

Active Noise Control refers to the systems that use external power sources to reduce effectively sound levels. A natural idea when introducing external energy is to modify the conservative properties of a passive system. The most straightforward approach is to adapt resonator parameters such as cavity volume, neck cross-section, or length, thereby creating adaptive resonators. This has been mainly achieved by modifying the volume of the cavity of Helmholtz resonators, hence varying the equivalent stiffness [108, 40, 80], or by modifying the neck length or cross-section, hence varying the equivalent mass [117]. However, these techniques are quite complex, heavy, bulky, and necessitate a high energy consumption.

Differing from the adaptive resonator method, the Active Noise Cancellation (ANC) is the most well-known method to the general public, as it is commonly integrated in headphones, cars, and planes.

From Rayleigh's tuning forks to the Active Impedance Control

The start of Active Noise Cancellation Active noise cancellation technology emerged from the seminal work of Rayleigh's experiment in 1878 involving the superposition of sound fields using two synchronized tuning forks

[130]. The concept of ANC began with the patent of Henri Coanda [75, 34] in 1931. The development of active noise mitigation continued in 1936 with Lueg's patent [103], which proposed an experimental setup, illustrated in Fig. 2.16a, that was insufficient for demonstrating the ANC principle [110]. The Active Noise Cancellation principle relies on the superposition of two identical waves that differ of a 180 degrees phase shift. This phase shift causes destructive interference, effectively canceling the original incident sound wave. To effectively realize ANC, two approaches exist:

- The feedforward approach: a reference microphone measures the pressure of an incident wave and an acoustic source generates an opposite-phase wave in the same direction. As a result, the waves cancel each other after the loudspeaker's position.
- The feedback approach: an error microphone measures the pressure at a position, and an acoustic source generates an opposite-phase wave to cancel the incident waves at the microphone location.

Figure 2.15 illustrates the concept of ANC at a given instant time $t \in [0,T]$ with $T > 0$ inside an infinite tube extending along z-axis. The blue and red curves represent the displacement of air particles for the incident sound wave and for the anti-phase wave, respectively. Both waves propagate in the direction of increasing $z \in]-\infty,+\infty[$, as indicated by the green arrow. Below the curves, a schematic depicts the movement of air particles within the tube. Notice that the locations where the concentration in air particles are the highest and the lowest correspond to the maximum pressure locations (in absolute value). The lowest concentration point in particles for the incident wave aligns with the highest concentration point in particles for the created opposite-phase wave. When these waves interfere, the particle concentration along the z-axis becomes uniform, resulting in destructive interference which prevents the wave from propagating through the medium.

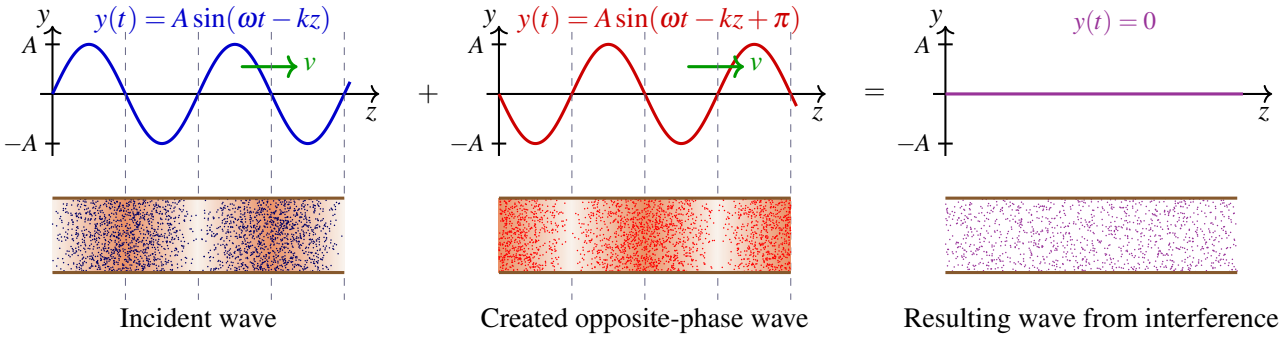

Fig. 2.15 Schematic of the ANC principle with the description of the displacement of air particles.

This phenomenon illustrates that the generated wave with opposite phase must match the incident wave in amplitude and frequency, but be shifted by 180 degrees in phase. Despite the simplicity of this principle, the practical realization of ANC has faced many experimental challenges. Indeed, Lueg [103] proposed to measure the incident pressure inside a duct, and to generate an opposite-phase sound wave using a secondary source placed downstream. The signal coming from the microphone is processed through an electronic device that computes the opposite-phase wave while compensating for the acoustic delay between the microphone and the source for the traveling wave. This configuration is referred to as feed-forward control, as of the microphone is positioned upstream of the loudspeaker relative to the wave propagation direction. However, since the microphone does not measure the resulting cancellation, the quality of ANC cannot be directly assessed.

Active Noise Cancellation, Impedance Control, and their relations A major breakthrough came in the early 1950s with the work of Olson and May [122], who developed the first functioning ANC device. Their approach placed the microphone directly in front of the loudspeaker (Fig. 2.16b), creating a feedback control configuration in which the microphone is used as an error sensor. The idea of the collocation of the actuator (the loudspeaker) and sensor (the microphone) allowed a more robust design, while placing the microphone downstream relative to the wave propagation direction. This configuration enables the measurement of the resulting wave formed by the superposition of the incident and generated opposite-phase waves [122, 121]. Olson and May's experiments demonstrated significant noise reduction performance, hence opening the modern field of ANC.

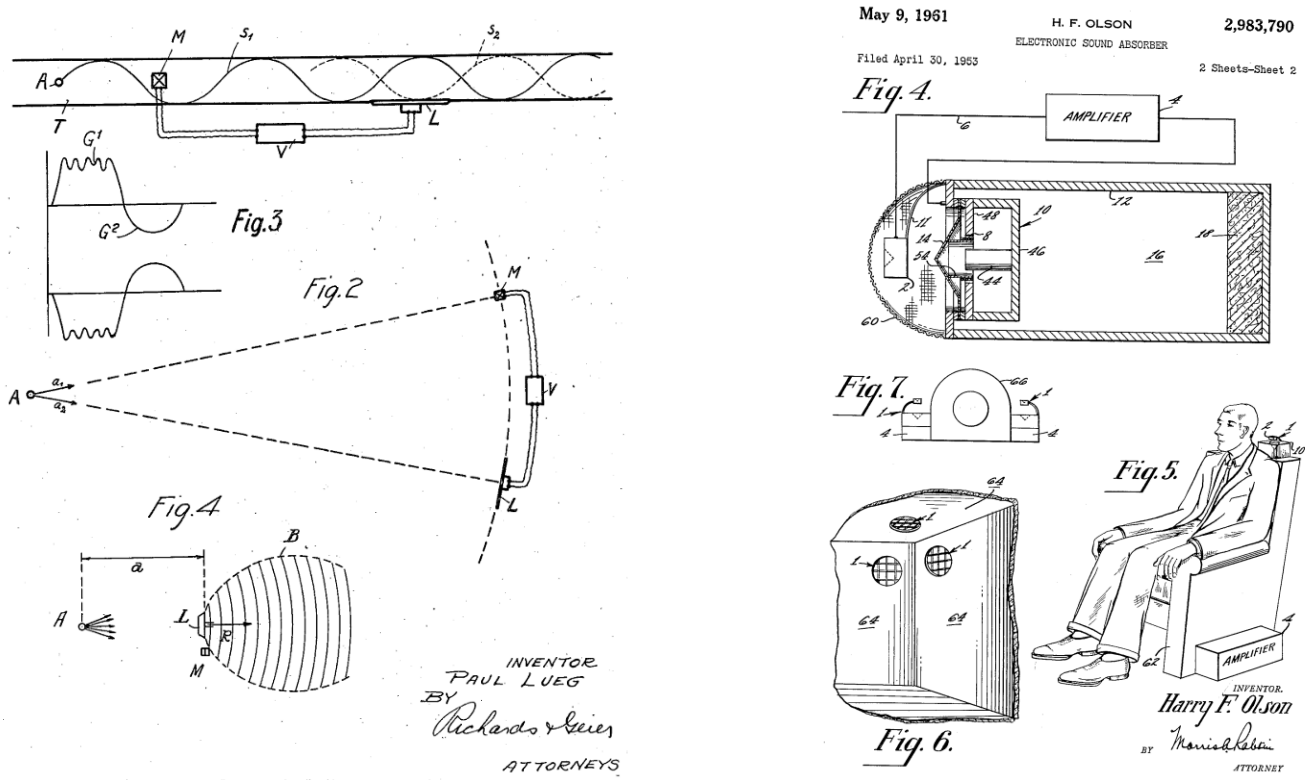

(a) (b)

Fig. 2.16 Patents of (a) Lueg [103] ; (b) Olson [121].

The main difference between Lueg's work and Olson's work lies on the placement of the microphone and the use of its measurement. In Olson's approach, the microphone is collocated with the loudspeaker and used as an error microphone (defining the feedback approach), whereas in Lueg's setup, the microphone serves as a reference one, placed upstream. While Olson and May successfully described and created a "quiet zone" around the error microphone, they also introduced the Impedance Control (IC) principle. They aimed at controlling the overall impedance of a porous layer coupled to the "Electronic Sound Absorber" in order to enhance low-frequency acoustic dissipation. This was achieved by reducing the pressure behind a porous or cloth material [122], thereby increasing the pressure gradient across the porous material, resulting in better performance of the material at lower frequencies.

Following this work, Guicking and Galland further advanced Active IC techniques [77, 76, 60, 153]. Building on Olson and May's concept, a porous plate placed in front of the electroacoustic device is investigated by Guicking *et al.* in [77] and developed an active equivalent of a quarter-wavelength resonator at low frequencies, pictured in Fig. 2.17a. Furthermore, Galland *et al.* in [61] later designed a liner of quarter-wavelength resonators with electroacoustic absorbers, carefully engineered to reduce thickness while increasing efficiency (Fig. 2.17b).

Both Guicking's and Galland's devices aim to reduce the pressure at the error microphone by generating an opposite-phase wave, therefore emulating a quarter-wavelength resonator and simultaneously increasing the efficiency of the porous material, achieving broadband sound reduction.

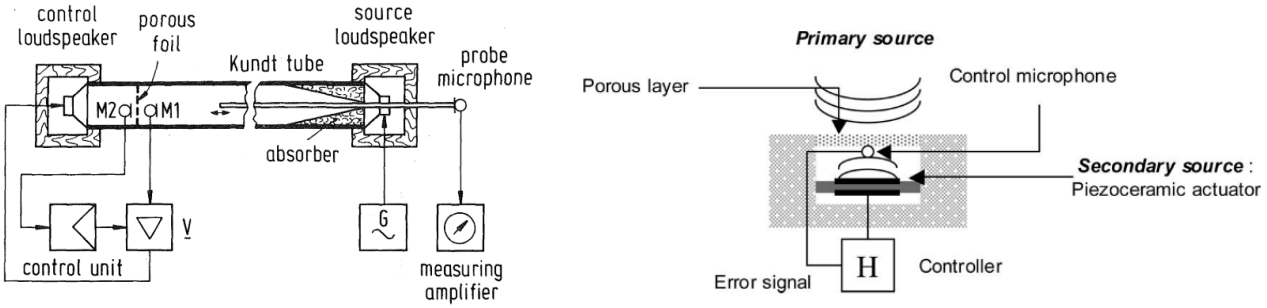

(a) (b)

Fig. 2.17 (a) Scheme of the experimental arrangement of active porous-plate absorbers, from [77] ; (b) Scheme of one cell hybrid absorber, from [61].

Nowadays, ANC technology is widely applied in real-life situations [75]. Despite its success, ANC faces a fundamental limitation: it requires generating an opposite-phase wave with the same amplitude as the incident one, leading to high energy consumption (depending on the incident amplitude: from a few mW (for active noise cancellation headphones) to 10 W and more). In addition, while the ANC concept in one dimension is relatively straightforward to understand and realize, the situation becomes much more complex in three-dimensional environments. In such cases, constructive interference can be formed by the superposition of the opposite-wave phase and the incident one in spatial regions, similarly to the interference patterns seen in the double-slit experiment. As a result, in open environments, the pressure reduction achieved at the microphone location may be accompanied by pressure increases elsewhere. These limitations motivated the exploration of an alternative approach: the Impedance Control (IC), which achieves noise mitigation by targeting the acoustic impedance of a surface rather than by producing additional sound waves. Research into IC began to develop in parallel with further advances in ANC.

Impedance Control It has been previously seen that Impedance Control can be achieved by the production of waves using a secondary source, which enables to drive the pressure to zero in particular points of space. It allows to choose the effective impedance of a porous material. This application shows how Active Noise Cancellation can be used to realize Impedance Control. However, IC can be achieved through multiple types of methods, not limited to the one presented previously. The techniques presented in this section do not rely on a secondary source, but rather on modifying the mechano-acoustical impedance of an acoustic interface, given in this case by the loudspeaker's membrane. This method largely differs from previous ones as it is an entirely acoustically-passive process. To begin with, the IC principle starts from a material point of view. The acoustic impedance of a material defines the interactions of a wave with the medium. The acoustic impedance Z is set as:

$$Z = \frac{p}{v_n} \tag{2.9}$$

with p the pressure, and v_n the normal outwards component of the particles velocity relative to the surface. As a result, Z is expressed in Pa.s.m^{-1}. One can see that the acoustic impedance contains both the force applied on the fluid particles (through the pressure p), and the response to this force through the particles velocity v, resulting in

an extremely practical formulation to describe the pressure needed to move the particles. It is worth noting that the acoustic impedance can only be defined in media where linear approximations hold. In a homogeneous fluid medium, the wave (or characteristic) acoustic impedance of the medium is:

$$Z = \rho c \tag{2.10}$$

with ρ and c standing for, respectively, the density of the fluid medium and the velocity of waves in the medium. However, if the propagation of waves is studied in a finite medium, boundary conditions arise, that can model either solid or fluid media (or hybrid behaviors in case of porous media).
At the interface between two media, a surface impedance can be defined, which characterizes how the surface dissipates, reflects, or transmits the wave's energy. As a result, the entire internal behavior of the solid structure can be ignored (though it may also be studied using continuum mechanics), and the solid structure is effectively studied through its interactions with the fluid medium. Interactions with structural modes will lead to non-local impedance operator connected to the trace of the partial derivative equation governing the mechanical system dynamics.
The surface impedance can be estimated by considering the velocity of the solid interface and the pressure in its immediate vicinity. This estimation relies on the assumption that the fluid particles near the interface follow the same velocity, due to velocity continuity, the fluid particles are "pulled" and "pushed" by the interface.
However, a more complex and accurate approach models the solid structure explicitly, treating the incident pressure as an external excitation force on the structure. In the same way, the acoustic medium receives a response contribution from the solid structure. First suggested by Morse [116], the surface acoustic impedance – commonly a complex variable $Z \in \mathbb{C}$ – depends on the wave frequency, the wave incidence angle with the interface, and the internal behavior of the solid structure.

The principle of Impedance Control lies in targeting the surface impedance to regulate the conditions of transmission, absorption and reflection of the acoustic waves. In practical applications such as ducts, the grazing incidence condition presents additional complexities compared to normal incidence conditions. This grazing incidence problem was first investigated by Cremer in [37] to analytically seek optimal values of the surface impedance, later extended by Tester in [151, 152]. Figure 2.18 depicts the grazing incidence and the normal incidence scenarios along a one-dimensional axis $z \in \mathbb{R}$.

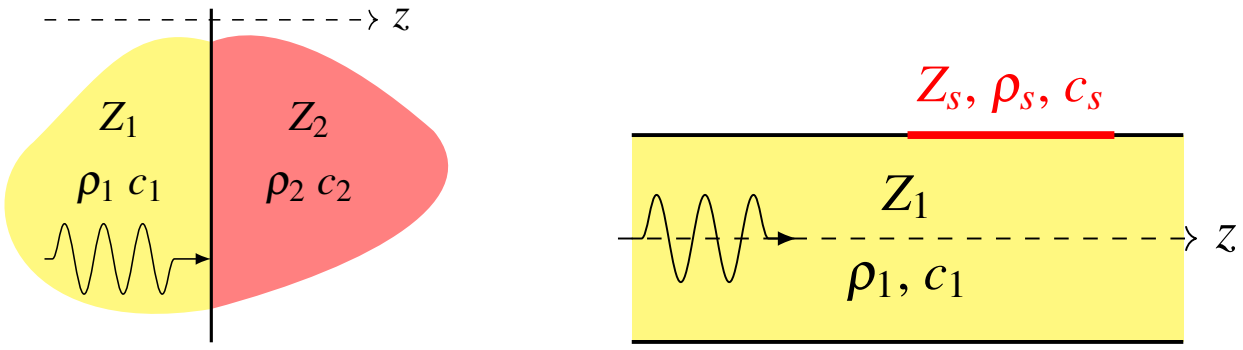

(a) (b)

Fig. 2.18 Scheme of (a) normal incidence conditions ; (b) grazing incidence conditions.

Let us consider a simple case for grasping the principle of IC. For simplicity, consider two media with characteristic acoustic impedances Z_1 and Z_2, each occupying semi-infinite domains unbounded at $z \longrightarrow -\infty$ and $z \longrightarrow \infty$ as pictured in Fig. 2.18a. In this 1 dimensional setting, traveling plane waves can be described in terms of particle velocity v and pressure p as:

- Incident wave:

$$p_i(z,t) = f\left(t - \frac{z}{c_1}\right) \tag{2.11}$$

$$v_i(z,t) = \frac{1}{Z_1} f\left(t - \frac{z}{c_1}\right) \tag{2.12}$$

- Reflected wave:

$$p_r(z,t) = g\left(t + \frac{z}{c_1}\right) \tag{2.13}$$

$$v_r(z,t) = -\frac{1}{Z_1} g\left(t + \frac{z}{c_1}\right) \tag{2.14}$$

- Transmitted wave:

$$p_t(z,t) = h\left(t - \frac{z}{c_2}\right) \tag{2.15}$$

$$v_t(z,t) = \frac{1}{Z_2} h\left(t - \frac{z}{c_2}\right) \tag{2.16}$$

with the subscripts i, r and t refer to respectively the incident, reflected and transmitted subscripts. The functions f, g and h are general solutions of d'Alembert wave equation, while c_1 and c_2 denote the wave speed in each acoustic medium. The continuity conditions at the interface $z = 0$ require that both the particle velocity and the pressure are continuous across the boundary, which can be expressed as:

$$\frac{1}{Z_1}(f(t) - g(t)) = \frac{1}{Z_2} h(t) \tag{2.17a}$$

$$f(t) + g(t) = h(t) \tag{2.17b}$$

By defining the reflection r_v and transmitted t_v coefficient in terms of particles velocity such as:

$$r_v = \frac{\mathbf{v}_r.\mathbf{u}_z}{\mathbf{v}_i.\mathbf{u}_z} = -\frac{v_r}{v_i} = -\frac{p_r}{p_i} \tag{2.18a}$$

$$t_v = \frac{\mathbf{v}_t}{\mathbf{v}_i} = \frac{v_t}{v_i} = \frac{Z_1}{Z_2}\frac{p_t}{p_i} \tag{2.18b}$$

By solving the system of Eq.s 2.17, it gives the following coefficients:

$$r_v = \frac{Z_1 - Z_2}{Z_1 + Z_2} \tag{2.19a}$$

$$t_v = \frac{2Z_2}{Z_1 + Z_2} \tag{2.19b}$$

Multiple cases arise, depending on the difference between Z_1 and Z_2:

- If $Z_1 >> Z_2$, then $r_v = 1$ and $t_v = 0$. The interface behaves like a rigid wall from the perspective of the first medium. In this case, all acoustic energy is reflected back into medium 1, without transmitted energy into medium 2.

- If $Z_2 >> Z_1$, then $r_v = -1$ and $t_v = 2$. A similar reflection-dominated behavior occurs, but with the roles of the media reversed. The interpretation of $t_v = 2$ can be realized by the power balance between incident, reflected and transmitted energies.

These limiting cases correspond to maximal reflection, where the acoustic energy is confined in one medium.

- If $Z_1 = Z_2$, then $r_v = 0$ and $t_v = 1$ (which would give the pressure coefficients $r_p = 0$ and $t_p = 1$). The waves do not interact with the interface and pass without energy loss or reflection. As a result, the acoustic waves do not remain in the first medium, reducing the acoustic energy in this one.

This concept is referred to impedance matching or impedance adaptation, which is a fundamental concept for ensuring maximal transmission across interfaces in electromagnetics such as optical fibers, and plays a major role in electrical wire connections for example. In acoustics, controlling impedance at boundaries enables the selection of the conditions of reflection, transmission, and absorption, forming the basis of the IC principle discussed here. These results highlight the use of impedance matching for acoustic dissipation in enclosed spaces such as rooms. If the surface impedance can match the acoustic impedance of air, incident acoustic waves are not reflected, therefore they are absorbed or transmitted through the surface. If the goal is to increase reverberation time, one could choose to target high reflection coefficients by mismatching the impedances. Therefore, controlling the acoustic impedance of a surface enables the choice of the reflection, absorption (if damping is invloved), and transmission coefficients.

Bardos *et al.* [12] demonstrated that, under certain conditions on the controller, it is possible to achieve exact control of the solutions of the wave equation within a closed domain by placing a controller at its boundary. As a result, to realize efficient IC, the choice of the surface treated by the target impedance remains important.

Two main transducers are used in the literature: the electrodynamic loudspeaker, and the piezoelectric diaphragm [105]. Recently, a new type of electroacoustic absorber has emerged for noise mitigation, based on the ionization of a thin air layer that acts as a actuator [140]. This innovative actuator offers several advantages over conventional transducers. Notably, it is not limited by mechanical resonances or the inertia of diaphragms, enabling high absorption coefficients to be achieved at very low frequencies over a broad frequency range. However, there are practical limitations: the operating amplitudes for sound absorption are lower than those achievable by classical actuators, it requires an O_3 molecules trap as the ionization generates Ozone, and the high voltage involved can create electric arcs. In this literature review, we focus on the electrodynamic loudspeaker as it is extensively used throughout this thesis, but the novelties proposed in this thesis could be applied to any of the above mentioned actuators. As a result, the model of the electrodynamic loudspeaker, and the links to its acoustic impedance is presented.

An electrodynamic loudspeaker is usually composed of a membrane closed at the center with a dust cap. The membrane is suspended to a basket using a spider, and carries a voice coil of length l, as in Fig. 2.19. Under the assumptions that the loudspeaker operates in its linear regime (low excitation amplitudes), and that the loudspeaker's membrane exhibits a locally-reacting behavior (low excitation frequencies), it can be modeled as a mass-spring system of mass M_0 and stiffness K_0. Additionally, a permanent magnet of magnetic field B lies on the non-moving part of the loudspeaker and surrounds the voice coil. When an electrical current i flows in the voice coil, the Lorentz force Bli creates the motion x of the membrane. In addition, the pressure gradient between the front pressure p_f and the back pressure p_b (caused by incident pressure waves for example) creates a force on the

membrane of effective area S_d. To account for energy dissipation, a general viscous damping R_0 can be used to model multi-physical damping mechanisms.

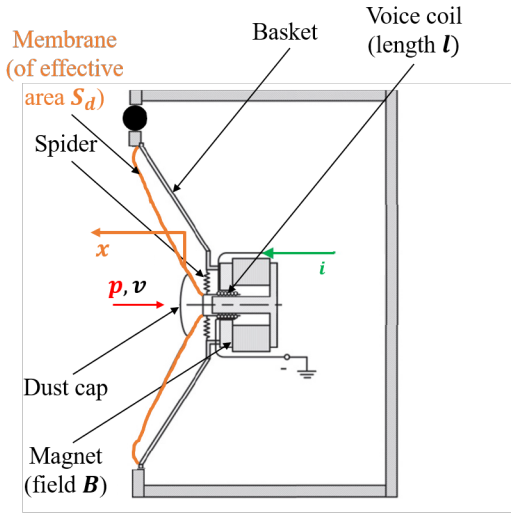

Fig. 2.19 Scheme of a loudspeaker with a back-cavity, from [41].

The equation of motion (detailed in many articles, and in the extensive review from Mallejac *et al.* [105]) of the membrane writes for $t \in [0,T]$, $T > 0$:

$$M_0\ddot{x}(t) + R_0\dot{x}(t) + K_0x(t) = S_d(p_f(t) - p_b(t)) - Bli(t) \tag{2.20}$$

Two types of loudspeaker are mainly used: with and without a back-cavity. With the same calculations as in Chapter 4, the pressure inside the back-cavity can be calculated as being proportional to the volume variations of the back-cavity at low frequencies (induced by the motion of the membrane). As a result, the pressure in the back-cavity p_b is expressed as:

$$p_b(t) = \frac{\rho c^2}{V_c} S_d x(t) \tag{2.21}$$

with V_c the volume of the back-cavity when the membrane rests $x = 0$, and ρ and c being the density and velocity of waves in the fluid. It enables to substitute in the loudspeaker's equation of motion:

$$M_0\ddot{x}(t) + R_0\dot{x}(t) + x(t)\left(K_0 + \frac{\rho c^2 S_d^2}{V_c}\right) = S_d p_f(t) - Bli(t) \tag{2.22}$$

Observe that it provides an additional stiffness to the loudspeaker's behavior. An equivalent stiffness $\tilde{K}_0 = K_0 + \frac{\rho c^2 S_d^2}{V_c}$ can be defined so that:

$$M_0\ddot{x}(t) + R_0\dot{x}(t) + \tilde{K}_0x(t) = S_d p_f(t) - Bli(t) \tag{2.23}$$

In case of an open loudspeaker (without a back-cavity), the expression is similar, as the pressure gradient comes from incident pressure waves (considering no mean flow and a homogeneous mean pressure). For simplicity, the equivalent stiffness $\tilde{K}_0$ is noted K_0 throughout the manuscript. From this equation, the impedance Z of the closed-box loudspeaker without applied current $i = 0$ can be derived by applying a Laplace transform:

$$Z_{a0}(s) = \frac{\tilde{p}_f(s)}{\tilde{v}(s)} = \frac{M_0}{S_d}s + \frac{R_0}{S_d} + \frac{K_0}{S_d}\frac{1}{s} \tag{2.24}$$

where $\tilde{\bullet}$ denotes the Laplace transform of variable $\bullet$, $s \in \mathbb{C}$ stands for the Laplace variable, and v represents the velocity of the membrane $\dot{x}$.
In the context of loudspeakers, IC involves modifying this impedance through the electrical current i from the Lorentz force Bli. For electrical shunting and control purposes, most studies in the literature require identifying the electrical impedance of the circuit (inductance and resistance of the coil), due to the applied voltage to the speaker terminals being the control variable. This step is not mandatory if a Howland current pump [126] is placed at the speaker terminals, enabling to pilot the electrical current, which acts directly in the mechanical dynamics of the loudspeaker (Eq. (2.23)).

The most straightforward method of controlling a loudspeaker's impedance is to measure both the membrane velocity and the nearby acoustic pressure. This combination of measurements forms the basis of 'Direct Impedance Control' (DIC), which will be detailed in the following. Alternative techniques for impedance control that do not require direct velocity measurement will be discussed later in the section.

With the measurements of pressure and velocity via external sensors
The measure of both the pressure and velocity to control the impedance of a loudspeaker is known as 'Direct Impedance Control' (DIC). In this approach, the pressure is retrieved through the use of a microphone, while velocity can be obtained using multiple different methods, detailed below. The impedance is targeted using a feedback control method that compares the measured apparent impedance with the targeted one, implemented through the control of the membrane's velocity.
Guicking *et al.* [76] and Orduna-Bustamante *et al.* [123] created the DIC strategy by measuring the impedance with the two microphones method in a cylindrical Kundt's tube, therefore showing the possibility of choosing the termination impedance, i.e. the reflection coefficient at normal incidence that can be chosen between 0 and 1.5 [76]. To enable to the practical use of the device, both studies from Thenail *et al.* [153] and Furstoss *et al.* [60] used an accelerometer to retrieve the membrane's velocity, as represented in Fig. 2.20a. Thenail [153] experimentally showed again with this method that the optimized impedance for acoustic absorption in air under normal incidence conditions is $Z = \rho_0 c_0$ with ρ_0 and c_0 being respectively the density of air and velocity of sound waves in air. Furstoss [60] extended the method to oblique incidence and recreated a quarter-wavelength resonator, following earlier approaches.
Other techniques to realize Direct Impedance Control by measuring the membrane's velocity are accounted:

- with a vibrometer [100] whose experimental set-up is pictured in Fig. 2.20c,
- with a second coil to measure the induced voltage that is proportional to the membrane's velocity [57, 133] depicted in Fig. 2.20d,
- with an additional microphone placed inside the loudspeaker's back cavity [159, 78], as shown in Fig. 2.20b.The measurement of the pressure inside the loudspeaker's back-cavity enables to approximately estimate the displacement of the membrane thanks to the added stiffness of the trapped air.

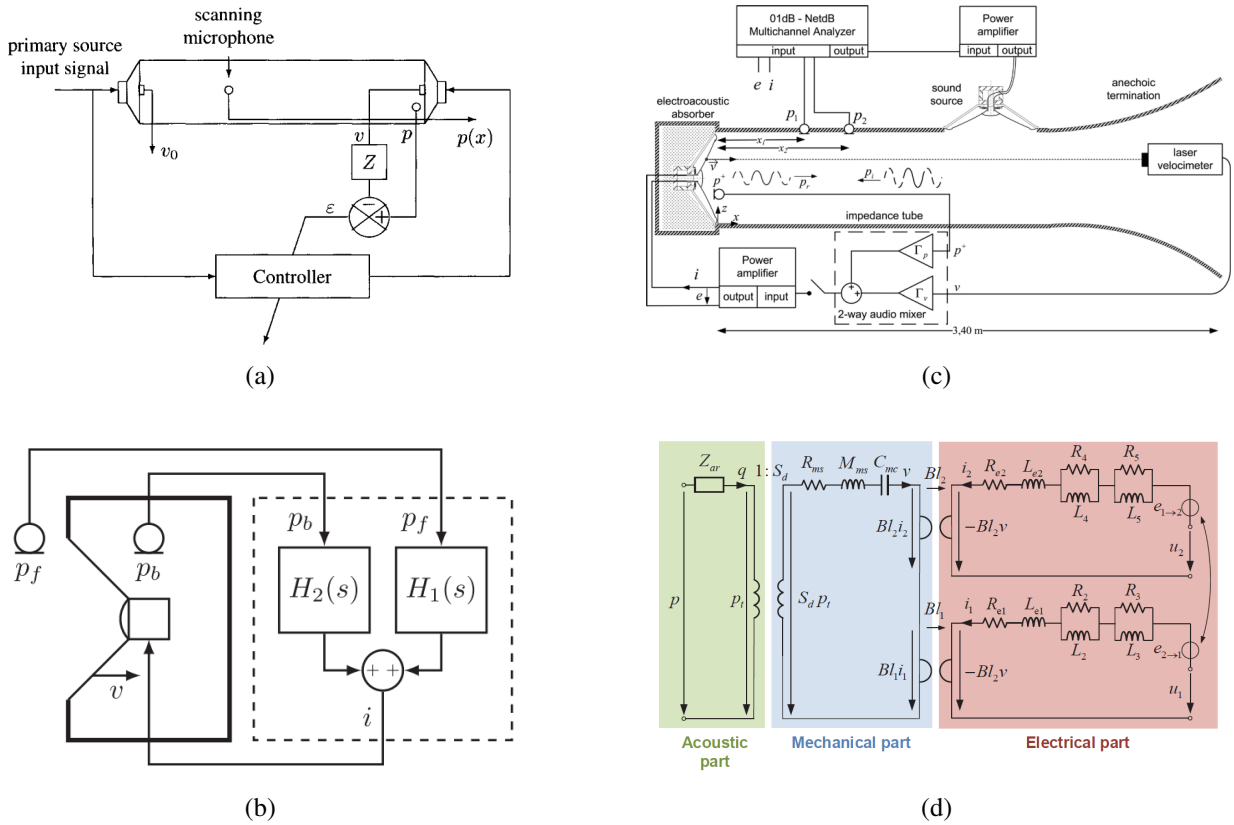

Fig. 2.20 (a) Scheme of the experimental set-up featuring an accelerometer for velocity sensing, from [153]; (b) Scheme of the experimental set-up featuring amicrophone in the loudspeaker's back-cavity for velocity sensing, from [159]; (c) Scheme of the experimental set-up featuring a vibrometer for velocity sensing, from [100]; (d) Model of the dual coil electrodynamic loudspeaker, from [133].

The type of measurement – impedance measurement or velocity measurement – implies different control strategies – proportional impedance control or velocity feedback control – that present their own downsides and limitations. The main drawback of both methods comes from the velocity sensors that are bulky and are not suited for practical implementations. In an attempt to simplify and develop light, thin and adaptive devices for sound absorption, sensorless control methods has been developed through self-sensing strategies and electrical shunt configurations.

Sensorless devices

For creating sensorless electroacoustic absorbers, two main practices can be distinguished: the electrical shunt (usually passive) and the digitally controlled shunts (electro-active). Both techniques estimate the acoustic pressure from the electrical current induced in the loudspeaker's coil. In a passive shunt, this current is processed by an electrical network designed to yield the desired dynamic response and, therefore, the target acoustic impedance. In an electro-active shunt, a digital controller emulates the electrical behavior of the passive circuit, allowing greater adaptability.

Fleming *et al.* [58] realized the control of sound fields by the shunting of a loudspeaker using both methods: active and passive shunting. Fleming simulated the response of a Helmholtz resonator, while maintaining the optimal performance even with variations in the acoustic response of the environment, which is a benefit of the active shunt outlined by Fleming. A key benefit of the shunt approach is that the acoustical passivity of the loudspeaker remains assured. In 2011, Lissek *et al.* [100] demonstrated the equivalence between DIC (feedback-based acoustic impedance control) and electrical shunting by proposing a common framework, unifying them under the

concept of the "Electroacoustic Absorber" (EA). They outlined that active controls can experience instability through the feedback gains depending on the components of the loudspeaker, particularly the electric inductance. To address this limitation, the use of a Howland current pump, first introduced by Rivet *et al.* in 2016 [134], allows direct control of the coil current and voltage. This configuration solves the stability issues encountered with the electrical components of the loudspeaker. Consequently, Boulandet *et al.* [30] also incorporated a Howland current pump [126], applying the electrical current equal to the voltage command to the loudspeaker's coil and conversely. This configuration makes it straightforward to synthesize an electrical shunt digitally, with the controller's filter directly perceived as an electrical impedance by the loudspeaker. Experimental results showed good sound level reduction at low frequencies, in a narrow frequency band around resonance (20 dB ref 1 Pa V^{-1} at the resonance frequency). To broaden this effective bandwidth, Bitar *et al.* [20, 19] proposed a nonlinear analog electrical shunt, supported by analytical and numerical studies, though experimental implementation proved to be challenging.

A drawback of passive shunting remains its limited adaptability: once built, the impedance cannot easily be modified, and precise tuning is further complicated by impedance mismatch, which is aggravated by the presence of a strong feedthrough term that masks the effective electromechanical coupling.

With the measurement of the pressure nearby the membrane via an external sensor

A more recent approach focuses on controlling the loudspeaker impedance by measuring only the acoustic pressure in the vicinity of the membrane, without the knowledge of the membrane's velocity, displacement or acceleration. Early work from Collet *et al.* used this method for implementing the Advection Boundary Law (ABL) in distributed systems [36, 39]. Later works leveraged the Howland current pump [126] that enables the control to be made via the electrical current sent into the voice coil, initiated by Rivet *et al.* in [134] (from the same team as Boulandet [30], exploring both sensorless and sensor-based configurations). The experimental set-up from Rivet *et al.* [134] is represented in Fig. 2.21 with the Howland current pump (the experimental set-up of [30] uses a shunting technique instead of the microphone). The electrical impedance no longer needs to be identified, simplifying the control strategy. It consists in a single measure of pressure in front of the loudspeaker's membrane coupled to a feed-forward controller that computes the electrical current to send to the loudspeaker.

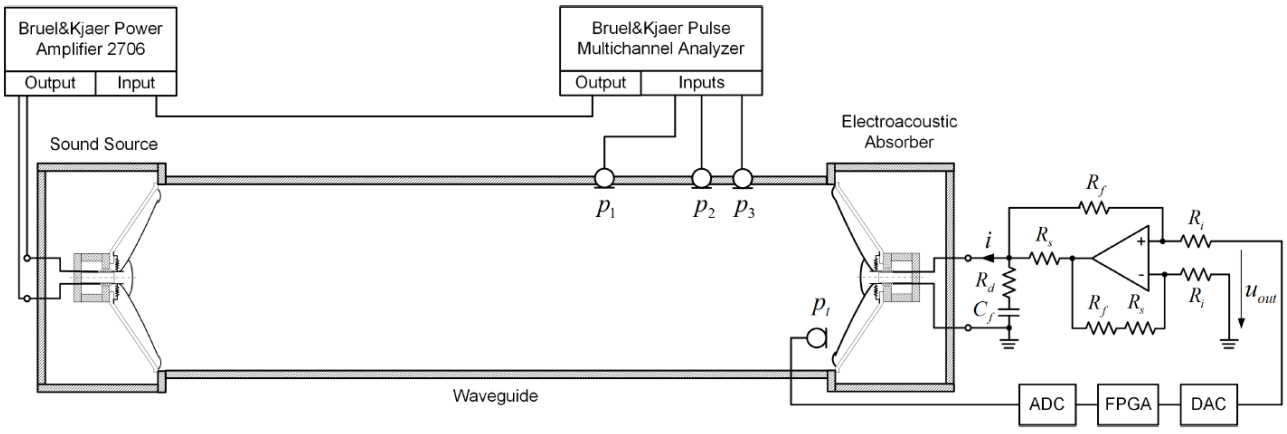

Fig. 2.21 Scheme of the experimental setup with the Howland current pump enabling a electrical current driven control, from [134].

The control strategy implemented in these articles can be found by model-inversion. To build a feed-forward controller, the desired setpoint and the plant model must be known. The loudspeaker is modeled by its acoustic impedance Z_{a0} in the absence of an applied electrical current. Applying the Laplace transform, the equation of

motion in the presence of an electrical current i can be expressed as:

$$Z_{a0}(s)\tilde{v}(s) = \tilde{p}_f(s) - \frac{Bl}{S_d}\tilde{i}(s) \tag{2.25}$$

Let us define a targeted acoustic impedance with targeted mass M_t, damping R_t and stiffness K_t, with the desired displacement, speed and acceleration x_t, $\dot{x}_t$ and $\ddot{x}_t$:

$$Z_{at} = \frac{\tilde{p}_f(s)}{\tilde{v}_t(s)} = \frac{M_t}{S_d}s + \frac{R_t}{S_d} + \frac{K_t}{S_d}\frac{1}{s} \tag{2.26}$$

where $\tilde{v}_t$ is the Laplace transform of the targeted membrane velocity $\dot{x}_t$. To determine the expression of the electrical current to send into the loudspeaker's coil to enforce a target velocity, displacement and acceleration, let us impose that the actual velocity is the targeted one $\tilde{v} = \tilde{v}_t$ in Eq. 2.25:

$$Z_{a0}(s)\tilde{v}_t(s) = \tilde{p}_f(s) - \frac{Bl}{S_d}\tilde{i}(s) \tag{2.27}$$

Which yields after some manipulations:

$$\tilde{i}(s) = \tilde{p}_f(s)\frac{S_d}{Bl}\left(1 - \frac{Z_{a0}(s)}{Z_{at}(s)}\right) \tag{2.28}$$

It results in the following transfer function:

$$H(s) = \frac{\tilde{i}(s)}{\tilde{p}_f(s)} = \frac{S_d}{Bl}\left(1 - \frac{Z_{a0}(s)}{Z_{at}(s)}\right) \tag{2.29}$$

The electrical current to send into the loudspeaker's coil to enforce a targeted acoustic impedance by controlling the velocity can be calculated via Eq. 2.28. As a result, the controller modifies the membrane velocity to attain the targeted impedance, relying solely on the measured pressure. This feed-forward control strategy, referred to as a pressure-based current-driven control, is currently at the core of numerous recent studies [18, 26, 28, 27, 29], due to its straightforward implementation and robustness.

The control strategy has demonstrated great potential for room modal modal equalization [135] and has been explored in ducts under grazing incidence by Boulandet *et al.* in [29]. More recently, a liner of programmable feed-forward Electroacoustic Absorbers has been assessed in a turbofan under high excitation levels by De Bono *et al.* in [28].

The presented control strategy also enables breaking acoustic reciprocity, allowing identical waves to propagate differently in ducts depending on their propagation direction by implementing the Advection Boundary Law (ABL) [87, 26, 27]. Figure 2.22 illustrates excellent results where acoustic energy is transmitted over a wide frequency band in the backward direction while being blocked in the forward direction. It is worth noting that the ABL has been first introduced by Collet *et al.* for active acoustic impedance control in [36].

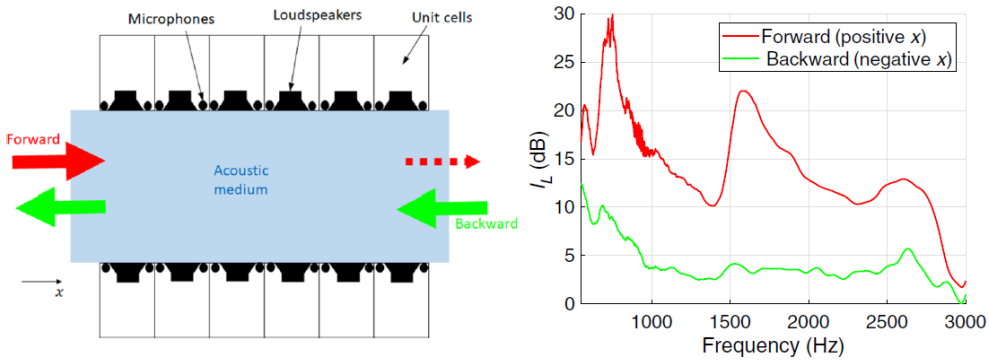

Fig. 2.22 Scheme of the waveguide, and Insertion Loss (I_L) measurements relative to incident waves directions, from [87].

However, the presented method is limited by stability issues coming from uncertainties in the characterization of the loudspeaker's dynamics, in addition to the digital delays [42] that limits the working frequency range. To address these challenges, Volery *et al.* [159] proposed a mixed feedforward-feedback control architecture, improving the robustness of such control strategy, but at the cost of increased complexity, requiring more precise tuning and higher computational resources.

This control strategy still requires improvements to broaden its effective bandwidth, and would benefit from incorporating nonlinear behavior to enhance sound absorption across a wider frequency bandwidth. Moreover, nonlinear dynamics enable faster transient decrease rate, and phenomena such as bifurcations, quasi-periodic behavior, and Targeted Energy Transfer that are useful for noise mitigation, as seen previously. However, conventional transfer function approaches and the Infinite Impulse Response implementations struggle to enforce nonlinear control laws due to folding singularities. To overcome this, Guo *et al.* in [78] successfully developed a nonlinear resonator operating at moderate and low excitation amplitudes by adding a nonlinear contribution to the above pressure-based current-driven control strategy $i = i_L + i_{NL}$. The calculation of the added nonlinear electrical current requires the addition of a microphone in the back-cavity of the loudspeaker (similarly to the proposition of [159]), which estimates the membrane's displacement (using Eq. 2.21) and adds an electrical current proportional to the cube of the membrane's displacement. The results show the enlargement of the efficiency bandwidth of the resonance. However, this approach only generates polynomial nonlinearities and presents challenges in controllability since the nonlinearity depends on the membrane's velocity, which itself is regulated by the underlying linear control law, limiting flexibility in driving the nonlinear response. Following this work, an acoustic metacrystal has been developed with electroacoustic absorbers to create an active acoustic Su-Schrieffer-Heeger-like metamaerial [125].

As a result, De Bono *et al.* [43] proposed a nonlinear electroacoustic resonator at low excitation amplitudes based on a real-time approach. This innovative method is introduced, extended, and thoroughly analyzed in this work (Chapters 3, 4, 5 and 6). Although parameter optimization has been developed [115], it is not detailed here, but the corresponding journal article is provided in Appendix D. Further advancements of the method have been carried out to enhance the performance of the nonlinear resonator, including the realization of a liner composed of nonlinear electroacoustic resonators.

The state of the art of Noise Control is illustrated in Fig. 2.23.

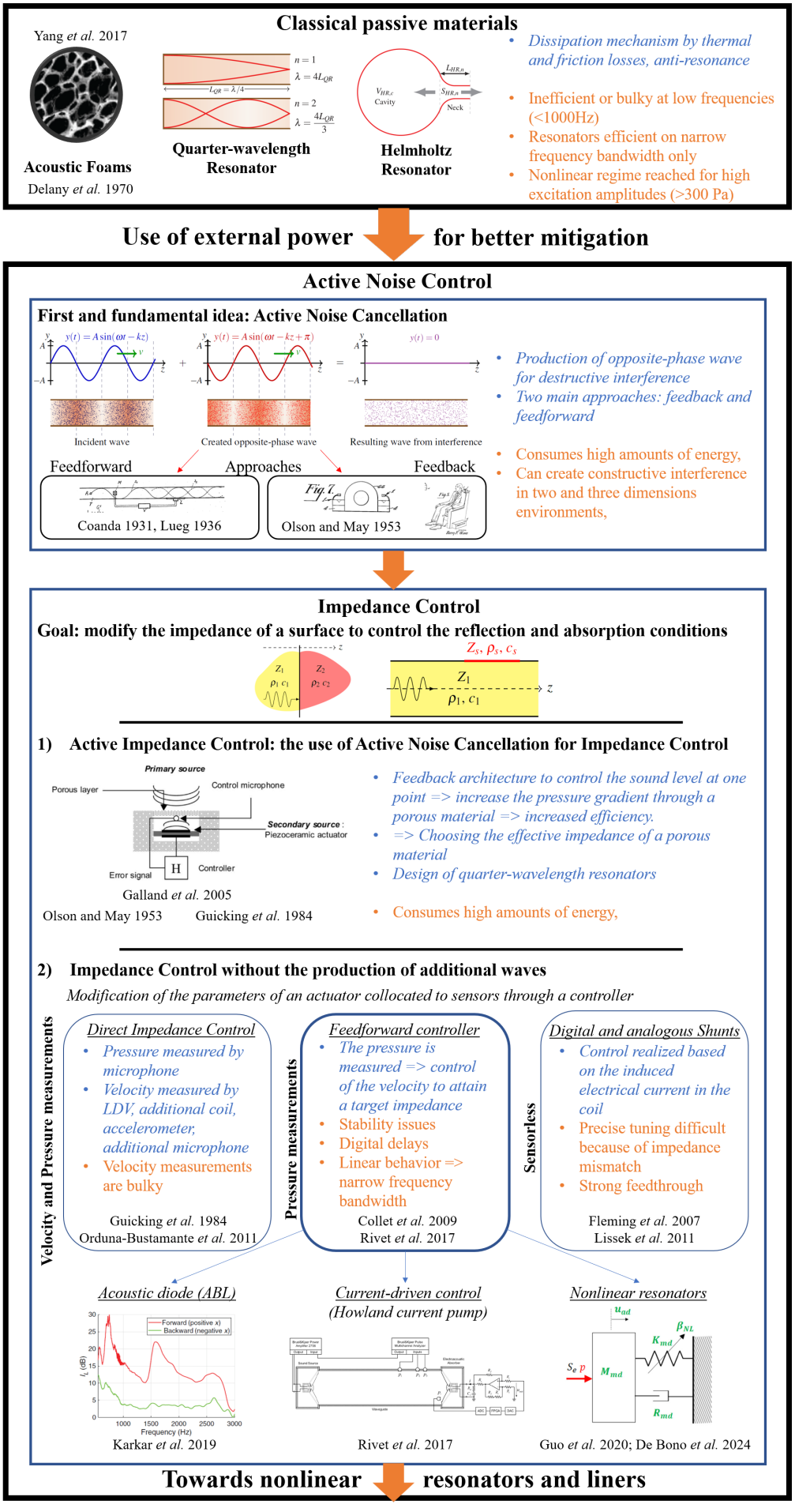

Fig. 2.23 Illustration of the state of the art of Active Noise Control

2.4 Problem

The presented literature highlights the stakes for improving noise control, and the importance of drawing inspiration from the field of mechanical vibration control field. The mechanical vibration mitigation field highlights key points for the use of external devices:

- The mitigation of vibrations meets the need for great adaptability to extreme variations of parameters.
- Linear resonators do not provide the needed adaptability.
- Consequently, nonlinear resonators have been developed to benefit from their phenomena such as bifurcations, fast transient energy decrease, self-tuning, or large frequency bandwidth of efficiency. However, they present behaviors that can be undesirable (even if some of the unwanted effects are currently under study for improving the vibration mitigation capabilities), such as detached resonance curves, energy scattering, chaotic behaviors, or the folding phenomena that creates a dependence of the mitigation to initial conditions.

The key points of the literature are summarized in the following:

- Noise Control is one of the main issues to be tackled.
- Passive noise control systems show limitations for acoustic mitigation at low frequencies by being inefficient, bulky, or efficient in narrow bandwidths. Moreover, these materials do not offer adaptable behaviors depending on the situation.
- To overcome this, passive nonlinear noise control resonators have been studied, with the goal of benefiting from the adaptability and extended bandwidth offered by nonlinear phenomena. However, the amplitude threshold for activating this regime is high, making its real-life applications difficult.
- The Active Noise Cancellation device offers an extreme adaptability, but features high energy consumption while being efficient only in small spatial zones due to its acoustically active nature.
- To benefit from adaptability, without consuming high amount of energy, Impedance Control emerged. Nevertheless, despite stability issues that can arise, the programming of nonlinear behaviors is challenging due to the frequency-based approaches, limiting the method to linear behaviors for now. This prevents the method from benefiting of nonlinear phenomena. The linear behavior presents the same limitations as the Tuned Mass Damper (in mechanics) and the Helmholtz Resonator (in acoustics).

This doctoral thesis fits into this framework, and aims to enabling the creation of nonlinear behaviors within the Impedance Control method, while remaining at low excitation amplitudes (under 110 dB).

2.5 Manuscript outline

To achieve this goal, the manuscript is composed of 4 additional Chapters:

- Chapter 3 aims at defining the control strategy and validate it by numerical and experimental means. The Chapter proposes the development of a real-time based approach to extend the model-inversion feedforward controller to the creation of nonlinear dynamics of an actuator at all excitation amplitudes. The mathematical formalization of the method is proposed. The control strategy is then applied to an acoustic application with the creation of nonlinear Electroacoustic Resonators (ER), and the stability of the method

is demonstrated for this case. The control strategy is validated by comparison of numerical simulations with analytical results. Additionally, the experimental validation is realized through the comparison to an Infinite Input Response linear implementation, and nonlinear dynamics are synthesized and typical behaviors are demonstrated.

- Chapter 4 aims at verifying that the synthesized nonlinear ER is able to dissipate acoustic energy. Another significant challenge is to demonstrate that the control strategy allows for the implementation of multiple and various nonlinearities, while ensuring that the experimental behavior corresponds to the desired one. For this purpose, the ER is coupled to an acoustic mode of a tube, and the model of the experiment is detailed. Analytical developments using the Multiple Scale Method are derived from the model for determining the key parameters, their influence on the behaviors, and the possibility for acoustic dissipation. Numerical and experimental studies were carried out to confirm that the nonlinear ER is able to control the tube acoustic mode with better performance than linear ER. Experiments are conducted with various nonlinear behaviors and compared with good agreement to the numerical solution of the model, confirming that obtained experimental behaviors corresponds to the ideal desired behaviors.

- Chapter 5 aims to guarantee the best possible acoustic performances for the nonlinear ER by enabling the selection of the equilibrium point when folding arises. For this purpose, two distinct method for the modification of the control strategy with the addition of synthetic variables are proposed in the general framework set in Chapter 3. The modified control strategy is validated through numerical computation to ensure that all initial conditions lead to the targeted equilibrium point. The experimental validation of the modified strategy is carried out on the two distinct experiments proposed in Chapters 3 and 4, and for the two proposed methods.

- Chapter 6 aims at developing a nonlinear metamaterial composed of nonlinear ER for proposing innovative solutions for acoustic control. An analogous electrical model is presented along with a Finite Element Model of an experiment designed for assessing the performances of the developed nonlinear metamaterial. Experiments are conducted and compared with numerical results. The analogous electrical model is studied for the creation of edge solitons in the medium.

Chapter 3

Programming nonlinearity

This chapter presents a method for implementing nonlinear behavior in actuators at low excitation amplitudes. Although the impedance control method has been studied for many years [122, 100, 39, 87], the principle of the presented control strategy for enforcing nonlinear behaviors can be difficult to grasp. Hence, this chapter focuses on establishing the mathematical framework of the control strategy and exploring its possibilities and limitations. This chapter examines the following:

- The mathematical formalization of the control is realized for an n degree-of-freedom system;
- The application of the mathematical frame to an electroacoustic resonator is introduced, along with the needed basic assumptions;
- The validation of the control strategy is performed through numerical investigations and experimental tests.

Parts of this chapter are currently under review as a submitted journal article, while some results have already been communicated in [43].

3.1 Principle and formulation of the problem

We seek to create a feed-forward impedance control method that allows to digitally program nonlinear behaviors for the plant to exhibit, at low excitation amplitudes.
Instead of reducing the energy in a domain, the impedance control method involves controlling the impedance of a system to absorb energy from the domain without knowledge of the domain where the absorbing device is placed. Considering a nonlinear nature of the problem, a real-time-based approach is employed.

Let us consider the plant model for a general system, linear or nonlinear, with $n \in \mathbb{N}^*$ degrees of freedom:

$$\dot{X}(t) = A(X(t), t, f_{ext}(t), u_d(t)) \tag{3.1}$$

where $X \in \mathbb{R}^n$ stands for the state vector, $f_{ext} \in \mathbb{R}^n$ denotes the vector of exterior forces, $u_d \in \mathbb{R}^n$ is the vector of the desired control commands, $t \in [0,T]$ with $T > 0$ represents the time and the upper dot ($\dot{\bullet}$) the time derivative. As a result, the vector function A describes the evolution of the system states and is defined as $A : (\mathbb{R}^n \times [0,T] \times \mathbb{R}^n \times \mathbb{R}^n) \longrightarrow \mathbb{R}^n$.

3.1.1 The set-point

For each plant to control, a set point is the desired state of the plant to achieve. We aim at enforcing nonlinear behaviors into linear systems at low excitation amplitudes, but the general formulation proposed in this study could be designed to target linear responses in nonlinear systems. The opposite path consisting of creating linear resonators from nonlinear ones is more difficult to realize, and is not explored here.

To implement nonlinear behaviors into linear systems, the method proposed in this paper involves introducing an ExoSystem (ES) fed by measurements. The ES is a numerical oscillator corresponding to the desired behavior of the plant, and governed by the equation:

$$\dot{X}_d(t) = F(X_d(t), t, f_{ext}^{ES}(t)) \tag{3.2}$$

where $X_d \in \mathbb{R}^n$ stands for the desired vector of system states and the vector function $F : (\mathbb{R}^n \times [0,T] \times \mathbb{R}^n) \longrightarrow \mathbb{R}^n$ describes the mathematical model of the desired behavior of the plant. The numerical system receives the vector of exterior forces f_{ext}^{ES}, which can be taken as the measured vector of exterior forces f_{ext}^{m}. The ES is the target dynamics informed by the external forces applied to the plant. As a result, solving the ES dynamics provides the desired vector state X_d. Hence, the objective of the controller is to enforce the ES vector states into the plant. If the desired dynamics F is nonlinear, multiple stable solutions of Eq. (3.2) can be featured, and the solution exhibited by the ES will depend upon the initial conditions referred to as $X_d(t_0) = X_{d0}$.

3.1.2 A model-inversion based feed-forward controller

To enforce the desired behavior provided by the ES, a feed-forward controller is employed suiting the available experimental architecture. A way to build a feed-forward controller is to invert the plant system dynamics. Let us define the function g in Eq. (3.3). The dynamical trajectory is solution of the implicit equation $g = 0$ such that g writes:

$$g(\dot{X}(t), X(t), t, f_{ext}(t), u_d(t)) = \dot{X}(t) - A(X(t), t, f_{ext}(t), u_d(t)). \tag{3.3}$$

According to the implicit function theorem [167], the function g must respect some assumptions in order to be able to obtain the explicit form of the controller u_d. First of all, we can assign the Banach spaces $H = \mathbb{R}^n$ and $E = \mathbb{R}^n \times \mathbb{R}^n \times [0,T] \times \mathbb{R}^n$, respectively to u_d and the remaining variables $(\dot{X}(t), X(t), t, f_{ext}(t))$ (grouped in $l = (\dot{X}(t), X(t), t, f_{ext}(t))$) of g. Then, we can assume that $\exists (l_0, u_{d,0}) \in E \times H$ such that $g(l_0, u_{d,0}) = 0$. So, according to the implicit function theorem [167], if the application g is of class C^k, $k \geq 1$, and the matrices:

$$\left(\frac{\partial g_p}{\partial (u_d)_q} \bigg|_{l=l_0, u_d=u_{d,0}} \right)_{1 \leq p \leq n,\ n+1 \leq q \leq 2n} \tag{3.4}$$

are invertible, with continuous inverses, then the neighbourhoods E' of l_0 and H' of $u_{d,0}$ exist so that:

$$\exists \varphi \in C^k(E', H')\ , \forall (l, u_d) \in E' \times H', \quad g(l, u_d) = 0 \Leftrightarrow u_d = \varphi(l). \tag{3.5}$$

This means that, if the function g is continuously differentiable, and its derivatives with respect to u_d are invertible, and such inverses are continuous, then we can express explicitly u_d as a function of the remaining variables l: $u_d = \varphi(l)$. In that case, the expression $u_d = \varphi(l)$ can be exploited to synthesize a feed-forward controller, according to the so-called model-inversion control (MIC) method. Observe that the above theorem is valid for

either linear or nonlinear plants: a model-inversion-based feed-forward controller can be synthesized as long as the actuation variable respects the above assumptions.

Let us suppose that the setpoint X_d is known (by integration of Eq. (3.2)), the controller u_d being able to track such setpoint in the plant, is obtained by imposing $\forall t \in [0,T]\ X(t) = X_d(t)$ in the plant Eq. (3.1). Therefore:

$$\forall (X_d, t, f_{ext}, u_d) \in E' \times H', \quad \dot{X}_d(t) = A(X_d(t), t, f^m_{ext}(t), u_d(t)) \Leftrightarrow\ u_d = \varphi(\dot{X}_d(t), X_d(t), t, f^m_{ext}(t)). \tag{3.6}$$

This imposes the additional condition that X_d satisfies the equation of the plant Eq. (3.1) $\forall t \in [0,T]$.

3.1.3 General formulation

Based on described procedures in the previous sections, under the assumptions of the implicit function theorem, the entire controlled system (the plant and the controller) is described by the following system of equations:

$$\dot{X}(t) = A(X(t), t, f_{ext}(t), u_d(t)) \tag{3.7a}$$

$$\dot{X}_d(t) = F(X_d(t), t, f^m_{ext}(t)). \tag{3.7b}$$

$$u_d(t) = \varphi(\dot{X}_d(t), X_d(t), t, f^m_{ext}(t)). \tag{3.7c}$$

If Eq. (3.7c) is obtained from Eq. (3.7a), by model-inversion (see Section 3.1.2) and supposing $f^m_{ext} \approx f_{ext}$, since Eq. (3.7a) describes an asymptotically converging physical system, then:

$$\lim_{t \longrightarrow \infty} X(t) = X_d(t) \tag{3.8}$$

3.1.4 Algorithm

Algorithm principle

The algorithm used to implement the controller, as given by Eqs. (3.7b) and (3.7c), is composed of two main tasks. The first task consists of obtaining the set-point, i.e., integrating the ES of Eq. (3.7b) fed with the measured external forces by using a numerical scheme. At each step t_{n-1}, the numerical scheme allows for the prediction of the vector state X_d at the next time step t_n. The second task follows the first one, i.e. it is performed at time step t_n, and consists of writing the control variable u_d according to Eq. (3.7c). Below, the two steps are detailed, starting from t_n. For the sake of clarity, the variables computed at t_{n-1} corresponding to the prediction at t_n, will be noted $\bullet^{n-1}_n$.

1. From Eq. (3.7a), taking $\dot{X}_d \equiv \dot{X}^n_{d,n}$, $X_d \equiv X^{n-1}_{d,n}$ and $f^m_{ext} \equiv f^m_{ext}(t_n)$, we directly compute $\dot{X}^n_{d,n}$. Hence, we can get $u_d(t_n)$ by Eq. (3.7c).

2. Solve Eq. (3.7b) using a numerical scheme, based on the state vector determined at the preceding time step $X^{n-1}_{d,n}$, and the measured external forces $f^m_{ext}(t_n)$. This operation gives the state vector $X^{n+1}_{d,n}$.

Observe that, if functions φ and F are both linear, a Laplace transform allows to get $\tilde{X}_d(s)$ as function of $\tilde{f}^{ES}_{ext}(s) = \tilde{f}^m_{ext}(s)$ where $s \in \mathbb{C}$ is the frequency domain complex variable (set $\tilde{\bullet}$ denotes the Laplace transform of variable $\bullet$). Therefore, the controller $\tilde{u}_d(s)$ can be directly related to $\tilde{f}^m_{ext}(s)$ by a corrector transfer function $H(s)$, and the two steps described above merge into a single one, which is the digital synthesis of $\tilde{u}_d(s) = H(s)\tilde{f}^m_{ext}(s)$. This digital synthesis can be performed by any recursive scheme such as the Infinite Impulse Response (IIR)

[69]. Nevertheless, if either φ or F are nonlinear, the convolution operators cannot be employed, and the two steps described above, involving a real-time integration of the ES, must be retained. For this reason, such model-inversion control strategy has been labeled as a Real-Time-Integration (RTI) scheme [43, 114, 112], while the choice of the specific integration scheme should be made based upon the experimental hardware at disposal.

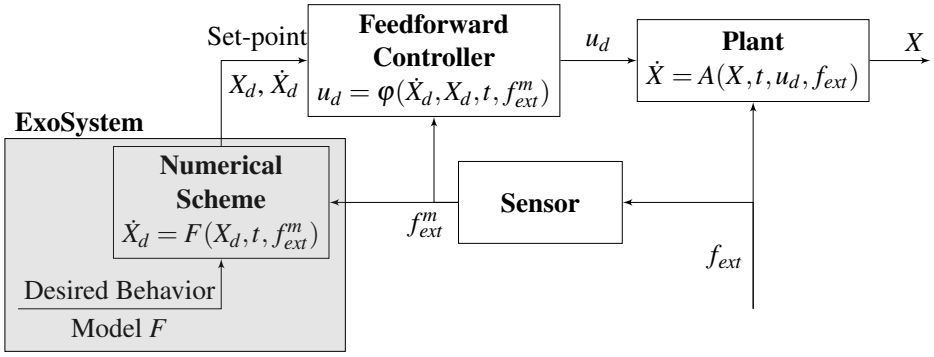

Fig. 3.1 Block diagram of the open-loop control

The numerical scheme

In such RTI control strategy, the numerical scheme plays a critical role. Striking a balance between computational efficiency, accuracy, and stability can significantly enhance the overall performance of the control approach.
A fourth-order Runge-Kutta (RK4)-like scheme is considered here. To properly use a RK4 scheme, the parameters values must be known at the intermediate stages within the time-step t_n, $t_n + h_n/2$, and $t_n + h_n$, with $h_n = t_{n+1} - t_n$. This requirement implies that external forces should be measured at these corresponding time instants. However, both the $t_n + h_n/2$ and $t_n + h_n$ external forces measurements are generally unknown during the numerical integration in real time. To address this limitation, the external forces are assumed to remain constant throughout the integration interval: $f^m_{ext}(t_n) = f^m_{ext}(t_n + h_n/2) = f^m_{ext}(t_n + h_n)$. Under this assumption, the RK4-like scheme can be formulated as follows:

$$X_d(t_n + h_n) = X_d(t_n) + h_n \left(\frac{1}{6} k_1(t_n, X_d(t_n), h_n, f^m_{ext}(t_n)) + \frac{1}{3} k_2(t_n, X_d(t_n), h_n, f^m_{ext}(t_n)) + \frac{1}{3} k_3(t_n, X_d(t_n), h_n, f^m_{ext}(t_n)) + \frac{1}{6} k_4(t_n, X_d(t_n), h_n, f^m_{ext}(t_n)) \right) \tag{3.9a}$$

$$\begin{cases} k_1\left(t_n, X_d(t_n), h_n, f^m_{ext}(t_n)\right) = F\left(X_d(t_n), t_n, f^m_{ext}(t_n)\right) \\ k_2\left(t_n, X_d(t_n), h_n, f^m_{ext}(t_n)\right) = F\left(X_d(t_n) + \frac{h_n}{2} k_1\left(t_n, X_d(t_n), h_n, f^m_{ext}(t_n)\right), t_n + \frac{h_n}{2}, f^m_{ext}(t_n)\right) \\ k_3\left(t_n, X_d(t_n), h_n, f^m_{ext}(t_n)\right) = F\left(X_d(t_n) + \frac{h_n}{2} k_2\left(t_n, X_d(t_n), h_n, f^m_{ext}(t_n)\right), t_n + \frac{h_n}{2}, f^m_{ext}(t_n)\right) \\ k_4\left(t_n, X_d(t_n), h_n, f^m_{ext}(t_n)\right) = F\left(X_d(t_n) + h_n k_3\left(t_n, X_d(t_n), h_n, f^m_{ext}(t_n)\right), t_n + h_n, f^m_{ext}(t_n)\right) \end{cases} \tag{3.9b}$$

An alternative explicit integration scheme can be employed to determine the set-point X_d. Selecting a first-order integration scheme, such as the Euler method, implies assuming that external forces remain constant over the time step, unlike the RK4-like method that requires intermediate force values. However, the Euler scheme demands a higher sampling frequency to achieve similar accuracy. Given the limitations of the experimental setup in terms of sampling frequency, the RK4-like scheme seemed a more suitable option.

The experimental implementation of an implicit integration scheme is more challenging and should be expressed as an explicit scheme beforehand, for example, or combined with an explicit scheme.

3.2 Application to the case of the electroacoustic resonator

3.2.1 The plant and the controller

After outlining the mathematical framework of the control strategy to achieve a desired equilibrium point of a nonlinear impedance operator, we consider the specific application of a digitally programmable ER under low-noise excitation amplitudes. The two following assumptions are realized:

Assumption 3.1 *The loudspeaker's membrane undergoes low external sound pressure excitation. As a result, the loudspeaker's dynamics are considered linear.*

Assumption 3.2 *The loudspeaker undergoes low excitation frequencies. As a result, the loudspeaker's dynamics are considered to be dominated by its first mode.*

Assumption 3.2 is based on the underlying hypothesis that the size of the membrane is small compared to the operating wavelengths. Hence, a locally reacting behavior of the loudspeaker membrane is assumed.
As a result, the loudspeaker mechanical dynamics can be described by the one-degree-of-freedom ($n = 1$) mathematical model [17]:

$$M_0\ddot{x}(t) + R_0\dot{x}(t) + K_0x(t) = f_{ext}(t) - Blu_d(t), \tag{3.10}$$

where the variable x is the modal coordinate of the loudspeaker's first mode. The left-hand side represents the classical single degree-of-freedom model with the modal mass M_0, damping R_0, and stiffness K_0. The force induced by the sound pressure on the membrane surface is denoted by $f_{ext}(t) = S_d p(t)$ where p is the sound pressure, and S_d is the so-called effective surface area of the loudspeaker's membrane. The pressure at the surface of the loudspeaker membrane can be measured using one or more microphones [42]. The control is applied by the Laplace force $-Blu_d(t)$, where l is the length of a solenoid through which the electric current u_d (the controller) flows, and B is the permanent magnetic field generated by the magnet immersed in the solenoid.
The model of the plant satisfies the conditions of the implicit function theorem, as detailed in Section 3.1.2, because the control variable is linear with respect to the model of the plant, as shown in Eq. (3.10). Hence, from Eq. (3.7c), we can easily write the feed-forward controller expression:

$$u_d(t) = \frac{1}{Bl}(-M_0\ddot{x}_d(t) - R_0\dot{x}_d(t) - K_0x_d(t) + f^m_{ext}(t)) \tag{3.11}$$

where $x_d \in \mathbb{R}$ is the desired modal coordinate determined by the ES. Observe that the ES is assumed to have the same number of degrees of freedom $n = 1$ as the plant. Now, let us particularize Eq. (3.7b) for an ES target dynamics of the type:

$$M_d\ddot{x}_d(t) + R_d\dot{x}_d(t) + F_{NL}(x_d,t) = f^m_{ext}(t), \tag{3.12}$$

where M_d is the desired modal mass, R_d is the desired modal damping, while $F_{NL} : \mathbb{R} \times [0,T] \longrightarrow \mathbb{R}$ is a nonlinear restoring force function. For simplicity, we consider that F_{NL} contains a linear stiffness component, that we call K_d. Clearly, the choice of the desired modal parameters and of F_{NL} should respect the classical constraint of causality and stability (bounded response).
It is worth noting that the damping or mass can also be chosen to be nonlinear:

$$M_d\ddot{x}_d(t) + C_{\mathrm{NL}}(\dot{x}_d,t) + F_{NL}(x_d,t) = f^m_{ext}(t), \tag{3.13}$$

where C_{NL} is a nonlinear damping function. However, in this study, only a nonlinear stiffness function is considered.

3.2.2 Asymptotic Convergence

In this section, we verify the asymptotic convergence condition Eq. (3.8) for the above mentioned control scheme. Assuming that the pressure measurements are perfectly accurate $f_{ext}^m = f_{ext}$, and replacing u_d in Eq. (3.10) by Eq. (3.11), we have $\forall t \in [0,T]$:

$$M_0\ddot{x}(t) + R_0\dot{x}(t) + K_0x(t) = M_0\ddot{x}_d(t) + R_0\dot{x}_d(t) + K_0x_d(t). \tag{3.14}$$

Let us set $y = x - x_d$, it leads to a homogeneous second-order ordinary differential equation:

$$M_0\ddot{y}(t) + R_0\dot{y}(t) + K_0y(t) = 0. \tag{3.15}$$

Assuming two complex conjugate roots r_1 and r_2 for the characteristic equation of Eq. (3.15), the solution writes:

$$\forall t \in [0,T] \quad y(t) = \mathrm{e}^{\Re(r_1)t}(A\cos(\Im(r_1)t) + B\sin(\Im(r_1)t)), \tag{3.16}$$

where $\Re(z)$ and $\Im(z)$ stand for the real and imaginary parts of a complex number $z \in \mathbb{C}$, respectively. Since the loudspeaker is positively damped as a physical system, it gives a negative coefficient $\Re(r_1) = -R_0/(2M_0)$. In addition, utilizing the triangle inequality, one may observe the behavior of the solution when $t \longrightarrow +\infty$:

$$\lim_{t\longrightarrow+\infty} \mathrm{e}^{\Re(r_1)t} = 0 \tag{3.17a}$$

$$\forall t \in [0,T] \cup \{+\infty\} \quad |A\cos(\Im(r_1)t) + B\sin(\Im(r_1)t)| \leq |A| + |B|. \tag{3.17b}$$

Eq (3.17b) shows that $y(t)$ is bounded, which means that the product limit is 0. It yields:

$$\lim_{t\longrightarrow+\infty} y(t) = 0 \quad \Rightarrow \quad \lim_{t\longrightarrow+\infty} x(t) = x_d(t). \tag{3.18}$$

Therefore, the designed control satisfies the condition of asymptotic convergence, ensuring that the loudspeaker dynamics tend to the one conceived for the ES.

3.2.3 Design of the desired dynamic behavior

This section presents the basic equations and conditions for selecting the various parameters to achieve a desired nonlinear behavior. Let us set the following dimensionless parameters η_M, η_K and η_R so that:

$$M_d = \eta_K M_0 \tag{3.19a}$$

$$R_d = \eta_R R_0 \tag{3.19b}$$

$$K_d = \eta_K K_0 \tag{3.19c}$$

Let f_d be the targeted frequency of the linear resonance of the ER, and f_0 be the frequency of the intrinsic mode of the ER. The parameter η_K can be found using the following equation, knowing the targeted frequency:

$$\frac{\eta_K}{\eta_M} = \left(\frac{f_d}{f_0}\right)^2 \tag{3.20}$$

Choosing the value of the coefficient of the nonlinearity defines the amplitude of the ER's membrane at which the ER will exhibit a nonlinear behavior.

3.3 Numerical simulations

This section aims to validate the proposed strategy through the study of numerical simulations.

3.3.1 Method

The numerical simulations are built to simulate the behavior of the control by considering the vector of state X, of the state of the ES X_d, and the electrical current u_d. The numerical simulation consists of following the steps detailed in 3.1.4 under an arbitrary pressure. We set $f_{ext}^{ES} = f_{ext}^{m} = f_{ext}$. Notice that the feedback of the acoustic environment is not modeled, as it has been done in [43]. Hence, the simulated ER is excited by an acoustic signal that is not influenced by the ER's response. The simulations are realized with a 50 000 Hz sampling frequency (being the same as the experimental device's frequency).

At each time step, the ES given by Eq. (3.13) is integrated using a Runge-Kutta numerical scheme. Its solution x_d is injected in the electrical current provided by Eq. (3.11), as extensively detailed in Section 3.1.4 and in [43]. Then, the obtained electrical current is used in the plant, as shown in Eq. (3.10), which is integrated using a classical numerical scheme to provide the ER's simulated response, x.

Parameter	Value	Unit
M_0	3.89×10^{-4}	kg
R_0	2.63×10^{-1}	$\mathrm{kg.s^{-1}}$
K_0	4.34×10^{3}	$\mathrm{kg.s^{-2}}$
Bl/S_d	136.7	$\mathrm{kg.m^{-1}.A^{-1}.s^{-2}}$
S_d	1.3×10^{-3}	$\mathrm{m^2}$

Table 3.1 Thiele-Small parameters of the ER.

The Thiele-Small parameters [17], to insert in the plant Eq. (3.10), of the loudspeaker are given in Table 3.1. These parameters have been obtained from the measurements conducted on the experimental bench following the procedure described in Appendix A.

For the results analysis, let us define the envelope $\hat{Y}$ of a time signal Y as the modulus of the Hilbert transform H of the time histories:

$$\hat{Y}(f(t)) = |H(Y)(t)|. \tag{3.21}$$

Sine frequency sweeps can be used for excitation signals. As the sine sweep associates an excitation frequency at each time t, the envelope can be expressed as a function of the excitation frequency denoted f: $\hat{Y}(f(t))$.

3.3.2 The synthesis of linear resonators

First, let us study the synthesis of linear resonators. In order to do so, we consider the following ES:

$$M_d\ddot{x}_d(t) + R_d\dot{x}_d(t) + K_d x_d(t) = f_{ext}^{ES}(t), \quad \text{with } f_{ext}^{ES}(t) = f_{ext}^{m}(t), \tag{3.22}$$

where M_d, R_d and K_d denote the desired modal parameters of the ES dynamics. Setting $\eta_M = \eta_K = \eta_R = 1$ enables the verification of the control strategy in a trivial case study, where the computed electrical current is expected to be zero, as we look to achieve the same impedance featured by the loudspeaker in open circuit. The excitation signal consists of a sine sweep with a linearly increasing frequency from 200 Hz to 1500 Hz to excite around the loudspeaker's first mode. Figure. 3.2 depicts the electrical current, and the envelopes of the ES displacement $\hat{x}_d$ and the actual displacement $\hat{x}$ of the membrane. Observe that the actual and ES displacements are in agreement. Furthermore, the system exhibits a linear resonance at the loudspeakers natural frequency of 531 Hz, which is consistent with the choice $\eta_K = \eta_M = 1$. As anticipated, the computed electrical current remains extremely close to zero throughout the excitation. Although the electrical current is extremely small, an increase of the amplitude is still present at the first mode's natural frequency.

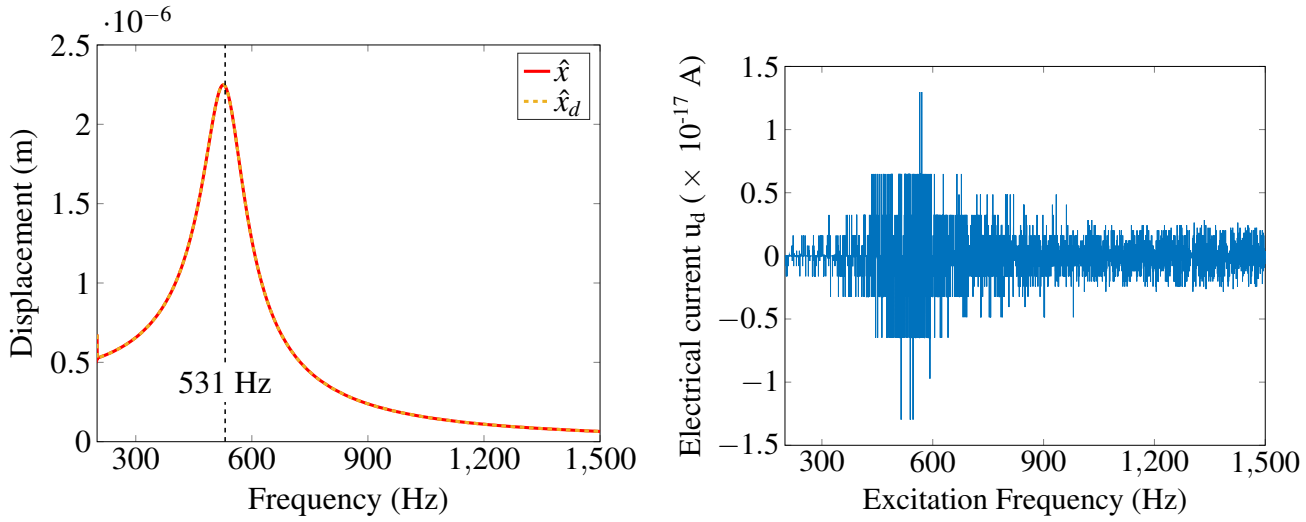

(a) (b)

Fig. 3.2 (a) Envelopes of the actual displacement $\hat{x}$ and the ES displacement $\hat{x}_d$; (b) Electrical current computed during the simulation with $\eta_M = \eta_K = \eta_R = 1$.

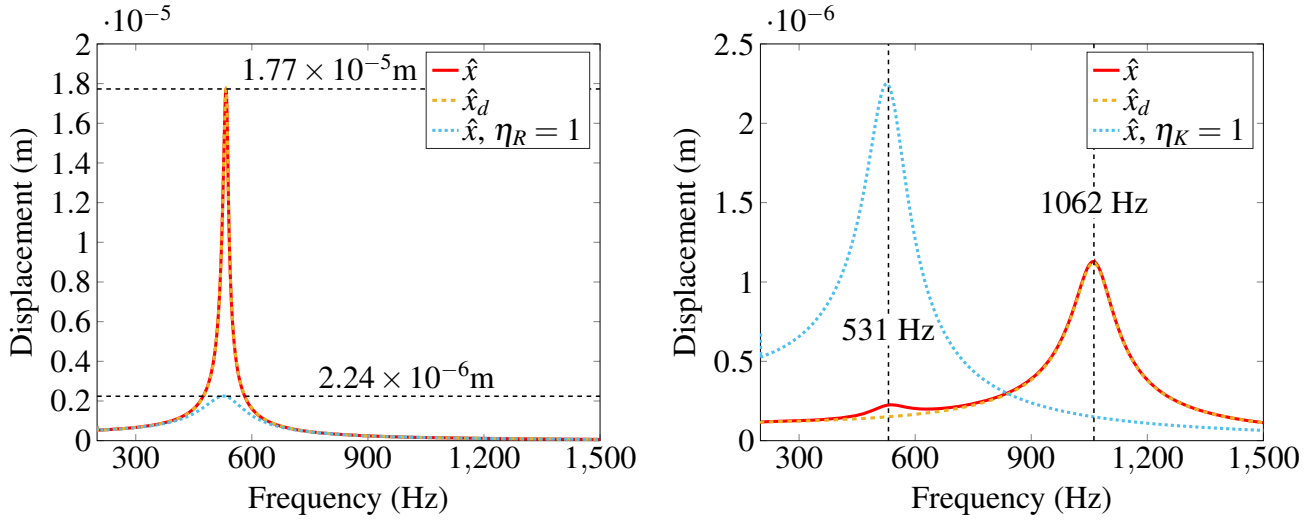

(a) $\eta_R = 1/8$, $\eta_K = 1$ (b) $\eta_R = 1$, $\eta_K = 4$

Fig. 3.3 Envelopes of the actual displacement $\hat{x}$ and the ES displacement $\hat{x}_d$ with $\eta_M = 1$

Figure 3.3 plots the envelopes of the ES displacement and the actual displacement of the ER for two distinct scenarios: one with $\eta_M = \eta_K = 1$ and $\eta_R = 1/8$ (Fig. 3.3a) and another with $\eta_M = \eta_R = 1$ and $\eta_K = 4$ (Fig. 3.3b). Observe in Fig. 3.3a that the resonance is amplified by nearly a factor of 8 ($1.77 \times 10^{-5}/2.24 \times 10^{-6} \approx 7.9$). The ES displacement and the actual displacement curves coincide, indicating that the control strategy successfully enforces the desired behavior in the ER. In the second scenario, setting $\eta_K = 4$ leads to a desired resonance frequency of $f_d = 1062$ Hz. As shown in Fig. 3.3b, the resonance peak is accurately positioned at this target frequency. However, a noticeable discrepancy between the ES displacement and the actual displacement occurs at the loudspeaker's natural frequency $f_0 = 531$ Hz. This discrepancy is attributed to the limitations inherent to the numerical scheme of the ES, detailed below. As a result, the desired behavior defined by the ES does not include this unwanted response. Additionally, the figure shows that the resonance amplitude peak at 1062 Hz is lower than the one at 531 Hz, indicating that driving the desired resonance frequency at higher frequencies from its natural frequency reduces the displacement amplitude (but not the impedance), as expected.

The control strategy effectively enforces the desired behavior into the system. However, the natural resonance of the system cannot be completely eliminated using this method, as a residual contribution from the loudspeaker's natural resonance can still be observed. This unexpected behavior stems from the prediction of the vector state X_d using the previous time step, as detailed in Sec. 3.1.4. Specifically, the algorithm does not estimate the pressure at different increments of the numerical scheme, as required by a proper RK4 method. Instead, the numerical scheme assumes the pressure remains constant throughout the time step, which alters the accuracy of the integration scheme. Consequently, the pressures acting on the ER's membrane differ from those used in the numerical prediction, leading to numerical errors in the integration scheme, causing the persistence of the loudspeaker's natural frequency. During numerical simulations, where the pressure is known and the influence of the ER on the acoustic field is not modeled, the RK4-like scheme can be replaced with a RK4 scheme that takes into account the evolution of the pressure at the intermediate stages $t_n + h_n/2$ and $t_n + h_n$. The outcome is plotted in Fig. 3.4 in the case of $\eta_M = \eta_R = 1$ and $\eta_K = 4$. Notice that both $\hat{x}$ and $\hat{x}_d$ follow the same trajectory, without the residual resonance at the natural frequency of the loudspeaker's first mode.

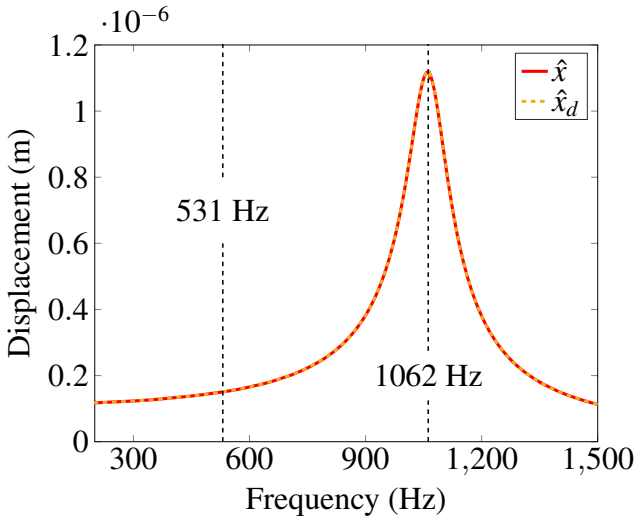

Fig. 3.4 Envelopes of the actual displacement $\hat{x}$ and the ES displacement $\hat{x}_d$ with $\eta_M = \eta_R = 1$ and $\eta_K = 4$ for a RK4 scheme that takes into account the evolution of the pressure at the intermediate stages. The sampling frequency is 50 kHz.

Two main approaches exist to address this issue: modifying the numerical scheme or mitigating the residual effects through the use of an additional controller. The first possible solution involves adapting the numerical scheme itself. By dissociating the calculation steps and the measurement steps, the pressure could be measured at the half-time step $t_n + h/2$ (or at additional points), allowing these measurements to be incorporated into the numerical integration process to correct the predictions. Alternatively, the control strategy could utilize a first-order integration scheme (such as the Euler scheme), which does not rely on this assumption. However, the Euler scheme requires smaller time steps to ensure convergence. Figure 3.5a illustrates that the Euler scheme diverges with a 50 kHz sampling rate, preventing its experimental use. In Fig. 3.5b, the Euler scheme at a 500 kHz sampling frequency produces acceptable results. Nonetheless, a slight discrepancy between $\hat{x}$ and $\hat{x}_d$ appears despite the high sampling frequency. These findings highlight the need for the RK4-like algorithm, which offers a balance between accuracy and the constraints of the experimental hardware. As a result, it is the algorithm used throughout the manuscript.

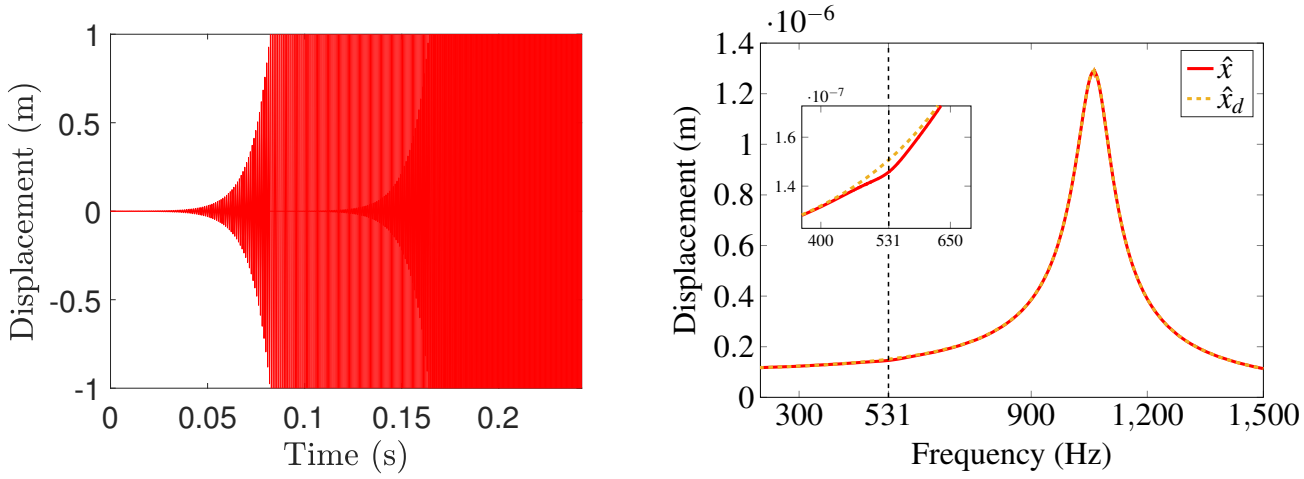

(a) Sampling frequency : 50 kHz

(b) Sampling frequency : 500 kHz

Fig. 3.5 Envelopes of the actual displacement $\hat{x}$ and the ES displacement $\hat{x}_d$ with $\eta_M = \eta_R = 1$ and $\eta_K = 4$ for a Euler scheme at different sampling frequencies.

Another possible approach is to numerically predict the pressure – instead of measuring it, as previously suggested – at $t_n + h/2$ and $t_n + h$ to increase the precision of the numerical scheme. If these solutions do not work, the reduction of the remaining resonance amplitude can be realized by adding a feedback controller to the feed-forward one [134]. Nevertheless, a feedback loop would require a real-time measurement of the state vector X, i.e. the measurement of the displacement (or the velocity, or the acceleration) of the loudspeaker's membrane, therefore increasing the robustness of the control [159]. This could be achieved by placing a microphone in the back cavity of the loudspeaker [78] or by placing an accelerometer on the ER membrane's surface (preferably from the cavity side). It should be noted, though, that placing an accelerometer directly on the membrane would increase the modal mass of the loudspeakers first mode, potentially affecting its dynamic behavior.

3.3.3 The effect of time delay

This subsection aims to briefly explore the effect of time delay on the proposed control strategy. Such an analysis is essential, as digital implementation inevitably introduces a delay in the response. An extensive study on the influence of delay in IIR-based implementation has been conducted by De Bono [42]. Here, the effect of the time delay on a RTI implementation is investigated by comparing it to the solutions without delay. The experimental

delay of the control is estimated in [135] to be at least one time step: $\tau = 2 \times 10^{-5}$ s. This value serves for assessing the influence of the digital latency. Figure 3.6 presents the envelopes of the actual displacement $\hat{x}$ with and without delay in the previous studied cases:

- $\eta_M = \eta_R = \eta_K = 1$ (Fig. 3.6a)
- $\eta_M = \eta_K = 1$ and $\eta_R = 1/8$ (Fig. 3.6b)
- $\eta_M = \eta_R = 1$ and $\eta_K = 4$ (Fig. 3.6c)

For the first two configurations where $\eta_K = 1$, the presence of delay does not noticeably affect the system response, as the displacement trajectories with and without delay are nearly identical (Figs.3.6a and 3.6b). However, Fig. 3.6c with $\eta_K = 4$ reveals that the residual linear natural resonance at $f_0 = 531$ Hz is amplified in the presence of delay. Additionally, the amplitude of the actual displacement of the 1062 Hz resonance peak is slightly higher than the ES displacement amplitude of the resonance peak, suggesting that the time delay subtly alters the ER behavior. This is due to the phase lag between the incident pressure and the electrical current equal to the delay that induces a different pressure between the control calculations and the actual one applying on the membrane.

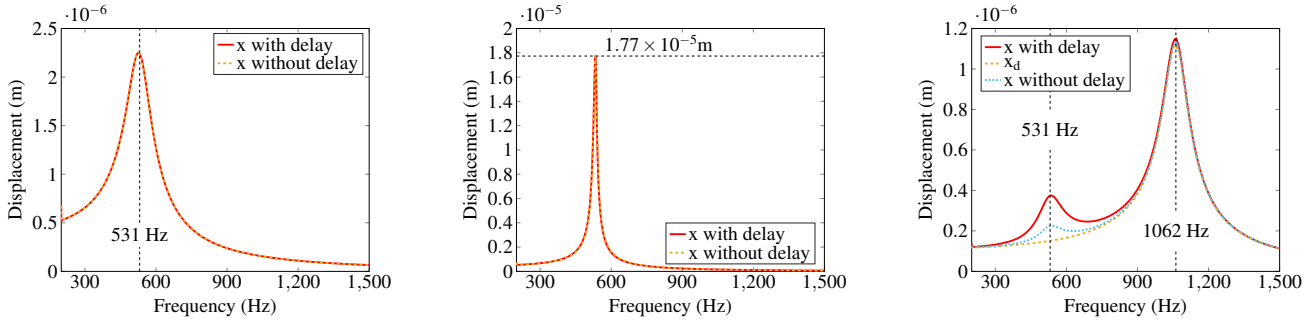

(a) $\eta_R = 1$, $\eta_K = 1$ (b) $\eta_R = 1/8$, $\eta_K = 1$ (c) $\eta_R = 1$, $\eta_K = 4$

Fig. 3.6 Envelopes of the actual displacement $\hat{x}$ with $\eta_M = 1$ with and without the time delay $\tau = 2 \times 10^{-5}$ s

3.3.4 Validation of the synthesis of nonlinear resonators by a comparison to an analytical solution

To begin with, let us compare the numerical simulations, Eq. (3.7), to an analytical solution obtained using the harmonic balance method (HBM) with truncation to the first harmonic. The ES dynamics considered in this section is a Duffing-like oscillator, with $F_{NL}(x_d,t) = K_d x_d(t) + K_d \beta_{\text{NL}} x_d^3(t)$, but other nonlinear stiffness functions $F_{NL}(x_d,t)$ might be considered, as done in [114]. Hence, the ES dynamics is described by the following equation:

$$M_d \ddot{x}_d(t) + R_d \dot{x}_d(t) + K_d x_d(t) + K_d \beta_{\text{NL}} x_d^3(t) = f_{ext}^{ES}(t), \tag{3.23}$$

with the parameters $\eta_M = \eta_K = 1$, and $\eta_R = 1/8$, and $\beta_{\text{NL}} = 10^{10}$ m^{-2} is the coefficient of the cubic stiffness. Note that the choice of β_{NL} is motivated by the low displacement amplitudes of the loudspeaker. The excitation is chosen as a frequency sine sweep lasting 30 seconds, from 350 Hz to 900 Hz (to contain the first mode of the plant), and the excitation amplitude is arbitrarily chosen as 1.5 Pa. Additional simulations are performed using a mono-frequency sine signal excitation lasting 5 seconds. The initial conditions for all the simulations are taken as $x(0) = x_d(0) = 0$ and $\dot{x}(0) = \dot{x}_d(0) = 0$.

Let us define the high, low and unstable equilibrium points of the response of a Duffing equation featuring a hardening behavior as the defined points in Fig. 3.7.

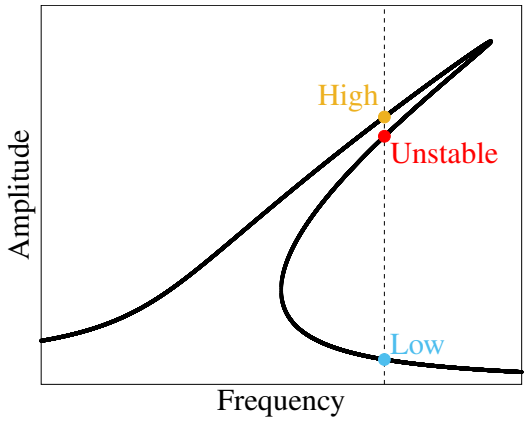

Fig. 3.7 Amplitude response of the Duffing equation featuring a hardening behavior with linear and cubic stiffness.

The frequency spectra in the stationary regime of $\hat{x}_d$ and $\hat{x}$, corresponding to the amplitudes of the target displacement x_d and of the response of the ER x, respectively, are plotted in Fig. 3.8. Both $\hat{x}_d$ and $\hat{x}$ are compared to the HBM solution of Eq. (3.7b) for an increasing frequency sweep (Fig. 3.8a) and a decreasing frequency sweep (Fig. 3.8b). It can be seen that the solution to the ES equation is well approximated using the numerical scheme, as it closely matches the results obtained from HBM. Both Fig. 3.8a and Fig. 3.8b show that $\hat{x}_d$ perfectly overlaps with $\hat{x}$, validating the control algorithm in simulations. Moreover, the ER's stationary response under mono-harmonic excitations (represented by black points) shows that the low energy equilibrium point is the steady-state solution for the considered initial conditions.

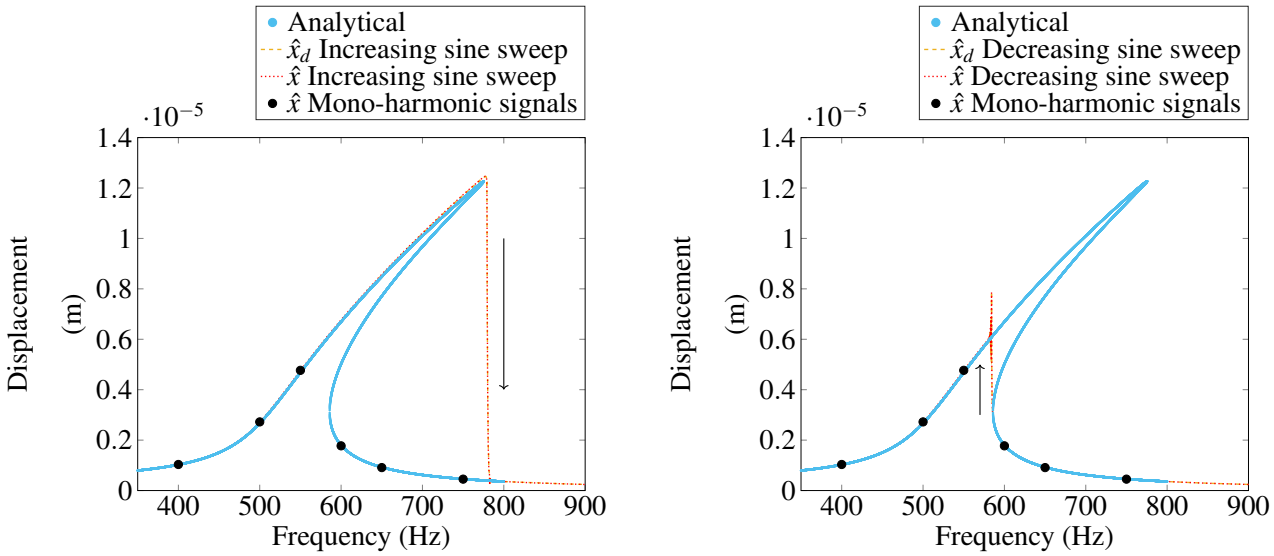

(a) (b)

Fig. 3.8 Comparison between the analytical solution of Eq. (3.7b) obtained by Harmonic Balance Method (HBM), and the envelopes $\hat{x}_d$ and $\hat{x}$ of the simulated ES targeted displacement x_d and of the ER response x respectively, in case of (a) increasing or (b) decreasing frequency sweep excitation.

In Fig. 3.9, the basins of attraction of the ES are computed using a Poincaré map, depending on the initial conditions $x_{0d} = x_d(0)$ and $\dot{x}_{0d} = \dot{x}_d(0)$, for a monoharmonic excitation at 650 Hz and with the same parameters as the ones of the simulations. The black zone corresponds to the higher energy equilibrium point, while the white zone corresponds to the lower energy equilibrium point. Figure 3.9 shows that for initial conditions in the vicinity of the ones chosen in the simulations $(x_0, \dot{x}_0) = (0,0)$, the system's response tends to the low energy equilibrium

point, in agreement with the black dots of Fig. 3.8. In the following experiment, and in the next Chapters, it is observed that it is an issue for noise mitigation purposes. A modified control strategy to choose the equilibrium point regardless of the initial conditions is proposed in Chapter 5.

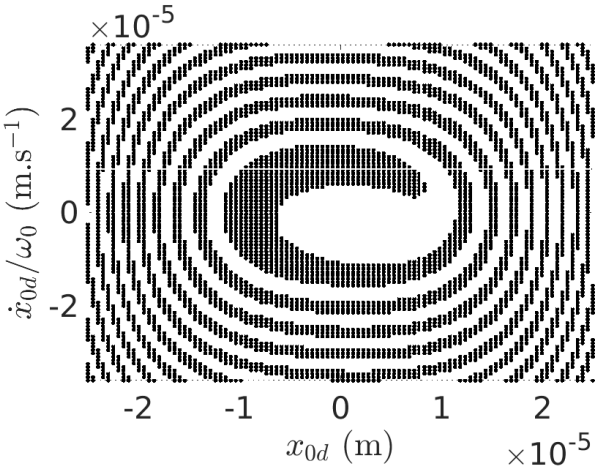

Fig. 3.9 Basins of attraction of the ES Eq. 5.1b. The black (respectively, white) color zone indicates that the system tends towards the high (respectively, low) energy equilibrium point.

3.4 Experimental validation

The objective of this section is to validate the nonlinear impedance control strategy experimentally. In this experiment, the ER is placed in a quasi-open acoustic field.

3.4.1 Experimental set-up

The ER is composed of a loudspeaker Visaton®K50WP 8Ω of membrane effective area S_d, collocated to an externally polarized 1/4" Bruël&Kjaer©microphone, and linked to a d-SPACE©MicroLabBox DS1202 device for the real-time implementation of the RTI control algorithm. The sampling frequency for both acquisition and control is 50 kHz. The control signal output from the d-SPACE©device provides a voltage command to the loudspeaker equal to the desired electrical current u_d. Indeed, the ER is equipped with a Howland current pump [43, 41] assuring that the electrical current sent to the loudspeaker's coil is equal to the voltage command [126]. The velocity $v = \dot{x}$ of the ER's membrane is measured using a Laser Doppler Velocimeter (LDV) Polytec©CLV 3D, while the pressure p on the ER is retrieved by the same microphone employed for the control. The experimental setup is depicted in Fig. 3.10. The external acoustic source is excited at low amplitudes (under 110 dB), such that the ER response remains confined to the linear regime without the controller. Also, the excitation frequencies are sufficiently low to assume a locally-reacting behaviour of the speaker membrane around the piston-mode resonance, as described in Section 3.2 (the wavelength is large compared to the size of the loudspeaker's membrane). The excitation signals on the external acoustic source can be linearly increasing/decreasing frequency sweeps from 350 Hz to 800 Hz, lasting 30 seconds, or monoharmonic sines, lasting 5 seconds. Sine sweeps from 100 Hz until 1500 Hz or 3000 Hz are also realized with a duration of 60 seconds. In the case of monoharmonic excitations of the external sound source, the ER pressure and velocity are recorded for an additional 2 seconds to observe the transient regime.

The modal parameters of the loudspeaker's first mode and the Laplace force factor Bl/S_d are measured using the method presented in Appendix A, and are detailed in Table 3.1.

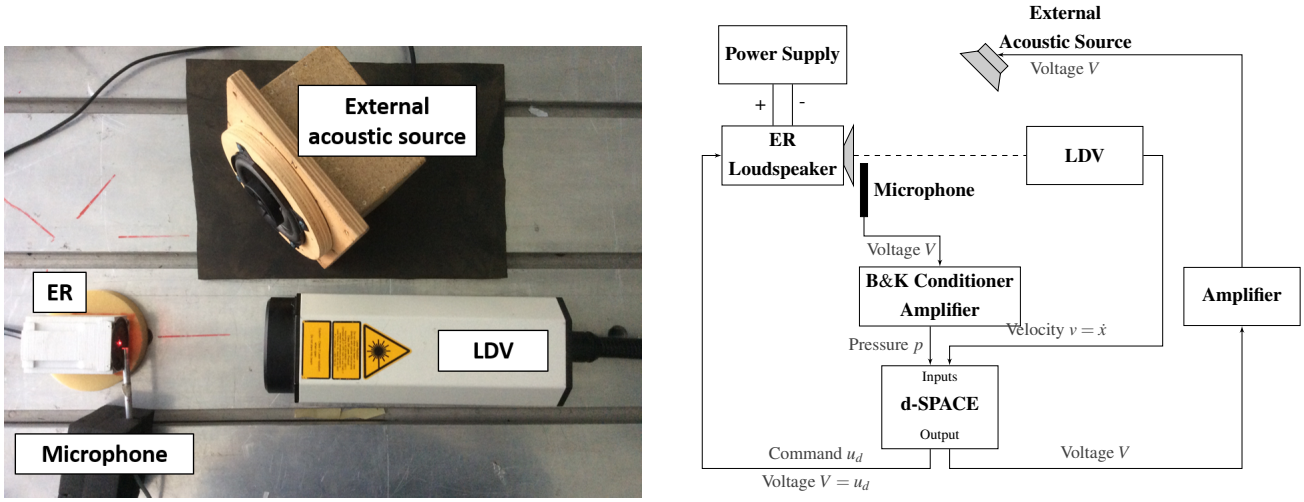

(a) (b)

Fig. 3.10 (a) Picture and (b) scheme of the open-field experimental set-up.

3.4.2 Experimental validation of the control strategy

Linear target dynamics

To experimentally validate the RTI control algorithm, the ER response controlled by the RTI strategy is first compared to that obtained by a classical IIR implementation. The desired ES dynamics is assumed as a linear SDOF resonator as in Eq. (3.24):

$$M_d\ddot{x}_d(t) + R_d\dot{x}_d(t) + K_d x_d(t) = f_{ext}^m(t) \tag{3.24}$$

The transfer function applied through the IIR method is detailed in [43]. The ER is excited using sine sweeps ranging from 100 Hz to 3000 Hz lasting 60 seconds. The ER's response is illustrated in Fig. 3.11, which presents the amplitude, phase and coherence of the mobility transfer function $Y(s) = v(s)/p(s)$ for various cases, where v stands for the measured membrane velocity, and p denotes the measured pressure near the membrane. In Fig. (3.11a), the mobility transfer function is presented in the case of $\eta_K = 1$, $\eta_R = 1/8$, and $\eta_M = 1$. Observe that the first mode of the loudspeaker is clearly recognizable, and located at its resonance frequency (531 Hz). For both the IIR and RTI control implementations, the ER behave as expected: the resonance frequency remains unchanged by either control method. The phase further confirms the presence of the resonance at 531 Hz. Additionally, a reduction in the coherence is observed at the resonance frequency, which was to be expected.

In Fig. 3.11b, the ER's response is compared across three cases:

- without control (Open Circuit (OC)): without closing the circuit. Therefore, the electrical current caused by induction from the incoming pressure is deleted;
- with $\eta_M = \eta_K = 1$ and $\eta_R = 1/8$;
- with $R_d/S_d = \rho_0 c_0 = 418.46$ kg.m.s^{-2}, meaning that $\eta_R \approx 2.068$, and with $\eta_K = \eta_M = 1$.

In Fig. 3.11a, the ER's response with $\eta_R = 1/8$ show a significant increase in amplitude, as expected due to the reduced damping. Compared to the OC case, the resonance is considerably amplified. Notice that the resonance for the $\eta_R = 2.068$ is more damped in this case than in the OC case, as the original damping is multiplied by 2. The resonance frequency appears to shift to higher frequencies, although this shift is small due

to the increased damping, which broadens and flattens the resonance peak. The particular case of $R_d = \rho_0 c_0$ enables targeting the impedance $Z(s) = \rho_0 c_0$. The horizontal black dashed lines in the amplitude plot indicate the target impedance values $Z = R_0/S_d$, $Z = R_0/8S_d$ and $Z = \rho_0 c_0$. The control strategy, both with IIR and RTI, successfully brings the ER's response to the targeted impedance at resonance for each measurement. Achieving the $\rho_0 c_0$ impedance in linear acoustic resonators enables efficient sound absorption under normal incidence conditions.

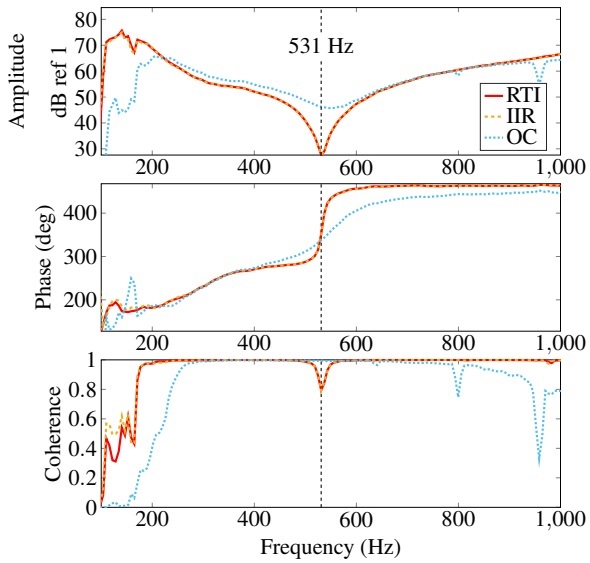

(a) $\eta_K = 1$, $\eta_R = 1/8$, $\eta_M = 1$

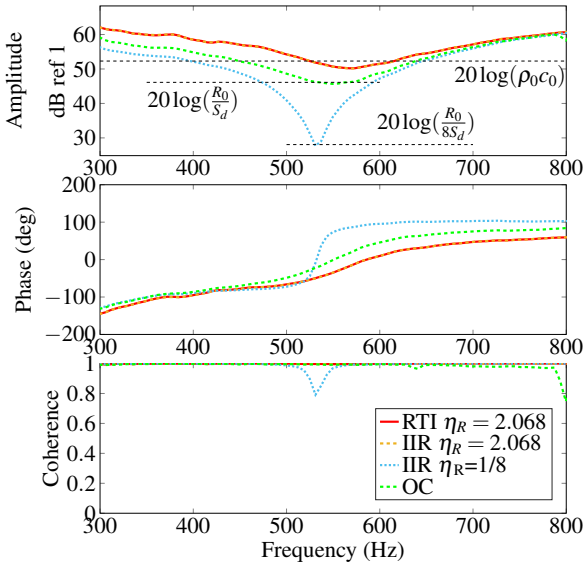

(b) $\eta_K = 1$, $\eta_R = 2.068 \Leftrightarrow R_d = \rho_0 c_0$, $\eta_M = 1$

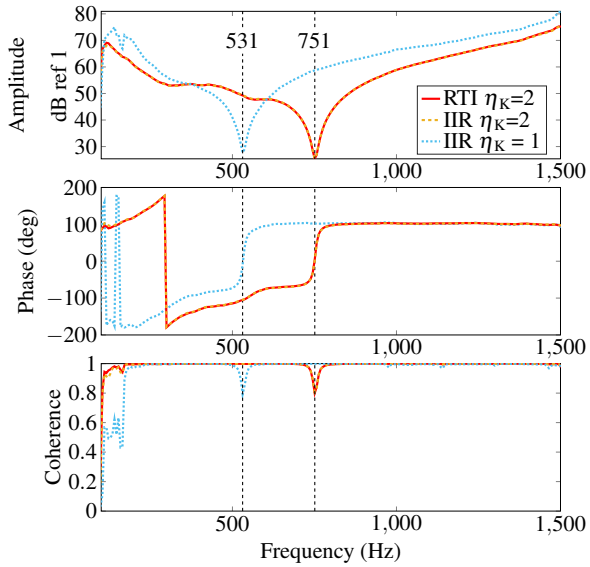

(c) $\eta_K = 2$, $\eta_R = 1/8$, $\eta_M = 1$

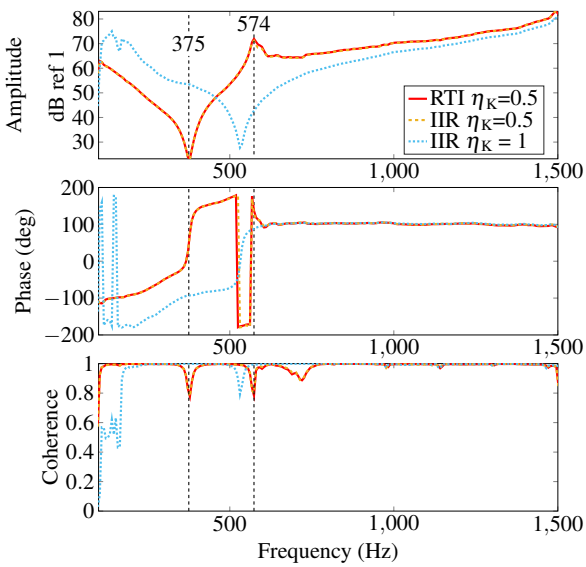

(d) $\eta_K = 0.5$, $\eta_R = 1/8$, $\eta_M = 1$

Fig. 3.11 Amplitude, phase and coherence of the mobility $Y(s) = v(s)/p(s)$ for different cases.

Figures 3.11c and 3.11d present the mobility transfer function with two different values of η_K: $\eta_K = 2$ or $\eta_K = 0.5$, while keeping $\eta_M = 1$ and $\eta_R = 1/8$ in both cases. Changing the η_K parameter enables the adjustment of the effective stiffness, thereby modifying the frequency of the ER's resonance, as shown in both figures. Targeting $\eta_K = 2$ yields the desired frequency $f_d = \sqrt{\eta_K} f_0 = f_0\sqrt{2} \approx 751$ Hz. As shown in Fig.3.11c, the experimentally measured resonance frequency is 750.7 Hz, confirming the high precision of the control strategy in increasing the effective stiffness. Conversely, reducing $\eta_K = 0.5$ should lead to a decrease in the target

resonance frequency, calculated as $f_d \approx 375$. Figure3.11d confirms that the experimental system effectively reaches this target, with the resonance peak observed at approximately 375 Hz. These results highlight the ability of the control strategy to accurately shift the resonance frequency in both directions, towards higher and lower frequencies, by tuning the stiffness parameter. Notice that the IIR and RTI methods exhibit the same behavior across the entire frequency bandwidth, which validates the accuracy and behavior of the developed RTI-based approach. However, in both configurations, the first eigenmode of the loudspeaker disrupts the control outcome at its resonance frequency. Observe that the phase of the transfer functions show perfectly normal behaviors with phase inversion at resonances for all parameters 3.11.

For the case of $\eta_K = 2$, a resonance appears slightly above the eigen resonance frequency f_0, underlining that the inherent first mode of the loudspeaker is not deleted by the control strategy for both IIR and RTI methods. This behavior is consistent with the predictions of the numerical simulations. A small localized increase in the mobility is also observed just before 500 Hz. In addition, a slight loss of coherence and a modification of the phase can be observed. In the case of $\eta_K = 0.5$, a peak appears after the eigen resonance frequency of the loudspeaker at 574 Hz, followed by a significant loss of coherence. These effects are attributable to various main causes:

- The control strategy's inability to eliminate structural eigenmodes;
- Uncertainties in the loudspeaker's model lead to an imperfect targeted resonator;
- Acoustic feedback and environmental influence, that are not modeled in the numerical predictions here.

The RTI and IIR control methods both demonstrate an excellent precision in targeting desired resonance frequencies and acoustic impedances. The validity of the RTI implementation is confirmed through direct comparison with the IIR approach, showing consistent frequency responses across a wide frequency range. However, both methods are unable to delete the loudspeaker's inherent eigenmode. This phenomenon is a result of the control's inherent nature. The suppression of the remaining resonance might be realized through various approaches.

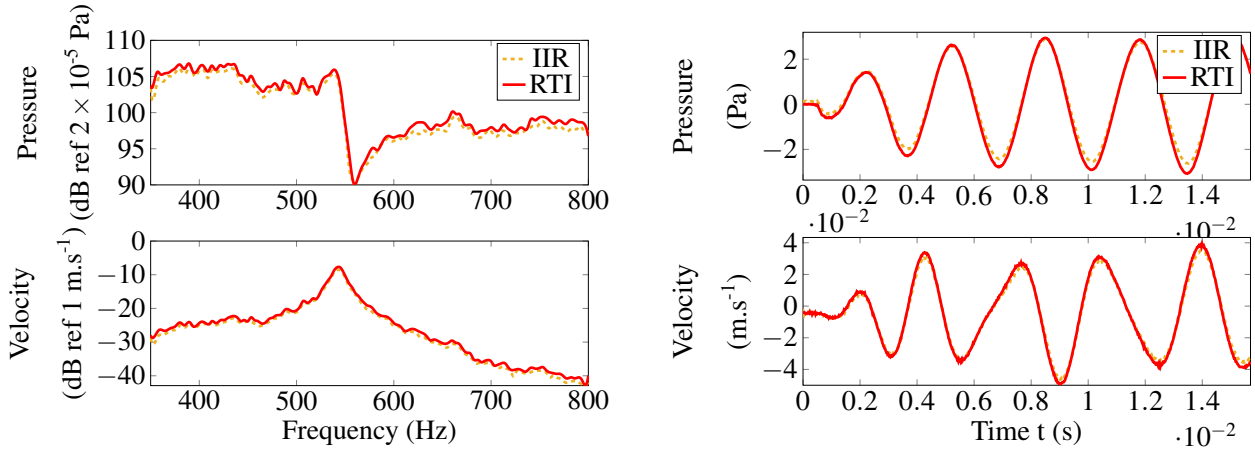

(a) (b)

Fig. 3.12 Comparison of the ER responses in pressure and velocity, controlled by either RTI or IIR algorithms in case of (a) stationary regime, and (b) transient regime.

The target parameters are selected to match those of the numerical simulations: $\eta_M = \eta_K = 1$ and $\eta_R = 1/8$. The ER responses in terms of the membrane velocity and the nearby pressure are plotted in Fig. 3.12, showing excellent agreement both for the envelops of the stationary solutions (Fig. 3.12a) within the frequency range of

external excitation, and for the transient regime (Fig. 3.12b). The frequency plots in Fig. 3.12a feature a linear resonance at these excitation amplitudes for both methods. Additionally, the time plots in Fig. 3.12b highlight an extremely close transient behavior of both methods. These results validate the RTI control for linear target dynamics in the transient regime as well.

Nonlinear target dynamics

To confirm that a nonlinear behavior can be synthesized using the presented method, the desired dynamics is taken as a nonlinear SDOF resonator as described in Eq. (3.23) with $\eta_M = 1$ and $\eta_R = 1/8$. Both increasing and decreasing frequency sweeps are performed. The envelopes of the membrane velocity, the nearby pressure and the computed electrical current during the experiment are presented in Fig. 3.13 for two distinct cases: with $\beta_{\mathrm{NL}} = 10^{10}$ m^{-2} (Fig. 3.10b) and $\beta_{\mathrm{NL}} = -10^{10}$ m^{-2} (Fig. 3.13b). In both cases, the ER's response exhibits a distinct response depending on the direction of the frequency sweep, which is typical of nonlinear resonators. Specifically, in Fig. 3.13a, the ER's response reveals a hardening behavior, as expected from the positive value of β_{NL}, whereas a softening behavior can be observed in Fig. 3.13b resulting from the negative value of β_{NL}. It indicates that the control strategy enables the creation of nonlinear resonators at identical amplitudes (under 110 dB) as the preceding linear control. Furthermore, the choice of the behavior, hardening or softening, can be selected by adjusting the sign of the nonlinear parameter β_{NL}. Notably, in the softening case, the desired linear frequency is set to $f_d = 751$ Hz, demonstrating that both the nonlinear behavior and the baseline linear frequency can be independently prescribed and simultaneously enforced on the ER.

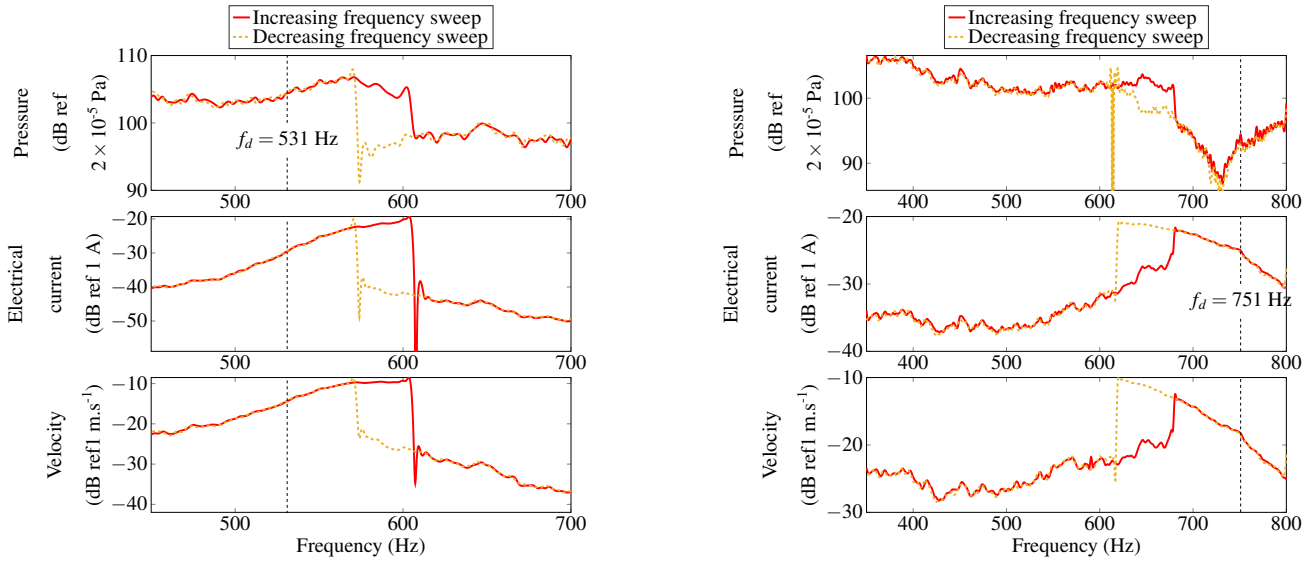

(a) $\eta_K = 1$, $\beta_{\mathrm{NL}} = 10^{10}$ m^{-2} (b) $\eta_K = 2$, $\beta_{\mathrm{NL}} = -10^{10}$ m^{-2}

Fig. 3.13 Envelopes of the velocity of the membrane, pressure close to it, and electrical current computed during the experiment under a sine sweep excitation with $\eta_M = 1$ and $\eta_R = 1/8$.

Another well-documented characteristic of nonlinear systems is their ability to scatter energy towards higher or/and lower harmonics. It is known that the nonlinear resonators scatter more energy towards higher frequencies [118]. The Power Spectrum Density (PSD) calculated from the Short Term Fourier Transform (STFT) (Spectrogram) of the pressure measured close to the ER's membrane for an increasing frequency sweep excitation are plotted in Fig. 3.14a. Observe that the ER's response is not purely monoharmonic: an additional harmonic component emerges between 12s and 17s. After 17s, the harmonic generation is stopped, coinciding with the

bifurcation at 17s shown in the time signal of the measured pressure depicted in Fig. 3.14b. Observe that the bifurcation stops the scattering of energy towards higher frequencies. The corresponding Fast Fourier Transform (FFT) of the measured pressure is presented in the same figure. The FFT reveals that higher harmonics are generated from 1400 Hz up to approximately 1820 Hz, with the bifurcation occurring at 605 Hz. Assuming the system produces third-order harmonics, a fundamental frequency of 605 Hz would yield a harmonic at $3 \times 605 = 1815$ Hz, which closely aligns with the observed upper harmonic bound. Furthermore, the presence of harmonics starting from 1400 Hz suggests that the ER produces higher-order components for lower fundamental frequencies, beginning around $1400/3 \approx 467$ Hz. This confirms that the nonlinear ER behaves similarly to a classical Duffing oscillator, exhibiting key features such as bifurcations, and energy scattering. Additionally, the resonance and bifurcation frequency are clearly identifiable on the FFT plot.

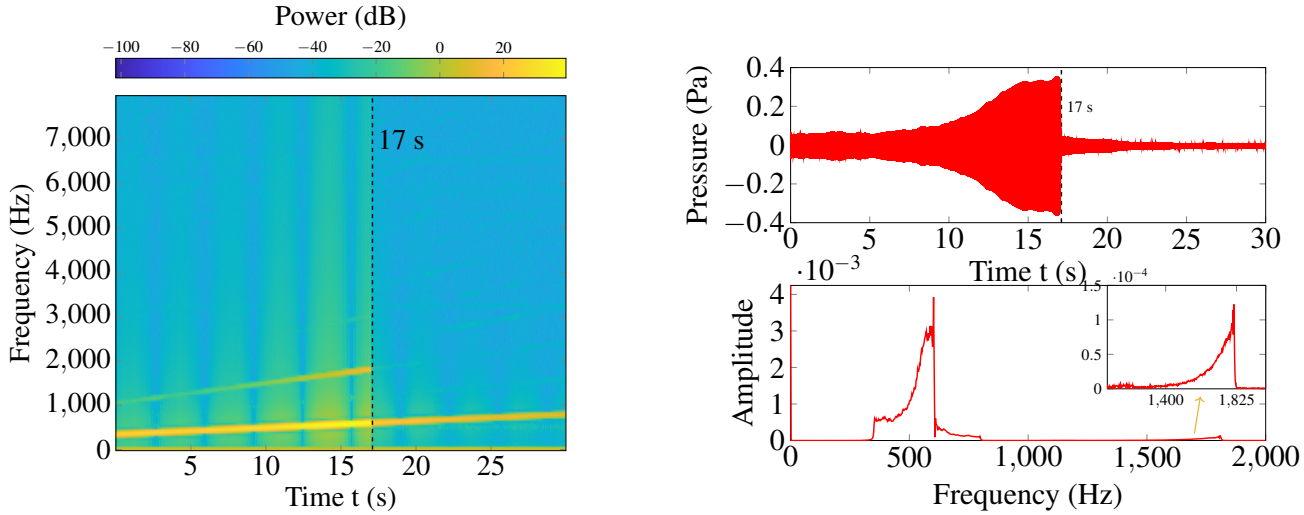

(a) Spectrogram of the measured pressure

(b) Time signal and FFT of the measured pressure

Fig. 3.14 Time signal, Spectrogram and FFT of the measured pressure close to the loudspeaker's membrane with $\eta_R = 1/8$, $\eta_K = \eta_M = 1$ and $\beta_{\text{NL}} = 10^{10}$ m^{-2}.

3.4.3 Study of the classical nonlinear behaviors

Let us define G the amplifying gain imposed to the excitation signal, until now equal to $G = 0.1$. To further validate that the proposed control strategy successfully synthesizes a nonlinear resonator exhibiting classical nonlinear behaviors, parametric study is conducted on the nonlinear parameter β_{NL} and on the excitation amplitude through the gain G. Figure 3.15a presents the normalized envelopes (normalized by G) of the measured membrane velocity for various values of β_{NL}, while Fig. 3.16a illustrates the effect of varying G. The results clearly demonstrate that increasing either β_{NL} or G leads to a shift of the bifurcation frequency toward higher values. Observe that the amplitude of the nonlinear resonance decreases with G and with β_{NL}. These phenomena are typical of nonlinear hardening resonators.

At low values of both the nonlinear parameter β_{NL} and the excitation gain G, the system's response does not feature a bifurcation. It is due to the nonlinear threshold value not being reached. Indeed, lower values of β_{NL} require higher excitation amplitudes to reach amplitudes enabling the jumping phenomena. Similarly, the nonlinear parameter must be chosen accordingly with the excitation amplitudes to maintain the same properties for all excitation amplitudes. It indicates that this control strategy works for all excitation amplitudes (from 80 dB Sound Pressure Level (dB SPL) to 115 dB SPL), provided the loudspeaker operates within its linear regime, in

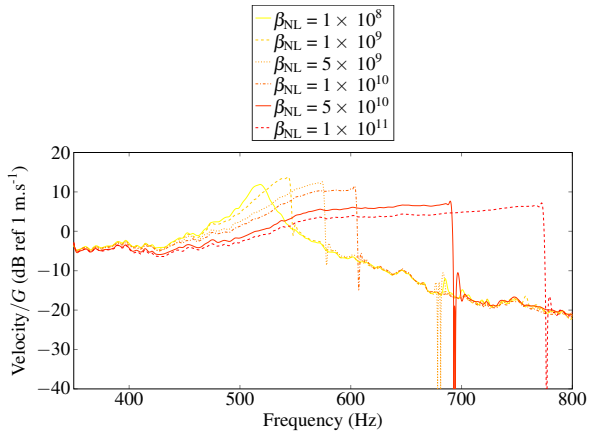

(a) Normalized envelopes of the measured velocity with $G = 0.1$.

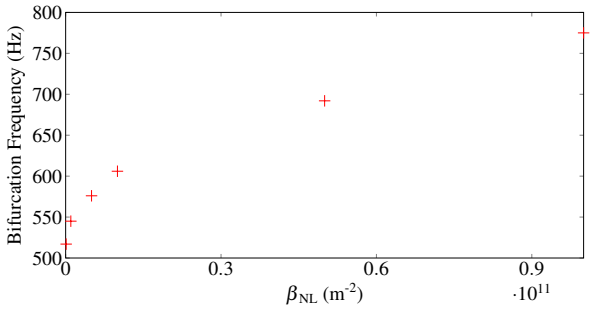

(b) Jumping frequency of the increasing frequency sweeps with respect to the value of the nonlinear parameter β_{NL}

Fig. 3.15 Parametric study of the nonlinear parameter: ER's membrane velocity envelopes and bifurcation frequencies with the parameters $\eta_M = 1$, $\eta_K = 1$, $\eta_R = 1/8$.

addition to the fact that the nonlinear parameter is chosen wisely. Indeed, the nonlinear phenomena observed for $G = 0.3$ can be reproduced at $G = 0.005$ with higher values of β_{NL}, provided that the sensor operates within its amplitude bandwidth of sensitivity. To further characterize the nonlinear behavior, the envelopes of the membrane velocity for varying excitation gains are plotted in Fig. 3.16b. The black points denote the estimated backbone curve of the system determined by the maximal amplitude point of the envelope of the frequency sweep. Observe that the backbone curve clearly shows the hardening behavior and complies with the classical shape of a backbone curve of a hardening Duffing oscillator. It is worth noting that this can not be strictly considered as the backbone curve of the system, as the jumping phenomenon can happen at lower frequencies than the actual bifurcation. The proper investigation of the nonlinear resonator can be realized through the use of experimental continuation, either by Control-Based-Continuation [144] or by Phase-Locked-Loop [1]. Here, frequency sweeps are used, as the modal parameters of the nonlinear resonator do not need to be identified. However, their identification could have been done to compare with the desired ones, and to determine the bifurcation frequency more accurately [1]. This study is left to future investigations.

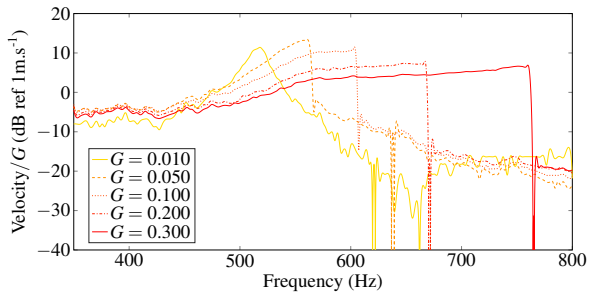

(a) Normalized envelopes of the velocity with $\beta_{NL} = 10^{10}$.

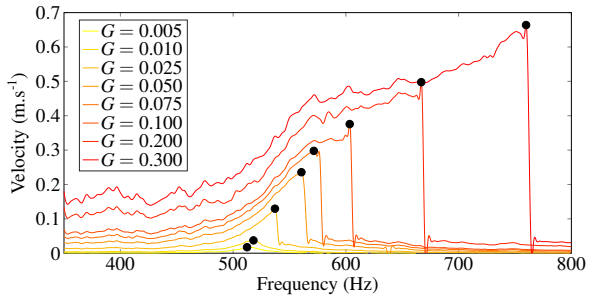

(b) Envelopes of the velocity with $\beta_{NL} = 10^{10}$, and backbone curve of the system.

Fig. 3.16 Parametric study of the excitation amplitudes: envelopes of the ER's membrane measured velocity with the desired parameters $\eta_M = 1$, $\eta_K = 1$, $\eta_R = 1/8$.

Figure 3.15b presents the evolution of the jumping frequency with respect to the value of β_{NL}. It can be seen that the jumping frequency increases with β_{NL}, highlighting the hardening behavior. The nonlinear behavior of

the controlled system aligns with the classical behaviors of Duffing oscillators in terms of the nonlinear parameter and the excitation amplitudes. Figure 3.17 presents a parametric study of the damping coefficient by plotting the envelopes of the ER membrane velocity and the nearby pressure for various values of η_R, under both increasing and decreasing frequency sweeps. A nonlinear resonance region, characterized by the coexistence of two stable equilibrium points, can be identified for $\eta_R = 1/4$ (Fig. 3.17a). This behavior is no longer observable for higher damping values: for $\eta_R = 1/2$ (Fig. 3.17b), $\eta_R = 1$ (Fig. 3.17c), and $\eta_R = 2.068$ (Fig. 3.17d). However, this zone created by the nonlinear resonance is narrowed by the reduction of η_R, compared to the $\eta_R = 1/8$ case (Fig. 4.14a). Additionally, the $\eta_R = 1/2$ case exhibits a resonance that shifts toward the high frequencies despite the loss of the jump. Furthermore, both $\eta_R = 1$ and $\eta_R = 2.068$ cases feature a damped linear response. As a result, the phenomena induced by the nonlinear behaviors can be deleted due to the high values of damping. This effect is demonstrated by the theory and well-known from the literature.

However, it is possible to create nonlinear behaviors with high levels of damping by increasing the nonlinear parameter β_{NL}. To illustrate this case, Fig. 3.18 introduces the envelopes of the ER's membrane velocity and nearby presure, and of the computed electrical current during the experiment for a case with $\eta_M = \eta_K = 1$, a high damping $\eta_R = 2.068$, and a large nonlinear parameter $\beta_{\mathrm{NL}} = 5 \times 10^{13}$ m^{-2}. The nonlinear hardening behavior is clearly observed in the electrical current and membrane velocity signals. However, the pressure does not evidently show the nonlinear behavior featured by the ER. This discrepancy may be attributed to the reduced membrane motion: lower values of displacement, velocity, and acceleration of the ER's membrane during resonance, resulting from the high damping. In addition, the linear absorption of the resonator is enhanced (due to the damping value $\eta_R = 2.068$), which reduces the sound pressure, resulting in a lower resonance amplitude. These observations demonstrate that nonlinear resonators can still be synthesized even under significant damping. Such configurations are particularly valuable in scenarios where high damping is desirable, for instance, to mitigate stability concerns [42].

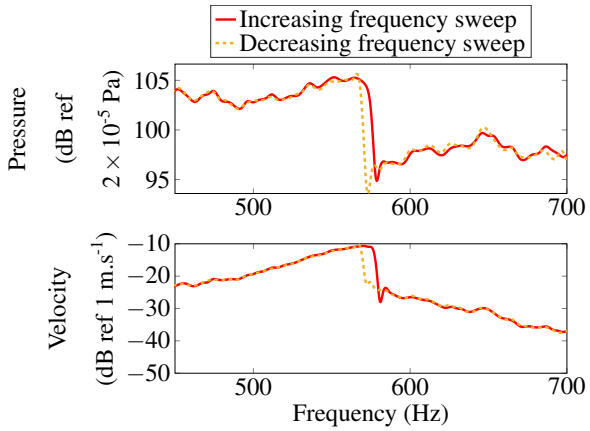

(a) $\eta_R = 1/4$

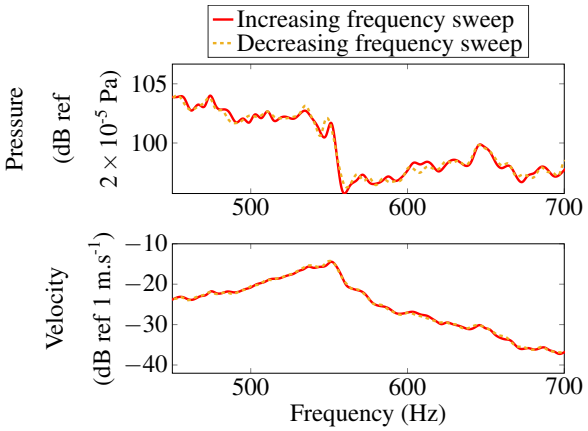

(b) $\eta_R = 1/2$

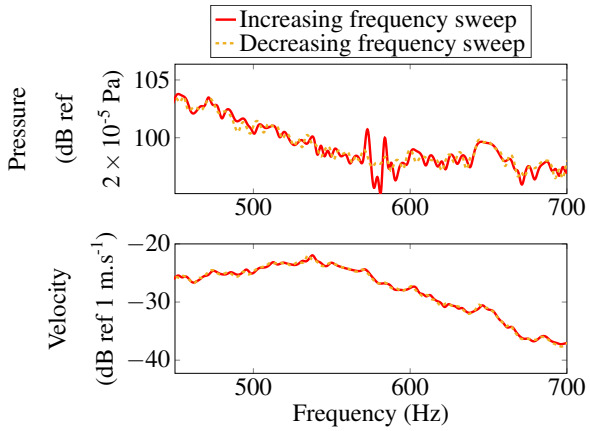

(c) $\eta_R = 1$

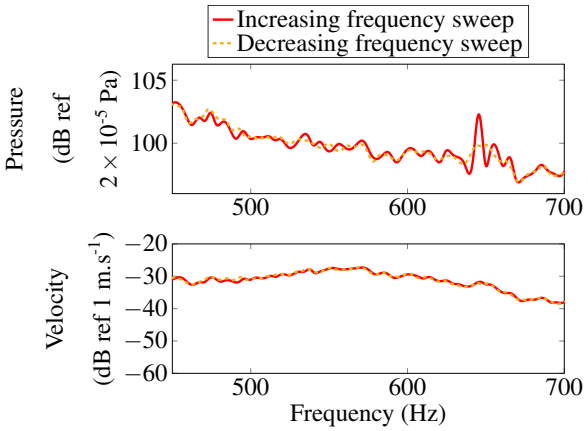

(d) $\eta_R = 2.068 \Leftrightarrow R_d = \rho_0 c_0$

Fig. 3.17 Parametric study of the damping parameter: envelopes of the pressure and velocity of the ER's membrane with $\eta_K = 1$, $\eta_M = 1$ and $\beta_{\text{NL}} = 10^{10}$ m^{-2}

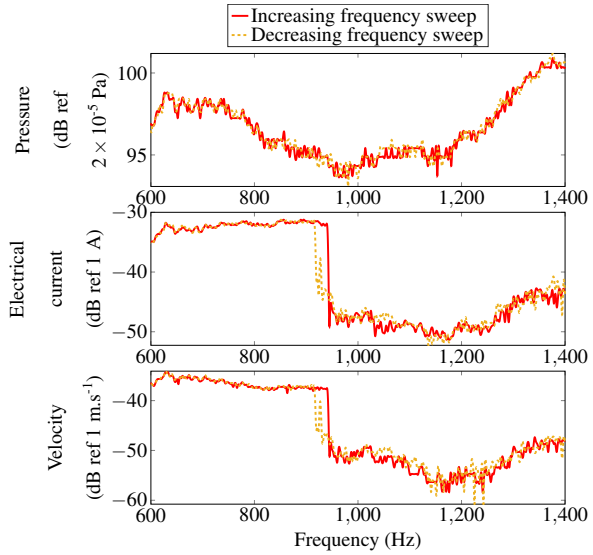

Fig. 3.18 Envelopes of the ER's membrane velocity and pressure close to it and electrical current computed during the experiment with $\eta_M = \eta_K = 1$, $\eta_R = 2.068$, and $\beta_{\text{NL}} = 5 \times 10^{13}$ m^{-2}.

Conclusion of the chapter

This chapter provides the mathematical framework and basic assumptions of the designed control strategy. Numerical and experimental tests validate the theoretical developments, while highlighting the limitations of the control strategy. The main contributions are:

- The mathematical framework that gives the needed assumptions and conditions to use the model inversion strategy with a setpoint defined by an exosystem;
- The analytical demonstration of the asymptotic convergence showing the unconditional convergence of the control strategy;
- The creation of digitally programmable nonlinear resonators at low excitation amplitudes (under 110 dB).

Although the chapter covers the main results, some perspectives can be highlighted:

- Prove the asymptotic convergence Eq. (3.8) for the general formulation of the control strategy;
- The application of the control strategy for other goals and transducers, such as the artificial creation of nonlinear sensors at low excitation amplitudes for adaptive sensibilities. Moreover, the application of such control strategy to the plasmacoustic transducers from [140], or to piezoelectric materials would open interesting behaviors to investigate;
- Develop a method enabling the overcoming of the appearance of the remaining resonance due to the numerical scheme. Many possibilities can be considered:
  - By dissociating the calculation time-steps with the measurement ones to feed the numerical scheme at intermediate stages;
  - By numerically estimating the pressure at the intermediate stages;
  - By increasing the sampling frequency and using a first-order numerical scheme;
  - By reducing the amplitude of the remaining resonance by adding a feedback loop that necessitates an additional measurement.

  The dissociation of the calculation time-steps from the measurements ones treats the cause of the problem and might be easy to implement. Indeed, it does not require additional sensors, or another acquisition and control device. However, adding a feedback loop with an additional measurement would increase the overall accuracy of the control and can be considered in parallel to the previous proposed improvement.
- The stability of the control strategy applied to the ER must be studied, along with its robustness for targeting its use for applications. The stability of the linear ER with the IIR filter has been conducted in the literature [42, 159], and its extension to the targeting of nonlinear behavior is essential.

Chapter 4

An acoustic two degree of freedom system

This chapter introduces the coupling of the NER with an acoustic mode of a tube. The goals of this chapter are:

- Investigating the capability of the control strategy to accurately enforce an extremely various range of nonlinear behaviors,
- Investigating the capability of the NER to absorb energy and to control an acoustic mode of a tube, and comparing to optimized Tuned Mass Dampers enforced in the ER.

To achieve these two goals, experimental results are produced with three main nonlinear behaviors: a cubic restoring force function (softening and hardening), a logarithmic potential restoring force function and piecewise linear restoring force functions with continuous and discontinuous behaviors. The produced experimental results are studied through analytical methods and numerical simulations.
This chapter is mainly composed of two published journal articles:

- Morell M., Gourdon E., Collet M., Ture Savadkoohi A., De Bono E., Lamarque C.-H. (2024). Towards digitally created electroacoustic resonators for low amplitude sound pressure levels: Modeling and experiments. *Journal of Sound and Vibration*, 548:118437. [114]
- Morell M., Collet M., Gourdon E., Ture Savadkoohi A., De Bono E. (2025). Experimental validation of the analytical modelling of a digitally created duffing acoustic nonlinear oscillator at low amplitudes. *Mechanics & Industry*. 26:2. [112]

4.1 Considered system

4.1.1 Principle and experimental set-up

This section aims at modeling the experimental acoustic set-up in order to predict the system behavior. The experimental set-up has been designed such that it can be modeled as a two-degrees-of-freedom system [35, 16]. The scheme of the experiment is presented in Fig. 4.1 and its model has been widely studied in previous works [16, 35, 74]. It is composed of a circular reduced cross-section tube with radius r_t and length L_t, linked to the ER through a circular cross-section coupling box with radius r_{cb} and length L_{cb}. A coupling box consists of connecting a wider tube to the considered tube, permitting the establishment of a relation between the pressure and the volume variations caused by the displacement of the air particles of the reduced section tube and the displacement of the membrane of the ER. The system is excited through an external loudspeaker which plays the role of an Acoustic Source (AS) placed at the opposite end of the tube. The microphone placed in the reduced section tube is employed to verify the noise attenuation performance achieved by our nonlinear ER, and it does not play a role in the programming. In the following parts, each segment of the experimental set-up will be explained in detail and will be modeled.

For the clarity of the following developments , we define here $I = \mathbb{R} \times [-\pi;\pi] \times [0;L_t + L_{\text{cb}}]$ such that $\mathbf{Y} = (r,\theta,z) \in I$ are the polar coordinates. The orthonormal basis of the polar base coordinates are denoted $(\mathbf{e_r},\mathbf{e}_\theta,\mathbf{e_z}) \in \mathbb{R}^3$. We set the time $t \in \mathbb{R}_+$.

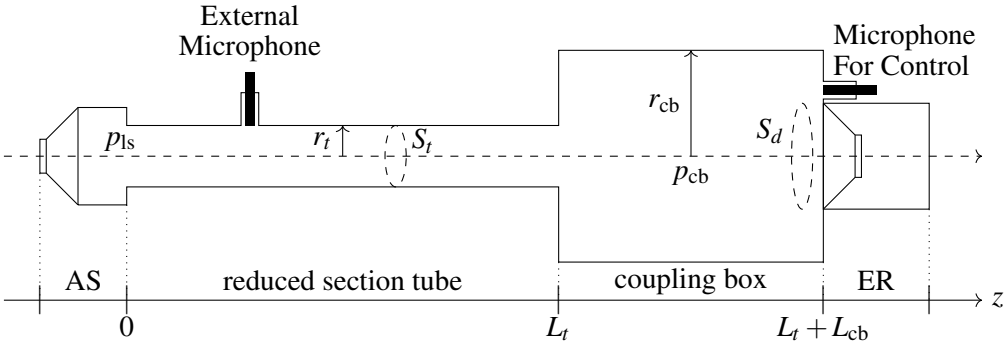

Fig. 4.1 Experimental scheme

4.1.2 Model General Hypotheses

The main general hypotheses classically considered in linear acoustics are reminded in the following. Let us define the main variables of pressure p, velocity $\mathbf{v}$ and mass density ρ as consisting of a constant part (the mean value) and a fluctuating part:

$$\forall(\mathbf{Y},t) \in I \times \mathbb{R}_+ \qquad \begin{cases} p_T(\mathbf{Y},t) = p_0 + p(\mathbf{Y},t) \\ \mathbf{v}_T(\mathbf{Y},t) = \mathbf{v_0} + \mathbf{v}(\mathbf{Y},t) \\ \rho_T(\mathbf{Y},t) = \rho_0 + \rho(\mathbf{Y},t) \end{cases} \tag{4.1}$$

where $p_T : (\mathbf{Y},t) \in I \times \mathbb{R}_+ \longrightarrow \mathbb{R}$ denotes the total pressure. Moreover, $\rho_T : (\mathbf{Y},t) \in I \times \mathbb{R}_+ \longrightarrow \mathbb{R}$ stands for the total mass density of the air, and $\mathbf{v}_T : (\mathbf{Y},t) \in I \times \mathbb{R}_+ \longrightarrow \mathbb{R}^3$ represents the total velocity of the air particles.

Assumption 4.1 *No flow is applied to the fluid, i.e. the fluid is at rest excepted for acoustic waves. Considering Eqs. (4.1), the constant velocity can be supposed equal to 0 such that:*

$$\forall(\mathbf{Y},t) \in I \times \mathbb{R}_+ \qquad \mathbf{v}(\mathbf{Y},t) = \mathbf{v_0} + \mathbf{v}(\mathbf{Y},t), \qquad \textit{where} \qquad \mathbf{v_0} = \mathbf{0}$$

Assumption 4.2 *Fluctuations of pressure, velocity and mass density are small compared to characteristic values. It implies that the medium has a linear response. To satisfy this assumption, the following conditions concerning the fluctuating components of the main variables have to be met [137]:*

$$\forall(\mathbf{Y},t) \in I \times \mathbb{R}_+ \qquad \begin{cases} p(\mathbf{Y},t) << (\rho_0 c^2) \\ ||\mathbf{v}(\mathbf{Y},t)|| << c \\ \rho(\mathbf{Y},t) << \rho_0 \end{cases}$$

where c is the celerity of the acoustic waves. Second-order terms are neglected in the calculations.

Assumption 4.3 *The heat exchange at the events of compression and expansion of a fluid volume subjected to acoustic waves is neglected. We assume that the transformations are adiabatic.*

Assumption 4.4 *The fluid (the air) is considered ideal, i.e viscosity and heat conduction are neglected.*

Assumption 4.5 *The waves are considered to be plane:*

$$\forall(\mathbf{Y},t) \in I \times \mathbb{R} \qquad \begin{cases} p(\mathbf{Y},t) = p(z,t) \\ \mathbf{v}(\mathbf{Y},t) = \mathbf{v}(z,t) \\ v_r(z,t) = v_\theta(z,t) = 0 \\ \rho(\mathbf{Y},t) = \rho(z,t) \end{cases}$$

The section of the largest tube of the experiment allows the first transverse modes to appear above 2 kHz. Nonlinear resonators scatter energy through higher and lower harmonics. While lower harmonics feature higher wavelength, higher harmonics don't and can invalidate this hypothesis. However, depending on the nonlinearity, energy scattering can be neglected as the scattering effect is small. The energy scattering at higher frequencies is left for the study of future works. It ensures plane waves below this excitation frequency.

4.1.3 The acoustic source model

One of the innovations introduced in this work is the functionality of the proposed system at low excitation amplitude. As previously mentioned, acoustic resonators usually need to be excited at high excitation amplitudes to activate their nonlinear behaviors [3, 74, 16]. These sound pressure levels range from 120 dB to 160 dB depending on the characteristics of the device. Part of these amplitudes are not the target amplitudes of this work, as we aim low excitation amplitudes (under 110 dB) in order to obtain a linear acoustic medium and remain within the loudspeaker's linear regime. Indeed, high amplitudes would place the ER loudspeaker in its nonlinear regime, leading to a significant discrepancy between the behavior and the supposed model of the ER loudspeaker. Consequently, low excitation regime is an assumption made for the control of the ER loudspeaker in Sections 3.2 and 4.1.2.

As a result, the considered amplitudes of work are from 70 dB to 105 dB to remain in linear acoustics (a demonstration at 120 dB is realized in the following also). The working frequency is chosen to bound the frequencies of the reduced section tube's first acoustic mode: from 350 Hz to 800 Hz. The lower operating wavelength corresponds to the higher considered frequency, meaning that a 800 Hz frequency signal has a 0.43 m long wavelength, which can be considered relatively large compared to the size of the membrane. This falls under the cutoff frequency of the largest tube (2 kHz).

The acoustic source is modeled as an incident pressure at $z = 0$ (see Fig. 4.1), named p_{ls}.

4.1.4 The reduced section tube model

The model of the reduced section is developed in the following. First, let us consider the mass conservation equation :

$$\frac{\partial \rho_T}{\partial t} + \boldsymbol{\nabla}(\rho_T \mathbf{v}_T) = 0 \tag{4.2}$$

Separating the constant from the fluctuating parts as shown in Eqs. (4.1), replacing the variables in Eq. (4.2), and considering the linear approximation (Assumption 4.2), it reads:

$$\frac{\partial (\rho_0 + \rho)}{\partial t} + \boldsymbol{\nabla}\left(\rho_0 \mathbf{v_0} + \rho_0 \mathbf{v} + \rho \mathbf{v_0}\right) = 0 \tag{4.3}$$

Considering the assumptions that there is no flow (Assumption 4.1) and that the waves are plane (Assumption 4.5), the mass conservation equation simplifies:

$$\frac{\partial \rho}{\partial t}(z,t) + \rho_0 \frac{\partial v_z}{\partial z}(z,t) = 0 \tag{4.4}$$

where v_z denotes the air particles velocity in the z direction, defined by $v_z : (z,t) \mapsto \mathbf{v}(z,t).\mathbf{e_z}$. The air equation of state inside the cavity can be obtained using the adiabatic transformations assumption 4.3 in the limitations of the linear approximation assumption 4.2. It states that:

$$\frac{\partial p}{\partial \rho} = c_0^2 \tag{4.5}$$

where $c_0 = \sqrt{(\gamma p_0)/\rho_0} = \sqrt{\gamma RT/M}$ with γ the specific heat ratio, M the molar mass of the fluid and R the perfect gas constant. It can be seen that the velocity of acoustic waves is directly dependent of the temperature. We replace the preceeding expression in Eq. (4.4), and we set that $\mathbf{u} : (\mathbf{Y},t) \in I \times \mathbb{R}_+ \longrightarrow \mathbb{R}^3$ stands for the air particles displacement such that $v_z = \dfrac{\partial u_z}{\partial t}$. The expression yields:

$$\frac{1}{c_0^2}\frac{\partial p}{\partial t}(z,t) + \rho_0 \frac{\partial^2 u_z}{\partial t \partial z}(z,t) = 0 \tag{4.6}$$

Integrating with respect to time $t \in \mathbb{R}_+$ does not introduce non-zero constant as the mean value of the fluctuating part is equal to 0. Considering only fluctuating variables in stationary regimes, the constant can always be considered as being zero. It gives:

$$p(z,t) = -\rho_0 c_0^2 \frac{\partial u_z}{\partial z}(z,t) \tag{4.7}$$

The linearized Euler equation for a non-viscous fluid, with plane waves (Assumption 4.5) and without flow (Assumption 4.1) reads:

$$\rho_0 \frac{\partial^2 u_z}{\partial t^2}(z,t) = -\frac{\partial p}{\partial z}(z,t) \tag{4.8}$$

By replacing Eq. (4.7) in Eq. (4.8), one can obtain:

$$\rho_0 \frac{\partial^2 u_z}{\partial t^2}(z,t) = \rho_0 c_0^2 \frac{\partial^2 u_z}{\partial z^2}(z,t) \tag{4.9}$$

A weak formulation is derived to study the system. Let $u_z^* : (z,t) \in H^1([0;L_t]\times\mathbb{R}) \longrightarrow \mathbb{R}$ be a virtual displacement field that is kinematically admissible, continuous, and differentiable with respect to coordinate z and time t. Multiplying Eq. (4.9) by u_z^* and integrating over the volume yields the variational formulation of Eq. (4.9):

$$\int_0^{L_t} \rho_0 \frac{\partial^2 u_z}{\partial t^2} S_t u_z^* \mathrm{d}z = \int_0^{L_t} \rho_0 c_0^2 \frac{\partial^2 u_z}{\partial z^2} S_t u_z^* \mathrm{d}z \tag{4.10}$$

After an integration by parts and using Eq. (4.7) at $z=0$, and $z=L_t$, this yields:

$$\int_0^{L_t} \rho_0 \frac{\partial^2 u_z}{\partial t^2} S_t u_z^* \mathrm{d}z = -\int_0^{L_t} \rho_0 c_0^2 S_t \frac{\partial u_z}{\partial z}\frac{\partial u_z^*}{\partial z}\mathrm{d}z - S_t u_z^*(L_t,t) p_{\mathrm{cb}} + S_t u_z^*(0,t) p_{\mathrm{ls}} \tag{4.11}$$

Let us consider the boundary conditions at each end of the reduced section tube:

$$\begin{cases} u_z(0,t) = -u_{\mathrm{ls}}(t) \\ u_z(L_t,t) = u_{\mathrm{cb}}(t) \end{cases} \tag{4.12}$$

where the displacement is positive when the air goes out of the tube.
Let us suppose that the response of the system is dominated by its first mode (Assumption 3.2). This assumption is reasonable as the operating excitation frequencies are chosen accordingly. We suppose the additional assumption:

Assumption 4.6 *The shape function of the first mode's response of the reduced section tube with the boundary conditions Eqs. (4.12) is similar to the shape function with the conditions:*

$$\forall t \in \mathbb{R}_+ \qquad p(0,t) = p(L_t,t) = 0$$

Taking into account the assumption, the assumed shape function of the first mode is calculated using an open-open tube. We use a Rayleigh-Ritz [16] method considering that:

$$u_z(z,t) = u_a(t)\Phi_1(z) = u_a(t)\left(-\cos\left(\frac{\pi z}{L_t}\right)\right) \tag{4.13}$$

where $\Phi_1 : [0;L_t] \longrightarrow \mathbb{R}$ is the shape function (which represents also the first acoustic mode of the tube), and $u_a : \mathbb{R}_+ \longrightarrow \mathbb{R}$ stands for the modal coordinates. The same considerations are applied to the virtual displacement. The projection of Eq. (4.11) on the mode yields:

$$\left(\frac{\rho_0 S_t L_t}{2}\right)\ddot{u}_a(t) + \left(\frac{\rho_0 c_0^2 S_t \pi^2}{2L_t}\right)u_a(t) = -S_t\left(p_{\mathrm{cb}}(t) + p_{\mathrm{ls}}(t)\right) \tag{4.14}$$

The objective of a model is to closely represents the reality. However, the experiments revealed the need to model a damping coefficient. The choice of linear viscous damping is arbitrary. In typical structural or fluid-structure dynamics problems [22], it is often assigned a viscous term to synthesize the multi-physical

phenomena contributing to the modal dissipation (such as mechanical damping and visco-thermal losses). The corresponding modal viscous coefficient is then usually estimated experimentally [52]. This formalism is kept in the reduced model by introducing a viscosity contribution in Eq. (4.14), proportional to c_a. This parameter is obtained by experimental measurements and a brief study of its influence on the numerical results is presented in B.3. We obtain:

$$m_a\ddot{u}_a(t) + c_a\dot{u}_a(t) + k_a u_a(t) = -S_t\big(p_{\text{cb}}(t) + p_{\text{ls}}(t)\big) \tag{4.15}$$

The modal mass m_a and modal stiffness k_a of the first acoustic mode of the reduced section tube reads:

$$\begin{cases} m_a = \dfrac{\rho_0 S_t L_t}{2} \\ k_a = \dfrac{\rho_0 c_0^2 S_t \pi^2}{2L_t} \end{cases} \tag{4.16}$$

4.1.5 The coupling box model

A weak coupling between two systems allows to compare with theoretical work from the literature, in addition to the difficulty to create a strong coupling with the acoustic resonator. The goal of introducing the coupling box into the system is to maintain a weak coupling between the primary system to be controlled (the reduced section tube) and the added system (the ER). The air inside the coupling box is either compressed or expanded, thereby increasing or reducing the air particle density. The variations in the particles density generate a pressure force proportional to the amount of displaced air, either in the outward or inward direction respectively. This mechanism is extremely similar to the force of a spring.

To achieve such a condition through the coupling box, a compromise between length and section has to be found. The coupling box's volume should be large in order to create a weak coupling. Moreover, its section is chosen to be large enough compared to the ones of the narrowed tube section and the membrane of the ER. Additionally, the length of the coupling box should be kept relatively short compared to the wavelengths of the working frequencies to use the following assumption:

Assumption 4.7 *The spatial distribution of pressure along the z axis within the coupling box is constant.*

We aim to establish the relationship between the pressure inside the coupling box and its volume variations. Let us consider the previously proven Eq. (4.7). The pressure is expressed as a being proportional to the gradient of the air particles displacement. It can be seen as proportional to a rate of compression or expansion of the air particles. Let us consider the entire length of the coupling box (defined by the interval $[L_t; L_t + L_{\text{cb}}]$), the pressure in the coupling box, denoted p_{cb}, can be expressed as a function of its volume variation:

$$p_{\text{cb}}(t) = -\rho_0 c_0^2 \frac{\Delta V_{\text{cb}}(t)}{V_{\text{cb},0}} \tag{4.17}$$

where $V_{\text{cb},0}$ represents the initial volume of the coupling box, ρ_0 is the air density, and c_0 is the velocity of the sound in the air. The variation of volume ΔV_{cb} can be described in terms of displacements of the membrane of the ER and of the modal air mass of the tube with a reduced-section. A positive displacement u_a of the tube acoustic mode participates in decreasing the volume of the coupling box, while a positive displacement of the ER x in increasing the volume. It gives:

$$\Delta V_{\text{cb}}(t) = -S_t u_a(t) + S_d x(t) \tag{4.18}$$

Finally, Eq. (4.17) reads:

$$p_{\mathrm{cb}}(t) = k_b\Big(S_t u_a(t) - S_d x(t)\Big) \tag{4.19}$$

with $k_b = \dfrac{\rho_0 c_0^2}{V_{\mathrm{cb},0}}$.

4.1.6 Coupled equations of the two-degree-of-freedom model

Each segment of the overall system has been described individually. Equations of the coupled systems can be constructed by incorporating boundary conditions. The considered ER model is given by the desired behavior equation Eq. (3.13) in the tube with the compatibility condition $p = p_{\mathrm{cb}}$:

$$M_d\ddot{x}(t) + R_d\dot{x}(t) + F_{\mathrm{NL}}(t,x) = S_d p_{\mathrm{cb}}(t) \tag{4.20}$$

Equations (4.15) and (4.20) yield the system of equations:

$$\begin{cases} m_a\ddot{u}_a(t) + c_a\dot{u}_a(t) + k_a u_a(t) = -S_t\big(p_{\mathrm{cb}}(t) + p_{\mathrm{ls}}(t)\big) \\ M_d\ddot{x}(t) + R_d\dot{x}(t) + F_{\mathrm{NL}}(t,x) = S_d p_{\mathrm{cb}}(t) \end{cases} \tag{4.21}$$

Introducing Eq. (4.19) into Eq. (4.21) yields the weakly coupled two-degree-of-freedom system of equations:

$$\begin{cases} m_a\ddot{u}_a(t) + c_a\dot{u}_a(t) + k_a u_a(t) + S_t\big(k_b\big(S_t u_a(t) - S_d x(t)\big)\big) = -S_t(t) p_{\mathrm{ls}}(t) \\ M_d\ddot{x}(t) + R_d\dot{x}(t) + F_{\mathrm{NL}}(t,x) - S_d\big(k_b\big(S_t u_a(t) - S_d x(t)\big)\big) = 0 \end{cases} \tag{4.22}$$

We set $\gamma = k_b S_t S_d$ and $\alpha = S_d/S_t$. The system can be further rearranged as:

$$\begin{cases} m_a\ddot{u}_a(t) + c_a\dot{u}_a(t) + k_a u_a(t) + \dfrac{\gamma}{\alpha}\big(u_a(t) - \alpha x(t)\big) = -S_t p_{\mathrm{ls}}(t) \\ M_d\ddot{x}(t) + R_d\dot{x}(t) + F_{\mathrm{NL}}(t,x) + \gamma\big(\alpha x(t) - u_a(t)\big) = 0 \end{cases} \tag{4.23}$$

This system appears to be close to a weakly coupled two-degree-of freedom system. However, it is worth noting that the weak coupling in this system appears to be non-reciprocal. This is a consequence of formulating the equations in terms of forces. The formulation in terms of pressure, which is the common acoustic approach, results in a reciprocal coupling. In fact, the system of equations can be expressed using the acoustic parameters m_a/S_t, c_a/S_t, k_a/S_t, M_d/S_d and R_d/S_d:

$$\begin{cases} \dfrac{m_a}{S_t}\ddot{u}_a(t) + \dfrac{c_a}{S_t}\dot{u}_a(t) + \dfrac{k_a}{S_t}u_a(t) + \dfrac{\gamma}{S_d}\big(u_a(t) - \alpha x(t)\big) = -p_{\mathrm{ls}}(t) \\ \dfrac{M_d}{S_d}\ddot{x}(t) + \dfrac{R_d}{S_d}\dot{x}(t) + \dfrac{1}{S_d}F_{\mathrm{NL}}(t,x) + \dfrac{\gamma}{S_d}\big(\alpha x(t) - u_a(t)\big) = 0 \end{cases} \tag{4.24}$$

The coupling between the mechanical behavior of the ER, and the acoustic behavior of the tube allows one to choose either of the formulations. In the following, the formulation in terms of forces defined Eq. (4.23) is employed.

4.2 Numerical Simulations

The model has been studied to enable the prediction and optimization of the coupled system's behavior. Using the model, the parameters for the equal-peak design of a Tuned Mass Damper (TMD) programmed as a linear

oscillator $F_{NL}(t,x) = K_d x(t)$ can be computed by numerical optimization, for comparing nonlinear resonators to linear ones. It enables to check that the nonlinear behaviors can be used for acoustic absorption.
Moreover, as the control strategy is not included in the model (it assumes that the control strategy enables the desired behavior to be perfectly applied), the imperfections of the control strategy and of the delay of the numerical scheme does not appear on the numerical simulations. However, it permits the comparison of the obtained behavior with the desired one. As a result, the comparison of the results can confirm that the obtained experimental behavior is close to the desired one: is the non-linear behavior precisely obtained, or only an approximated behavior can be obtained with this method ?

To obtain the closest comparison, the model presented in Eq.s (4.24) is solved using a 4th order Runge-Kutta scheme with a 50 kHz sampling frequency. The parameters of the model are retrieved from the characterization of the experiment, and the desired parameters programmed in the resonator. Many parameters can influence the quality of the simulation results as it is seen below: S_d, c_a, m_a... As a result, a sensitivity analysis could be of great interest in this work. However, as c_a has a great influence on the solution, only a sensitivity analysis of the c_a parameter is proposed in Appendix B, along with the analysis of the influence of a non-modeled anti-resonance. The FRC of the rigid-termination configuration is also demonstrated in Appendix B. As seen in the following, the results are in good agreement with the experimental ones, lowering the interest of the sensitivity analysis.

To compare the results obtained from numerical simulations and from the experiment, two main characteristics arise:

- Observe that the experimental microphone is not placed at the middle of the reduced section tube (S_t-tube), which require the additional correction of the numerical results. The model assumes the mode shape of the acoustic mode of the tube, resulting in the assumption that the displacement is maximum at the middle of the tube. The variable separation from the Rayleigh-Ritz method enables to compute the displacement at another location z of the tube:
$$u_z(z,t) = u_a(t)\left(-\cos\left(\frac{\pi z}{L_t}\right)\right) \tag{4.25}$$
Knowing that the microphone is placed at $z = 5.5$cm, the displacement obtained by numerical simulations is calculated at the microphone location afterwards for comparison to the experimental data. Notice that the mode shape is obtained under the assumption of an open-open tube model, which is false in practice (e.g. the coupling box pressure is not zero). As a result, the maximum amplitude is not exactly in the middle of the tube, which is an additional uncertainty of the model.

- Observe that the numerical simulations are obtained from a model formulated in terms of displacement of the modal masses. However, the experimental data is retrieved from a microphone that gives the pressure inside the reduced section tube. As a result, the conversion of the numerical results from displacement to pressure is needed to make the comparison. For that purpose, the following formula (valid for propagative waves) can be used:
$$p(x,t) = \rho_0 c_0 \frac{\partial u_z}{\partial t}(x,t) = \rho_0 c_0 \left(-\cos\left(\frac{\pi z}{L_t}\right)\right)\frac{\partial u_a}{\partial t}(t) \tag{4.26}$$
This formula is sufficient in this case, but an extended version that takes into account the incident and reflected waves could be used.

The comparison of the numerical results with the experimental ones are presented in the next section, validating the model.

4.3 Analytical study

The model Eqs. (4.24) are studied through an analytical method : the Multiple Scale Method (MSM) [118] with the use of the Complex variables of Manevitch [107]. The calculations for a general nonlinear stiffness are conducted and detailed in Appendix C in Section C.1. This section aims at briefly summarizing the principle of the method and the main results that are developed in the Appendix.

To simplify the analytical developments, Eqs. (4.24) are reduced to a dimensionless form, via the following changes of variables:

$$\tau = \omega_0 t = \sqrt{\frac{k_a}{m_a}} t \tag{4.27}$$

The variables u_a (subscript $a \equiv$ air) and x are re-scaled such as $u_a = O(1)$ and $x = O(1)$ with the following:

$$\begin{cases} u_a \to \chi u_a \\ x \to \chi x \end{cases} \tag{4.28}$$

Finally, to conduct the Multiple Scale Method, a book-keeping parameter $\varepsilon << 1$ is defined such as:

$$\begin{cases} \dfrac{c_a}{\sqrt{k_a m_a}} = \varepsilon \xi_a \\ \dfrac{\gamma}{\alpha k_a} = \varepsilon \gamma_0 \\ \dfrac{S_t P}{k_a \chi} = \varepsilon f \\ \dfrac{R_t}{M_t}\sqrt{\dfrac{m_a}{k_a}} = \xi_m \\ \dfrac{\gamma}{\alpha k_a}\dfrac{m_a \alpha}{M_t} = \gamma_0 \mu \\ \dfrac{m_a}{M_d k_a \xi} F_{\mathrm{NL}}(\tau, \xi x) = \zeta \tilde{F}_{\mathrm{NL}} \end{cases} \tag{4.29}$$

where $\tilde{F}_{\mathrm{NL}}$ is the nonlinear restoring force after re-scaling equations. It yields the following equations:

$$\begin{cases} u_a'' + \varepsilon \xi_a u_a' + u_a + \varepsilon \gamma_0 (u_a - \alpha x) = -\varepsilon f \sin(\nu \tau) \\ \varepsilon \left(x'' + \xi_m x' + \zeta \tilde{F}_{\mathrm{NL}}(t, x) + \gamma_0 \mu (\alpha x - u_a) \right) = 0 \end{cases} \tag{4.30}$$

Where the parameters ξ_a, γ_0, f, ξ_m, ζ and $\gamma_0 \mu$ should be order $O(1)$ (with the subscript $m \equiv$ membrane), and where ν is the normalized pulsation of the excitation pulsation Ω defined as depending of σ the detuning parameter, meaning that the solution is studied around the resonance of the system:

$$\nu = \frac{\Omega}{\omega_0} = 1 + \sigma \varepsilon \tag{4.31}$$

The MSM approach is introduced here by the decomposition of the time τ in new time scales as:

$$T_k = \varepsilon^k \tau \ \in \mathbb{R}_+ \qquad ; \qquad k \in [\![0 \ ; \ N]\!] \tag{4.32}$$

Let us introduce the complex variables of Manevitch which are functions of new time scales T_k [107] such that (with $i^2 = -1$):

$$\begin{cases} u_a' + i\nu u_a = \varphi_a(T_0, ..., T_N)\, e^{i\nu\tau} \\ x' + i\nu x = \varphi_m(T_0, ..., T_N)\, e^{i\nu\tau} \end{cases} \tag{4.33}$$

where the complex variables can be expressed in the polar domain with the amplitudes $(N_a, N_m) \in {\mathbb{R}_+}^2$ and $(\delta_a, \delta_m) \in [-\pi; \pi]^2$:

$$\begin{cases} \varphi_a(T_1, ..., T_N) = N_a(T_1, ..., T_N)\, e^{i\delta_a(T_1, ..., T_N)} \\ \varphi_m(T_0, ..., T_N) = N_m(T_0, ..., T_N)\, e^{i\delta_m(T_0, ..., T_N)} \end{cases} \tag{4.34}$$

After a Galerkin method to project the obtained system onto the first harmonics, equations at mutliple scales are obtained. The first scale at $O(\varepsilon^0)$ describes the fast system dynamics and is written:

$$O(\varepsilon^0) : \begin{cases} \dfrac{\partial \varphi_a}{\partial T_0} + i\dfrac{\varphi_a}{2} + \dfrac{\varphi_a}{2i} = 0 \\ \dfrac{\partial \varphi_m}{\partial T_0} + i\dfrac{\varphi_m}{2} + \xi_m \dfrac{\varphi_m}{2} + \zeta R_1(\varphi_m, \varphi_m^*) + \dfrac{\gamma_0 \mu}{2i}(\alpha\varphi_m - \varphi_a) = 0 \end{cases} \tag{4.35}$$

Solving this set of equations leads to the Slow Invariant Manifold (SIM) W that defines the fixed points of the dynamical system:

$$W = \{(\varphi_a, \varphi_m) \in \mathbb{C}^2 \quad / \quad \mathscr{H}(\varphi_a, \varphi_a^*, \varphi_m, \varphi_m^*) = 0\} \tag{4.36}$$

Additionally, the unstable points of the SIM can be obtained by perturbation of the variable φ_m.

The scale at $O(\varepsilon)$ can also be studied, describing the slow time scale. The first equation of (4.30) at order $O(\varepsilon)$ gives:

$$\frac{\partial \varphi_a}{\partial T_1} + \frac{i\varphi_a}{2}(2\sigma - \gamma_0 - i\xi_a) + \frac{i\alpha\gamma_0}{2}\varphi_m = \frac{if}{2} \tag{4.37}$$

The implicit equation $\mathscr{E}(\varphi_a, \varphi_a^*, \varphi_m, \varphi_m^*) = 0$ is obtained by Eq. (4.37), defining a manifold E such as:

$$E = \{(\varphi_a, \varphi_m) \in \mathbb{C}^2 \quad / \quad \mathscr{E}(\varphi_a, \varphi_a^*, \varphi_m, \varphi_m^*) = 0\} \tag{4.38}$$

Defining the jacobian matrix of $(\mathscr{H}, \mathscr{H}^*)$ regarding the variables φ_m and φ_m^*, the equilibrium points can be obtained by the following condition:

$$W \cap E \cap \{(\varphi_a, \varphi_m) \in \mathbb{C}^2 / \det(\mathbf{A}) \neq 0\} \Longleftrightarrow \begin{cases} \mathscr{E}(\varphi_a, \varphi_m, \varphi_a^*, \varphi_m^*) = 0 \\ \mathscr{H}(\varphi_a, \varphi_m, \varphi_a^*, \varphi_m^*) = 0 \\ \det(\mathbf{A}) \neq 0 \end{cases} \tag{4.39}$$

And the singular points can be obtained by the following condition:

$$W \cap E \cap \{(\varphi_a, \varphi_m) \in \mathbb{C}^2 / \det(\mathbf{A}) = 0\} \Longleftrightarrow \begin{cases} \mathscr{E}(\varphi_a, \varphi_m, \varphi_a^*, \varphi_m^*) = 0 \\ \mathscr{H}(\varphi_a, \varphi_m, \varphi_a^*, \varphi_m^*) = 0 \\ \det(\mathbf{A}) = 0 \end{cases} \tag{4.40}$$

The presented method is used for the study of the system in the following. For extensive details on the method and calculations, refer to the Appendix C.

4.4 Experimental set-up and methods

4.4.1 Experimental set-up

The ER is placed at the end of a cylindrical cavity with a cross-section S_{cb} (radius r_{cb}) and of length L_{cb}, which is linked to a cylindrical tube with a narrow cross-section S_t (radius r_t) of length L_t at the other end, as pictured in the photos of Fig. 4.2a and in the sketch of Fig. 4.2. The ER can be replaced with a rigid termination for creating a reference measure. The narrow cross-section tube (S_t-tube) is terminated with the acoustic source: an external loudspeaker delivering a sound pressure excitation p_{ls}. The S_t-tube is considered as the main system whose first acoustic mode must be attenuated by the ER. The connections between the devices are represented in the scheme 4.2b. The dimensions of the experiment are presented in Table 4.1.

	Dimension	Value	Unit
Tube	r_t	1.45×10^{-2}	m
	S_t	6.61×10^{-4}	m^2
	L_t	0.204	m
Coupling box	r_{cb}	0.02	m
	L_{cb}	0.125	m
ER	S_d	1.3×10^{-3}	m^2

Table 4.1 Dimensions of the experiment.

The system is assembled from multiple pieces of other experiments. The surfaces are not all of the same material, and 3D printing has been needed to assemble the final experiment. The reduced section tube is a part of a Bruël&Kjaer©Kundt's tube. The coupling box is a brass material cylindrical tube. The junction between the coupling box section and the Kundt's tube section is a 3D printed adaptator. The same type of 3D printed adaptator fills the gap between the Acoustic Source and the Kundt's tube. A 3D printed cylindrical termination is placed at the end of the coupling box, with a reserved space for the ER, or for a printed rigid termination: each junction is sealed using Teflon to limit the acoustic leakage. The coupling box is isolated from vibrations coming from other components of the experiment (such that the acoustic source) that could travel through the basis by placing rubber material behind it.

The digital programming of the ER is done using a d-SPACE©MicroLabBox DS1202, which is also used as the acquisition system, working at 50 kHz.

The sensing devices for control and for data analysis, are externally polarized 1/4" Bruël&Kjaer©microphones. The microphones provide the voltage signal to the d-Space device after going through the Bruel&Kjaer©conditioner.

The electrical current signal to send into the ER loudspeaker is provided by the calculations made by the d-Space device. The ER's electrical circuits (containing the Howland current pump) is power-supplied using a 10 V amplitude voltage. The Howland current pump allows to send into the loudspeaker's coil an electrical current proportional to the provided voltage $V(t) = Gi(t)$. It is noteworthy that the electrical current is not amplified between the controlling device and the ER as the calculated electrical current should be proportional to the electrical current to be injected into the loudspeaker coil. However, to ensure stability and the best possible

performances, it might be considered as a control parameter to optimize. The actuation gain as a control parameter is not studied in this work, and is kept to 1.
The excitation is provided by an acoustic source being an external loudspeaker linked to the d-SPACE device through an amplifier. Most of the following experiments are done using an acoustic excitation lasting 60 seconds in the form of a linear chirp from 350 Hz to 800 Hz with either increasing or decreasing frequencies. Other types of excitations are used as mono-harmonic signals composed of a 5-second long sinus, while the acquisition system also records the transient regime of the system.
Reference measures for all considered excitation signals are made using a rigid termination instead of the ER.

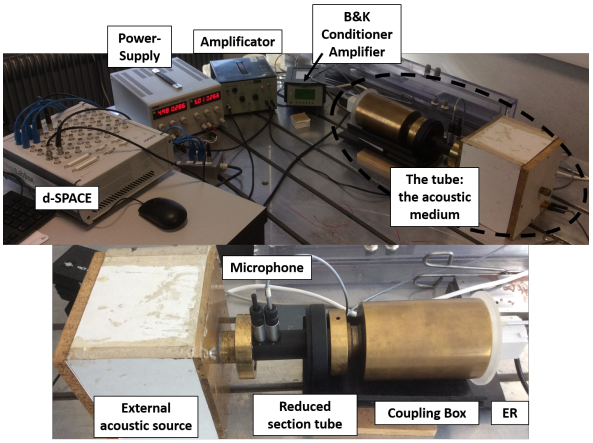

(a) Global experimental set-up

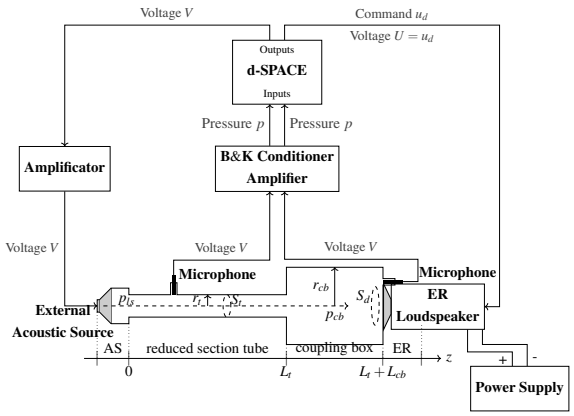

(b) Scheme of the experimental set-up and the connections

Fig. 4.2 Experimental setup

4.4.2 Parameters of the experimental bench

The parameters in the system of equations (4.23) are either directly measured or estimated using the model. The estimated parameters are those that do not require experimental measurements, they are calculated based on the dimensions of the experiment using the expressions:

$$\begin{cases} m_a = \dfrac{\rho_0 c_0 L_t}{2} \\ k_b = \dfrac{\rho_0 c_0^2}{V_{\text{cb},0}} \end{cases} \tag{4.41}$$

The rigid-termination set-up is presented in Appendix B and in Fig. B.1. Analytically calculating m_a or k_a enables the determination of the other. The parameter m_a is arbitrarily chosen to be the calculated parameter, and k_a to be the measured one. Assuming that the experimental bench is placed in standard conditions: a static air pressure 1013.25hPa and temperature 20°C, these parameters are calculated and presented in Table (4.2).

The measured parameters are directly measured using the experiment. These parameters can rely on calculated parameters such as the modal mass m_a, and are presented in Table 4.3. The measured parameters are the mean value of a set of measurements (described in Appendix B), along with the standard deviation of the set of measurements. Notice that the curve-fitting of the analytical solution of the rigid-termination configuration could have been also used.

Parameter	Expression	Value	Unit
m_a	$\frac{\rho_0 S_t L_t}{2}$	8.22×10^{-5}	kg
k_b	$\frac{\rho_0 c_0^2}{V_{\mathrm{cb},0}}$	1.46×10^{8}	$\mathrm{kg\,m^{-4}/s^2}$
γ	$k_b S_t S_d$	125.54	$\mathrm{kg\,s^{-2}}$

Table 4.2 The calculated parameters of the model under standard conditions: the static air pressure 1013.25hPa and temperature 20°C.

Three configurations, designated A, B, and C, are proposed, and the measured values for characterizing the experiment are presented. These configurations correspond to three sets of measurements that have been conducted throughout the course of the work. The measurements were taken at different times of year, which revealed fluctuations in the humidity rate (and thus the molar mass of air) and temperature, resulting in variations in the air velocity ($c_0 = \sqrt{\gamma RT/M}$). These parameters exert a considerable influence on the parameters of the experiment. Furthermore, the experiment has been dismantled and rebuilt between configurations, introducing additional variability in the length of each experimental segment and consequently affecting the parameters. The configuration used for the production of the results is directly displayed in the corner of figures along within the title of the figures.

	Configuration			
	A	**B**	**C**	Unit
f_0	596.82 ± 0.78	559.10 ± 0.26	575.56 ± 0.026	Hz
c_a	$3.86 \times 10^{-2} \pm 7.82 \times 10^{-5}$	$3.65 \times 10^{-2} \pm 2.21 \times 10^{-5}$	$3.77 \times 10^{-2} \pm 3.26 \times 10^{-4}$	$\mathrm{kg\,s^{-1}}$
k_a	1155.90 ± 3.02	1014.40 ± 0.95	1075.01 ± 0.097	$\mathrm{kg\,s^{-2}}$

Table 4.3 The measured parameters of the model (mean value of the estimated parameters of the set of measurements) $\pm$ the standard deviation of the estimated values of the set of measurements.

4.5 Targeting a cubic restoring force function

4.5.1 Design

As a first example, a cubic restoring forcing function is employed here to demonstrate the functionality of the nonlinear programming. Configurations A and B are considered regarding this restoring force. The specific form of the nonlinear restoring force is given by:

$$F_{\mathrm{NL}}(t,x) = K_d(x + \beta_{\mathrm{NL}} x^3) \tag{4.42}$$

Where β_{NL} represents an adjustable nonlinear parameter. The value of the parameter β_{NL} plays a crucial role in determining whether the stiffness force composed of the linear part $K_d x$ and of the nonlinear part $K_d \beta_{\mathrm{NL}} x^3$ exhibits nonlinear phenomena across the considered range of amplitudes. The order of magnitude of these two parts weighs in the activation of nonlinear behavior. The sign of β_{NL} gives the sign of the force that determines

whether the programmed behavior results in either a hardening or softening behavior.

The choice of the damping parameter η_R is motivated by the need to create bifurcations. Indeed, a condition on the existence of the bifurcations emerges from the calculations of stability of equilibrium points, from Eq. C.73:

$$(1-\zeta-\alpha\gamma_0\mu)^2-\xi_m^2>0 \tag{4.43}$$

The given condition is expressed as a function of the linear stiffness and of the damping of the resonator. Throughout the study of the cubic restoring force, the choice of $\eta_R = 1/8$ ensures the existence of the bifurcation.

The choice of the linear stiffness parameter η_K is motivated by the necessity to align the nonlinear resonance frequencies of the ER with the frequencies of the acoustic mode of the tube. If this is not realized, higher amplitudes would be needed to benefit from the nonlinear resonance of the ER. For all the proposed nonlinear behaviors, the backbone of the ER must intersect with the straight backbone of the linear acoustic oscillator, as seen in Section 2.2.2. Indeed, the nonlinear softening behavior involves large amplitude oscillations of the ER at lower frequencies than the linear resonance frequency. As a result, the ER is more efficient within the considered frequency bandwidth. The opposite effect can be seen for hardening behaviors, which benefit from large oscillations at higher frequencies than the linear frequency of the resonator. The choice of η_K determines the frequency of the linear resonance of the ER. It allows the selection of the targeted linear mode frequency of the resonator. Choosing an appropriate η_K is essential to tune the ER nonlinear resonance with the acoustic tube resonance for improved sound absorption. We choose $\eta_M = 1$ to allow to tune the linear frequency of the resonator by a simple calculation described Eq. (3.20).

Hardening behavior

To obtain a hardening behavior, the parameter β_{NL} is taken positive, the restoring force function is plotted in Fig. 4.3. The order of magnitude of the nonlinear term, and the gap from the resonance frequency of the primary system lead to the choice of the pair of parameters $(\eta_K, \beta_{\mathrm{NL}})$. The pair of parameters has been chosen by empirical and numerical means. For both Configurations A and B, the η_K parameter is chosen equal to 1, such that only the β_{NL} parameter is to be found. We are able to proceed in such manner because the linear resonance frequency of the ER is close to, and is lower than the resonance frequency of the primary system.

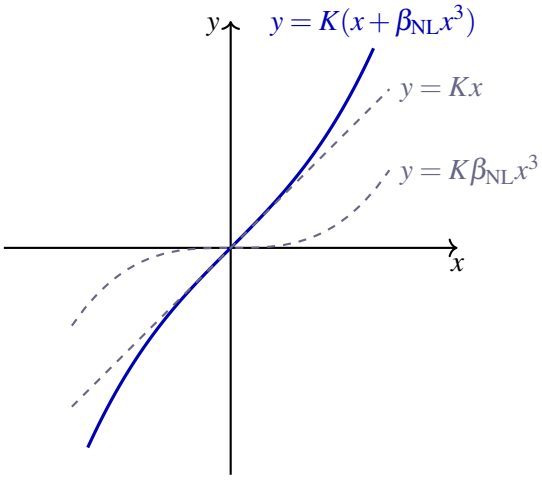

Fig. 4.3 Design of Cubic behavior

For Configuration A, we choose $\beta_{\text{NL}} = 2 \times 10^{11}$ m^{-2}, and for Configuration B, $\beta_{\text{NL}} = 5 \times 10^{10}$ m^{-2}. We can see that given the same ER modal parameters, the β_{NL} parameter of Configuration B is lower than the one of Configuration A. It is due to the higher gap between the ER linear frequency and the primary system resonance frequency for Configuration A. At constant amplitudes, higher values of β_{NL} enlarges the ER nonlinear resonance frequencies towards higher frequencies. It also permits to use the β_{NL} as a tuning parameter. It is worth noting that excitation amplitudes play a major role, as the nonlinear resonance also enlarges with increasing excitation amplitudes. Moreover, the ER normalized amplitudes of oscillations (the ratio between the ER amplitude and the excitation amplitude) decrease when the nonlinear parameter values increase at constant frequency. It may lead to a less efficient ER despite a broadened frequency bandwith. The retained parameters are described for Configurations A and B in Table (4.4).

Configuration	Parameter	Value	Unit
A	η_M	1	
	η_K	1	
	f_d	531	Hz
	η_R	$1/8$	
	β_{NL}	2×10^{11}	m^{-2}
B	η_M	1	
	η_K	1	
	f_d	531	Hz
	η_R	$1/8$	
	β_{NL}	5×10^{10}	m^{-2}

Table 4.4 Parameter values for the cubic hardening restoring force results (f_d being the desired resonance frequency).

Softening behavior

To obtain a softening behavior, the parameter β_{NL} is taken negative: $\beta_{\text{NL}} \rightarrow -\beta_{\text{NL}}$, $\beta_{\text{NL}} > 0$. The restoring force function is plotted in Fig. 4.4.

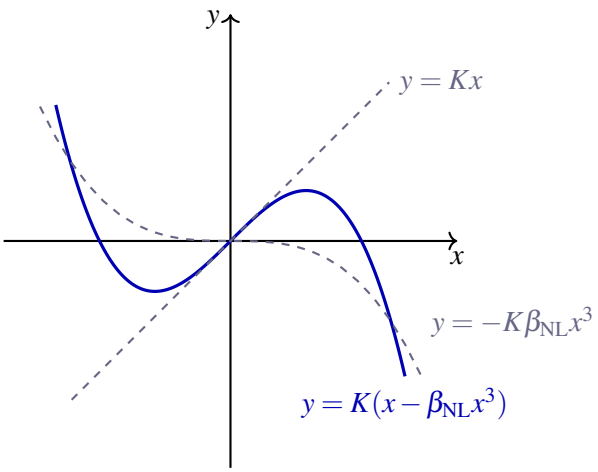

Fig. 4.4 Design of Cubic behavior

In the case of the softening behavior, the overall potential can become positive at high oscillating amplitudes, leading to possible instability due to the injection of energy into the system. This case is used for illustrative purposes. Nevertheless, the logarithmic potential restoring force, later considered in this paper, solves the instability issue.

Taking $\eta_M = 1$, the choice of η_K can be done using Eq. (3.20). In order to make the softening behavior useful in such applications, the ER linear resonance frequency has to be at higher frequencies than the resonance frequency of the system to control, see Section 2.2.2. We choose the parameters of the ER such that the softening behavior parameters describe a similar situation as the hardening behavior one. For Configuration A, knowing that $f_0 = f_d = 531$ Hz (f_d being the desired frequency), the frequency gap between the linear first mode of the ER and the acoustic mode of the tube (596 Hz) is 65 Hz. In order to produce the nonlinear softening behavior, the parameter η_K is chosen such as the frequency gap between the mode of the ER and the acoustic mode of the tube should be close to 65 Hz. Consequently, $f_d = 660$ Hz, which gives the parameters $\eta_M = 1$, $\eta_K = 1.5496$, and $\eta_R = 1/8$ for producing the softening behavior. The same method is applied to calculate the η_K coefficient for Configuration B. The parameters for both configurations are detailed in Table (4.5).

Configuration	Parameter	Value	Unit
A	η_M	1	
	η_K	1.5496	
	f_d	660	Hz
	η_R	$1/8$	
	β_{NL}	-3×10^{11}	m^{-2}
B	η_M	1	
	η_K	1.222	
	f_d	531	Hz
	η_R	$1/8$	
	β_{NL}	-5×10^{10}	m^{-2}

Table 4.5 Parameter values for the cubic softening restoring force results.

4.5.2 Analytical predictions

The analytical calculations are briefly summarized in Section 4.3. The application of the general analytical results to the cubic nonlinearity is detailed in the Appendix Section C.2. Appendix C presents the analytical study that enables the calculation of the Slow Invariant Manifold (SIM) that predicts the global dynamic of the system and its stability. From the SIM, the existence of bifurcations can be derived. The calculations are then continued at higher orders, enabling the calculations of the equilibrium and fixed points, along with the estimation of their stability. These methods are well-known and widely documented in the literature. Here, we start with the Configuration **B**, as the differences between Configurations are the parameters of the experimental set-up (mainly modal parameters of the tube, and of the excitation amplitude).

Configuration B

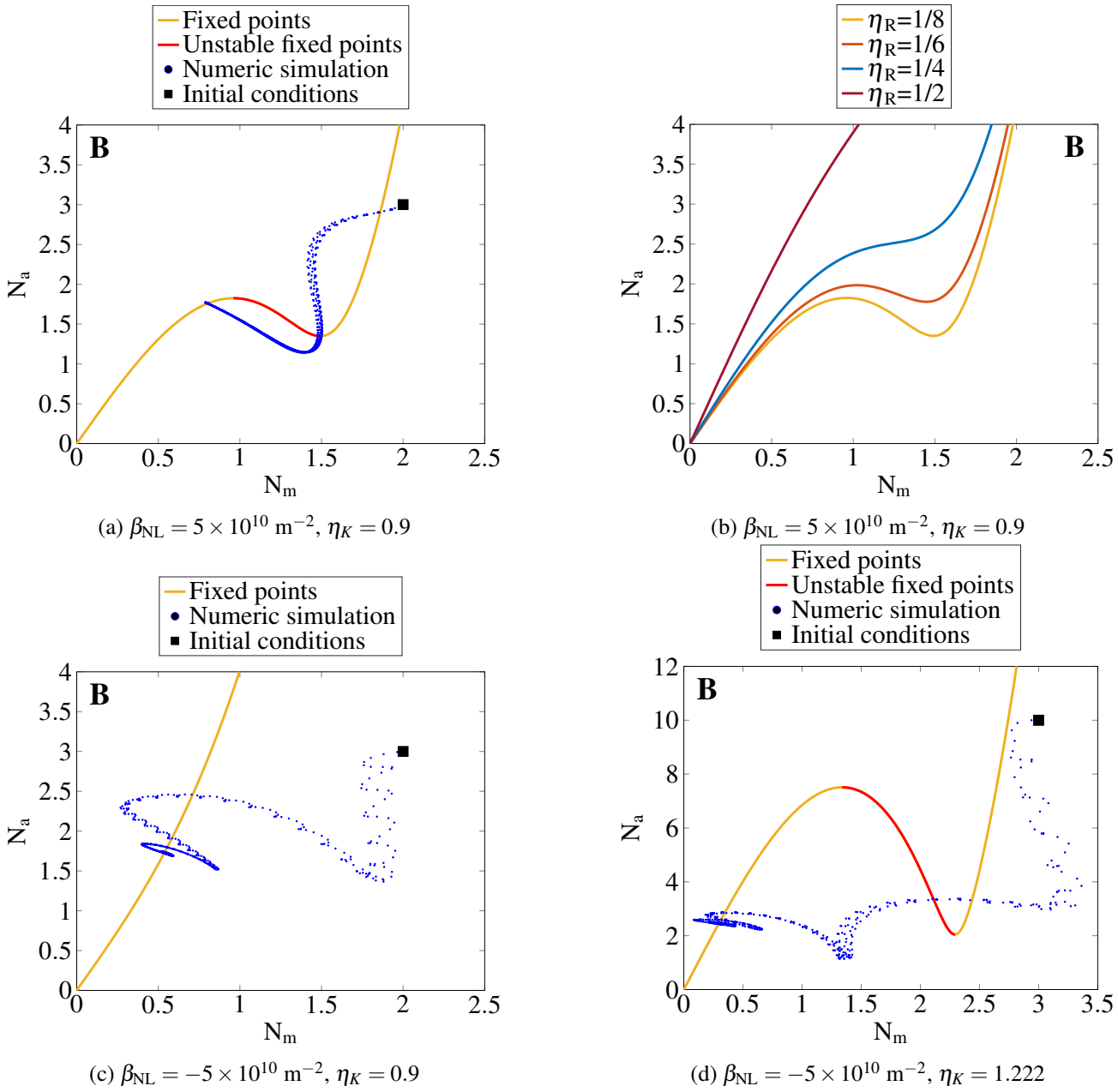

(a) $\beta_{NL} = 5 \times 10^{10}$ m^{-2}, $\eta_K = 0.9$

(b) $\beta_{NL} = 5 \times 10^{10}$ m^{-2}, $\eta_K = 0.9$

(c) $\beta_{NL} = -5 \times 10^{10}$ m^{-2}, $\eta_K = 0.9$

(d) $\beta_{NL} = -5 \times 10^{10}$ m^{-2}, $\eta_K = 1.222$

Fig. 4.5 Figures of the SIM of the two degree of freedom system defined by equations (C.25,4.36), with $P = 0.5$ Pa. Predictions made with parameters from Configuration B.

Let us study the results given by the analytical calculations in the case of the measured and defined parameters of Configuration **B**. Each analytical results are supported by numerical simulations. Multiple phenomena can be anticipated using analytic and numeric approaches. The SIM is a representation of the asymptotic states of the equilibria of the system, and plots the variable N_a as a function of N_m, being respectively the envelopes of the modal displacement of the acoustic mode and of the ER membrane. The SIM presented Eqs. (C.25, 4.36) in Appendix C with the stability boundary conditions introduced Eq. (C.72) is depicted in Figure 4.5a with the given parameters and $\eta_K = 0.9$. The unstable fixed points whose existence indicates eventual bifurcations are indicated in red. In fact, the condition of intersection of the backbone with the primary oscillator's resonance frequency (about η_K) can be observed: if the linear frequency of the ER is not tuned with the frequency of the

acoustic mode of the tube, the bifurcation can not happen. It is due to the coupling between the pressure inside the reduced-section tube and the ER, such as the pressure needs to reach the activation threshold of the nonlinear behavior of the ER. Indeed, the linear frequency of the ER should be chosen such as the nonlinear resonance coincides with the acoustic mode of the tube. Taking $\eta_K = 0.9$ lowers the linear frequency of the ER which tunes the nonlinear resonance with the resonance of the reduced-section tube since the behavior is hardening. This effect can also be observed by taking an interest in the softening behavior. If we set $\beta_{\text{NL}} = -5 \times 10^{10}$ m^{-2} and we keep $\eta_K = 0.9$, the bifurcation can not happen as presented in Figure 4.5c. However, if we set $\eta_K = 1.222$, the linear frequency is placed at higher frequencies than the frequency of the reduced-section tube resonance, leading to the tuning of the nonlinear resonance of the ER with the frequency of the reduced-section tube resonance. It causes the existence of unstable fixed points, resulting in possible bifurcations as depicted in Figure 4.5d. Additionally, the condition of existence of unstable zones given equation (C.73) is verified in Figure 4.5b. In fact, the critical damping parameter with the considered parameters is $\xi_{2,c} = 0.0444$, which yields $\eta_R = 0.2232$. It can be seen that the SIM with $\eta_R = 1/4$ does not include unstable zones, while the SIMs for $\eta_R = 1/8$ and $\eta_R = 1/6$ do. The qualitative behavior of the analytical results corresponds to the one found with numerical simulations, but shifts in the jumps and amplitudes are observed due to the choice of parameters orders through the choice of ε (see Appendix C), and by the additional harmonics that are not taken into account in the analytical calculations.

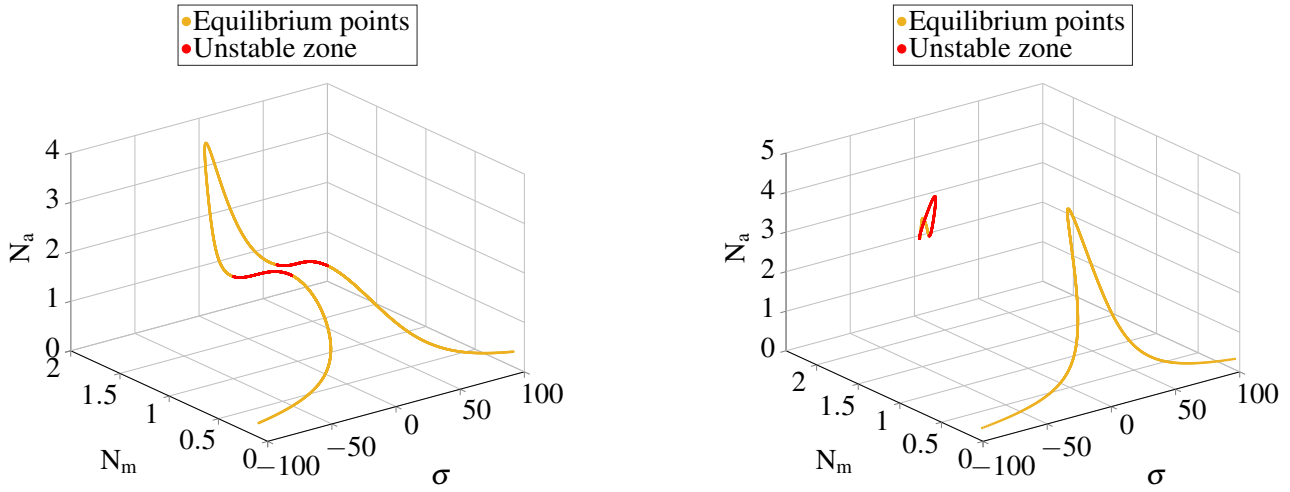

(a) $\beta_{\text{NL}} = 5 \times 10^{10}$ m^{-2}, $\eta_K = 0.9$ (b) $\beta_{\text{NL}} = -5 \times 10^{10}$ m^{-2}, $\eta_K = 1.222$

Fig. 4.6 Figures of the equilibrium points of the two degree of freedom system defined by equation (C.53), with $P = 0.8468$ Pa. Predictions made with parameters from Configuration B.

Let us plot the equilibrium points of the two degrees of freedom system with both the softening and hardening restoring forces. The results are plotted in Figure 4.6 with incident pressure $P = 0.8486$ Pa which is the numerical input that suits the experimental pressure input for the Configuration **B**. Figure 4.7 presents the projection of the results of Fig. 4.6 onto the 2-dimensional planes with respect to σ for both the hardening (Figs. 4.7a and 4.7b) and softening (Figs. 4.7c and 4.7d) behaviors.

Observe in Figs. 4.6 and 4.7 that both behaviors do not demonstrate quasi-periodic regime with initial conditions set to 0, as stable fixed points exist for all frequencies (e.g. $\sigma = 20$ for the hardening case). A non-zero initial condition of the system is needed to attain quasi-periodic regimes. Moreover, possible bifurcations can be expected from the system with hardening behavior with the given parameters due to the unstable zones of the main branch, as it can be seen in Figure 4.6a. Additionally, the Figure 4.7a predicts that a bifurcation may happen around $\sigma = 20$ (knowing that σ is defined such as $\nu = \Omega/\omega_0 = 1 + \sigma\varepsilon$ with Ω being the the pulsation of the excitation sine wave).

Regarding the softening case in Figure 4.6b, observe an isolated branch of equilibrium points that is far from the main branch. However, Figure 4.7c shows that the isolated branch is situated at lower energy than the main branch for the acoustic mode, and at higher energy than the main branch for the ER (Figure 4.7d). Indeed, the larger the amplitudes of the ER, the lower the amplitudes of the acoustic mode, as the ER can absorb more energy with large oscillations. In this particular case, attaining the equilibrium points of the isola may be extremely beneficial for the reduction of the energy of the acoustic mode of the tube. This result is particularly interesting as most of studies in the literature obtains isolas that increase the amplitudes of the primary system, leading to unwanted responses.

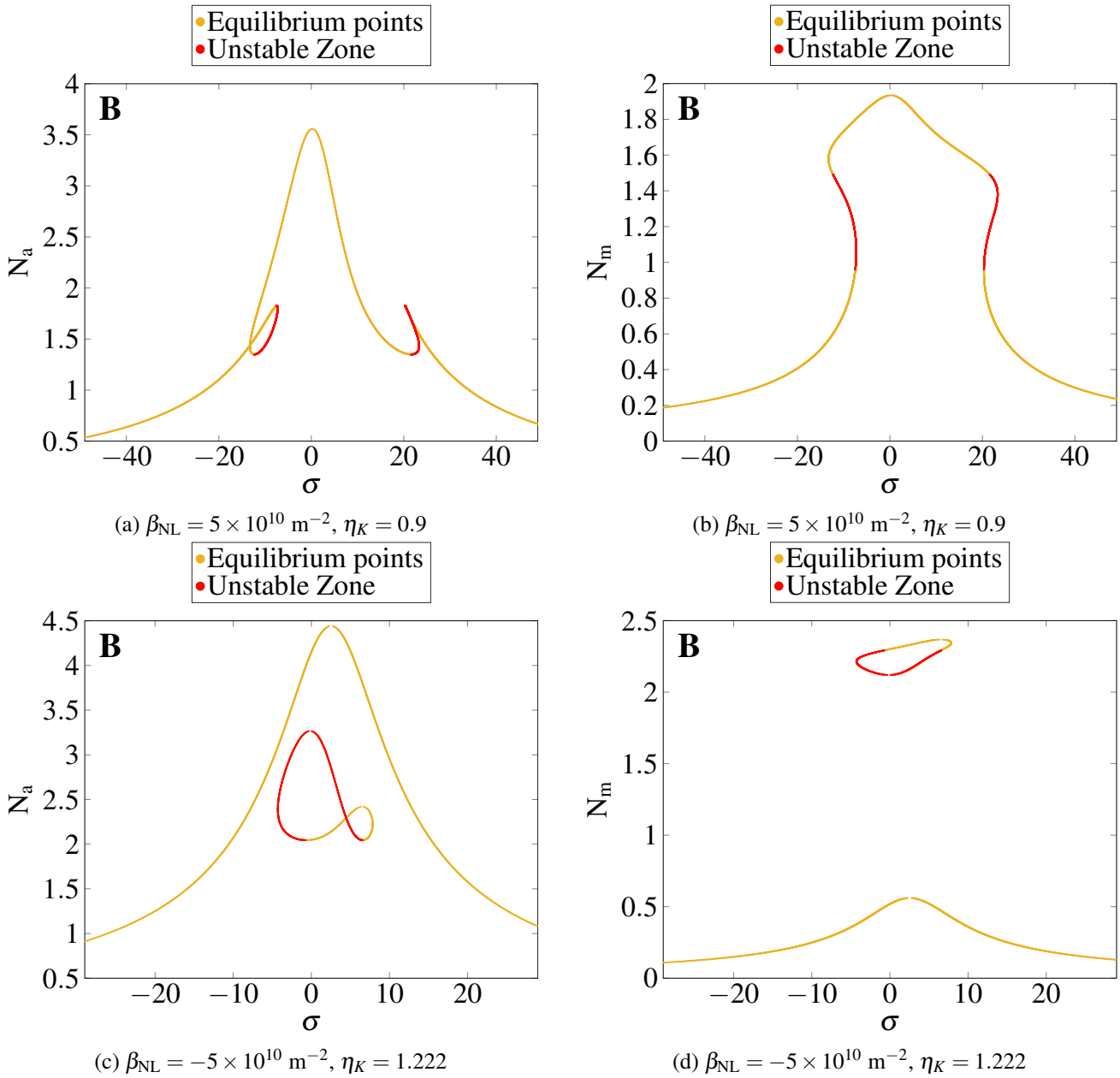

(a) $\beta_{NL} = 5 \times 10^{10}$ m^{-2}, $\eta_K = 0.9$

(b) $\beta_{NL} = 5 \times 10^{10}$ m^{-2}, $\eta_K = 0.9$

(c) $\beta_{NL} = -5 \times 10^{10}$ m^{-2}, $\eta_K = 1.222$

(d) $\beta_{NL} = -5 \times 10^{10}$ m^{-2}, $\eta_K = 1.222$

Fig. 4.7 Figures of the equilibrium points of the two degree of freedom system defined by equation (C.53), with $P = 0.8468$ Pa for both hardening (a,b) and softening (c,d) behaviors. Predictions made with parameters from Configuration B.

Configuration A

The results obtained with the parameters defined in Configuration **A** are plotted in Fig. 4.8. The SIM is defined in Fig. 4.8a. Notice that the analytical results predict a bifurcation with $\eta_K = 1$, while the Configuration **B** results for the hardening behavior needs $\eta_K = 0.9$ to obtain a qualitative behavior showing a nonlinear jumping phenomena. This is due to the higher resonance frequency of the acoustic mode of the tube, which naturally coincides with the nonlinear resonance of the ER.

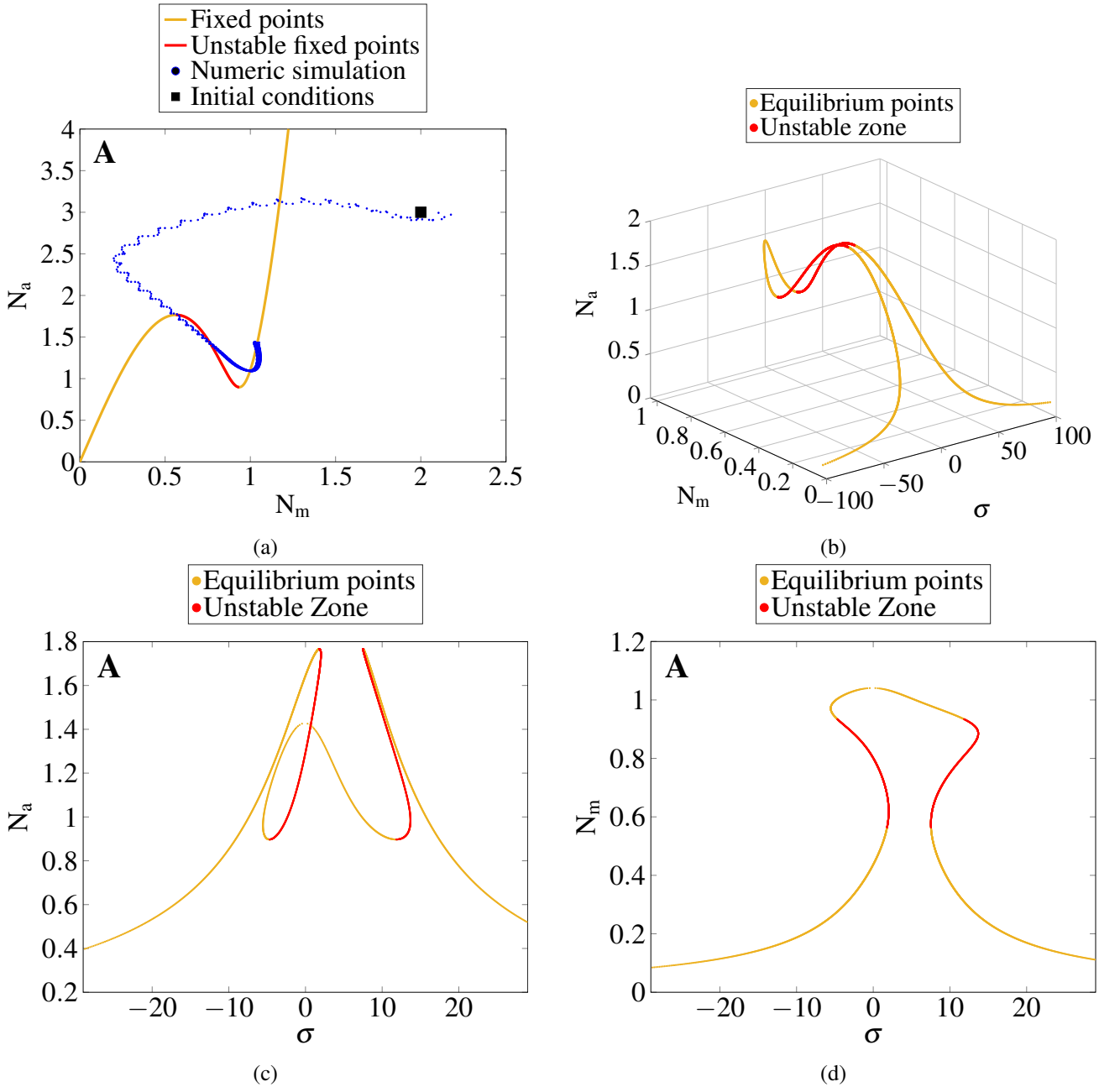

Fig. 4.8 Figures of the equilibrium points of the two degree of freedom system defined by equation (C.53), with $P = 0.4418$ Pa. (a) The SIM and the numerical integration; (b) The equilibrium points in the (σ, N_m, N_a) plane; (c,d) Projections of the equilibrium points in the (σ, N_a) (c) and (σ, N_m) (d) planes. Predictions made with parameters from Configuration A, with $\beta_{\mathrm{NL}} = 2 \times 10^{11}$ m^{-2}, $\eta_K = 1$.

The 3 dimensional plot of the equilibrium points is illustrated in Fig. 4.8b, which confirms the activation of the nonlinear behavior of the two degree of freedom system once a threshold is reached. Moreover, the nonlinear

behavior of the resonator featured in Fig. 4.8c expects bifurcations to happen with a frequency sweep excitation. The primary oscillator's response is plotted in Fig. 4.8d. Observe that the behavior presents multiple bifurcations possibilities at the frequencies of the bifurcations featured in the ER's response. As a result, the nonlinear behavior should be exhibited in the response of the primary oscillator. The response of the primary oscillator shows a significant reduction of the energy at the frequencies of high amplitude of the nonlinear resonator. As a result, the nonlinear resonator seems to be able to reduce the energy contained in the primary oscillator. The steady-state regime of the numerical simulations converge towards the fixed points defined by the SIM. However, observe that the time modulations are extremely slow (compared to the literature), which is due to the high modal damping of the acoustic mode of the tube (approximately 6%).

4.5.3 Experimental results

Experimental results and comparison to an optimized Tuned Mass Damper

The variation of the pressure and electrical current amplitudes are plotted in Fig. 4.9 for Configuration A for both increasing and decreasing frequency sweep, and for the programmed hardening and softening behaviors. Variations of the electrical current depicted in Fig. 4.9a (bottom) clearly indicate the programming of a hardening behavior. Indeed, in the case of increasing frequency excitation, the measured pressure jumps (at 596 Hz) to a lower energy stable equilibrium point, whereas, in the case of decreasing frequency excitation, the measured pressure jumps (at 563 Hz) to a higher energy equilibrium point. For the softening behavior, shown in Fig. 4.9b (bottom), the opposite phenomenon occurs. The decreasing frequency measurement experiences a jump to lower energy equilibrium points at lower frequencies (569 Hz), while the increasing frequency measurement jumps to a higher energy equilibrium point (638 Hz). The use of experimental continuation for multi-degrees of freedom system are under investigation and being perfectioned in the literature [161, 131]. The use of Control-Based-Continuation would enable a more accurate estimation of the bifurcation. Indeed, the jump does not ensure that the bifurcation is situated at this frequency, and continuation techniques would permit to stabilize the unstable points, and realize an excellent approximation of the bifurcation frequency.

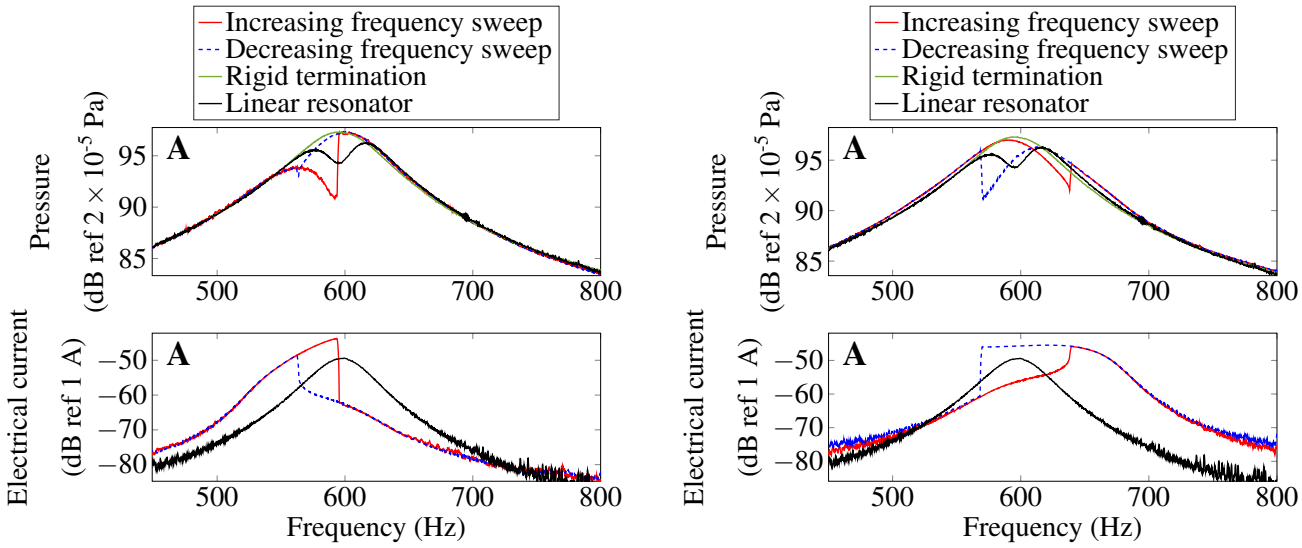

(a) Hardening behavior

(b) Softening behavior

Fig. 4.9 Experimental results for the cubic restoring force. Variation of the pressure amplitude inside the reduced section tube (top), and variation of the electrical current amplitude sent to the ER (bottom). Results obtained from Configuration A.

The pressure plotted in Figs. 4.9a (top) and 4.9b (top) presents the coupled behavior of the acoustic mode of the tube. The same phenomena occurs in both cases characterized by a significant reduction of the sound level in the tube at the frequencies corresponding to the nonlinear resonance. It is due to the activation of the ER nonlinear behavior that starts to act with large response amplitudes, and as a result it pumps the energy of the tube mode. However, from Fig. 4.9b (top) one can observe a slight increase in the sound level in the reduced section tube from 600 Hz to 700 Hz. This issue can be solved by optimization means, which are not considered in this work.

Moreover, either larger frequency bandwidth or better sound absorption are realized using these cubic restoring forces. The tuning parameters should be optimized in future studies. Experimental time histories of the pressure inside the reduced-section tube are plotted in Fig. 4.10 for both hardening and softening behaviors. One can see that the incident pressure level is divided by two for the increasing frequency sweep, which is coherent with the reduction of more than 6 dB seen in the frequency plots. The bifurcation is clearly recognizable.

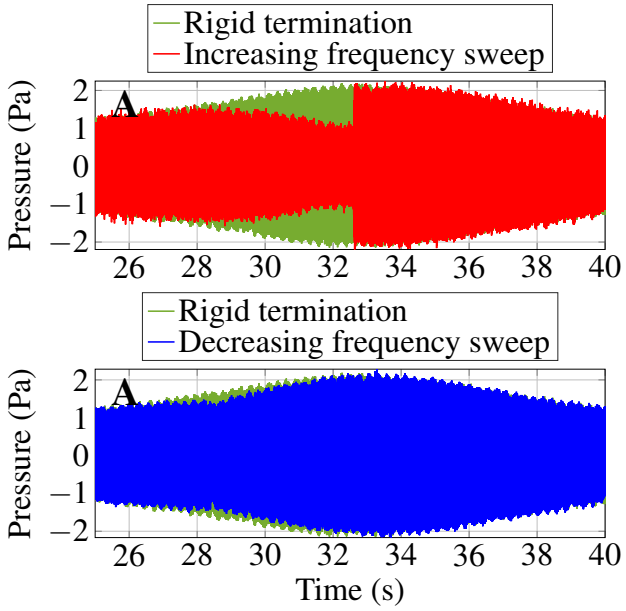

(a) Hardening behavior with (top) increasing frequency sweep (bottom) decreasing frequency sweep

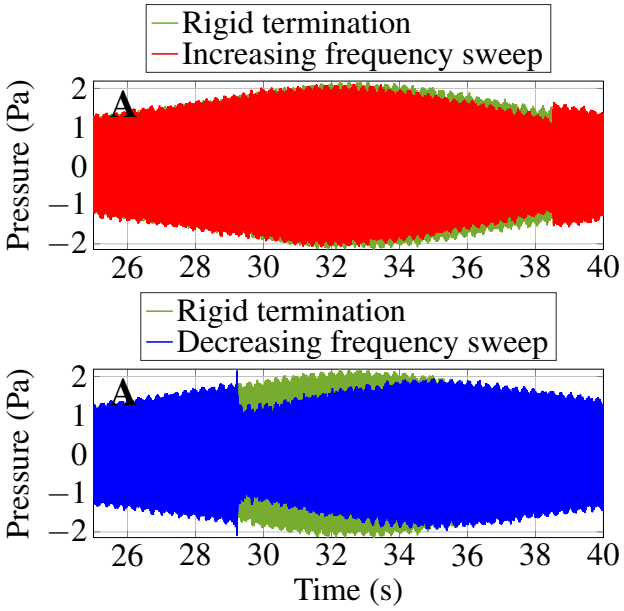

(b) Softening behavior with (top) increasing frequency sweep (bottom) decreasing frequency sweep

Fig. 4.10 Experimental time histories for the cubic restoring force: pressure inside the reduced-section tube. Results obtained from Configuration A.

Validation of the model

This section aims at validating the numerically solved model. The validation of the analytical model allows us to predict the behavior and the phenomena that could happen using other restoring forces for exemple. Additionally, the comparison of experimental data to numerical data permits to analyse the results coming from analytical studies more precisely. Indeed, the discrepancies between experimental data and analytical or numerical data can be classified as coming from the model, or from the analytical method. Let us compare the numerical and experimental data for both Configurations A and B.

The numerical excitation signal is taken as identical to the experimental one, i.e. a frequency sweep from 350 Hz to 800 Hz that lasts 60 seconds with either increasing or decreasing frequency sweeps. The numerical parameters for the ER are identical to the experimental ones.

The results obtained from the numerical integration of the model outlined in Section 4.2 are compared to the experimental ones, and the outcomes are presented in Fig. 4.11 for Configuration A. One can see that the model describes correctly the behavior of the coupled experimental system despite a noticeable frequency shift of the bifurcations illustrated in Fig 4.11. This shift can mainly be explained by model uncertainties. Among model uncertainties, an important role is played by the S_d parameter, which can differ significantly from the membrane surface area. In terms of modeling, it is worth highlighting that the parameter S_d imposes significant challenges when it comes to its estimation and measurement [17]. This parameter affects the coupling between the acoustic mode and the ER, and hence the bifurcation frequencies. The inaccurate approximation at low frequencies is due to the presence of a coupling of an anti-resonance at lower frequencies that is not modeled. It might also be responsible for the frequency shift of the bifurcations. The influence of the antiresonance is discussed in Appendix B.2. Nevertheless, despite the strong approximations employed in the reduced numerical model, it well captures the trends of the measured pressure. It confirms that the actual behavior of the ER is extremely close to the desired behavior.

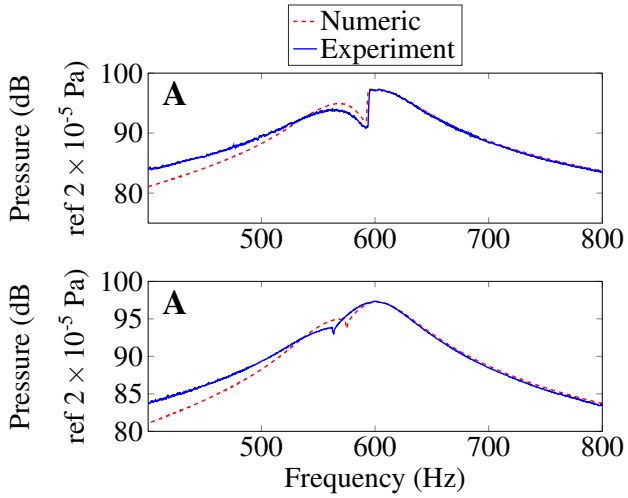

(a) Hardening behavior with (top) increasing frequency sweep, (bottom) decreasing frequency sweep

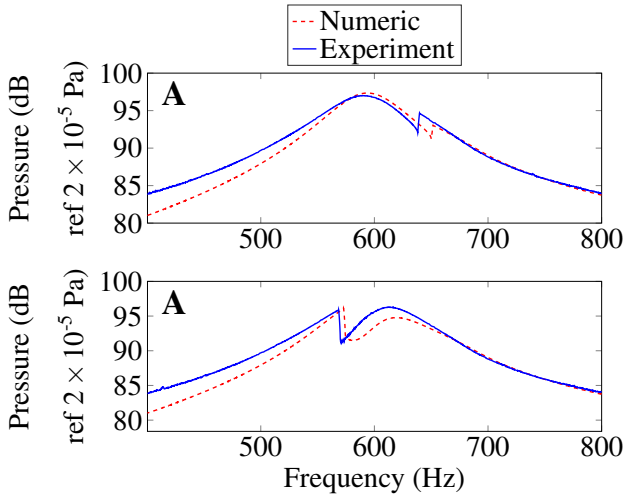

(b) Softening behavior with (top) increasing frequency sweep, (bottom) decreasing frequency sweep.

Fig. 4.11 Experimental and corresponding numerical results obtained from direct numerical integration of Eq. (4.23): variation of the pressure amplitude. Results obtained from Configuration A.

Let us apply the same procedure and analysis to Configuration B. Variations of pressure inside the reduced-section tube for both experimental and numerical results with increasing and decreasing frequency sweeps are presented in Fig. 4.12. For Configuration B, it can be observed that the numerical integration of the equations of the model is also very efficient in predicting the behavior of both hardening and softening behaviors with either increasing or decreasing frequency sweeps. The frequency of the bifurcation is also well-predicted in all cases. Nevertheless, one can observe in Fig. 4.12b (bottom) that the absorption of the ER for the softening behavior with the decreasing frequency sweep is better for the experiment than for the numerical simulation. It is caused by the residual intrinsic resonance of the ER loudspeaker which is close to the cavity resonance to control. Indeed, the intrinsic resonance of the ER loudspeaker is not considered in the reduced order model as the model does not include the behavior of the control (such as delay and influence of the numerical scheme). This issue has not been raised in Configuration A because the tube acoustic mode is at higher frequencies than in Configuration B, decoupling the intrinsic resonance of the ER loudspeaker from the acoustic mode.

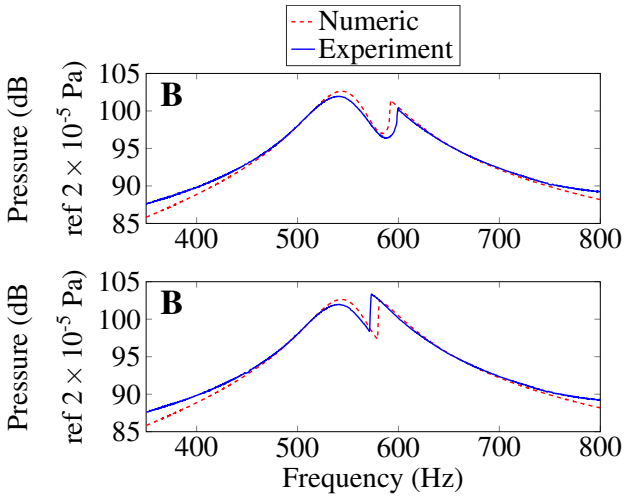

(a) Hardening behavior with (top) increasing frequency sweep, (bottom) decreasing frequency sweep

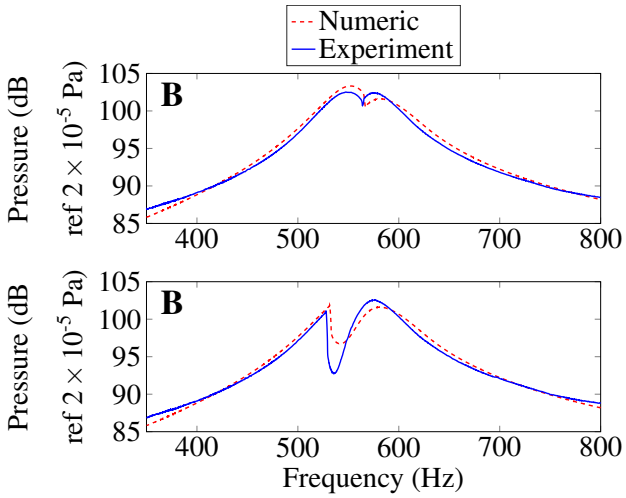

(b) Softening behavior with (top) increasing frequency sweep, (bottom) decreasing frequency sweep.

Fig. 4.12 Experimental and corresponding numerical results obtained from direct numerical integration of Eq. (4.23): variation of the pressure amplitude. Results obtained from Configuration B.

The results from both Configurations reveal a good agreement between numerical and experimental results. The model is accurate and is able to predict the behavior of the coupled system. Moreover, it also shows that the programmed control of the ER is efficient in providing cubic nonlinear oscillators at low excitation amplitudes (under 110 dB). However, some discrepancies between experimental and numerical data appear, and the causes are identified and enumerated here:

- They might come from experimental realization. Uncertainties in the model of the loudspeaker may lead to an imperfect cubic resonator, as the MIC method is based upon an assumed model (Assumptions 3.1 and 3.2).
- Another type of model uncertainties come from the estimation of the physical parameters used for the numerical simulations, e.g. S_d, c_a, k_a or m_a.
- Moreover, non-modeled experimental coupling or phenomena may also have a significant influence, such as the non-modeled low frequency anti-resonance.
- Additionally, assumptions may not be entirely verified, and could create differences between experimental and numerical data. Here, the model assumes a truncation of the modal response to the first mode, which seems to be reasonable here (as the first mode is well decoupled from the other ones in this frequency bandwidth). Another significant assumption lies on the mode shape of the first acoustic mode of the loudspeaker : Assumption 4.6. The assumption of a open-open tube mode shape is not entirely verified, which demonstration is trivial (e.g. the pressure inside the coupling box is not zero). Despite the assumption, the model succeeds to predict the behavior of the coupled system.
- Furthermore, the controller is not included in the model, resulting in the loss of the influences of the delay or of the numerical scheme. The controller can be added in the model in future investigations for better accuracy.

Comparison to the analytical predictions

As presented in Appendix Section C.1.3, the bifurcation only exists within a range of the resonator damping values. To study this condition, the system is excited using a frequency sweep with both increasing and decreasing frequency sweeps. Let us consider the hardening cubic behavior with a fixed linear stiffness such as $\eta_K = 0.9$, and multiple damping values η_R. The critical damping value calculated using the experimental data for Configuration B is $\mu_{R,c} = 0.2232$. Higher values of η_R prevent the bifurcations to occur. Variations of pressure inside the reduced section tube and electrical current injected into the loudspeaker's coil for various values of the damping parameter η_R are presented in Figure 4.13.

One can observe that the analytical results about the role of damping on the existence of bifurcations are accurate. Figures 4.13a and 4.13b show that bifurcations occur at lower values of damping $\eta_R = 1/8$ and $\eta_R = 1/6$ than the critical value $\mu_{R,c}$. Figure 4.13d presents a small bifurcation, even with a slightly larger value than $\eta_{R,c}$. Comparing the Fig. 4.13 with the results of Fig. 4.5b (which shows the apparition of the bifurcation as a function of the ER modal damping) exhibits a good agreement with the analytical predictions. Moreover, the frequency bandwidth of the existence of at least two stable equilibrium points is narrowed with higher η_R. From the analytical study, it is known that the unstable zone of the SIM becomes smaller with the rise of the damping value η_R. Nevertheless, bifurcations are smoothed when η_R approach the critical value $\mu_{R,c}$ as seen in Figures 4.13c and 4.13d, which is due to the two stable equilibrium points getting very close in amplitudes. This result can easily be interpreted with Eq. (C.72): when the damping increases, the imaginary parts of the two points delimiting the boundaries of the unstable zone are led towards 0, leading to the distance between the two points to be reduced. When the damping is superior to the critical damping, the bifurcations do not exist, and there is not a frequency bandwidth where two stable equilibrium points exist, as seen in Figures 4.13e and 4.13f. The agreement with analytical results is quite good, as the critical damping value is well predicted.

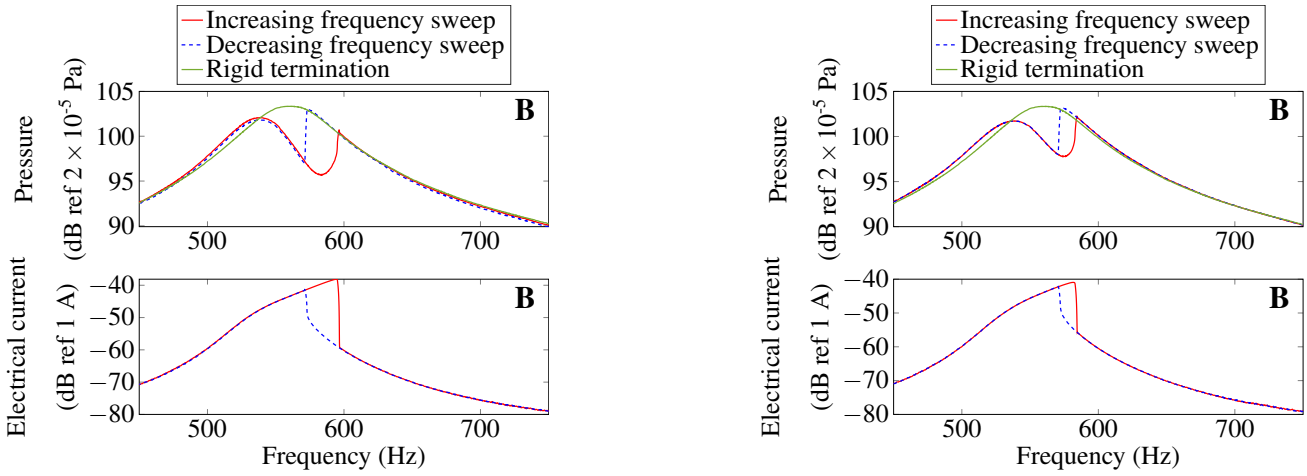

(a) $\eta_R = \frac{1}{8}$ (b) $\eta_R = \frac{1}{6}$

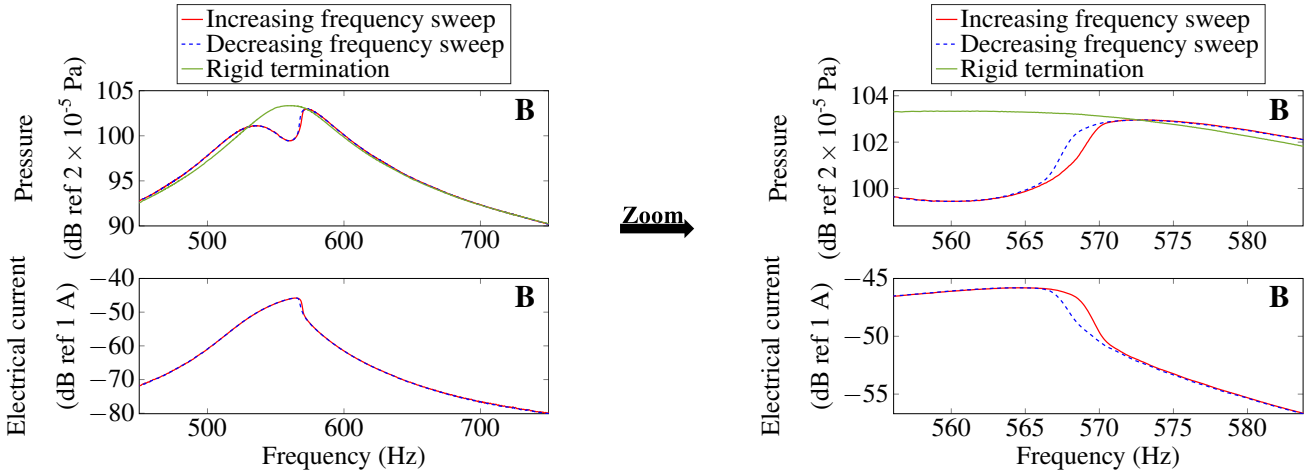

(c) $\eta_R = \frac{1}{4}$ (d) $\eta_R = \frac{1}{4}$

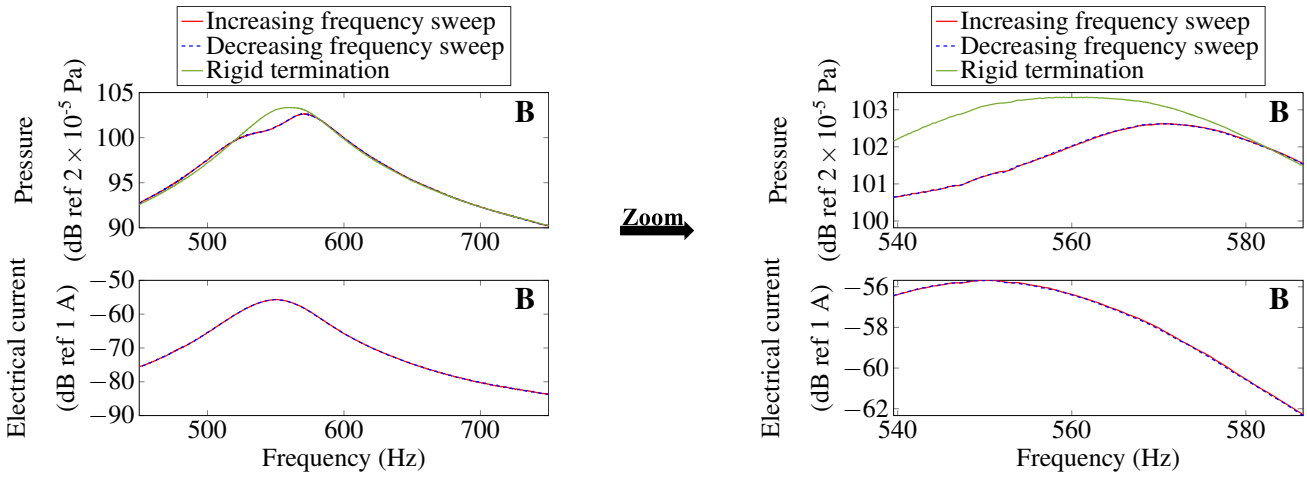

(e) $\eta_R = \frac{1}{2}$ (f) $\eta_R = \frac{1}{2}$

Fig. 4.13 Variations of pressure inside the reduced-section tube and electrical current injected in the ER under frequency sweeps excitation for different values of damping η_R. Results obtained from Configuration B.

In Fig. 4.14, in addition to the frequency sweeps, mono-harmonic signals are composed of a 5-second long sinus. The amplitude of the response to mono-harmonic signals is retrieved and is plotted with the frequency response to the sweeps at the corresponding frequency. Both hardening and softening behaviors are experimentally implemented. Variations of pressure inside the reduced-section tube and electrical current injected in the ER under frequency sweeps excitation are presented in Figure 4.14. It can be seen that mono-harmonic signals excite the lower branch in amplitude of the resonator, resulting in a higher pressure in the reduced-section tube. These observations mean that if the ER is not pre-stressed, i.e. has initial conditions without energy, the ER will select the lower branch of its equilibrium points. Therefore, the decreasing frequency sweep for the hardening behavior and the increasing frequency sweep for the softening behavior are equivalent to the response under mono-harmonic signals if the resonator is not pre-stressed. Nevertheless, the excitation signals that maximize the ER response, i.e. increasing frequency sweep for hardening behavior and decreasing frequency sweep for softening behavior could be obtained with pre-stressed resonators. The next Chapter explores the possibility of using the higher energy branch of the resonator to maximize the energy transfer from the primary system (the acoustic mode of the tube) to the nonlinear resonator, which is very important for creating an efficient control of real systems.

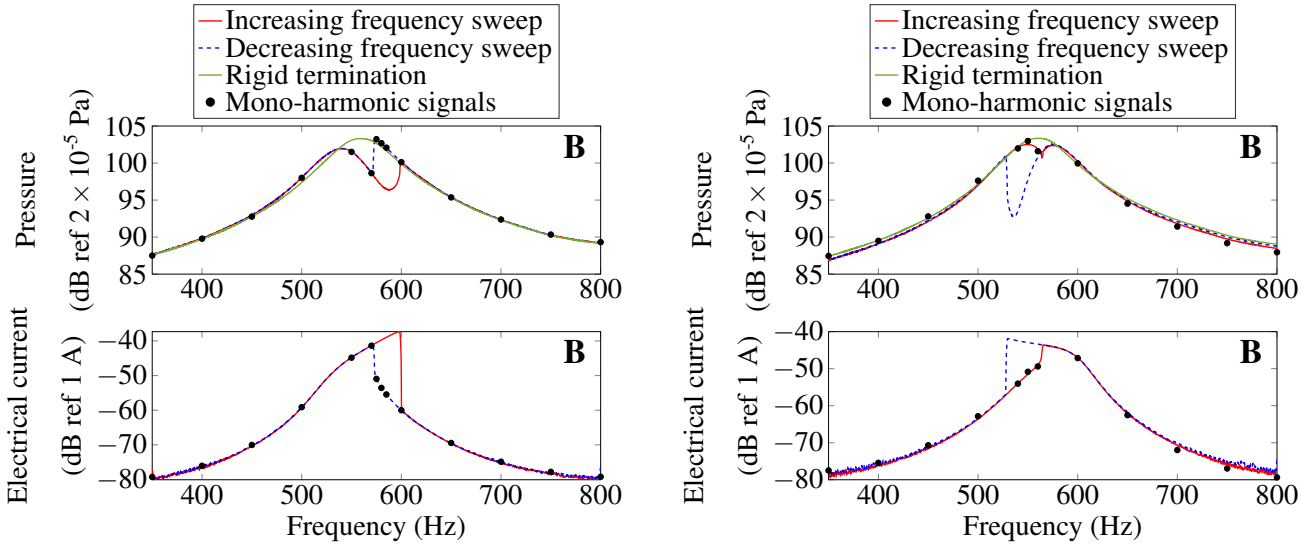

(a) With hardening restoring force function

(b) With softening restoring force function

Fig. 4.14 Experimental results: variations of pressure inside the reduced-section tube and electrical current injected in the ER under frequency sweeps excitation. Results obtained from Configuration B.

One can observe that the analytical results predict well the shape of the curves in the case of the hardening behavior, such as the Figure 4.7a which is to be compared to Figure 4.14a. The bifurcation is well localized (after the resonance), and towards higher amplitude. Notice that the equilibrium points obtained by analytical means describe a mono-harmonic response, and do not describe the response to the frequency sweep signal. However, the analytical results indicated that $\eta_K = 1$ does not allow unstable zones to exist. This shift can be explained by the hypothesis assumed during the analytical development on the scale of the coupling parameter. Additionally, the differences that we can observe between analytical and experimental data, such as the value of the parameter η_K, are probably not caused by the intrinsic resonance of the ER loudspeaker which is close to the cavity resonance to control as previously mentioned. Indeed, this discrepancy does not come from the model as the numerical simulations are more accurate than the analytical ones. As a result, it confirms that it is caused by the assumptions of the analytical study previously detailed.

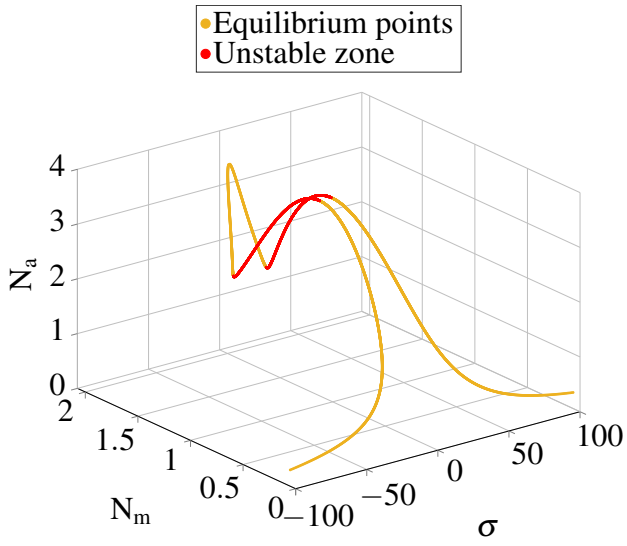

(a) $\beta_{NL} = -5 \times 10^{10}$ m^{-2}, $\eta_K = 1.122$

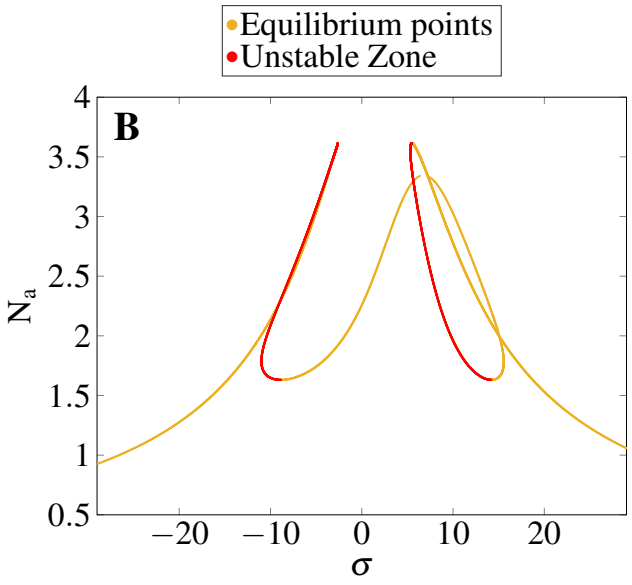

(b) $\beta_{NL} = -5 \times 10^{10}$ m^{-2}, $\eta_K = 1.122$

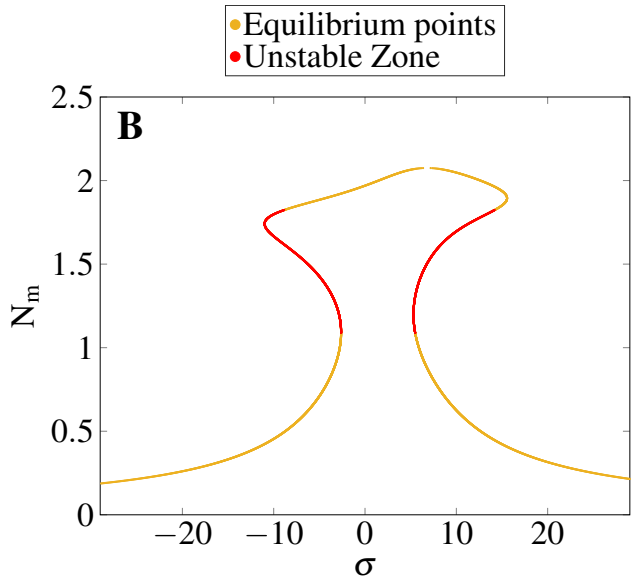

(c) $\beta_{NL} = -5 \times 10^{10}$ m^{-2}, $\eta_K = 1.122$

Fig. 4.15 Analytical predictions: figures of the equilibrium points of the two degree of freedom system defined by equation (C.53), with $P = 0.8468$ Pa. Equilibrium points in the (a) (σ, N_m, N_a) plane; (b) (σ, N_a) plane; (c) (σ, N_m) plane. Results obtained from Configuration B.

The same phenomena can be seen for the softening behavior presented in Figure 4.14b, as the parameter $\eta_K = 1.222$ does not describe well the experimental results. Choosing the parameter $\eta_K = 1.122$ to compute the analytical predictions (i.e. taking the same shift of -0.1 as for the hardening behavior) gives the Figure 4.15. A more accurate description of the phenomena is observed in Figure 4.15b. Indeed, the analytical predictions provide the same behavior as the measured pressure in Figure 4.14b, confirming that the analytical modelling is efficient for the softening behavior as well.

Study of the transient regime

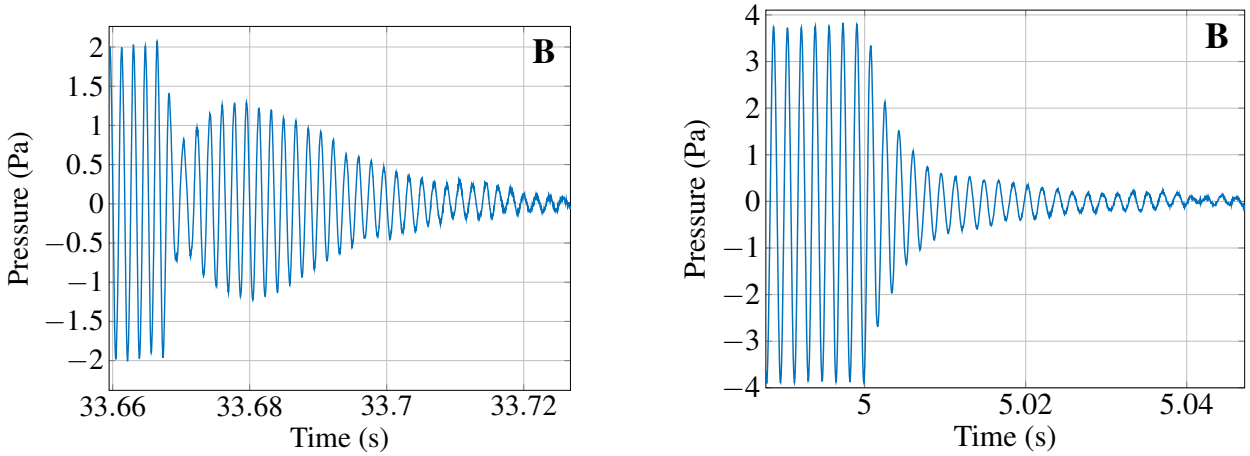

(a) Transient decrease from the higher branch of the ER (frequency sweep signal)

(b) Transient decrease from the lower branch of the ER (mono-harmonic signal)

Fig. 4.16 Experimental results: pressure inside the reduced-section tube at 580 Hz. Results obtained from Configuration B.

To study the transient regime, two different sets of measurements were carried out with two different excitation signals. The transient decrease analysis is realized from a mono-harmonic signal featuring a 5-second long sinus, and from a frequency sweep signal. The frequency sweep signal starts at 350 Hz and stops on a chosen frequency (here 580 Hz) for 3 seconds to obtain the steady response of the high energy equilibrium point. This excitation signal has been designed to enable the study of the transient regime while the ER state is placed on the higher amplitude branch. The two decreases from Figure 4.16 can be compared in terms of shape. The transient decrease of the primary system when the ER is placed on a high energy equilibrium point is presented in Figure 4.16a. It highlights a first decrease, and then an increase in amplitude can be noted. It leads to an exponential decrease until an amplitude of 0 Pa. The transient decrease of the primary system when the ER is placed on a low energy equilibrium point is presented in Figure 4.16b. Only an exponential decrease can be observed. The different phenomena are due to either the energy level of the ER is higher or lower than the bifurcation minimum energy. In the case of the higher energy equilibrium point decrease, it can be observed that the nonlinear resonator gives back energy to the primary oscillator as the energy grows in free regime. This behavior was expected as the resonator is not purely nonlinear and therefore can not display the features of a NES.

4.6 Targeting a non polynomial restoring force function

4.6.1 Design

The logarithmic potential restoring force has been investigated with numerical and analytical tools by Gendelman [66], showing that TET is featured by this non-polynomial law. To the best of our knowledge, the logarithmic potential force has not been experimentally implemented yet. Only Configuration A is considered regarding this restoring force. This particular form of restoring force would create softening behavior that cannot become unstable [66]. Let us introduce the following smooth potential function:

$$V(x) = -\frac{1}{2}K_d \ln(1+x^2) \tag{4.44}$$

A key point is that this force cannot cause unstable behaviors as the potential cannot become positive. It gives the equivalent nonlinear restoring force:

$$F_{\mathrm{NL}}(x) = \frac{K_d x}{1+x^2} \tag{4.45}$$

Nevertheless, this nonlinear force in its current state activates a nonlinear behavior at high excitation amplitudes. In order to enable the activation of a nonlinear behavior at lower excitation amplitudes, we introduce a coefficient β_{NL} as follows:

$$F_{\mathrm{NL}}(x) = \frac{K_d x}{1+\beta_{\mathrm{NL}} x^2} \tag{4.46}$$

The force is plotted Fig. 4.17.

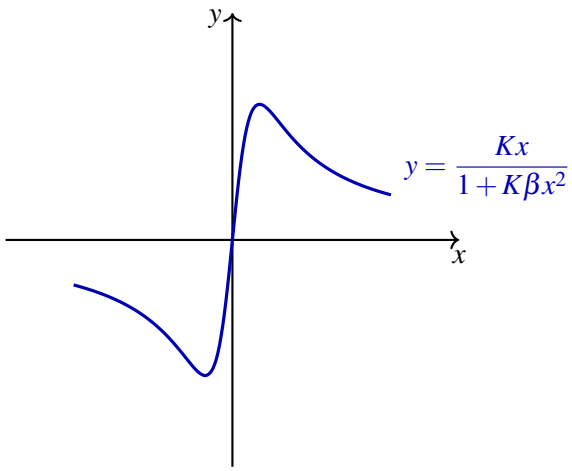

Fig. 4.17 Design of the logarithmic potential behavior.

The logarithmic potential restoring force can be briefly studied by developing the Taylor series of the force:

$$F_{\mathrm{NL}}(x) = \frac{K_d x}{1+\beta_{\mathrm{NL}} x^2} = \sum_{n=0}^{\infty} (-1)^n K_d \beta_{\mathrm{NL}}^n x^{2n+1} \tag{4.47}$$

The Taylor series of the force shows that logarithmic potential restoring force is equivalent to a cubic softening restoring force if the Taylor series is truncated to its two first terms. Therefore, the choice of a similar η_K than chosen for the cubic behavior should give similar results. Let us choose $\eta_K = 1.5496$ which is the same as the cubic softening restoring force. Nevertheless, the Taylor series highlights that the logarithmic potential restoring force is weaker than the cubic softening restoring force [66]. Both behaviors are compared in Fig. 4.18a for equal parameters $|\beta_{\mathrm{NL}}| = 3 \times 10^{11}$ m^{-2} and $\eta_K = 1$. One can observe that the significant softening behavior is activated at higher amplitudes for the logarithmic potential restoring force than the cubic softening restoring force for equal parameters. Therefore, the logarithmic potential softening restoring force is weaker than the cubic softening behavior, as expected. To solve this issue, the value of β_{NL} should be raised, as depicted in Fig. 4.18b for $\eta_K = 1$, and $\beta_{\mathrm{NL}} = 5 \times 10^{11}$ for the logarithmic potential restoring force and $\beta_{\mathrm{NL}} = -3 \times 10^{11}$ m^{-2} for the cubic softening restoring force.

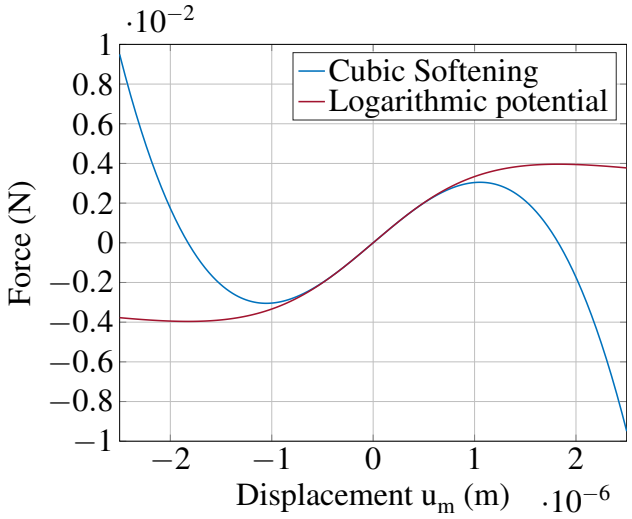

(a) $|\beta_{\text{NL}}| = 3 \times 10^{-11}$ m^{-2}

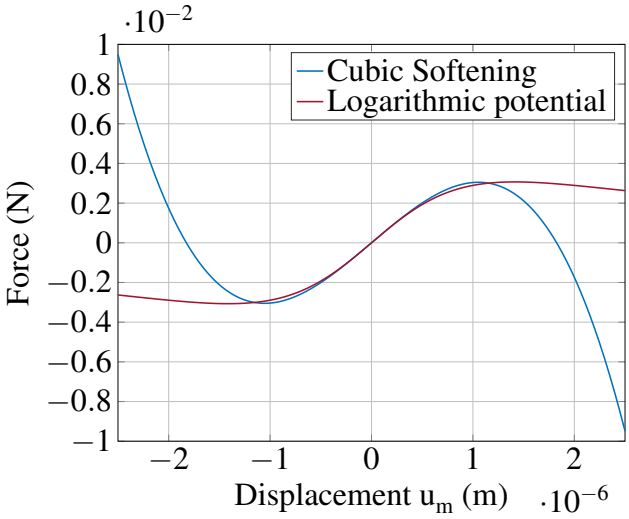

(b) $\beta_{\text{NL}} = 5 \times 10^{11}$ m^{-2} for the logarithmic potential restoring force and $\beta_{\text{NL}} = -3 \times 10^{11}$ m^{-2} for the cubic softening restoring force

Fig. 4.18 Restoring forces of the Logarithmic potential and Cubic Softening nonlinearities with different parameters.

The choice of parameters is detailed in Table (4.6). Two sets of measurements have been done at low and high excitation amplitudes with Configuration A.

Configuration	Parameter	Value		Unit
		Low amplitudes	High amplitudes	
A	η_M	1	1	
	η_K	1.5496	1.5496	
	η_R	$1/8$	$1/8$	
	β_{NL}	5×10^{11}	3×10^{9}	m^{-2}

Table 4.6 Parameter values for the logarithmic potential restoring force results.

4.6.2 Analytical predictions

The analytical predictions obtained by the MSM are presented here. The application of the general analytical results calculated in Appendix C to the logarithmic potential is detailed in the Appendix Section C.3.
The SIM for the parameters of Configuration **A** is plotted in Fig. 4.19a, featuring an unstable zone. The condition of existence of the unstable zone indicates the existence of the folding phenomena, therefore enables to predict the parameters to choose for enabling it. Observe that the nonlinear behavior is predicted, with a large bifurcation enabling a faster decrease of the energy. The numerical simulation steady response is located on the SIM, confirming the analytical calculations. However, the SIM for the parameters from Configuration **A**, but with the parameter $\eta_K = 1.3496$, illustrated in Fig. 4.19b, indicates that the folding phenomena is restricted to lower amplitudes. It results in a much slower decrease of the energy in the system as the bifurcation is tighter. This can be interpreted analytically using the condition of the unstable zones. Physically, this is due to the smaller frequency gap between the ER linear resonance frequency and the tube acoustic mode resonance frequency.

Indeed, if the ER linear resonance frequency is close to the primary system one, the distance between the two stable points of the folding is small, due to the intersection of the backbone curve with the linear resonance at lower amplitudes when the ER linear frequency decreases for softening behaviors. As a result, it is of great interest to be able to predict and optimize the coupled system's response accurately using analytical methods. It confirms the softening behavior expected from the design conclusions.

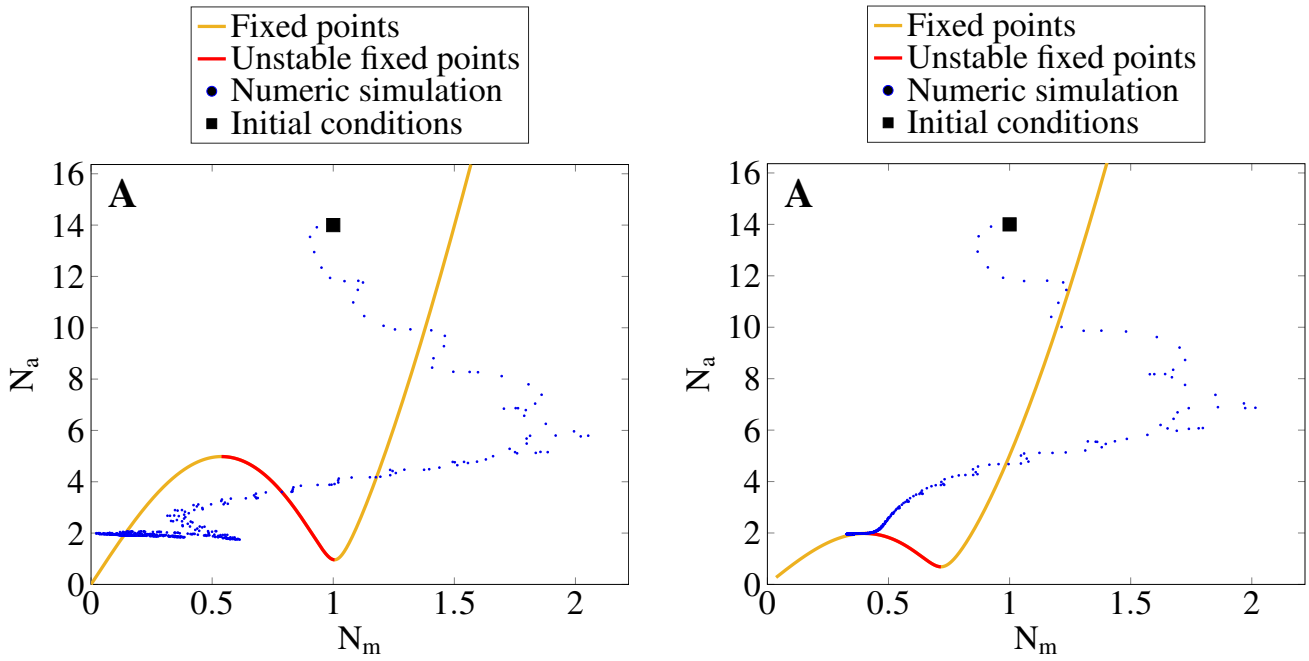

(a) $\beta_{NL} = 5 \times 10^{11}$ m^{-2}, $\eta_K = 1.5496$ (b) $\beta_{NL} = 5 \times 10^{11}$ m^{-2}, $\eta_K = 1.3496$

Fig. 4.19 Figures of the SIM of the two degree of freedom system defined by equation (C.85), with $P = 0.4418$ Pa. Predictions made with parameters from Configuration A.

The equilibrium points determined with the analytical work is illustrated in Fig. 4.20 for parameters defined for Configuration A. The complete equilibrium points in 3 dimensions (Fig. 4.20b) shows isolas, and confirms the nonlinear behavior of the system. This behavior is extremely similar to the softening cubic behavior seen above in Fig. 4.7. This behavior is relevant as a nonlinear behavior is created with an isola at lower amplitudes than the main branch, as seen for the cubic softening behavior. The different views are presented in Fig. 4.19. Previously, the results from Fig. 4.7 for the cubic softening behavior were not accurate to predict the experimental behavior. As a result, an arbitrary shift in the stiffness parameter is proposed: $\eta_K = 1.3496$ and the results are plotted in Fig. 4.21. Figure 4.21b plots the three dimensional plot. It shows that the isola is now attached to the main structure. Additionally, Figure 4.21d illustrates the N_m variable with respect to the frequency, and shows that bifurcations are to be expected in the ER's behavior. The behavior of the acoustic mode of the tube (Fig. 4.21c) predicts eventual bifurcations with a frequency sweep, with possible reduction of the energy of the primary oscillator. Even though it is not realized in this work, a method can be found in [91] for optimizing two degrees of freedom systems with nonlinear resonators to reduce the energy in the primary oscillator, and an experimental and numerical optimization is realized in [115].

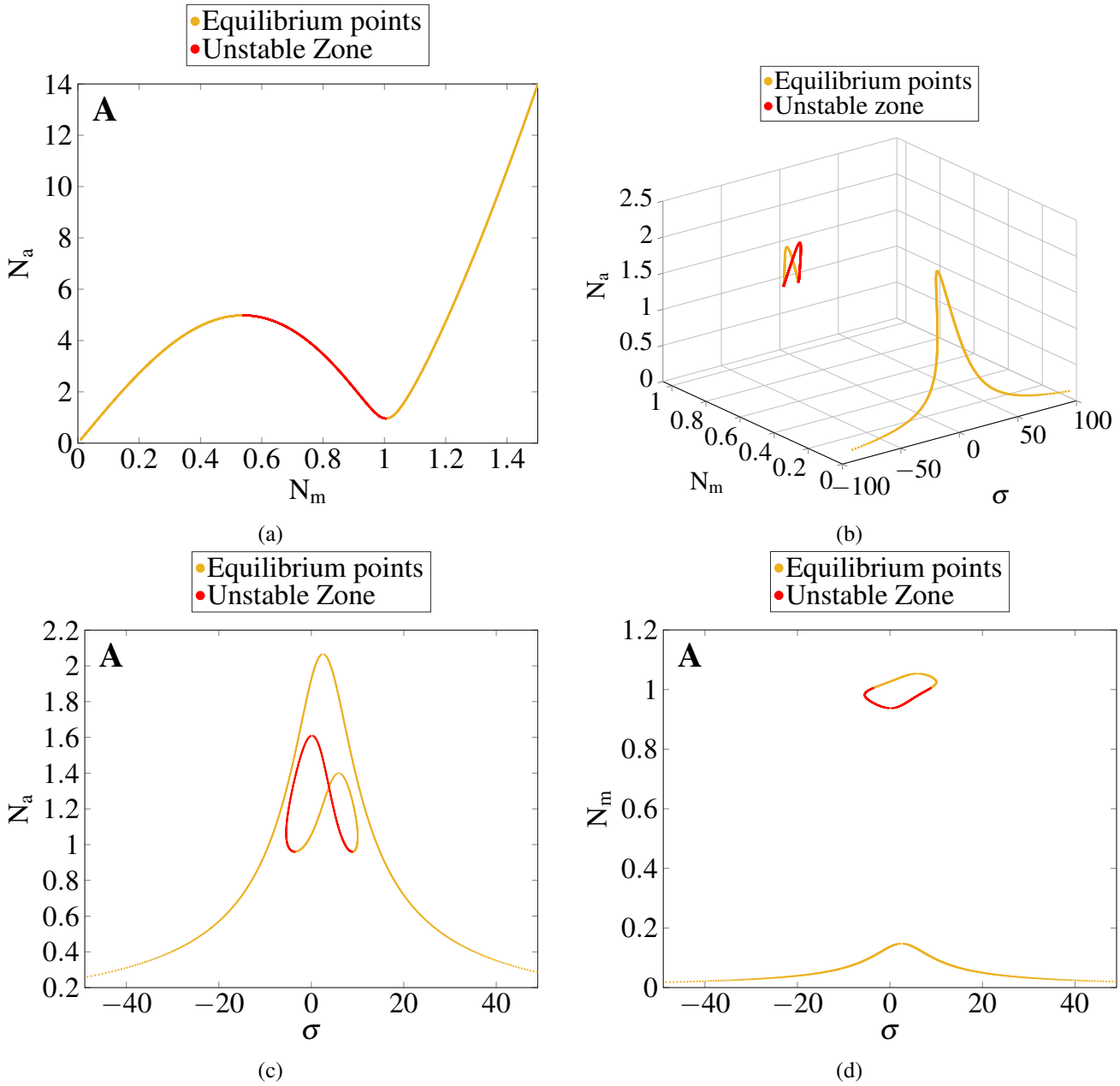

Fig. 4.20 Figures of the equilibrium points of the two degree of freedom system defined by equation (C.53), with $P = 0.4418$ Pa. (a) The SIM ; (b) The equilibrium points in the (σ, N_m, N_a) plane; (c,d) Projections of the equilibrium points in the (σ, N_a) (c) and (σ, N_m) (d) planes. Predictions made with parameters from Configuration A ($\eta_K = 1.5496$).

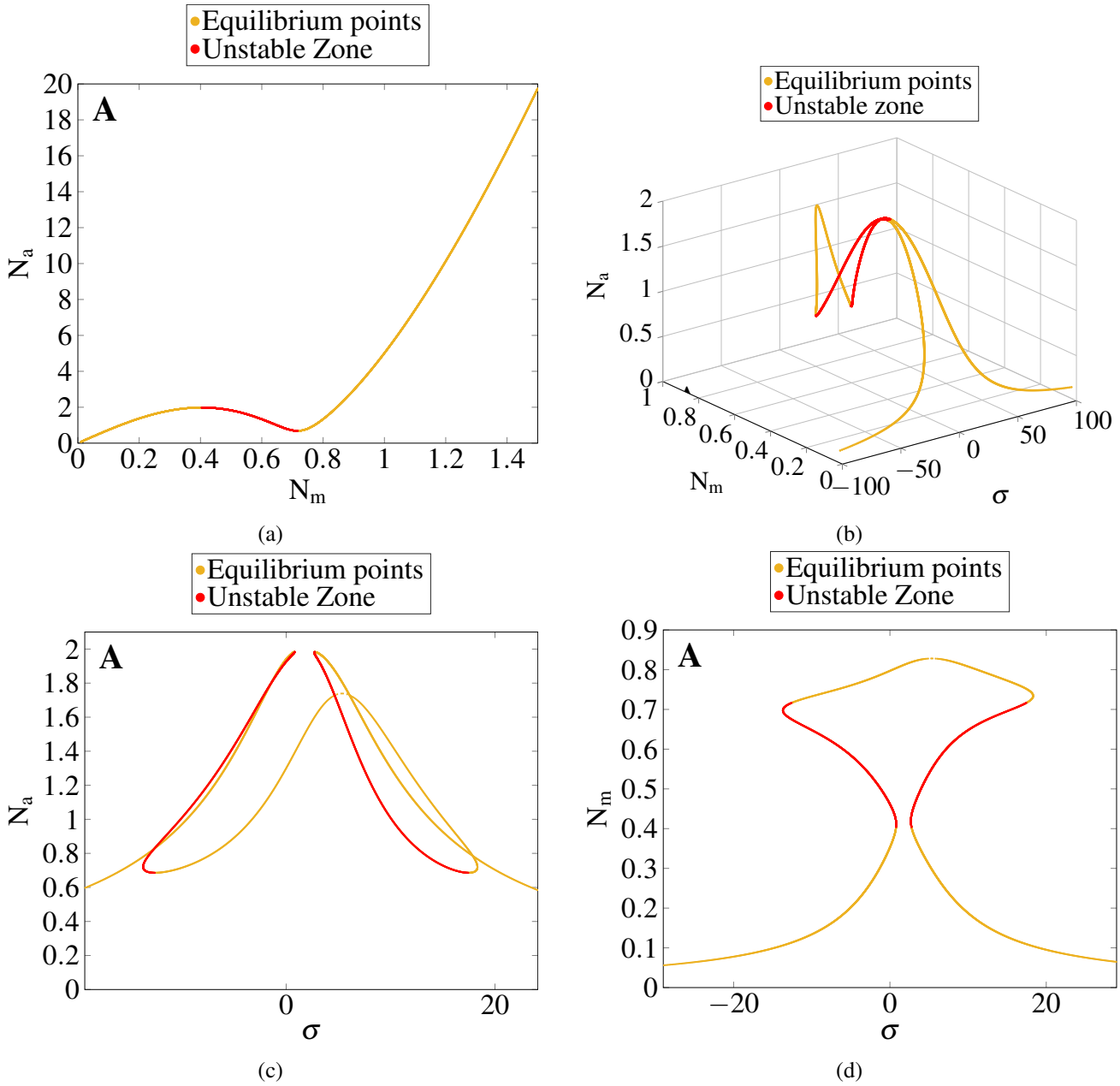

Fig. 4.21 Figures of the equilibrium points of the two degree of freedom system defined by equation (C.53), with $P = 0.4418$ Pa. (a) The SIM; (b) The equilibrium points in the (σ, N_m, N_a) plane; (c,d) Projections of the equilibrium points in the (σ, N_a) (c) and (σ, N_m) (d) planes. Predictions made with parameters from Configuration A (excepted for $\eta_K = 1.3496$).

4.6.3 Experimental results

The variations of the pressure and electrical current amplitudes are plotted in Fig. 4.22a for both increasing and decreasing frequency sweeps of the excitation. One can observe that the ER presents a softening behavior. Moreover, energy transfer from the acoustic mode of the tube to the nonlinear ER occurs at the frequencies of the nonlinear resonance, following the same phenomenon as the previous cases.

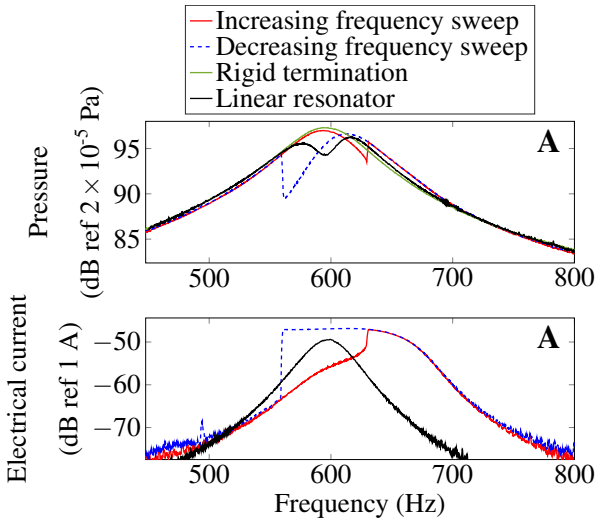

(a) Experimental results for the logarithmic potential restoring force: variation of (top) the pressure amplitude, (bottom) the electrical current.

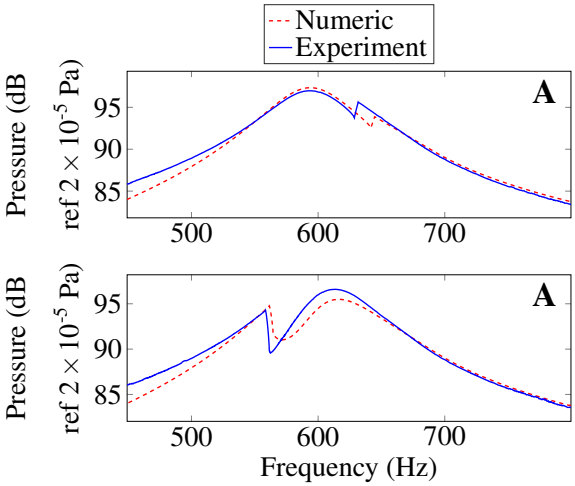

(b) Experimental and corresponding numerical results obtained from direct numerical integration of Eq. (4.23): variation of the pressure amplitude: (top) increasing frequency sweep (bottom) decreasing frequency sweep.

Fig. 4.22 Experimental and numerical results of the logarithmic potential restoring force at low excitation amplitudes. Results obtained from Configuration A.

The numerical results obtained from the integration of Eq. (4.23) are compared to experimental ones in Fig. 4.22b (top) for the increasing frequency sweep, and in Fig. 4.22b (bottom) for the decreasing frequency sweep. The numerical resolution of the model predicts well the behavior of the ER, despite the frequency shift of the jump, as for the other target behaviors. Despite the fractional nature of the restoring forcing function, it shows that the digital ER control is efficient in implementing the programmed nonlinear behaviors. The logarithmic potential restoring force shows great potential for sound absorption as the frequency bandwidth of efficiency is broadened. It also features sound absorption being equal to or greater than the linear oscillator.

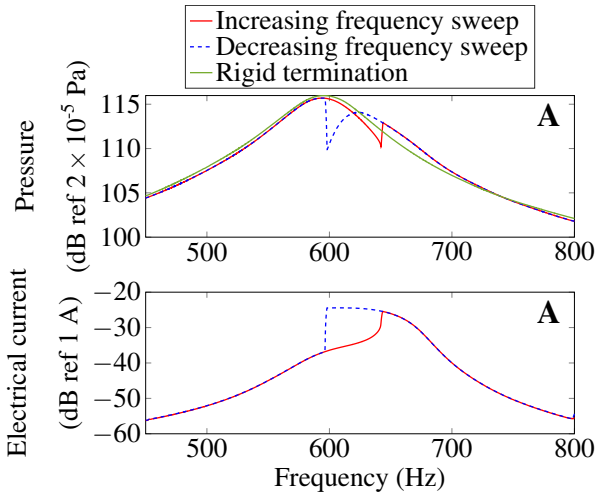

(a) Variation of (top) the pressure amplitude, (bottom) the electrical current.

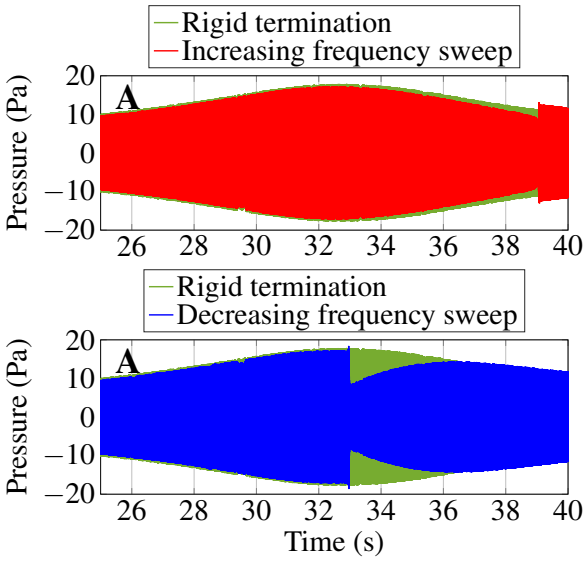

(b) Experimental time histories of the pressure inside the reduced-section tube with (top) increasing frequency sweep (bottom) decreasing frequency sweep.

Fig. 4.23 Experimental results for the logarithmic potential restoring force at high excitation amplitude with $\beta_{\mathrm{NL}} = 3\times10^{9}$ m^{-2}. Results obtained from Configuration A.

As previously mentioned, the nonlinear behavior can be attained at higher or lower excitation amplitudes. It is due to the nonlinear parameter β_{NL} which determines the magnitude of the nonlinear term. The nonlinear term activates the nonlinear response when its order of magnitude becomes similar to the one of the linear term. Based on this analysis, let us choose the parameters $\eta_M = 1$, $\eta_K = 1.5496$, $\eta_R = 1/8$ and $\beta_{\mathrm{NL}} = 3 \times 10^9$. The variations of the pressure and electrical current amplitudes are plotted in Fig. 4.23a. One can observe that the nonlinear phenomena are reproduced at higher excitation amplitudes. It highlights a softening behavior. The time histories of the pressure inside the reduced-section tube are plotted for both increasing and decreasing frequency sweeps in Fig. 4.23b.

4.7 Targeting a nonsmooth restoring force function

Targeting nonsmooth restoring force functions can be easily realized with mechanical devices, but is much more difficult to achieve with acoustic resonators. This section aims at targeting such behaviors, demonstrating the interest of digital controllers enabling the programming of the nonlinearities. Moreover, the use of not well-posed problems may enable quasi-periodic behaviors to appear, which have not been observed until now.

4.7.1 Design

Piecewise linear behavior

The linear piece-wise potential behavior, which has not been previously explored in the context of acoustics, is introduced in this study and illustrated in Fig. 4.24.

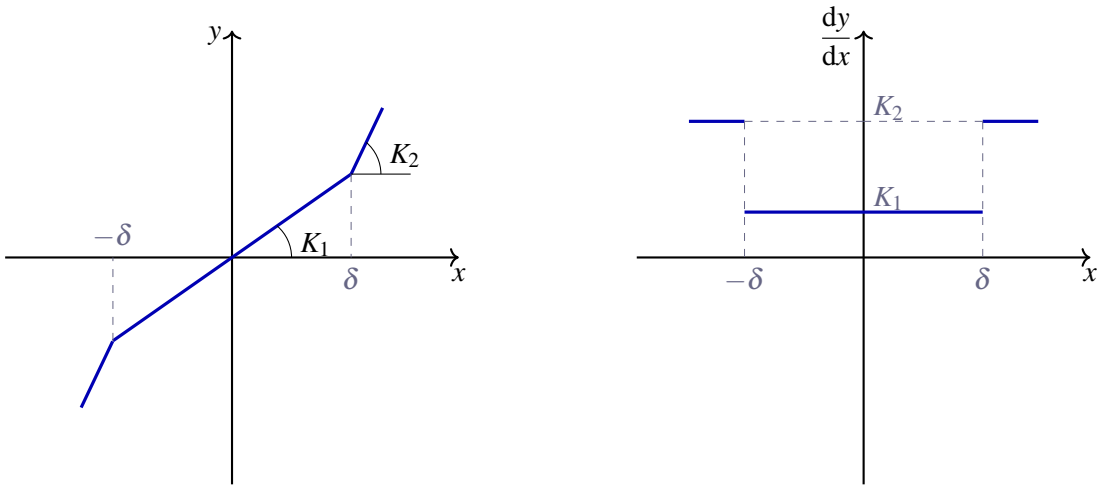

(a) Piecewise linear

(b) Piecewise linear derivative

Fig. 4.24 Design of Piecewise linear

This behavior shows that the method presented here is not limited to smooth restoring forcing functions and can be applied to synthesize non-smooth functions as well. Here, the goal is to create a system with a hardening behavior similar to a duffing-type behavior with 2 different slopes depending on a clearance of 2δ. The associated

restoring forcing function force plotted in Fig. 4.24 reads:

$$F_{\mathrm{NL}}(t,x) = \begin{cases} K_2 x - (K_1 - K_2)\delta & \text{if } x < -\delta \\ K_1 x & \text{if } -\delta < x < \delta \\ K_2 x + (K_1 - K_2)\delta & \text{if } \delta < x \end{cases} \tag{4.48}$$

where K_1 and K_2 stand for the slopes of the linear functions composing the nonlinear restoring force function.

This force is not differentiable on its whole definition domain, as in $x = \pm\delta$, where an infinite number of derivatives exist. The derivative of the force is a set-valued function, and is plotted in Fig. 4.24b. The clearance parameter 2δ defines the displacement of the membrane threshold at which nonlinear phenomena are initiated. The chosen parameters for the Configuration **A** are detailed in Table 4.7:

Configuration	Parameter	Value	Unit
A	η_M	1	
	η_K	1.2598	
	f_d	596	Hz
	η_R	$1/8$	
	K_1	K_d	$\mathrm{kg\,s^{-2}}$
	K_2	$5K_1$	$\mathrm{kg\,s^{-2}}$
	δ	8×10^{-7}	m

Table 4.7 Parameter values of the piece-wise linear restoring force experiment.

The selected parameters for the experiment are $\eta_M = 1$, $\eta_K = 1.2598$, and $\eta_R = 1/8$. The selection of η_K has been driven by the aim of aligning the linear resonance frequency of the ER with the acoustic mode of the tube.

Discontinuous piecewise linear behavior

The use of such a control strategy enables the creation of discontinuous piecewise behavior. Let us consider the following discontinuous piecewise linear restoring force:

$$F_{\mathrm{NL}}(t,x) = \begin{cases} K_2(x(t) + \delta) & \text{if } x < -\delta \\ K_1 x(t) & \text{if } -\delta < x < \delta \\ K_2(x(t) - \delta) & \text{if } \delta < x \end{cases} \tag{4.49}$$

The goal of creating a discontinuity between two linear parts is twofold. The effective stiffness appears extremely steep for the system, allowing to simulate an impact-like response, and the stiffness is almost zero in some regions of displacement x, which has proved to be difficult to synthesize using digital control. The restoring force function is plotted in Fig. 4.25.

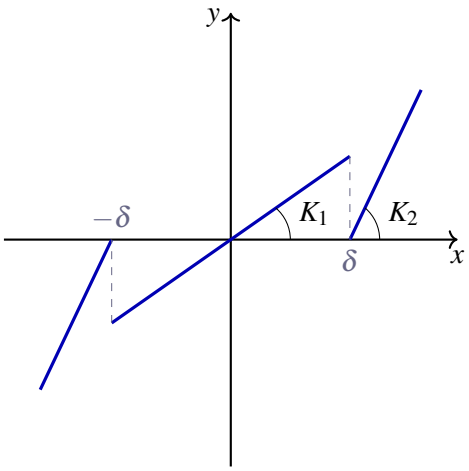

Fig. 4.25 Design of Piecewise linear discontinous

The configuration **C** is used for the experiments, and the chosen parameters in the digital programming of the control strategy are detailed in Table 4.8.

Configuration	Parameter	Value	Unit
C	η_M	1	
	η_K	1	
	f_d	531	Hz
	η_R	1/8	
	K_1	K_d	$\mathrm{kg\,s^{-2}}$
	K_2	$1.1K_d$	$\mathrm{kg\,s^{-2}}$
	δ	2×10^{-5}	m

Table 4.8 Parameter values of the piece-wise linear restoring force experiment.

4.7.2 Analytical predictions

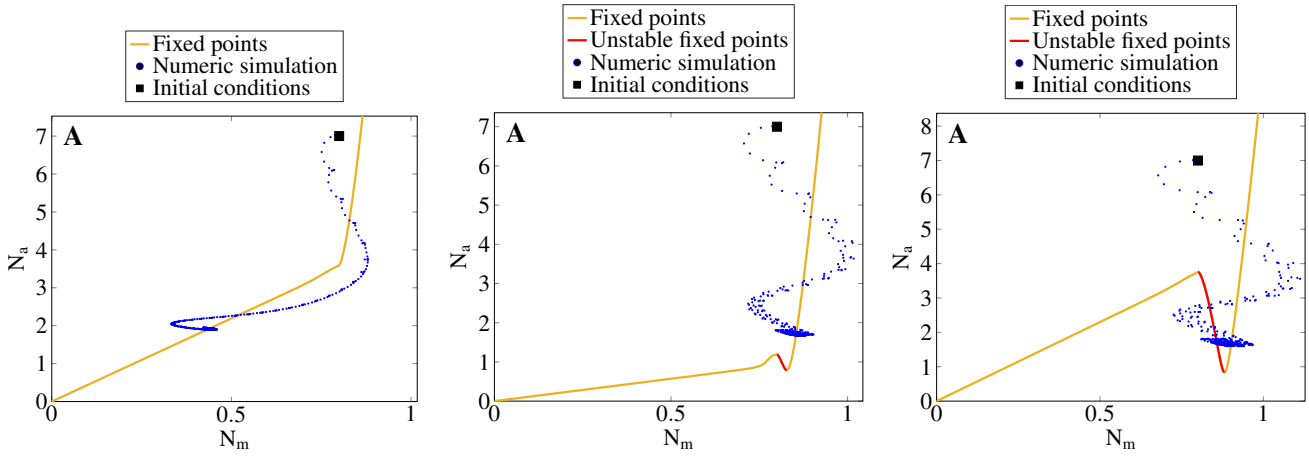

(a) $\eta_K = 1.2598$ (b) $\eta_K = 1.1$ (c) $\eta_K = 1$

Fig. 4.26 Predictions made with parameters from Configuration A.

The analytical predictions obtained by the MSM are presented here. The application of the general analytical results calculated in Appendix C to the piecewise nonlinearity is detailed in the Appendix Section C.4.
The MSM method used for analytical study struggles with discontinuous behaviors, and specific methods exist to treat them [8, 13]. As a result, the analytical study of the discontinuous configuration is not developed within this work. Only the piecewise continuous restoring force is here studied.

The analytical predictions of the SIM obtained with the continuous piecewise linear restoring force is illustrated in Fig. 4.26 for the defined parameters in Configuration A, with multiple values of $\eta_K = \{1.2598, 1, 1.1\}$.

- The $\eta_K = 1.2598$ case (Fig. 4.26a) illustrates the SIM for the values taken in the experimental tests. It predicts a linear behavior: the value of η_K aligns the linear resonance frequency of the NER with the one of the primary oscillator. It prevents the nonlinear behavior to happen as the nonlinear resonance is not aligned with the primary oscillator's resonance. However, it can be seen below that the experimental results exhibit nonlinear behavior despite this alignment. However, the modification of the slope of the restoring force can be clearly observed at $N_m = 0.8$.

- Building upon the previous analytical studies being compared to the experimental results, a shift in η_K should be made to enable the activation of nonlinear resonances. Here, $\eta_K = 1.1$ (Fig. 4.26b) is arbitrarily chosen, exhibiting possible bifurcations from a folding phenomenon. However, the bifurcation amplitude is low, and does not seem to enable an efficient transient energy decrease. This phenomena has been explained in Section 4.6.2. Additionally, the unstable zone starts at the defined clearance $N_m = 0.8$, enabling the precise choice of the apparition of nonlinear phenomena, increasing the controllability of the NER.

- By lowering $\eta_K = 1$ (Fig. 4.26c), the bifurcation amplitude increases, enabling an efficient transient decrease of the energy. However, the equilibrium points resulting from this set of parameters (Fig. 4.27) do not show an efficient decrease of the energy of the steady-state regime of the primary oscillator: an isola appears and the primary system mainly exhibits a linear behavior.

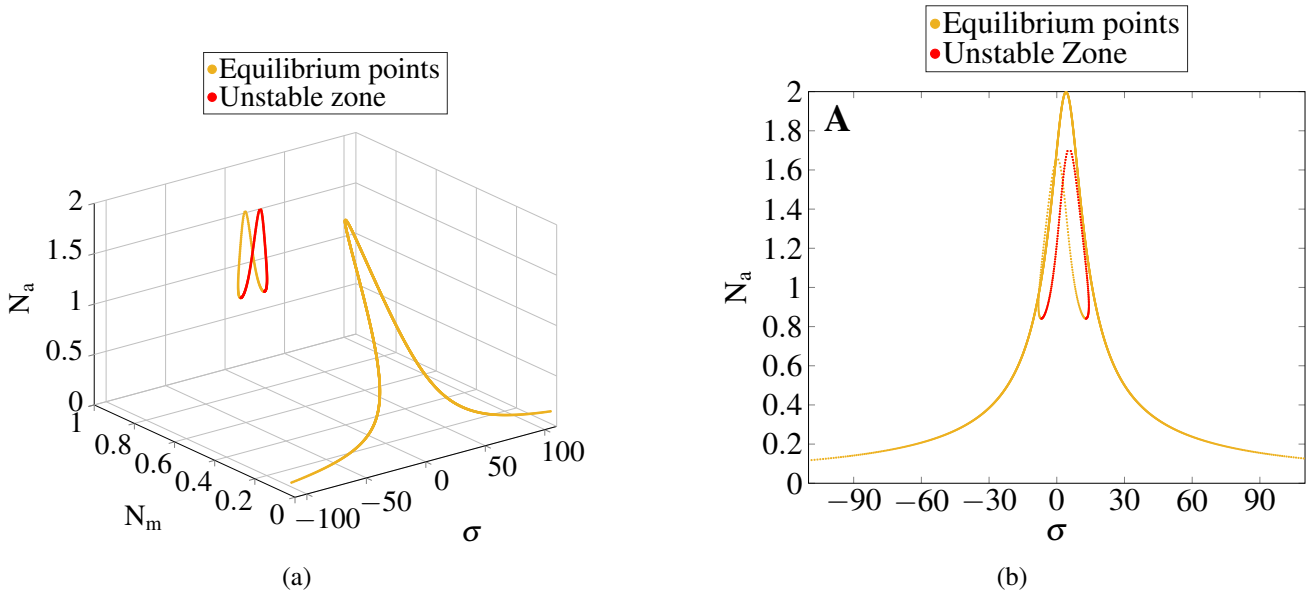

(a) (b)

Fig. 4.27 Figures of the equilibrium points (a) in the (σ, N_m, N_a) plane; (b) in the (σ, N_a) plane of the two degree of freedom system defined by equation (C.53), with $P = 0.4418$ Pa. Predictions made with parameters from Configuration A (excepted for $\eta_K = 1$).

For the three Figs 4.26a, 4.26b and 4.26c, the numerical integration of the model oscillates around the SIM, showing an agreement with the analytical results in addition to the steady-state response that is on the SIM. However, the damping ratio of the acoustic mode of the tube prevents the oscillations to follow the SIM precisely, in addition to the not verified assumption of the order of the coupling term. As a result, the behavior with $\eta_K = 1.1$ is studied through its equilibrium points, illustrated in Fig. 4.28. The main branch of equilibrium points exhibits a folding phenomenon, as it can be seen in the three dimensional Fig. 4.28b. Moreover, no isolated response curves are spotted. The NER response is plotted in Fig. 4.28d and shows eventual bifurcations. The response of the acoustic mode of the tube (Fig. 4.28c) also features bifurcations in its frequency response curve. It can be seen that the steady-state amplitude of response is lower than for $\eta_K = 1$. It shows the importance of evaluating the equilibrium points of the two degrees of freedom system.

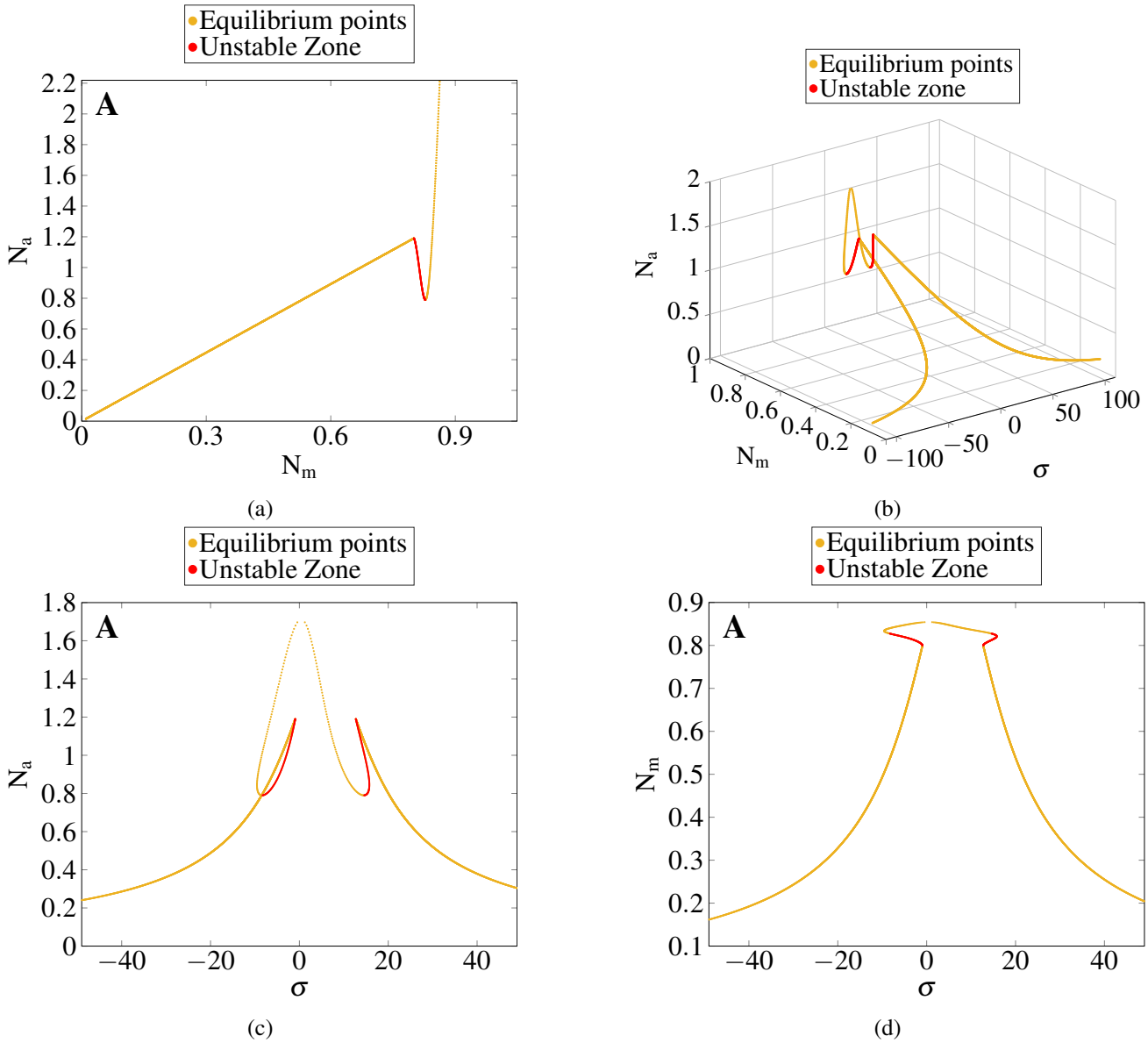

Fig. 4.28 Figures of the equilibrium points of the two degree of freedom system defined by equation (C.53), with $P = 0.4418$ Pa. Predictions made with parameters from Configuration A (excepted for $\eta_K = 1.1$).

4.7.3 Experimental results

Piecewise linear behavior

The variations of the pressure and electrical current amplitudes are plotted in Fig. 4.29a.

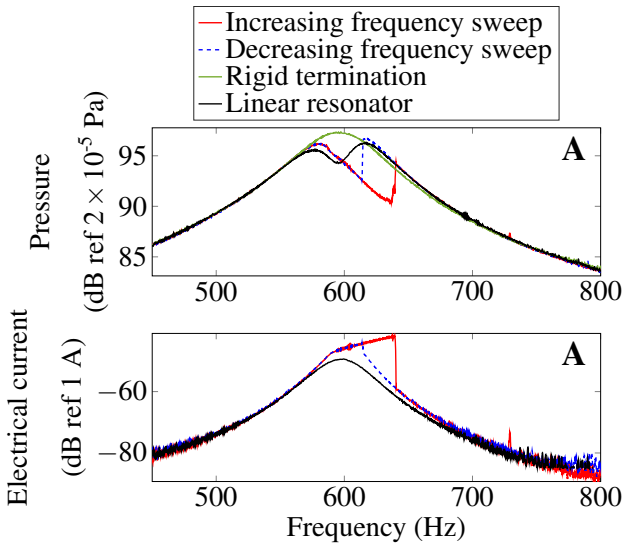

(a) Variation of (top) the pressure amplitude, (bottom) the electrical current.

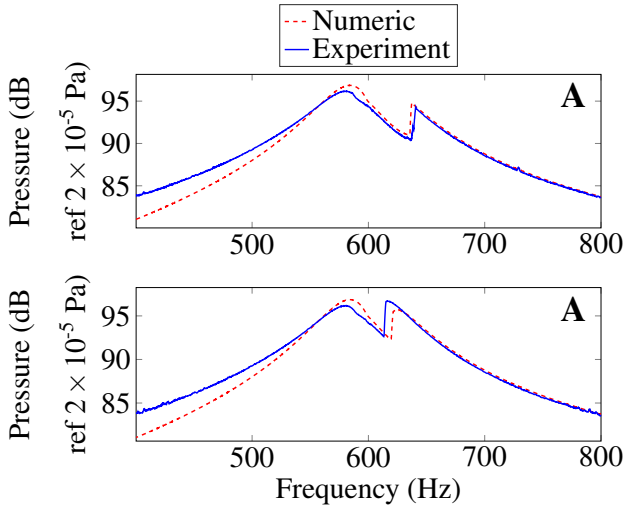

(b) Experimental and corresponding numerical results obtained from direct numerical integration of Eq. (4.23): variation of the pressure amplitude: (top) increasing frequency sweep (bottom) decreasing frequency sweep.

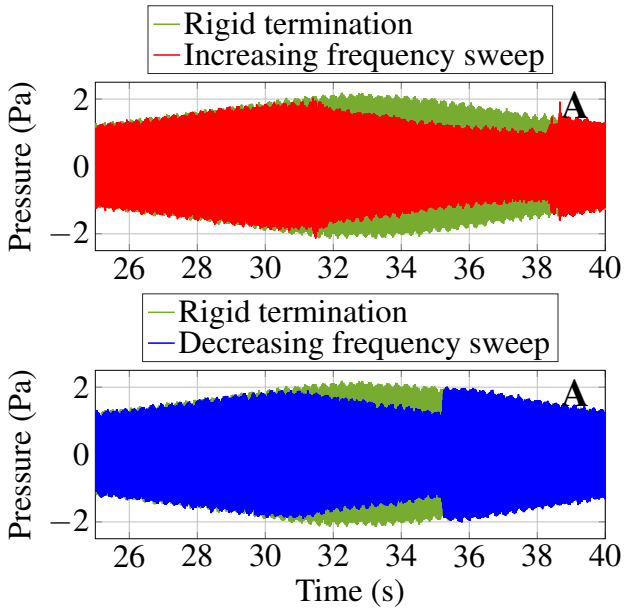

(c) Experimental time histories for the piecewise linear restoring force: pressure inside the reduced-section tube for the hardening behavior with (top) increasing frequency sweep (bottom) decreasing frequency sweep.

Fig. 4.29 Experimental results for the piece-wise linear restoring force. Results obtained from Configuration A.

One can observe in Fig. 4.29a (bottom) that the created behavior looks like a hardening duffing-type oscillator which is depicted in Fig. 4.9. Moreover, a significant reduction (of 5 dB ref 2×10^{-5} Pa) of the sound level can be seen and is not limited to the frequencies of the nonlinear resonance. It is explained by the linear nature

of the oscillator which is tuned to the frequency of the first mode of the primary system. The linear oscillator pumps the energy before activating its nonlinear behavior. This leads to a shift of the nonlinear behavior to higher frequencies, and as a result to energy pumping shifted from the maximum peak amplitude of the primary system. The experimental outcome is compared to results obtained from numerical integration of Eq. (4.23) for both increasing frequency sweep (top) and decreasing frequency sweep (bottom) in Fig. 4.29b. Both results fit closely the measurements, confirming that the actual behavior follows the programmed piece-wise linear behavior. These results show that via accurate choice of parameters, the programming of the piece-wise linear restoring forcing function can lead to promising results. Indeed, this behavior shows the potential of such nonlinear ER, as the performed sound absorption is greater than the linear ER for a larger frequency bandwidth. Experimental time histories of the pressure inside the reduced-section tube are plotted in Fig. 4.29c.

Discontinuous piecewise linear behavior

Frequency sweeps are used to evaluate the behavior and efficiency of the discontinuous piecewise linear restoring force function. The response of the acoustic first mode of the tube with a reduced section along with the computed electrical current are plotted in Fig. 4.30a. Notice that the computed electrical current with increasing and decreasing frequency sweeps are identical. Moreover, it can be seen that the amplitude response is modulated at the highest amplitude of the electrical current. The plot featuring the pressure amplitude reveals that the sound pressure is lowered at the ER resonance and that the performance is identical for both increasing and decreasing frequency sweeps. Furthermore, it presents modulations at the same frequencies as the electrical current. Finally, two peaks can be distinguished at lower and higher frequencies than the observed modulations. It is a similar behavior as a non-optimized Tuned Mass Damper, which can be expected as the behavior is piecewise linear.

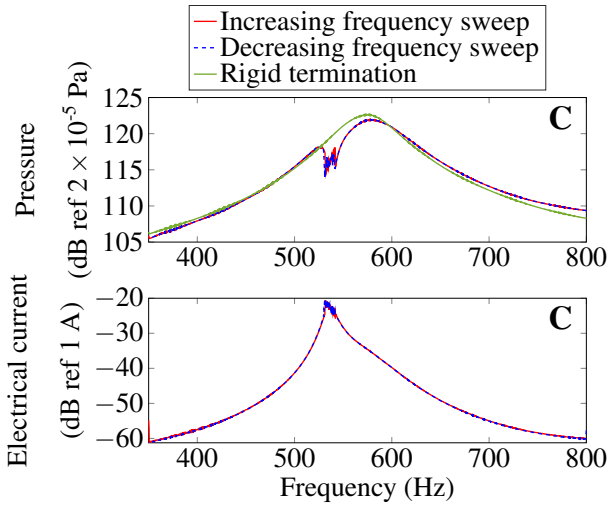

(a) Variation of (top) the pressure amplitude, (bottom) the electrical current.

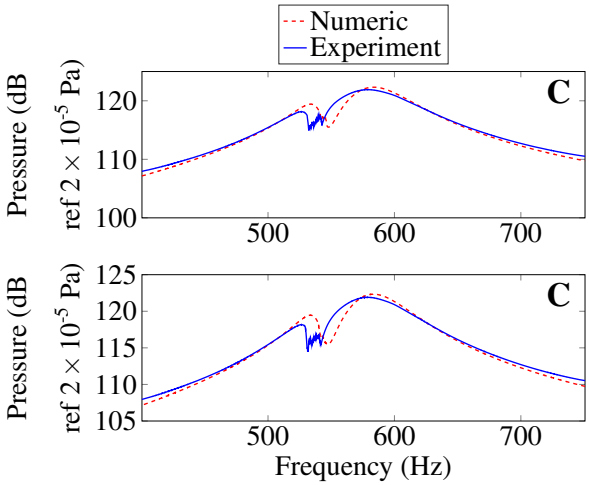

(b) Experimental and corresponding numerical results obtained from direct numerical integration of Eq. (4.23): variation of the pressure amplitude: (top) increasing frequency sweep (bottom) decreasing frequency sweep.

Fig. 4.30 Experimental results for the discontinuous piece-wise linear restoring force. Results obtained from Configuration C.

The comparison between numerical simulations and experimental results presents a reasonable accuracy for both increasing and decreasing frequency sweeps, presented in Fig. 4.30b. The behavior is well predicted as the numerical simulations features a lower sound pressure at the resonance of the ER. A quasi-periodic behavior is also detected on a narrower frequency bandwidth than the experimental one (see Fig. 4.31).

Figure 4.31a shows the sound pressure for a 537 Hz sinusoidal excitation (inside the frequency zone where modulations seem to exist) and for a 580 Hz sinusoidal excitation (outside the zone of the modulations). Observe that the response to the 537 Hz excitation is a quasi-periodic regime, confirmed by the Henon map in Fig. 4.31b. Indeed, the Henon map of the response to the 537 Hz excitation is a closed-form curve indicating quasi-periodic behavior. Furthermore, the 580 Hz excitation is a stationary regime as confirmed by Henon map also, as expected. As a result, the discontinuous piecewise linear restoring force function features quasi-periodic regime that is difficult to attain in this particular experiment with classical restoring force functions.

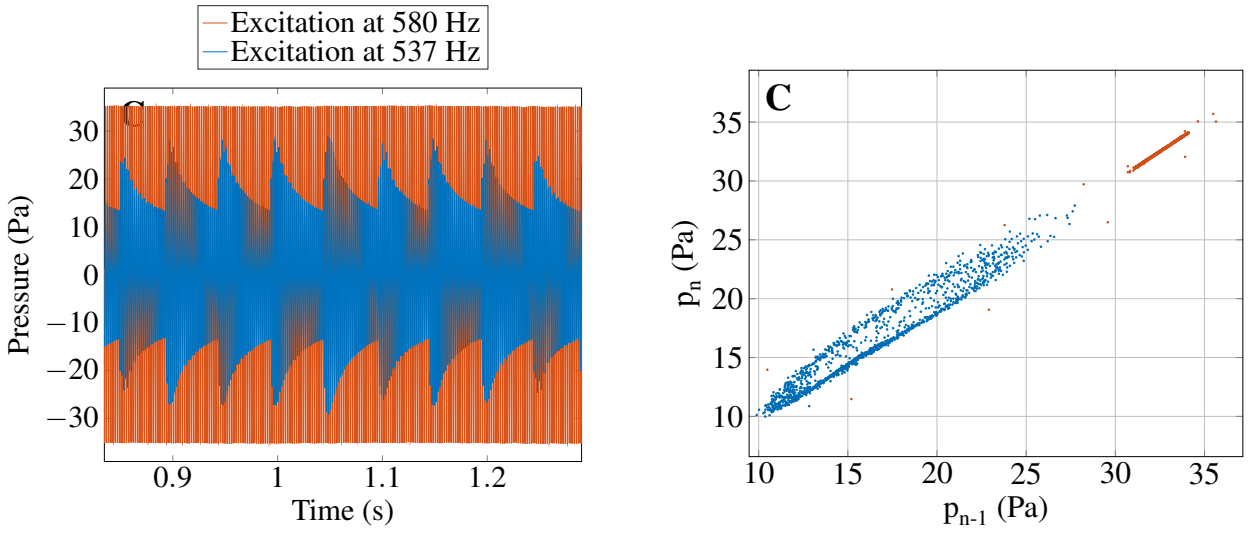

(a) (b)

Fig. 4.31 Experimental time histories for the discontinuous piecewise linear restoring force for sinusoidal excitation at 537 Hz and 580 Hz (a) and its Henon map (b).

However, discontinuous restoring force functions require, either adapted numerical schemes, or small time steps with classical schemes to minimize the errors. Here, the choice of classical numerical schemes are used to implement the discontinuous behavior, as adapted numerical schemes would be more precise, but would be of lower orders. The time histories from the discontinuous behavior measurement can be observed in Fig. 4.32. Notice that the electrical current computed during the experiment shows discontinuous behavior in Fig. 4.32a. This is due to the ES computed displacement that exceeds the clearance $\pm\delta$. Indeed, the behavior that is presented here is not well-posed, and induce these kind of behaviors. The electrical current and the ES computed acceleration (Fig. 4.32d) present discontinuous behaviors while the computed displacement (Fig. 4.32b) and velocity (Fig. 4.32c) display continuous (non differentiable) behaviors. As the electrical current is the sum of acceleration, displacement and velocity, it can be expected that if discontinuous behavior is observed in one of them, the electrical current will feature identical properties. This kind of behavior is usually defined as an issue to be resolved, but can indeed be useful to synthesize particular behaviors such as quasi-periodic regime. Moreover, a key point is that both increasing and decreasing behaviors are identical, which presents a better potential for use in unknown conditions.

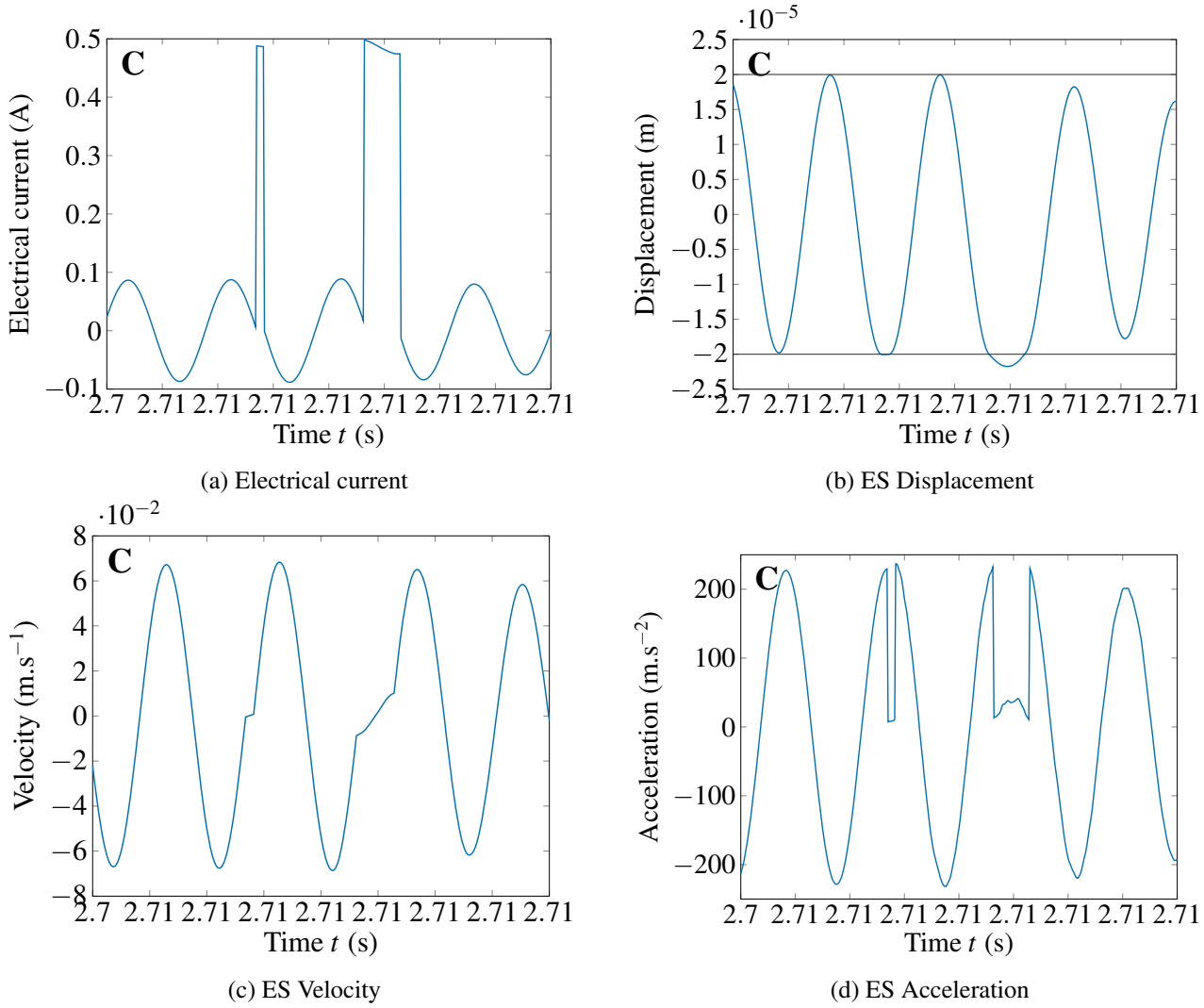

(a) Electrical current

(b) ES Displacement

(c) ES Velocity

(d) ES Acceleration

Fig. 4.32 Experimental time histories for the discontinuous piecewise linear restoring force of the computed variables during the experiment. Results obtained from Configuration **C**.

4.8 Conclusion of the chapter

This chapter highlights the potential of the presented control strategy of Chapter 3 for the digitally programming of a desired behavior. Even though the control strategy is limited by the mass and internal stiffness of the loudspeaker, these parameters can be modified and nonlinear behaviors can be enforced. This chapter demonstrated the main following results:

- The control strategy is capable of enforcing a desired digitally programmed behavior accurately. The diversity of the nonlinear behaviors is large, but the following behaviors have been programmed to showcase various different behaviors:
  - linear and cubic restoring force: softening and hardening behaviors;
  - non-polynomial restoring force: the logarithmic potential restoring force;
  - non-smooth restoring forces: continuous and discontinuous linear piecewise restoring forces;
  - nonlinear restoring forces featuring time-dependent coefficients (parametric forces). These restoring forces are not detailed in this manuscript, but has been developed and studied with a cubic stiffness

restoring force with a periodic time-dependent coefficient. The study has been published in an article shown in Appendix D [115].

- The NER is capable of controlling an acoustic mode of a tube, and therefore absorbing energy.
- The synthesized NER exhibits better performances in controlling the acoustic mode than a synthesized linear Tuned Mass Damper (see Appendix D).

To achieve these goals, an experiment is created where the NER is coupled to an acoustic mode of a tube through a coupling box. The model of the experiment, first developed by Bellet in [16], is adapted to the experimental means. The model is validated against the experimental results, and then studied through:

- Numerical simulations: the model predicts accurately the observed experimental behavior, despite strong hypotheses about the physics and control strategy involved. It validates the model and enables the full validation of the control strategy by confirming that the experimentally obtained behavior is the one desired and programmed.
- Analytical calculations realized using the MSM method coupled to the complex variables of Manevitch. Despite the validation of the model using numerical simulations, the analytical results do not give accurate predictions of the full behavior of the two degrees of freedom system. This discrepancy is due to the additional assumptions on the parameters orders of magnitude needed to realize the calculations. However, the qualitative behavior shown by the analytical results is in agreement with the experimental behavior, allowing of a deepest understanding of the phenomena at stake.

The complete analysis of the system enabled the previous conclusions. Moreover, it enables this experiment to become a test for unusual nonlinear behaviors before realizing expansive laboratory tests.

Until now, observe that the performances of the nonlinear resonator in controlling the acoustic mode is highly dependent of the branch of solutions adopted by the nonlinear resonator. As a result, to realize a fully controllable nonlinear resonator, the modification of the control strategy to enable the real-time selection of the equilibrium point is proposed in the next Chapter.

Chapter 5

Targeting specific equilibrium points

As it has been seen previously, the ER presents better energy absorption when placed on its high energy equilibrium point. Nonlinear mechanical systems can present complicated basin of attraction which depend on initial conditions [155]. As a result, depending on initial conditions, the forced nonlinear system can be attracted by different equilibria which affects dramatically the performances of the system.
The main objectives of this chapter is:

- Investigating the possibility and means to enable the RTI strategy described above to target specific stable equilibrium points, if more than one coexist at a single frequency,
- Investigating the capability of the designed method to realize energy absorption by selecting a targeted equilibrium.

However, on the one hand, to mechanically impose initial conditions on an ER is not a trivial task. On the other hand, classical control strategies do not contemplate the enforcing of initial conditions and the synthetic selection of one specific set-point when the system allows multiple stable solutions. As a result, to achieve these goals, the control strategy presented in Sections 3.1.2 and 3.1.3 allows to tackle this issue by forcing the ES to reach a specific equilibrium point, and is the main novelty of this chapter. Such achievement provides a significant breakthrough in the recent development of non-linear (generalized) impedance control techniques [78, 43, 114, 112], since the specific set-points introduced by synthetic nonlinearities have been, so far, only achievable under unrealistic external noise excitations (swept sines), as demonstrated in the two previous chapters.

This chapter is mainly taken from the following article, currently under review :

- Morell M., De Bono E., Gourdon E., Collet M., Ture Savadkoohi A., Lamarque C.-H. A model-inversion control strategy to attain desired equilibrium points when synthesizing nonlinear resonators. *Under review.*

5.1 Theoretical developments

Let us identify a target equilibrium point X_d^* of the desired dynamics F of the ES. Its basin of attraction is denoted $\mathscr{B}_F(X_d^*)$. In classical nonlinear systems where initial conditions are physically accessible, they can be properly set based on its basin of attraction $B_F(X_d^*)$, in order to realize the target equilibrium point [16]. For example, supposing to have multiple stable solutions and to target the highest energy equilibrium point, non-zero initial conditions can be forced by pre-constraining the system in order for it to settle on the desired high energy equilibrium point. During an active control process, accessing and imposing the initial conditions is a challenging

task, in addition to the basin of attraction that changes as a function of the forced excitation amplitude. To achieve the selection of the desired equilibrium point, two main manners have been found. Both manners involve creating synthetic parameters that are to be added to the ES system. The first method consists in adding synthetic added external forces to the measured ones in the ES equation. The second one lies in adding synthetic parameters to the vector of states of the ES. In both solutions, the ES state vector is computed using a numerical scheme at each time step based on fictive values composed of the actual value added with a synthetic one for a brief moment. The fictive values lead the numerical scheme to converge to a new solution which would be in the basin of attraction $\mathscr{B}_F(X_d^*)$ of the desired equilibrium point X_d^*. The fictive values are then dropped to 0, and the ES is attracted by the equilibrium point. The classical approach to reaching a desired equilibrium point is to select initial conditions within its basin of attraction $B_F(X_d^*)$. However, the basin of attraction depends on the excitation amplitude, which is generally unknown during experiments. As a result, the basin itself cannot be predetermined. A more straightforward strategy is therefore to actively drive the systems behavior toward the desired equilibrium point.

5.1.1 By adding synthetic external forces

The ES concept allows to dissociate the external force considered in the ES (f_{ext}^{ES}) from f_{ext}^m, and consider an $f_{ext}^{ES} = f_{ext}^m + f_{ext}^a$ in the ES, with f_{ext}^a an additional purely synthetic external force, which has the role to lead the ES to a fixed point lying in the basin of attraction $\mathscr{B}_F(X_d^*)$. As the goal is to drive the behavior of the system to the targeted fixed point, the additional purely synthetic external force f_{ext}^a should have transient character, such that to quickly extinguish after the desired equilibrium point has been reached by the plant. Notice that the extensions of the basin of attraction of each stable solution change with the amplitude of the actual external excitation f_{ext}, and the system is not autonomous. Nevertheless, if the amplitude of f_{ext}^a is properly devised based upon the amplitude of f_{ext}^m, the basin of attraction of the desired equilibrium can extend such that to fill the entire space of initial conditions physically realisable, and the achievement of the desired set-point is assured. The strategy is described in better details below.

By contemplating $f_{ext}^{ES} \neq f_{ext}^m$, the modified controlled system of Eq. (3.7), rewrites:

$$\dot{X}(t) = A(X(t), t, f_{ext}(t), u_d(t)) \tag{5.1a}$$

$$\dot{X}_d(t) = F(X_d(t), t, f_{ext}^m(t) + f_{ext}^a(t)) \tag{5.1b}$$

$$u_d(t) = \varphi(\dot{X}_d(t), X_d(t), t, f_{ext}^m(t)) \tag{5.1c}$$

Solving the ES Eq. (5.1b) yields the vector states X_d^f as a solution function of the variables $t \in [0, T]$ and $f_{ext}^{ES} = f_{ext}^m + f_{ext}^a$. The additional transient f_{ext}^a creates new attracting equilibrium points that correspond to solutions X_d for higher or lower excitation amplitudes. Supposing an additional synthetic force such that $\lim_{t \to +\infty} f_{ext}^a(t) = 0$, once the equilibrium point values X_d reach the basin of attraction $\mathscr{B}_F(X_d^*)$ of the targeted equilibrium point X_d^*, the equilibrium point adopted by the plant will stay on the desired trajectory, i.e.:

$$\lim_{t \to +\infty} X_d(t) = X_d^*. \tag{5.2}$$

In particular, the flow of the modified system (with $f_{ext}^{ES} \neq f_{ext}^m$) is equal to the flow of the unmodified dynamical system when f_{ext}^a extinguish. If the flow intersects a stable attracting fixed point of the unmodified system, the

system is attracted to it. To efficiently use this method, f_{ext}^{a} may be conceived as an offset smoothly decreasing to 0 with t to ensure that the flow quickly intersects with the desired equilibrium point.

5.1.2 By adding synthetic external displacement or speed

In this section, the choice of equilibrium point by the creation of a synthetic displacement, or speed is investigated. The external forces are chosen as the measured ones: $f_{ext}^{ES} = f_{ext}^{m}$. Let us discretize the time according to the algorithm time steps: $\forall n \in \mathbb{N}$, $t_n \in [0,T]$, $X_d(t_n)$, $f_{ext}^{m}(t_n)$, and $X_d^a(t_n)$ represents the added synthetic state vector. The time step $h_n = t_{n+1} - t_n$ is set constant. Let us suppose that the chosen numerical scheme $\Phi : ([0,T] \times \mathbb{R}) \longrightarrow \mathbb{R}$ is an explicit one-step scheme (as the RK4-like scheme), it writes:

$$\forall t_n \in [0,T] \quad X_d(t_{n+1}) = X_d(t_n) + h_n \Phi(t_n, X_d(t_n), f_{ext}^{ES}(t_n)) \tag{5.3}$$

The modified control involves:

$$\forall t_n \in [0,T] \quad X_d(t_n) \longrightarrow X_d(t_n) + X_d^a(t_n) \tag{5.4}$$

Substituting in Eq. (5.3), it yields $\forall t_n \in [0,T]$:

$$X_d(t_{n+1}) = (X_d(t_n) + X_d^a(t_n)) + h_n \Phi(t_n, X_d(t_n) + X_d^a(t_n), f_{ext}^{ES}(t_n)) \tag{5.5}$$

Let us name the term $X_d^{ES}(t_n) = X_d(t_n) + X_d^a(t_n)$. If the term $X_d^{ES}(t_n) = X_d(t_n) + X_d^a(t_n) \in \mathscr{B}_F(X_d^*)$, then $\lim_{n \to +\infty} X_d(t_n) = X_d^*$. As a result, the targeted equilibrium point is attained. In this case where the displacement or speed are driven by the fictive parameters, the flow can be easily driven to the high energy equilibrium point.

5.2 Numerical simulations

This section provides the numerical simulation to numerically validate the proposed strategy for targeting high energy fixed points.

As it has been demonstrated in Figs. 3.8 and 3.9 in Chapter 3, the equilibrium point attained under a mono-harmonic excitation highly depends on the initial conditions. Here we numerically validate the technique described in Section 5.1 to target a specific equilibrium point independently of the initial conditions.

5.2.1 By adding synthetic external forces

As presented in Section 5.1, the additional synthetic transient excitation f_{ext}^{a} needed to reach the desired equilibrium point, can be conceived as an offset smoothly decreasing to 0 with t, as in Eq. (5.6):

$$f_{ext}^{a}(t) = \frac{a}{2}\big(1 - \tanh(bt - 2)\big) \tag{5.6}$$

where $a \in \mathbb{R}_+$ is related to the amplitude of f_{ext}^{a} at $t = 0$ (the offset). The choice of this function form is explained by the need to drive the Exosystem's flow towards the flow of the desired fixed point. Note that the delay in which the system attains the equilibrium point can be optimized by the choice of b that determines the slope with which f_{ext}^{a} tends to the asymptotic value 0. For this study, b is set to 1. The additional synthetic transient f_{ext}^{a} is plotted in Fig. 5.1 for $a = 10$.

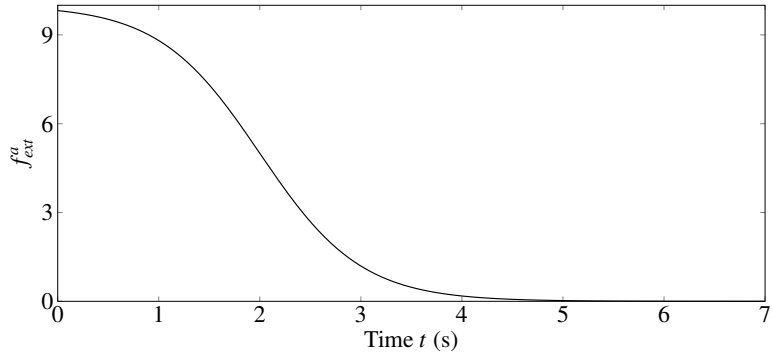

Fig. 5.1 Plot of the additional synthetic transient f_{ext}^a.

In the same manner as in Chapter 3, the basin of attraction defines the attained equilibrium point depending on the initial conditions in displacement and velocity. The black (respectively white) color zone indicates that the system tends to the high (respectively low) energy equilibrium point. The basin of attraction for $a = 0$, meaning that no synthetic variable is added to the control is pictured in Chapter 3, in Fig. 3.9.

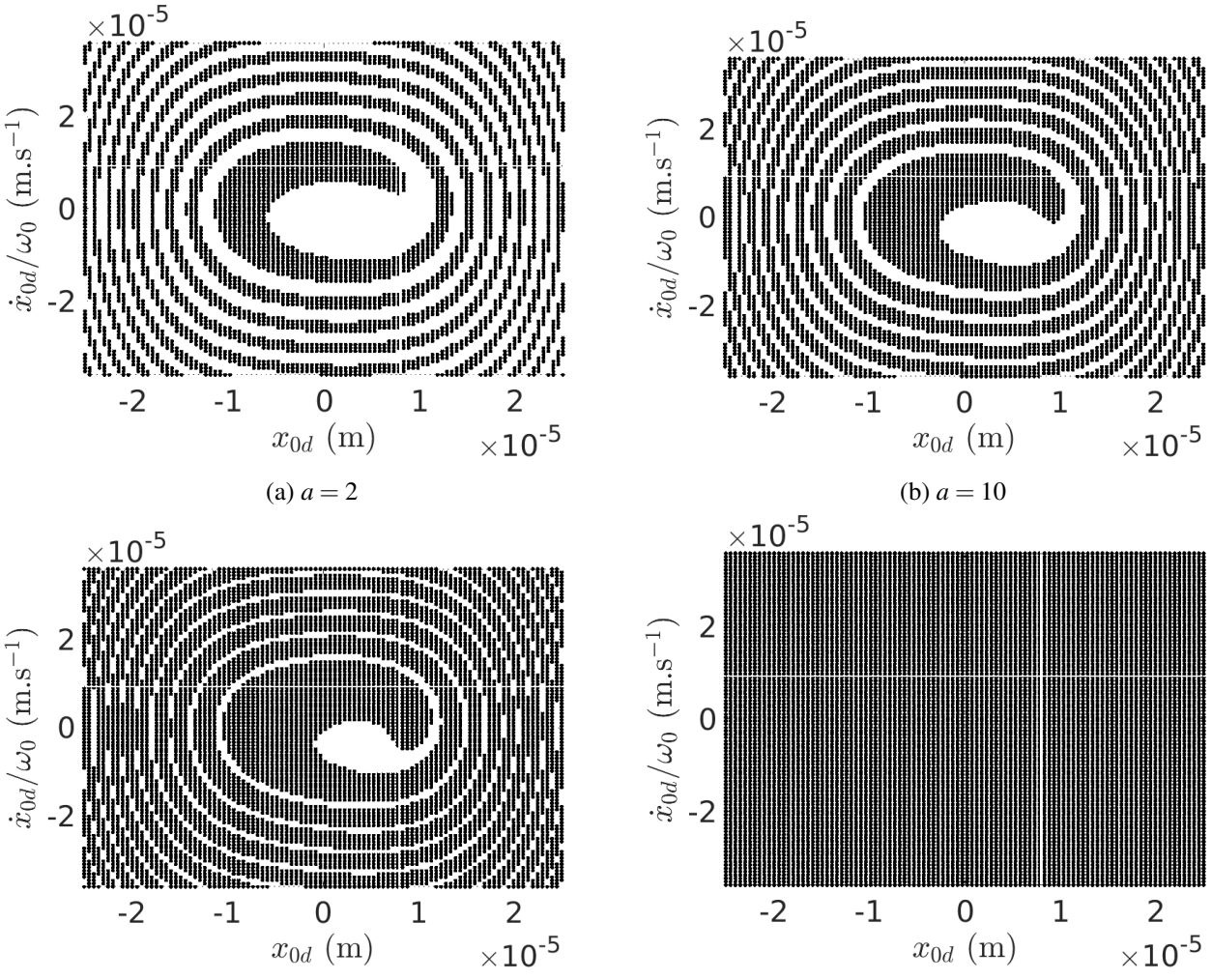

(a) $a = 2$

(b) $a = 10$

(c) $a = 12$

(d) $a = 14$

Fig. 5.2 Basins of attraction of the ES with the additional synthetic transient f_{ext}^a given by Eq. (5.6), for different amplitudes a. The black (respectively white) color zone indicates that the system tends to the high (respectively low) energy equilibrium point.

In Fig. 5.2, the ES basins of attraction for four different values a of f_{ext}^{a} are plotted, showing that the black zone (corresponding to the initial conditions leading to the high energy fixed point) enlarges with a. Moreover, a threshold value of a exists such that the entire space of initial conditions contemplated in Fig. 5.2, leads to the desired high energy equilibrium point. Therefore, for a given range of possible initial conditions, the parameter a should be selected higher than the threshold assuring the achievement of the high energy equilibrium point in the entire possible range of initial conditions.
Observe that, in case of more than 2 co-existing stable points, the choice of the parameter a is less straightforward, and functions different from the one of Eq. (5.6) might be explored. However, these speculations are left to future investigations.

5.2.2 By adding synthetic external displacement or speed

For the same reasons as adding synthetic external forces, x_d^a is chosen in the same form as in Eq. (5.6):

$$X_d^{ES}(t) = X_d(t) + X_d^a(t) \tag{5.7}$$

with $X_d^a = (x_d^a \quad \dot{x}_d^a)^t$ and $X_d^{ES} = (x_d^{ES} \quad \dot{x}_d^{ES})^t$, where x_d^a and $\dot{x}_d^a$ stand for the added synthetic displacement and velocity respectively. As a result, X_d^a is taken either in the form:

$$X_d^a(t) = \left(\frac{a}{2}(1-\tanh(bt-2))\right)\begin{pmatrix}1\\0\end{pmatrix} \tag{5.8}$$

Or in the form:

$$X_d^a(t) = \left(\frac{a}{2}(1-\tanh(bt-2))\right)\begin{pmatrix}0\\1\end{pmatrix} \tag{5.9}$$

A combination of both added variables in terms of velocity and displacement could be imagined, but is not studied in this work.

5.3 The quasi-open field experiment

The objective is to experimentally validate the nonlinear impedance control strategy introducing an additional synthetic transient f_{ext}^{a} in the ES, for the selection of the equilibrium point independently of the initial condition of the plant. In this first test, the ER is placed in a quasi-open acoustic field.
The experiment is identical as the one presented in Chapter 3, Section 3.4.1. Throughout the chapter, a nonlinear ES is chosen of the Duffing-type form:

$$M_d\ddot{x}_d(t) + R_d\dot{x}_d(t) + K_d x_d(t) + K_d\beta x_d^3(t) = f_{ext}^{ES}(t). \tag{5.10}$$

The desired parameters are selected as $\eta_R = 1/8$ and $\eta_M = \eta_K = 1$. The amplitude of the parameter β can be tuned to ensure that the ER display the nonlinearity under the low external noise excitation levels, while the sign of β determines whether the Duffing oscillator has a hardening ($\beta > 0$) or softening ($\beta < 0$) behavior. Here, we choose $\beta = 10^{10}$ m^{-2}.

5.3.1 Results for a added synthetic external forces

For the moment, we assume $f_{ext}^{ES} = f_{ext}^{m}$ in Eq. (5.10).
The response of the ER, excited by both increasing and decreasing frequency sweep, in terms of velocity and sound pressure on the ER's membrane, is plotted in Fig. 5.3. In addition, multiple monoharmonic sine signals across the frequency range are also employed as external sound excitations, and the corresponding stationary response envelopes are indicated by dots placed onto the frequency spectra in Fig. 5.3, as done in the simulations of Fig. 3.8. Both pressure and velocity spectra denote a hardening behavior of the ER, as desired. However, the ER responses to external sine excitations always lie on the lower amplitude branch, i.e. the lower energy equilibrium point, as predicted by the numerical simulations reported in Fig. 3.8. This is so, because in the experimental testing, initial conditions are close to 0 which, as demonstrated by the ES Poincaré map of Fig. 3.9, reside in the basin of attraction of the lower energy equilibrium point. From the acoustic point of view, the lower branch of the Duffing resonator response corresponds to lower amplitude of the resonance peak and also narrower frequency bandwidth of the ER response, which is undesirable for noise attenuation purposes.

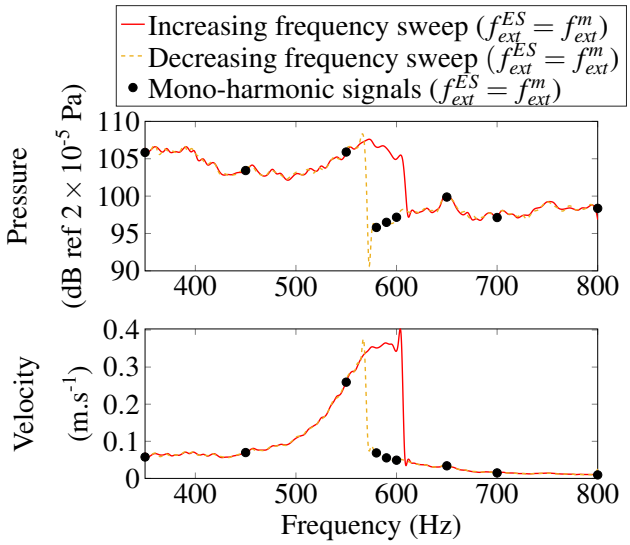

Fig. 5.3 Envelopes of the measured velocity and sound pressure on the ER's membrane, under increasing and decreasing frequency sweep excitations, or under mono-harmonic sine excitations, without employing additional synthetic transients in f_{ext}^{ES}.

Now, let us consider the possibility of having $f_{ext}^{ES} \neq f_{ext}^{m}$ and take as external sound excitations, 12 seconds long monoharmonic sine signals, with the ER's sound pressure and velocity measured for 14 seconds, i.e. for 2 additional seconds after the end of external sound excitations. During the 14 seconds-long measurement, different values are assigned to f_{ext}^{a}, in order for the ER to display different behaviors of interest under a sinusoidal external sound excitation. Finally, in the last 2 seconds of the experiment, the external sinusoidal excitation is turned off. Thus, the timeline of the experiment, from 0 to 14 seconds, is divided in different phases, as illustrated in Fig 5.4, in order to observe the changes in the equilibrium points the ER reaches when f_{ext}^{a} is varied. During phase A (from $t = 0$ to 2 seconds), f_{ext}^{a} is set to 0, while the ER quickly exhibits a stationary response under the external sine excitation. In phase B (from $t = 2$ to 6 seconds), an additional synthetic transient $f_{ext}^{a} \neq 0$ is taken into account such that the ER can reach the higher energy equilibrium point. Then, during phase C (from $t = 6$ to 8 seconds), f_{ext}^{a} is reset to 0. In phase D (from $t = 8$ to 9 seconds) instead, f_{ext}^{a} is set equal to the opposite of the measured pressure, i.e. $f_{ext}^{a} = -f_{ext}^{m}$. This means that $f_{ext}^{ES} = 0$, which should soon lead to an $x_d = 0$. Finally,

in phase E (from $t = 9$ to 12 seconds), the f_{ext}^a is set back to 0, and in phase F (from $t = 12$ to 14 seconds) the external sound excitation is turned off.

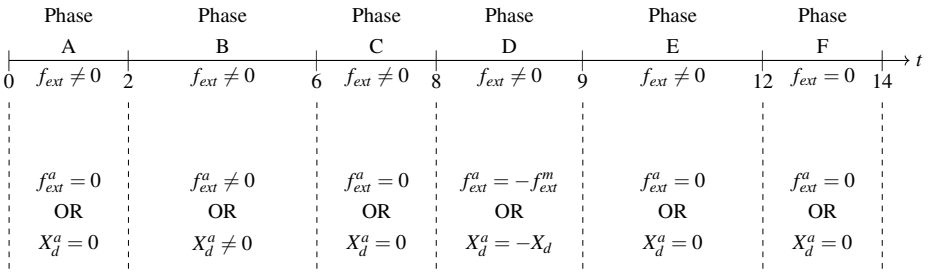

Fig. 5.4 Experimental procedure consisting of a sequence of 6 phases over a 14 seconds measurement.

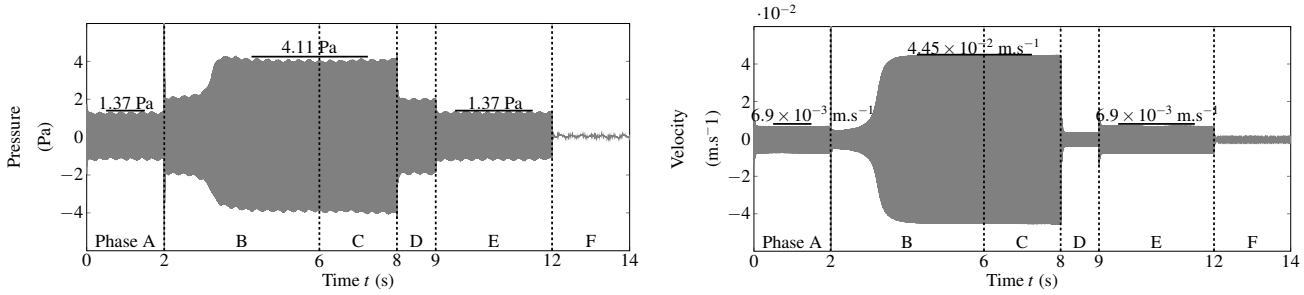

(a) (b)

Fig. 5.5 Measured sound pressure (a) and velocity (b) on the ER's membrane during the different phases along the timeline of Fig. 5.4, with $f_{ext} = f_{ext}^m + f_{ext}^a$ under a 590 Hz sinusoidal excitation.

The measured sound pressure and velocity of the ER's membrane during the different phases illustrated in the timeline of Fig. 5.4, are plotted in Fig. 5.5. The sinusoidal excitation is at 590 Hz. Observe that, during phase A, the lower equilibrium point is attained, as showed previously in Fig. 5.3. Then, in phase B, the higher energy equilibrium point (corresponding to larger oscillation both in pressure and velocity) is reached thanks to an f_{ext}^a given by Eq. (5.6) with $a = 200$ Pa. After the f_{ext}^a extinguishes, in phase C, the ER response is stably maintained on the high-energy equilibrium point. Indeed, after the application of the f_{ext}^a, the basin of attraction of the high-energy equilibrium point enlarges such that to include the current ES state. So, the ES's response and then the ER's one are attracted and stabilized to the desired equilibrium state, which is therefore endured even after that the additional synthetic transient extinguishes (in phase C). Then, in phase D we impose $f_{ext}^a = -f_{ext}^m$ which means $f_{ext}^{ES} = 0$. Therefore, the ER is forced towards the free response of the ES. This means a minimal velocity despite a significant sound excitation f_{ext}^m. Indeed, the actual external excitation is compensated by an $f_{ext}^a = -f_{ext}^m$. Then, in phase E, f_{ext}^a is brought back to 0, and we retrieve the same ER response as in phase A, as expected. Finally, in phase F, the external sinusoidal excitation is switched off. Notice that, in phase F, f_{ext}^m is almost zero (low background noise) as well as f_{ext}^a. This means that $f_{ext}^{ES} = 0$ as it was during phase D. Nevertheless, while the measured velocity during phase F falls into background noise, this is not so during phase D, where the velocity oscillations are very low in amplitude but not yet in the background noise levels. This is so because of the inevitable model uncertainties and physiological time delay in the digital control implementation [42], for which the model inversion is never perfectly accomplished. This explains the impossibility to reach a rigid ER behavior ($v = 0$) when $f_{ext}^{ES} = 0$.

The average values of the envelope of the stationary regime (phase C) for external sinusoidal excitation at four different frequencies (580 Hz, 590 Hz, 600 Hz, and 610 Hz) are reported with dots in Fig. 5.6. Those points

are compared to the spectra obtained with $f^a_{ext} = 0$, under increasing and decreasing frequency sweeps. Fig. 5.6 demonstrates that the high-energy equilibrium point has been reached thanks to the additional synthetic transient in the ES dynamics.

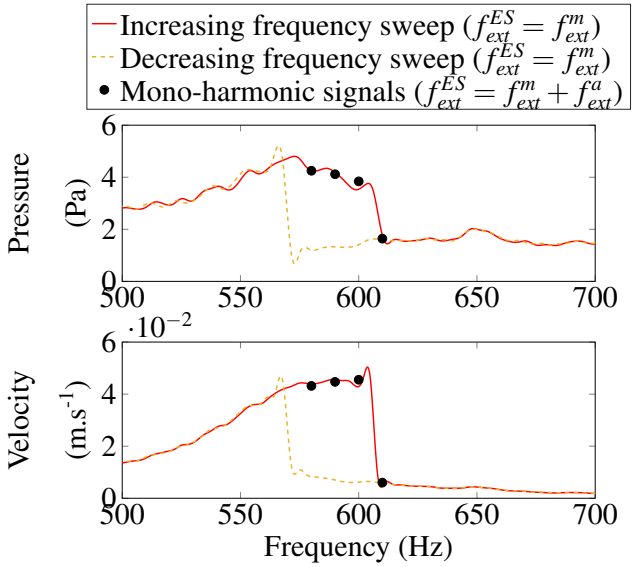

Fig. 5.6 Envelopes of sound pressure and velocity amplitudes on the ER's membrane under increasing (solid-line) and decreasing (dashed-line) frequency sweep external excitation, in case of $f^a_{ext} = 0$. On the same graphs, pressure and velocity amplitudes of the ER response with $f_{ext} \neq 0$, under sinusoidal excitations at 580 Hz, 590 Hz, 600 Hz, and 610 Hz are displayed as dots.

5.3.2 Results for a synthetic external displacement or speed

The same method is applied with a synthetic external displacement, and with a synthetic external velocity. In this section, the added synthetic external force is set to $f^a_{ext} = 0$ so that $f^{ES}_{ext} = f^m_{ext}$. The form of the added synthetic variable – displacement or velocity – corresponds to the one presented in Eq. (5.7).

The measured velocity of the ER's membrane and the measured pressure close to it with a 580 Hz sine excitation, in the case of the control with an added synthetic displacement x^a_d are plotted in Fig. 5.8. The higher equilibrium points for the frequencies 580 Hz, 590 Hz, 600 Hz and 610 Hz, are compared to the ER's response to both increasing and decreasing frequency sweep excitations without added variables in Fig. 5.7a. Notice that the result are identical to the ones obtained in the previous section: the higher equilibrium point is attained for each sinusoidal excitation. Figure 5.8 shows that an added synthetic displacement leads to attain a higher fixed point, which is the high equilibrium point of the ER's response (Fig. 5.7a). Observe in Figs. 5.8a and 5.8b that the time at which the synthetic variables are activated induces a transient large increase of the sound pressure and displacement of the ER. This phenomena arises because the energy injected in the system with the added variable is large compared to the one needed to attain the high energy equilibrium point. The lower equilibrium point may be attained from the higher one in phase E by following the strategy $x^a_d = -x_d$.

The same variables are plotted for a 600 Hz sinusoidal excitation in the case of added synthetic velocity $\dot{x}^a_d$ in Figs. 5.9 and 5.7b. The higher equilibrium point is attained in phase B, as expected. This case permits also to attain the lower equilibrium point from the higher one with the strategy $\dot{x}^a_d = -\dot{x}_d$.

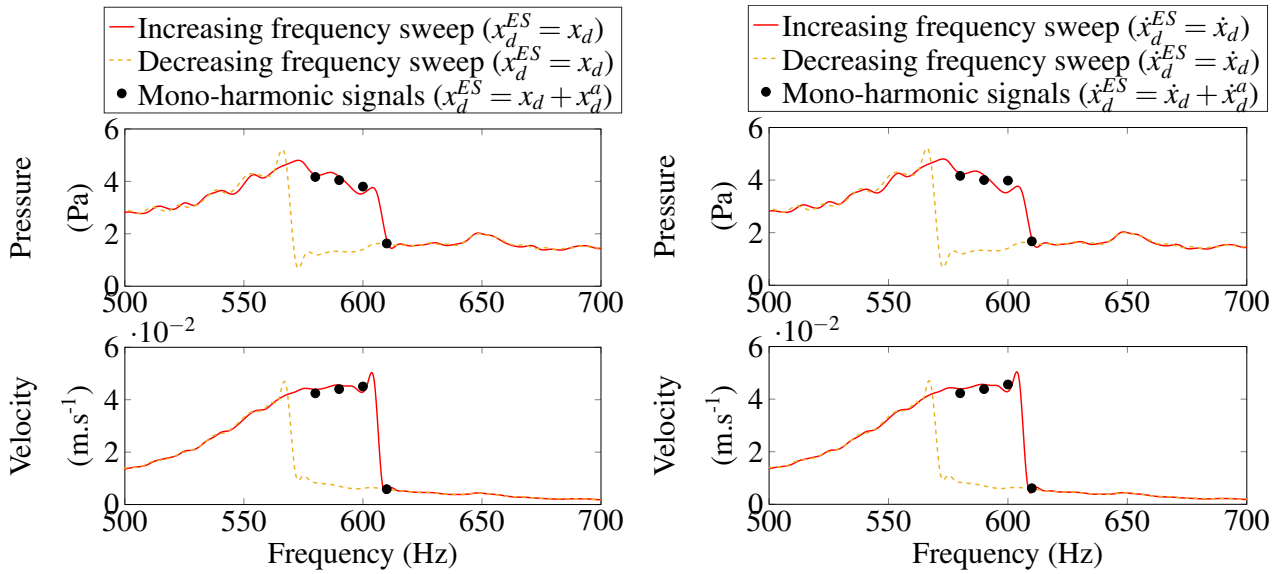

(a) (b)

Fig. 5.7 Envelopes of sound pressure and velocity amplitudes on the ER's membrane under increasing (solid-line) and decreasing (dashed-line) frequency sweep external excitation, in case of $x_d^a = 0$ and $\dot{x}_d^a = 0$. On the same graphs, pressure and velocity amplitude of the ER response under sinusoidal excitation (at 580 Hz, 590 Hz, 600 Hz, and 610 Hz) during phases B and C with adding an external synthetic (a) displacement $x_d^{ES} = x_d + x_d^a$ with $\dot{x}_d^a = 0$, (b) velocity $\dot{x}_d^{ES} = \dot{x}_d + \dot{x}_d^a$ with $x_d^a = 0$.

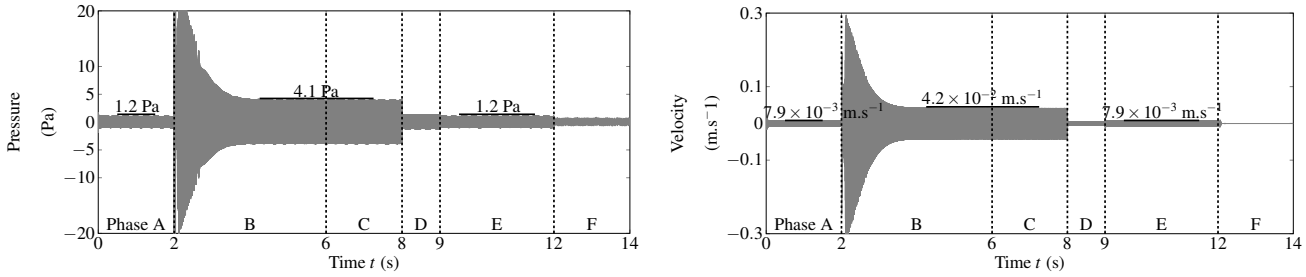

(a) (b)

Fig. 5.8 Measured sound pressure (a) and velocity (b) on the ER's membrane during the different phases along the timeline of Fig. 5.4, with $x_d^{ES} = x_d + x_d^a$, and $\dot{x}_d^a = 0$ under a 580 Hz sinusoidal excitation. The amplitude of the added variable synthetic displacement is fixed to $a = 2 \times 10^{-5}$ m.

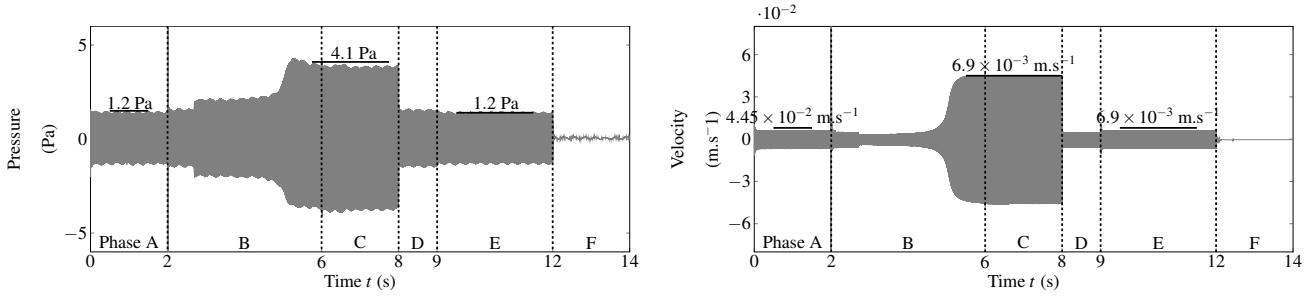

(a) (b)

Fig. 5.9 Measured sound pressure (a) and velocity (b) on the ER's membrane during the different phases along the timeline of Fig. 5.4, with $\dot{x}_d^{ES} = \dot{x}_d + \dot{x}_d^a$, and $x_d^a = 0$ under a 600 Hz sinusoidal excitation. The amplitude of the added variable synthetic velocity is fixed to $a = 0.25$ m.s^{-1}.

5.4 The coupled-tube experiment

The objective of the experiment is to validate that the modified control with the introduction of the fictive parameters permits to improve the acoustic energy absorption of the ER.

5.5 The coupled-tube experiment

In this second experiment, the ER is placed into an enclosed acoustic cavity, corresponding to the experimental test bench reported in Chapter 4, Section 4.4. Previously, the RTI algorithm's potential for acoustic mode attenuation, was outlined for different nonlinear synthetic dynamics. Nevertheless, so far, the equilibrium points exhibited by the ER could only be reached by properly adjusting the external sound excitation (increasing or decreasing frequency sweeps, for example), which are unrealistic in actual noise control scenarios. After having assessed the performances of our new control strategy (involving an $f_{ext}^{ES} = f_{ext}^{m} + f_{ext}^{a}$ or an $X_d^{ES} = X_d + X_d^a$) in quasi-open field, we now test the same concept when the ER is coupled to acoustic cavities.

5.5.1 Experimental set-up

The experimental set-up is identical as the one presented in Chapter 4 in Section 4.4. In this chapter, the experiments are realized with Configuration **D** detailed in Table 5.1. The same ES governing Eq. (5.10) is implemented, as for the open field experiment of Section 5.3, whose parameters are given in Eq. (5.10), with $\beta = 10^{10}$ m^{-2}, $\eta_K = \eta_M = 1$ and $\eta_R = 1/8$.
The same excitations as in the open field experiment Section 5.3 are used (chirp + mono-harmonic sinus), along with the excitation defined by the timeline of Fig. 5.4. The method for determining the parameters are presented in Appendix B.

Configuration	**D**	Unit
f_0	574.01 ± 0.19	Hz
c_a	$3.89 \times 10^{-2} \pm 1.74 \times 10^{-5}$	kg s^{-1}
k_a	1069.50 ± 0.71	kg s^{-2}

Table 5.1 The measured parameters of the model (mean value of the estimated parameters of the set of measurements) $\pm$ the standard deviation of the estimated values of the set of measurements.

5.5.2 Results for a fictive pressure

In Fig. 5.10a, we report the sound pressure measured inside the S_t-tube, and the displacement x_d of the ES estimated by the recursive integration of the ES dynamics (the first step of the control algorithm showed in Section 3.1.4).

The envelopes of the measured pressure inside the S_t-tube, and the ES displacement are plotted in Fig. 5.10a. Frequency sine sweep excitations have been employed with both increasing and decreasing frequencies, and a comparison with a rigid termination measurement is made. Moreover, the stationary responses of the system to single frequency sine signal are plotted for some frequencies. Observe that the ES displacement shows a nonlinear and hardening behavior. Moreover, the stationary responses to mono-harmonic signals are situated

on the lower energy branch. The measured pressure inside the S_t-tube shows that adding the ER at the end of the tube reduces the acoustic level in the tube. Observe that the measurements under a decreasing frequency sweep excitation corresponds to lower energy equilibrium points of the ES, and therefore to higher acoustic levels inside the S_t-tube. Indeed, when the ER's response is situated in the lower energy equilibrium point, the ER displacement amplitude, speed and acceleration are lower than for the high energy equilibrium points, leading to lower energy transfer from the primary system to the ER. As a result, to activate an efficient energy transfer from the primary system to the ER, and to enlarge the frequency bandwidth of efficient modal attenuation, the ER's response should be situated on the higher energy equilibrium points of the nonlinear resonance. This motivates the introduction of the strategy described above, involving an $f_{ext}^{ES} \neq f_{ext}^{m}$ to reach the desired equilibrium points.

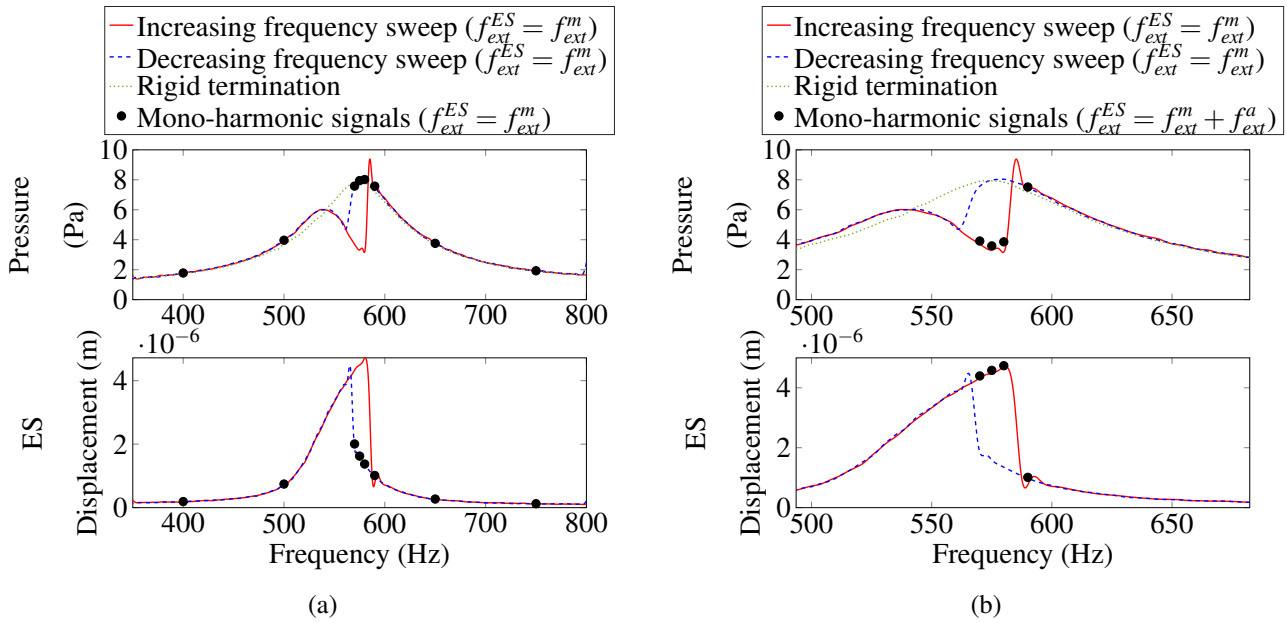

Fig. 5.10 Envelopes of the measured pressure inside the S_t-tube, and ES displacement under increasing and decreasing frequency sweep excitations in case of $f_{ext}^{ES} = f_{ext}^{m}$, along with the values obtained under mono-harmonic sine excitations (a) with $f_{ext}^{ES} = f_{ext}^{m}$; (b) with $f_{ext}^{ES} = f_{ext}^{m} + f_{ext}^{a}$ during phase C, after the extinguishment of f_{ext}^{a}.

Now, in order to validate the control strategy involving an $f_{ext}^{ES} \neq f_{ext}^{m}$, we test the system following the same experimental phases as those reported in the timeline sequence of Fig. 5.4. The amplitude of the added synthetic parameter is now fixed to $a = 200$ Pa. The envelopes of the stationary responses to mono-harmonic excitations at 570 Hz, 575 Hz, 580 Hz, and 590 Hz extracted from phases B and C (with the modified control) are plotted in Fig. 5.10b. The measured pressure inside the S_t-tube and the ES displacement computed in the control loop are plotted. It shows that the additional synthetic transient excitation f_{ext}^{a} leads the ER's response to attain the higher energy equilibrium point, resulting in better attenuation of the acoustic mode.

The time-histories of the measured pressure in the S_t-tube, of the measured pressure inside the S_{cb}-cavity, and of the ES displacement, are represented in Fig. 5.11 for a 580 Hz sine excitation. In phases B and C, it can be observed that the high energy equilibrium point in the ER's membrane displacement is attained, demonstrated by lower energy of the acoustic mode's response. The lower energy equilibrium point of the ER, instead, is reached in phase E in accordance with the results of the open-field experiment. Notice that, at the beginning of phase B we can observe an undesirable sudden increase of the ES displacement and of the measured pressures. However, this effect can be significantly reduced by properly adjusting the a parameter in the expression of f_{ext}^{a} of Eq. (5.6).

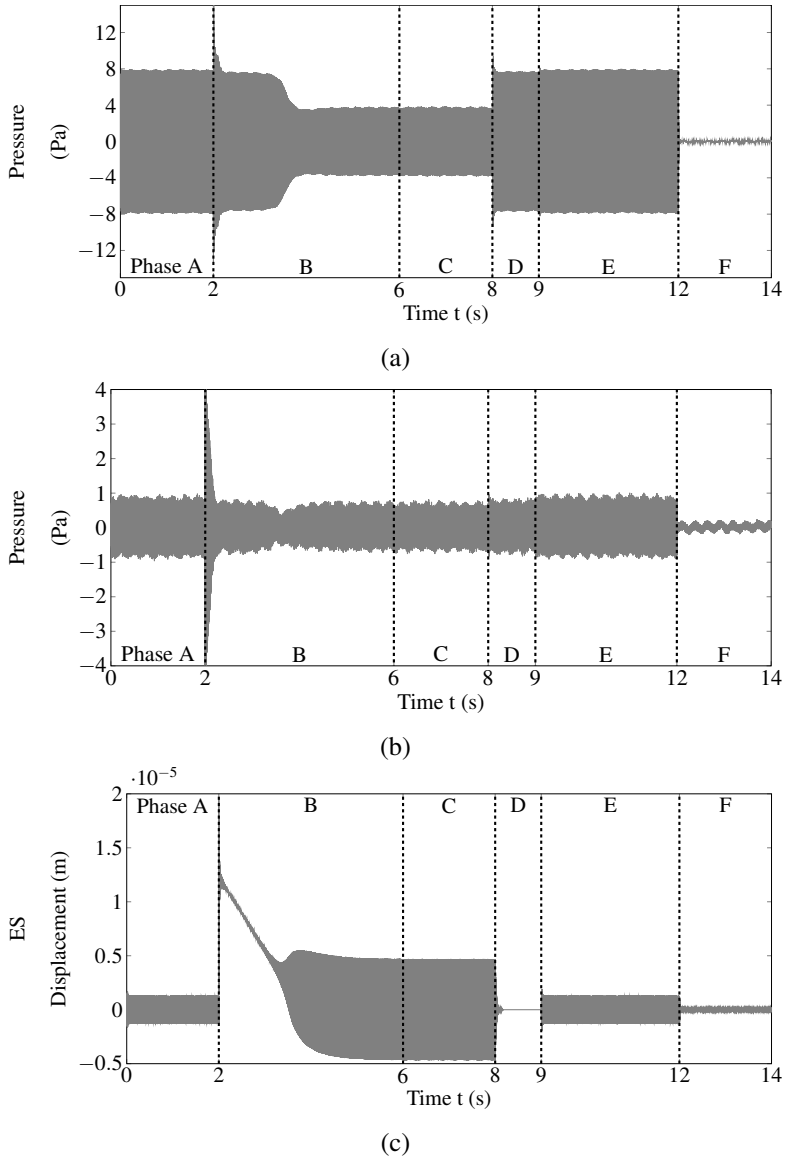

Fig. 5.11 Measured pressures (a) inside the tube with a reduced section and (b) inside the coupling box at the ER's membrane surface for a 580 Hz mono-harmonic signal ; (c) Estimated displacement of the ER's membrane computed in the control loop for a 580 Hz sine excitation signal.

The time histories of the measured pressure inside the S_t-tube and of the ES displacement are plotted in Fig. 5.12 for different values of the $a = \{6, 8, 15\}$ Pa, under a monoharmonic external sine excitation at 575 Hz. Fig.s 5.12a and 5.12b show that the value $a = 6$ Pa is not sufficient to bring the ER's response to the higher energy equilibrium point, while for $a \geq 8$ Pa the higher energy equilibrium point is reached, demonstrated by larger oscillation of the ES displacement, and lower amplitudes of the measured pressures in the S_t-tube in Fig.s 5.12c, 5.12d, 5.12e, 5.12f. As a result, the value of a needed to achieve the desired equilibrium point under the initial conditions of the present experimental testbench, should lie somewhere between $a = 6$ Pa and $a = 8$ Pa. Notice how the undesirable sudden increase of the ES displacement and of the measured pressure in the S_t-tube, at the beginning of phase B, is significantly weakened with respect to Fig. 5.11, where a was taken equal to 200 Pa. Moreover, as expected, the duration of f_{ext}^{a} increases with a. Therefore, by choosing the minimum value of a needed to attain the desired equilibrium point, the transient duration can be minimized as well. On the other hand, a proper selection of the parameter b appearing in Eq. (5.6), would also allow to minimize the transient duration

for a fixed value of a. The optimization of the form of f_{ext}^{a} is a interesting perspective.

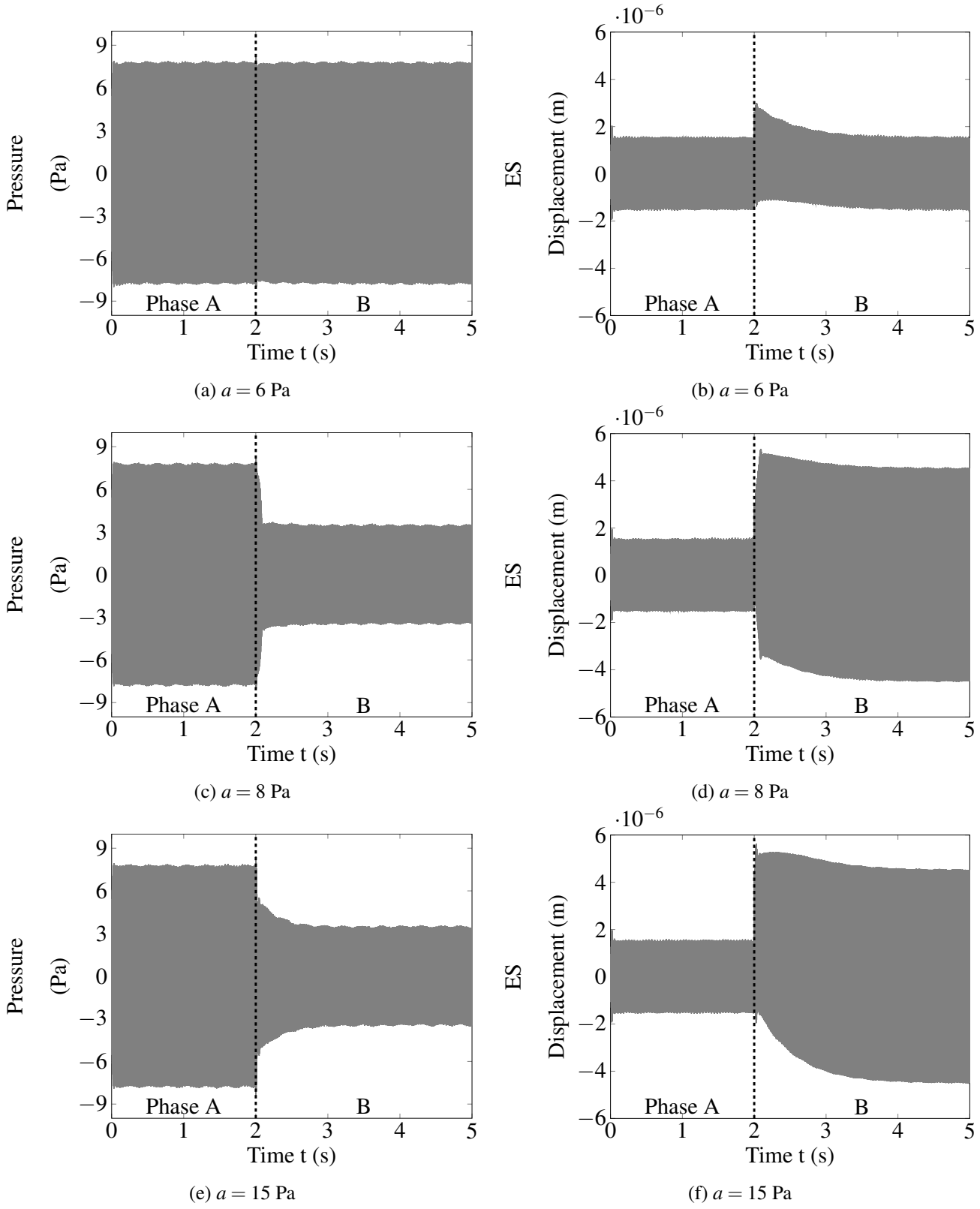

(a) $a = 6$ Pa

(b) $a = 6$ Pa

(c) $a = 8$ Pa

(d) $a = 8$ Pa

(e) $a = 15$ Pa

(f) $a = 15$ Pa

Fig. 5.12 Phases A and B of the measured pressure inside the reduced section tube (a,c,e), and estimated displacement of the ER's membrane computed in the control loop (b,d,f) for a 575 Hz sine excitation signal.

The experimental tests reported in this section prove the potential of the proposed strategy to target desired equilibrium points of Duffing-like dynamics, at low excitation levels, in an acoustic environment made by enclosed cavities, where higher energy equilibrium points are required for efficient noise attenuation. Moreover, as known from [42], the placement of the ER in small acoustic cavities induces acoustic feedback on the ER which might jeopardize the stability of the system, whenever the ER acoustical passivity is lost. The absence of any stability issue during the experimental tests reported in this section, reinforce the reliability of the proposed concept. The investigation on the impact of an $f_{ext}^{ES} \neq f_{ext}^{m}$ upon stability is a perspective of this work.

5.5.3 Results for a synthetic external displacement or speed

The same experimental conditions as for the preceding section are applied here. The synthetic external force is set to $f_{ext}^{a} = 0$, leading to $f_{ext}^{ES} = f_{ext}^{m}$, while the synthetic added vector state is set as $X_d^{ES} = X_d + X_d^a$. We arbitrarily choose that both variables x_d^a and $\dot{x}_d^a$ can not be different from 0 simultaneously. Figure 5.13 depicts the envelopes of the pressure inside the tube with a reduced section and of the ES displacement computed in the control for mono-harmonic sinusoidal excitations (black dots) in both cases: with an added synthetic displacement (Fig. 5.13a) and with an added synthetic velocity (Fig. 5.13b). The results are plotted against increasing and decreasing frequency sweeps realized without added variables, and a rigid termination measure. One can notice that in both cases, the higher equilibrium point is attained using the added synthetic variables. However, Fig. (5.13a) shows that the added synthetic variable failed to make the system attain the higher equilibrium point for a 580 Hz sinusoidal excitation. Notice that the frequency at which the control has not succeeded is extremely close to the end of the nonlinear zone, leading to one of the higher energy equilibrium points. This result might be induced by an insufficient amplitude of the added variables, or can be due to the vicinity of the bifurcation that destabilizes the equilibrium point.

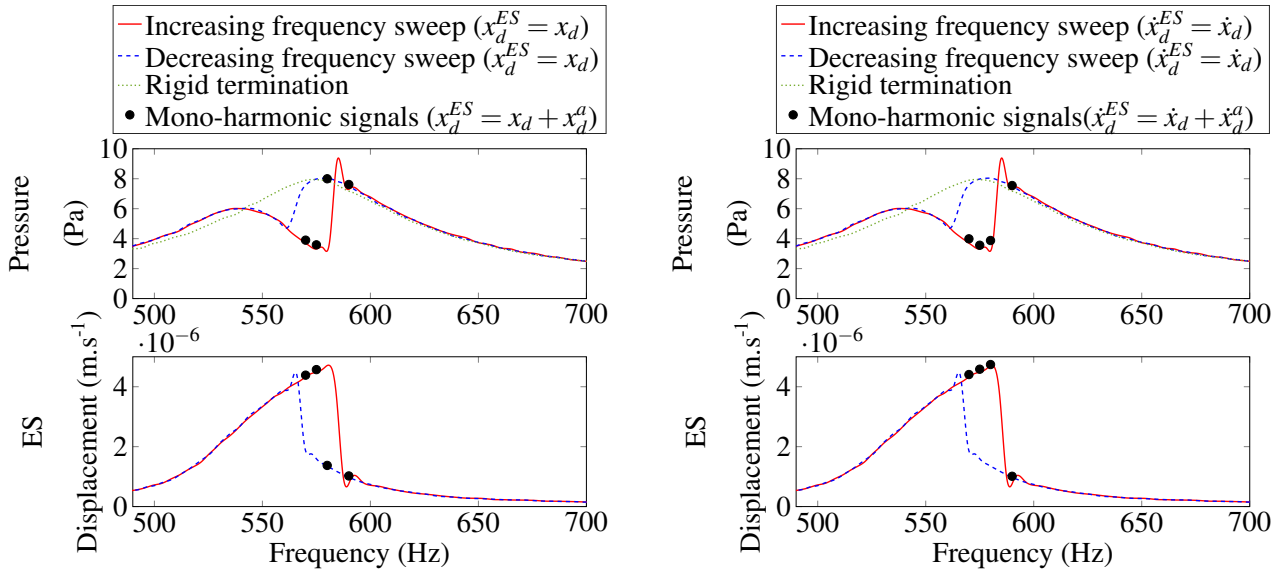

(a) $x_d^{ES} = x_d + x_d^a$ with $\dot{x}_d^a = 0$ (b) $\dot{x}_d^{ES} = \dot{x}_d + \dot{x}_d^a$ with $x_d^a = 0$

Fig. 5.13 Envelopes of sound pressure and velocity amplitudes on the ER's membrane under increasing (solid-line) and decreasing (dashed-line) frequency sweep external excitation, in case of $x_d^a = 0$ and $\dot{x}_d^a = 0$. On the same graphs, pressure and velocity amplitude of the ER response under sinusoidal excitation (at 580 Hz, 590 Hz, 600 Hz, and 610 Hz) during phases B and C with adding an external synthetic (a) displacement $x_d^{ES} = x_d + x_d^a$ with $\dot{x}_d^a = 0$, (b) velocity $\dot{x}_d^{ES} = \dot{x}_d + \dot{x}_d^a$ with $x_d^a = 0$.

Furthermore, Fig. 5.14 presents the time series of the pressure and ES displacement for the 575 Hz sinusoidal excitation in both synthetic added displacement (Figs. 5.14a and 5.14b) and velocity (Figs. 5.14c and 5.14d) cases. In both cases, the high equilibrium point is attained. However, the amplitude of the synthetic variable can induce acoustically active behaviors as one can notice from Fig. 5.14c in the beginning of phase B. It is explained by the ES displacement oscillating with large amplitudes while the added synthetic velocity decreases to 0. This unstable behavior should be addressed with caution while implementing added synthetic variables. The amplitude of the synthetic variable a seems to greatly influence the apparition of such phenomena.

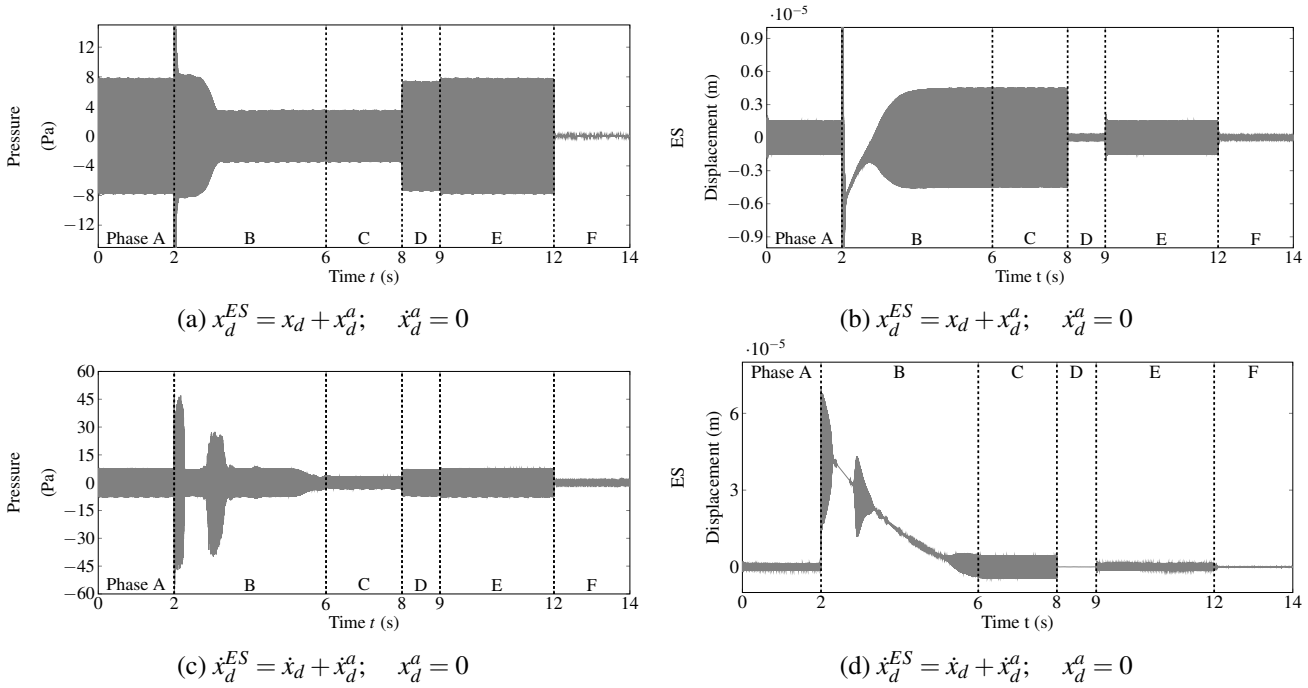

(a) $x_d^{ES} = x_d + x_d^a; \quad \dot{x}_d^a = 0$

(b) $x_d^{ES} = x_d + x_d^a; \quad \dot{x}_d^a = 0$

(c) $\dot{x}_d^{ES} = \dot{x}_d + \dot{x}_d^a; \quad x_d^a = 0$

(d) $\dot{x}_d^{ES} = \dot{x}_d + \dot{x}_d^a; \quad x_d^a = 0$

Fig. 5.14 Measured pressures (a,c) inside the tube with a reduced section for a 575 Hz mono-harmonic signal ; (c,d) Estimated displacement of the ER's membrane computed in the control loop for a 575 Hz sine excitation signal for both cases: (a,b) $x_d^{ES} = x_d + x_d^a, \quad \dot{x}_d^a = 0$; (c,d) $\dot{x}_d^{ES} = \dot{x}_d + \dot{x}_d^a, \quad x_d^a = 0$.

5.6 Conclusion

This chapter presents an extension of the control strategy presented in Chapter 3 that enables the selection of an equilibrium when two equilibrium points co-exist. Note that this extension of the control can be improved, both in terms of robustness and in terms of selection of equilibrium points in more complicated cases (for example if 5 equilibria exist). This chapter contains the following contributions:

- The conception of the modification of the model-inversion feedforward control strategy, that enables to synthesize specific equilibrium points of a desired nonlinear dynamics independently of the external excitation and for any initial condition.
  It is based upon the real-time integration of an ES dynamics described by a nonlinear Ordinary-Differential-Equation, where the energy needed to attain a desired equilibrium point is provided by adding a transient artificial synthetic variable.

- The validation of the control strategy by numerical simulations. It is shown that the additional synthetic external force allows to expand the basin of attraction of the target equilibrium point, therefore driving

the exhibited solution towards the desired trajectory which is showcased by the plant also after the extinguishment of the artificial transient.

Then, two experiments have been conducted to validate the extension of the control strategy and assess the performances of the control strategy applied to the Electroacoustic Resonator.

- The first experimental test is carried out in a quasi-open acoustic field environment and demonstrates the efficiency of the control concept to achieve desired equilibrium points of a Duffing-like target dynamics.
- The second one is carried out in an enclosed acoustic field, where the Electroacoustic Resonator is coupled to small acoustic cavities to assess the capability of the modified control to absorb energy and to realize mode control. Moreover, it allowed the assessment of the robustness of the proposed control strategy when strong acoustic feedback might endanger the stability of the coupled system [42].

In both experimental campaigns, the Electroacoustic Resonator achieved the desired equilibrium point under monoharmonic excitations. Future studies will be dedicated to the optimization of shape, amplitude and duration of the designed artificial transient, taking into account also multi-harmonic excitations, or different types of nonlinearities. Note that the added synthetic variable in terms of force highlight better and more reliable performances than with the added synthetic variable in terms of displacement or velocity.

Other future developments of the proposed control strategy might involve a feedback architecture, contemplating several collocated microphones. After having enlarged the spectra of classical impedances towards the domain of synthetic nonlinear operators [78, 114, 113, 43, 112], the work presented here is a fundamental step for the full controllability of digitally-programmed nonlinear impedances, further stimulating the scientific challenge of the inverse problem for the design of nonlinear optimal impedances for noise attenuation, in realistic scenarios. Thanks to the control strategy proposed here, indeed, the synthetic nonlinear behaviors implemented on Electroacoustic Resonators can finally find actual applications into realistic problem of noise control, such as for the attenuation of tonal noise in room acoustics.

Chapter 6

A Nonlinear Acoustic Metasurface

The objective of this chapter is to design and study a liner of nonlinear electroacoustic resonators (ERs) as an innovative solution for mitigating noise at low excitation amplitudes. The work proposed in this Chapter constitutes a preliminary step towards the development of nonlinear liners at low excitation amplitudes. As a result, this chapter aims at:

- Developing an experimental bench of a nonlinear liner, and assessing its performance in noise mitigation,
- Investigating nonlinear phenomena arising in nonlinear periodic media by experimental observation, and by analytical and numerical predictions,
- Modeling the experimental bench to predict the metasurface behavior (being the liner of nonlinear resonators), and being able to investigate nonlinear phenomena within this framework.

This preliminary study provides the foundation for future developments toward programmable nonlinear metasurfaces, a deeper understanding of nonlinear dynamics, and their practical application to noise mitigation.

6.1 Introduction

A periodic medium exhibits spatial periodicity either through its geometry or boundary conditions. Metamaterials are engineered structures that exploit such periodicity to achieve tailored properties, particularly for wave control and mitigation [84]. The periodic arrangement in metamaterials creates dispersive media, within which certain frequencies cannot propagate due to destructive interference. These frequency ranges are referred to as bandgaps. In linear media, two types of bandgaps are distinguished: Bragg bandgaps caused by spatial periodicity, and resonant bandgaps resulting from the periodic arrangement of resonators. hence, the periodic arrangement of resonators can create resonant bandgaps from the natural resonances, but also Bragg bandgaps from the spacing between resonators. The theoretical study of continuous periodic media traces back to Newton, who attempted to describe sound propagation in air using a chain of identical masses connected by identical springs [84, 31]. Acoustic metamaterials have since been realized through various periodic configurations, such as arrays of Helmholtz resonators [53], phononic crystals composed of identical elements to induce Bragg bandgaps [101, 99, 111], or periodic arrangement of membranes [25]. However, noise mitigation using Bragg bandgaps inherently depends on the spacing between unit cells, resulting in bulky metamaterials when targeting long wavelengths. Consequently, resonant metamaterials are better suited for mitigating low frequency noise, but often offers narrow frequency bandwidth of efficiency.
Periodicity can also be introduced through the boundary conditions, for example by using acoustic liners.

Acoustic liners treat the frontiers of a domain, commonly the walls of ducts, by incorporating periodic absorbing materials [36, 39]. Programmable liners composed of linear ERs have even been used to realize acoustic diodes [36, 87, 26, 27]. While linear metamaterials have been widely studied, nonlinear metamaterials feature complex and challenging behaviors to model [10], such as non-reciprocal transmission [128], breathers [50, 32], and solitons [2, 85, 48, 168, 46]. In addition, stiffness based nonlinearities typically exhibits chaotic passbands [54], quasi-periodic behavior and energy localization [81], which can be exploited for noise mitigation. Among these, solitons in nonlinear acoustic metamaterials have been experimentally demonstrated at high excitation amplitudes [2, 85].

The use of nonlinear phenomena obtained at high excitation amplitudes are of interest for acoustic mitigation at low excitation amplitudes. The control strategy previously presented enables the development of nonlinear resonators operating at low excitation levels. This capability opens the way to investigating and harnessing these nonlinear effects in practical noise mitigation applications.

6.2 Considered system

The goal of this chapter is to create a digitally programmable acoustic nonlinear metamaterial at low excitation amplitude. Building on the previous chapters, where various behaviors of individual electroacoustic resonator (ER) cells was investigated, it enables the choice of these behaviors for a nonlinear metamaterial, hence varying the global behavior of a general nonlinear metamaterial. In this work, the acoustic metamaterial is implemented under the form of a liner (creating a metasurface), enabling control over the boundary conditions of a waveguide, as illustrated in Fig. 6.1. The ERs are arranged side by side, with a minimal spacing between them, limiting the eventual Bragg bandgaps to the ones created by the size of an ER.

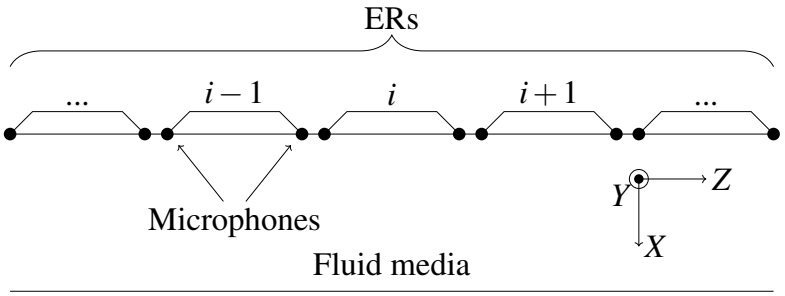

Fig. 6.1 Schematic of an asymmetric acoustic liner.

In this chapter, the considered waveguide features a square cross-section of area $S_{cs} = L_{cs}^2$. The variable $x : t \mapsto x(t) \in \mathbb{R}$ denotes the displacement of the ER's membrane. Both continuous and discrete models are considered in this chapter, resulting in the discrete notations that writes x_i as the displacement of the membrane of the i-th ER. The previous assumptions of linear medium approximation 4.2, low frequency 3.2, and low amplitude 3.1 stand, along with the piston mode approximation of the loudspeaker. The variable $p : (X,Y,Z,t) \mapsto p(X,Y,Z,t)$ denotes the pressure inside the waveguide, depending on the three coordinates $(X,Y,Z) \in [0,L_{cs}]^2 \times \mathbb{R}$ and the time $t \in [0,T]$, $T > 0$. The orthonormal basis of the Cartesian coordinates is written $(\mathbf{e_X},\mathbf{e_Y},\mathbf{e_Z}) \in \mathbb{R}^3$. This liner is studied through three main approaches:

- A numerical approach through temporal analysis of finite element modeling.
- An experimental test bench composed of an array of 7 ERs lining an acoustic waveguide.

- An analytical approach featuring an analogous model with an electric line for the study of possible solitons in the metamaterial.

6.3 A finite element model approach

The Finite Element (FE) model presented here aims at developing the essential characteristics of the nonlinear liner while minimizing the computational cost of the simulations. A similar reduction strategy has already been developed for linear liners and frequency-domain FE studies in [87]. Building on this approach, we extend the formulation to account for the boundary contributions of the nonlinear ERs, enabling an analysis of the liners behavior directly in the time domain.

A finite liner is placed within an infinite waveguide, whose domain is denoted by Ω. In this section, the variables are defined such that $t \in [0,T]$ and $(X,Y,Z) \in \Omega$. The origin of the coordinates (X,Y,Z) is chosen such that $Z = 0$ corresponds to the entrance of the liner. Within the waveguide, and under the assumptions of no mean flow and no dissipation, the acoustic pressure satisfies the classical wave equation:

$$\forall t \in [0,T],\ \forall (X,Y,Z) \in \Omega, \quad \frac{1}{c_0^2}\frac{\partial^2}{\partial t^2}p(X,Y,Z,t) - \Delta p(X,Y,Z,t) = 0 \tag{6.1}$$

where c_0 stands for the velocity of sound waves in the medium (air) under standard conditions, and Δ is the Laplace operator. By integrating over the cross-section, and decomposing the Laplace operator, it yields:

$$\frac{1}{S_{cs}}\iint_{S_{cs}}\left(\frac{1}{c_0^2}\frac{\partial^2}{\partial t^2}p(X,Y,Z,t) - \frac{\partial^2}{\partial Z^2}p(X,Y,Z,t)\right)dXdY = \frac{1}{S_{cs}}\iint_{S_{cs}}\left(\frac{\partial^2}{\partial X^2}p(X,Y,Z,t) + \frac{\partial^2}{\partial Y^2}p(X,Y,Z,t)\right)dXdY \tag{6.2}$$

In the left-hand-side of the equation, integral and derivative operators can be exchanged (as both operators do not apply on same variables). One sets the mean pressure $\tilde{p}$ over the cross-section:

$$\forall t \in [0,T],\ \forall Z \in \mathbb{R}, \quad \tilde{p}(Z,t) = \frac{1}{S_{cs}}\iint_{S_{cs}} p(X,Y,Z,t)dXdY \tag{6.3}$$

Moreover, one defines the following operator $\boldsymbol{\nabla}_\perp = \dfrac{\partial}{\partial X}\mathbf{e_X} + \dfrac{\partial}{\partial Y}\mathbf{e_Y}$. Consequently, the Eq. (6.2) gives:

$$\left(\frac{1}{c_0^2}\frac{\partial^2}{\partial t^2} - \frac{\partial^2}{\partial Z^2}\right)(\tilde{p}(Z,t)) = \frac{1}{S_{cs}}\iint_{S_{cs}}\left((\boldsymbol{\nabla}_\perp.\boldsymbol{\nabla}_\perp)p(X,Y,Z,t)\right)dXdY \tag{6.4}$$

From the divergence theorem, it writes:

$$\left(\frac{1}{c_0^2}\frac{\partial^2}{\partial t^2} - \frac{\partial^2}{\partial Z^2}\right)(\tilde{p}(Z,t)) = \frac{1}{S_{cs}}\oint_{\partial S_{cs}}\left(\boldsymbol{\nabla}_\perp p(X,Y,Z,t)\right)d\boldsymbol{\gamma} = \frac{1}{S_{cs}}\oint_{\partial S_{cs}}\left(\frac{\partial p}{\partial n}(X,Y,Z,t)\right)d\gamma \tag{6.5}$$

where ∂S_{cs} is the boundary of the domain S_{cs}, i.e. the frontiers of the waveguide, and $d\boldsymbol{\gamma} = \mathbf{n}d\gamma$, with $\mathbf{n}$ standing for the outward pointing unit normal and γ the curvilinear coordinate along ∂S_{cs}.
The projection of Euler's equation under the previous conditions on the normal vector $\mathbf{n}$ writes:

$$\rho_0\frac{\partial v_n}{\partial t} = -\frac{\partial p}{\partial n} \tag{6.6}$$

This relation links the normal acceleration of air particles to the gradient of pressure in the direction of the normal vector. As a result, the right-hand-side of the equation can be seen as an acoustic contribution of the boundaries. Consequently, the integral can be decomposed on two sub-spaces of ∂S_{cs}:

- where the surface is treated by the ER: $(\partial S_{cs})_{\text{ER}}$
- where the surface is rigid and does not interact with the medium: $(\partial S_{cs})_{\text{rigid}}$

It enables the reduction of the domain of the integral to $(\partial S_{cs})_{\text{ER}}$, as the normal acceleration of air particles at the boundaries that are not treated by the resonator is considered to be zero. In the waveguide with the liner's boundaries, the normal acceleration can be written using the equation governing the ER's dynamics. In this chapter, the behavior of the ER is supposed to perfectly match the one of the ExoSystem (ES). As a result, it writes $\forall t \in [0,T]$ and $\forall Z \in [(i-1)L_{res}, iL_{res}]$, $i \in [\![1,N]\!]$ with L_{res} the width of a resonator along the $Z-$axis, and $N \in \mathbb{N}^*$:

$$\frac{\partial v_n}{\partial t} = \ddot{x}_i(t) = -\frac{1}{M_d}\left(R\dot{x}_i(t) + F_{NL}(x_i(t)) - S_d p_b(t,\gamma)\right) \tag{6.7}$$

with p_b the acoustic pressure that applies at the boundary i.e on the ER's membrane. As a result, the metasurface can be seen as a surface with piecewise displacement along the $Z-$axis. Assume that the least attenuated duct modes (those who mostly contribute to the propagation) are symmetric with respect to both x and y axes. Hence, the pressure on the cross-section boundary is assumed uniform for $Z \in \mathbb{R}$. Hence, $\forall t \in [0,T],\ p_b(t,\gamma) = p_b(t)$. It reads:

$$\begin{aligned} &\forall t \in [0,T],\ \forall Z \in [(i-1)L_{res}, iL_{res}], \\ &\qquad \left(\frac{1}{c_0^2}\frac{\partial^2}{\partial t^2} - \frac{\partial^2}{\partial Z^2}\right)(\tilde{p}(Z,t)) = \frac{\rho_0}{M_d S_{cs}}\left(R\dot{x}_i(t) + F_{NL}(x_i(t)) - S_d p_b(t,Z_i)\right)\oint_{(\partial S_{cs})_{\text{ER}}} d\gamma \end{aligned} \tag{6.8}$$

with Z_i the coordinate Z of the center of the $i-$th ER: $Z_i = \dfrac{(2i-1)L_{res}}{2}$. By denoting L_p the length of the cross-section perimeter that is treated by the ER: $L_p = \oint_{(\partial S_{cs})_{\text{ER}}} d\gamma$, the following equations are to be solved simultaneously $\forall i \in [\![1,N]\!]$:

$$\begin{cases} \left(\dfrac{1}{c_0^2}\dfrac{\partial^2}{\partial t^2} - \dfrac{\partial^2}{\partial Z^2}\right)\tilde{p}(Z,t) = & \text{(6.9a)} \\ \qquad \dfrac{\rho_0 L_p}{M_d S_{cs}} \displaystyle\sum_{i=1}^{N} \Big(R\dot{x}_i(t) + F_{NL}(x_i(t)) - S_d p_b(t,Z_i)\Big)\Big(H(Z-(i-1)L_{res}) - H(Z-iL_{res})\Big) & \\ M_d\ddot{x}_i(t) + R\dot{x}_i(t) + F_{NL}(x_i(t)) = S_d p_b(t,Z_i) & \text{(6.9b)} \end{cases}$$

where H is the Heaviside function. These equations can be solved by finite differences for example, but the chosen approach is the use of the Finite Element Software COMSOL®. These analytical developments enable to model the system with a 1-dimensional domain governed by the wave equation which receives an acoustic contribution to model the liner.

Notice that the ER contribution scales linearly with the factor L_p, modeling the length treated with the ER. While L_p could in principle be taken as the physical length of the ER membrane, the coupling between the acoustic domain and the ER is usually defined using the S_d parameter, which represents the effective area of the fluid medium set into motion by the membrane. In practice, S_d corresponds to a portion of the total membrane surface. One way to model this could be to introduce spacing between the acoustic contributions in the Z-direction, and to take L_p as a fraction of the total width of the ER membrane associated with the effective area S_d. The model

adopted here assumes no spacing between ERs. Accordingly, the parameter L_p is estimated as the proportional part S_d relative to the total area attributed to the ER: a 5 cm square. Consequently, L_p is estimated as:

$$L_p = \frac{S_d}{L_{cs}^2} L_{cs} = \frac{S_d}{0.05^2} \times 0.05 = 0.026 \text{ m} \tag{6.10}$$

6.4 The experiment

6.4.1 Experimental set-up

The experiment aims at characterizing the Transmission Loss (TL) of the liner. For that purpose, a square cross-sectional tube of area S_{cs} is engineered and manufactured in 3 pieces. The two extremities are identical, of the same length L_e, with a circular opening at the middle fitted by acoustic sources being external loudspeakers Visaton©K50WP 8Ω. In Fig. 6.2, schemes and pictures of the experiment are presented. The letters **A** and **B** refer to the right and left sides of the experiment, respectively. Both excitation signals received by the external loudspeakers are amplified using 30W DataPhysics©amplifiers. The half-end of each tube are filled with acoustic foam in order to approach, as much as possible, quasi-anechoic conditions. Additionally, two 1/4" Bruël&Kjaer©Type 4988-A microphones, separated by $L_{\text{spacing}} = 4$ cm from each other, are placed at mid-distance L_m from the external sources LS-A/B and from the end of each tube to minimize the influence of evanescent waves as well as ensuring plane waves. These four microphones enable the use of the 4-Microphone-Method (4MM). The microphones are linked to a Conditioner PCB Piezotronics©482C. Between the two tubes **A** and **B**, the liner is positioned and consists into the same cross-sectional tube of length L_{lin}, with 7 openings on one face. These openings accommodate the Electroacoustic Resonators (ERs), which can alternatively be sealed with rigid terminations.

In this study, the ERs are built from Visaton©FRWS5 loudspeakers, each collocated with four embedded Knowles©WP-30113-P03 microphones, as shown in Fig. 6.3. These resonator cells were originally developed for a previous project implementing linear behaviors via a microcontroller integrated into each cells circuit. As a result, the micro-controllers were disconnected for this work, and new electrical connections were established to interface with an external acquisition and control system. Howland current pumps are also embedded in the electronic circuit of each cell to ensure that the voltage applied to the loudspeaker matches the one sent from the control device. The specifications, as well as characterization techniques and data for the 7 cells are presented in Appendix A.

The excitation signals, control trajectories and acquisition of all microphones signals and control variables are realized using a d-SPACE©MicroLabBox DS1203 (II).The dimensions of the experiment are detailed in Table 6.1:

Dimension	Value	Unit
L_e	1	m
S_{cs}	2.5×10^{-3}	m^2
L_m	0.125	m
L_{spacing}	0.04	m
L_{lin}	0.485	m

Table 6.1 Dimensions of the experiment

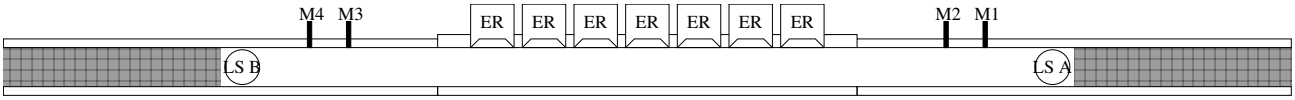

(a) Scheme of the tube.

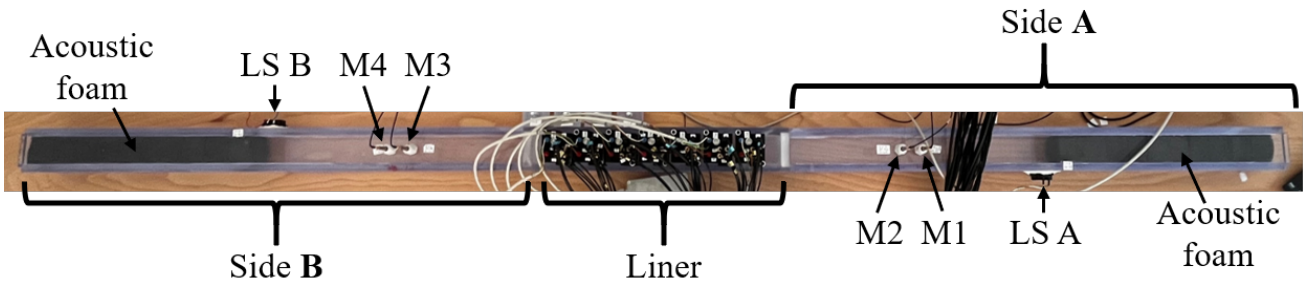

(b) Picture of the tube.

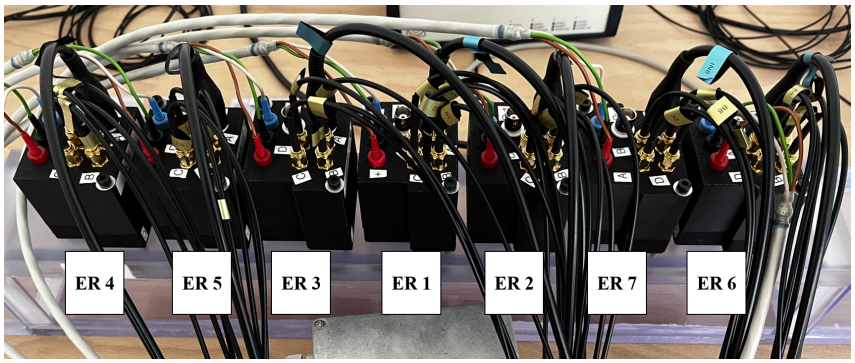

(c) Zoom on the liner.



(d) Picture of the inside of the liner, illustrating the grazing incidence.

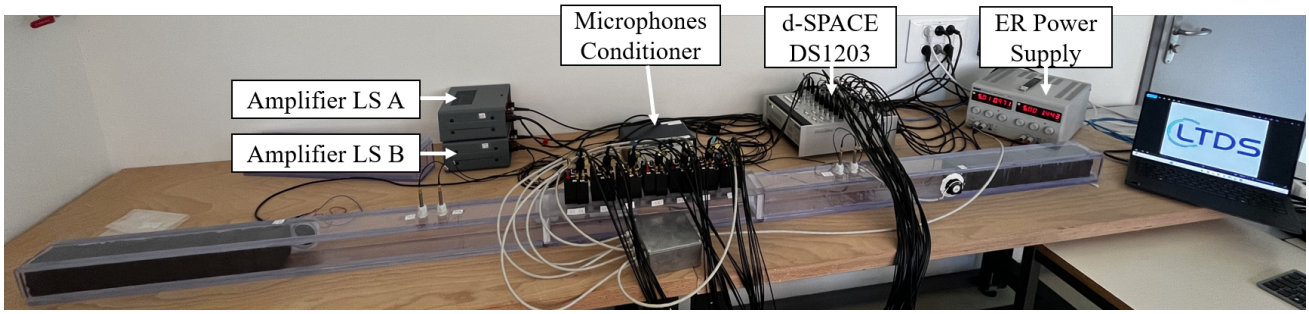

(e) Picture of the experimental bench.

Fig. 6.2 Experimental setup, with M1,M2,M3 and M4 being the 4 microphones used in the 4 Microphone Method (4MM), and LS A and LS B the loudspeakers of each side.

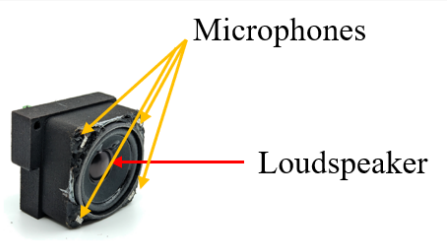

Fig. 6.3 Picture of the ER.

To calculate the cutoff frequency of the waveguide, rigid duct walls are considered. The cutoff frequency f_c, below which we can assume plane wave propagation and evanescent higher order duct modes, classically writes for a squared cross-section S_{cs}:

$$f_c = \frac{c_0}{2\sqrt{S_{cs}}} \tag{6.11}$$

In the case of the experiment, $\sqrt{S_{cs}} = L_{cs} = 5.5$ cm, which gives $f_c = 3118$ Hz. However, the cutoff frequency might change due to the modified boundary conditions of the ER.

6.4.2 Experimental tests and post-processing methods

In the present work, the liner under investigation is nonlinear, which does not fulfill the conditions of the experimental tests that are originally created for linear liners. Indeed, the 4MM determines the amplitudes of the waves going in the forward and backward directions on each side of the liner. It permits to determine the reflection and transmission coefficients of the liner in both directions. In principle, only three microphones would be sufficient in the presence of perfectly anechoic terminations. However, real anechoic terminations are imperfect and excite the waveguide modes, particularly at low frequencies where acoustic foams are less effective. A three-microphone approach could be implemented by modifying the acoustic load on one side of the setup, but in practice, the configuration with two loudspeakers and four microphones yields equivalent results while greatly simplifying the characterization of non-reciprocal liners.
Unlike linear liners, nonlinear liners scatter energy toward both lower and higher harmonics [160]. Quantifying the amount of energy redistributed across frequencies, and estimating an equivalent Transmission Loss (TL) require the use of additional acoustic loads at the tube extremities [23, 24]. Furthermore, frequency-sweep excitations cannot be used to estimate the TL, since the resulting scattering would render the measurements unusable. As a result, the liner is characterized exclusively using single-frequency sine excitations. In this framework, the determination of additional harmonics is neglected while using the characterization of the Transmission Loss of the liner. However, quantification of the production of harmonics can be realized using spectrograms, but the influence on the TL is left to future investigations.

The position of the microphones are referred to Z_{pj} with $j \in [\![1,4]\!]$, corresponding to the j-th microphone in Fig. 6.2a. At each position, the acoustic pressure is modeled as the superposition of waves propagating in the forward and backward directions. The scattering coefficients are estimated only at the fundamental harmonics, and the energy conversion towards higher and lower harmonics is neglected. Throughout the following work, this assumption is obviously not verified, but it enables the easy estimation of the TL. Spectrograms will be realized in order to estimate the quality of the assumption. The total pressure at each microphone position in the frequency domain reads as:

$$p(\omega, Z_{p1}) = p_1(t) = A_+(\omega)\,\mathrm{e}^{-ik_0 Z_{p1}} + A_-(\omega)\,\mathrm{e}^{ik_0 Z_{p1}} \tag{6.12a}$$

$$p(\omega, Z_{p2}) = p_2(t) = A_+(\omega)\,\mathrm{e}^{-ik_0 Z_{p2}} + A_-(\omega)\,\mathrm{e}^{ik_0 Z_{p2}} \tag{6.12b}$$

$$p(\omega, Z_{p3}) = p_3(t) = B_+(\omega)\,\mathrm{e}^{-ik_0 Z_{p3}} + B_-(\omega)\,\mathrm{e}^{ik_0 Z_{p3}} \tag{6.12c}$$

$$p(\omega, Z_{p4}) = p_4(t) = B_+(\omega)\,\mathrm{e}^{-ik_0 Z_{p4}} + B_-(\omega)\,\mathrm{e}^{ik_0 Z_{p4}} \tag{6.12d}$$

where ω corresponds to the excitation frequency, k_0 denotes the wave vector and A_+, A_-, B_+ and B_- stand for the pressure amplitude of the forward and backward waves, referred to with the subscript $+$ (*forward*) and $-$ (*backward*) on sides A and B. As the pressures are measured, and the amplitudes of forward and backward waves are unknown, the system can be solved for the amplitudes:

$$A_+(\omega) = i\frac{p_1(\omega)\,\mathrm{e}^{ik_0 Z_{p2}} - p_2(\omega)\,\mathrm{e}^{ik_0 Z_{p1}}}{2\sin(k_0(Z_{p1} - Z_{p2}))} \tag{6.13a}$$

$$A_-(\omega) = i\frac{p_2(\omega)\,\mathrm{e}^{-ik_0 Z_{p1}} - p_1(\omega)\,\mathrm{e}^{-ik_0 Z_{p2}}}{2\sin(k_0(Z_{p1} - Z_{p2}))} \tag{6.13b}$$

$$B_+(\omega) = i\frac{p_3(\omega)\,\mathrm{e}^{ik_0 Z_{p4}} - p_4(\omega)\,\mathrm{e}^{ik_0 Z_{p3}}}{2\sin(k_0(Z_{p3} - Z_{p4}))} \tag{6.13c}$$

$$B_-(\omega) = i\frac{p_4(\omega)\,\mathrm{e}^{-ik_0 Z_{p3}} - p_3(\omega)\,\mathrm{e}^{-ik_0 Z_{p4}}}{2\sin(k_0(Z_{p3} - Z_{p4}))} \tag{6.13d}$$

As a result, a single measurement is sufficient to determine the wave amplitudes, which is here realized using transfer functions estimation, following the Standard recommendations [147, 41]. To evaluate the Transmission Loss, the transmission coefficients must be identified first. These coefficients are obtained from two separate measurements, one with the acoustic source located on side **A** and the other with the source on side **B**. In the following, the superscripts $[A]$ and $[B]$ indicate the external acoustic source that has been used to realize the measurement. The relationship between the amplitudes of the incident waves and those of the reflected and transmitted waves can be expressed through the scattering matrix. This matrix contains the transmission and reflection coefficients in the forward and backward directions, denoted by T_+, R_+, T_- and R_-, and takes the form:

$$\begin{pmatrix} B_+^{[A]} & B_+^{[B]} \\ A_-^{[A]} & A_-^{[B]} \end{pmatrix} = \begin{pmatrix} T_+ & R_- \\ R_+ & T_- \end{pmatrix} \begin{pmatrix} A_+^{[A]} & A_+^{[B]} \\ B_-^{[A]} & B_-^{[B]} \end{pmatrix} \tag{6.14}$$

Solving the following system by inverting the last matrix, it yields the following solution:

$$T_+(\omega) = \frac{B_+^{[A]} B_-^{[B]} - B_+^{[B]} B_-^{[A]}}{A_+^{[A]} B_-^{[B]} - A_+^{[B]} B_-^{[A]}} \tag{6.15a}$$

$$R_-(\omega) = \frac{B_+^{[B]} A_+^{[A]} - B_+^{[A]} A_+^{[B]}}{A_+^{[A]} B_-^{[B]} - A_+^{[B]} B_-^{[A]}} \tag{6.15b}$$

$$R_+(\omega) = \frac{A_-^{[A]} B_-^{[B]} - A_-^{[B]} B_-^{[A]}}{A_+^{[A]} B_-^{[B]} - A_+^{[B]} B_-^{[A]}} \tag{6.15c}$$

$$T_-(\omega) = \frac{A_-^{[B]} A_+^{[A]} - A_-^{[A]} A_+^{[B]}}{A_+^{[A]} B_-^{[B]} - A_+^{[B]} B_-^{[A]}} \tag{6.15d}$$

Finally, the TL in both forward and backward directions can be expressed as:

$$TL_{\pm}(\omega) = 20\log\left(\frac{1}{|T_{\pm}|}\right) \tag{6.16}$$

In this work, each single-frequency sine excitation requires two measurements, providing the values of the forward and backward Transmission Loss (TL) as well as the corresponding coefficients at the excitation frequency. This procedure is repeated across the entire frequency bandwidth of interest.

Note that the excitation amplitudes from both acoustic sources (from sides **A** and **B**) need to be identical to ensure a valid estimation of the TL and of the coefficients in case of nonlinear liner. Indeed, in case of a nonlinear liner, the frequency response of the liner is dependent on the amplitude of the excitation. As experimental transducers are not perfectly identical, in addition to the terminations not being identical, an adjustment of the excitation signals is needed. Moreover, a constant excitation amplitude would enable a better comparison with numerical and analytical results. Consequently, an adaptive gain to apply to the excitation signal of each acoustic source is determined in the rigid liner configuration. The procedure and results of the excitation signals calibration are detailed in Appendix E.

The characterization and results of the rigid liner configuration are presented in Appendix E.

6.5 The linear metasurface

In this section, the linear metasurface performance and results are presented, and compared against the FE model. The analysis begins with the case of a single ER in order to address the grazing incidence problem, before extending to the case of multiple resonators. The objective is to compare the experimental findings with the FE predictions and with results available in the literature, where linear liners have been extensively investigated.

6.5.1 The single resonator problem

In this section, the single-resonator case under grazing incidence is examined. For the following, the denomination **C***j* denotes the *j*-th ER (Cell *j*). The **C1** ER is inserted into the tube, while the six remaining openings, for allocating the remaining ERs, are sealed with rigid caps. The first measurements are realized with an Open Circuit (OC) configuration, meaning that the equivalent parameters are $\eta_K = \eta_M = \eta_R = 1$.
The previously presented procedure is applied from 500 Hz to 1300 Hz with a 20 Hz step, and a 2 seconds duration for each step. Transmission Loss, power reflection and power absorption coefficients are presented in Fig. 6.4. The power reflection coefficient is classically obtained as $|R_{\pm}|^2$, while the power absorption coefficient in grazing incidence $\alpha_{\pm}$ is defined as the power left, as in [41]:

$$\alpha_{\pm} = 1 - |T_{\pm}|^2 - |R_{\pm}|^2 \tag{6.17}$$

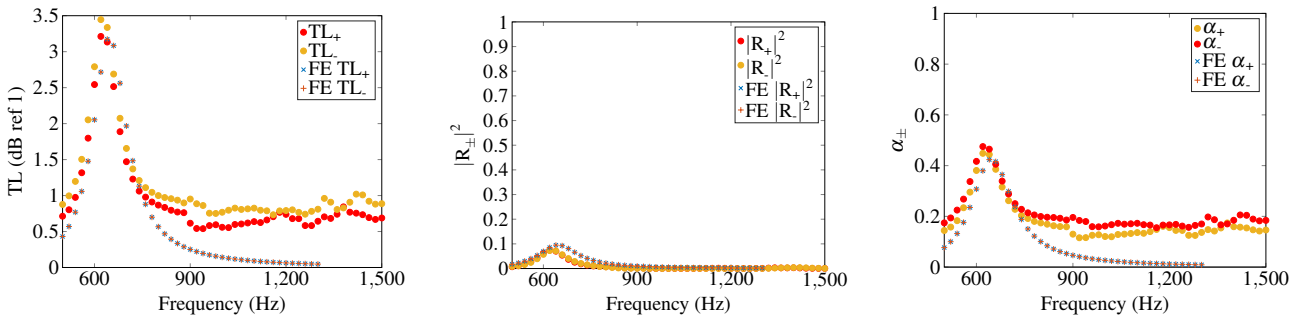

(a) (b) (c)

Fig. 6.4 Experimental and FE results obtained with 1 ER (OC configuration): (a) Transmission Loss, (b) Power Reflection coefficient, (c) Power Absorption coefficient.

It can be observed that the TL attains approximately 3.5 dB (Fig. 6.4a), and that the energy has mainly been absorbed (Fig. 6.4c), with very little energy reflected by the liner (Fig. 6.4b). Observe that the linear resonance of the ER (Cell C1) is aligned with the increase in TL, meaning that the ER absorbs the energy at its natural resonance. The numerical results are found to be in excellent agreement with the experimental ones for all three indicators, despite the simplifying assumptions of the FE model. However, FE predictions are expected to be less accurate for nonlinear resonators as their response strongly depends on the excitation amplitude, unlike linear resonators.

It is worth noting that stability issues may arise in the grazing incidence setup, since the ER directly faces a rigid wall, mainly due to the delay in the digital algorithm [42], as showed in Fig. 3.3.3. The empirical investigation of the performance and stability of the ER in this configuration is realized here by:

- modifying the damping parameter to the arbitrary value $\eta_R = 1/2$ and keeping $\eta_M = \eta_K = 1$, presented in Fig. 6.5,
- modifying the targeted resonance frequency of the resonator: $\eta_K = 3$ while keeping $\eta_M = \eta_R = 1$, presented in Fig. 6.6.

The modification of the damping led to the increase of the TL from 3.5 dB to 5.5 dB compared to the OC case (Fig. 6.5a). The electrical current increased the ER's amplitude response, enabling for the modification of the targeted impedance. This problem has been extensively treated in the literature [152, 28, 18]. The optimal impedance (and so the optimal damping in this case) depends on the characteristics of the liner, tube and medium. Here, diminishing the damping parameter enables to look for instabilities issues (that would be stabilized with higher values of damping). Here, no instabilities can be spotted, and the TL has been increased, mainly due to a higher amount of reflected energy (Fig. 6.5b) (as well as a slight increase in absorption (Fig. 6.5c)).

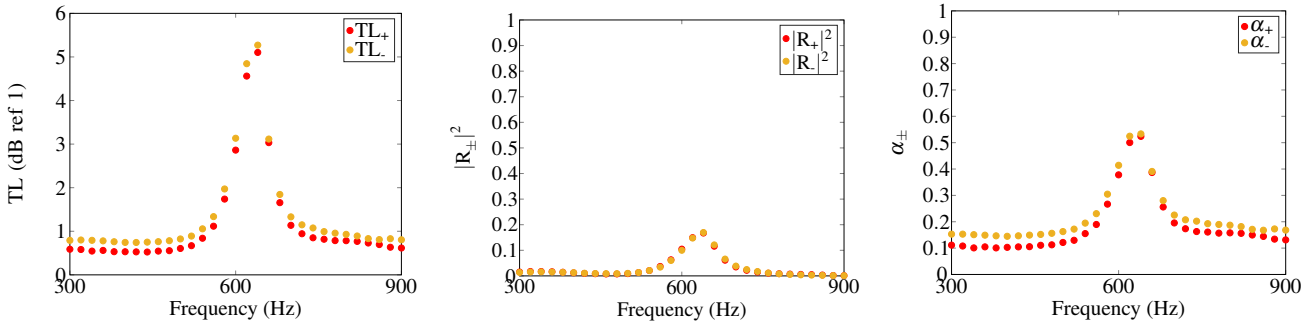

(a) (b) (c)

Fig. 6.5 Experimental results obtained with 1 ER with $\eta_R = 1/2$: (a) Transmission Loss, (b) Power Reflection coefficient, (c) Power Absorption coefficient.

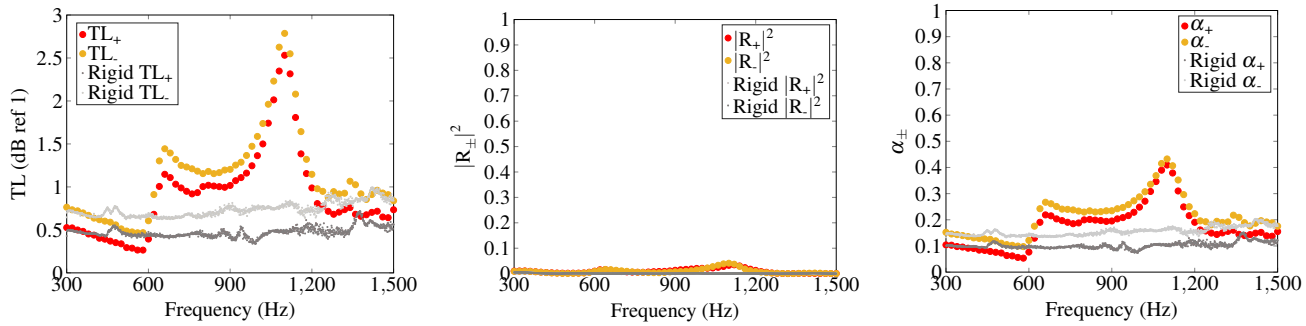

(a) (b) (c)

Fig. 6.6 Experimental results obtained with 1 ER with $\eta_K = 3$: (a) Transmission Loss, (b) Power Reflection coefficient, (c) Power Absorption coefficient.

The modification of the stiffness parameter, while keeping $\eta_M = 1$ allows for targeting the treatment of incident waves at the targeted resonance frequency. The modification of $\eta_K = 3$ targets the resonance frequency $f_d \approx 1106$ Hz. Figure 6.6a shows a significant increase in the TL at 1100 Hz compared to the OC case. At this frequency, a slight increase in the reflection coefficient can be observed (Fig. 6.6b), along with an important increase of the absorption coefficient (Fig. 6.6c). Consequently, the absorption capabilities of the ER are increased at the targeted frequency, as expected. However, an increased TL is observed at the loudspeaker's natural frequency compared to the Rigid configuration one, indicating that the membrane's natural resonance is not completely deleted by the control strategy (effect of time delay, as seen in Chapter 3). Moreover, the TL and absorption coefficient diminishes below the rigid configuration curves at 600 Hz (before the natural resonance) due to the change in resonance frequency, indicating that an instability can be spotted at this frequency.

These results allow to proceed for the construction of a distributed network of linear resonators. If stability issues does not arise from the coupling of the resonators through the acoustic medium, the performance should be improved.

6.5.2 The distributed network of resonators

In this section, a linear metasurface is created with the development of a liner of linear ERs. This has been extensively investigated previously with higher degrees of complexity, with and without flow [28], and by implementing the Advection Boundary Law (ABL) that breaks the acoustic reciprocity [87, 26, 27]. Here, a

straightforward approach is considered, aiming at validating basic steps regarding stability before the investigation of nonlinear behaviors. Seven nonlinear ERs are placed inside the tube. The parameters of each resonators are referred to $\eta_K^{[j]}$, $\eta_M^{[j]}$, $\eta_R^{[j]}$ with $j \in [\![1,7]\!]$ corresponding to the j-th ER.
The OC configuration is first investigated, meaning that the equivalent parameters are the natural ones. Remind that the proper modal mass, stiffness and damping slightly changes from one ER to another one, because they are not perfectly identical:

$$\forall j \in [\![1,7]\!], \quad \eta_K^{[j]} = \eta_M^{[j]} = \eta_R^{[j]} = 1 \tag{6.18}$$

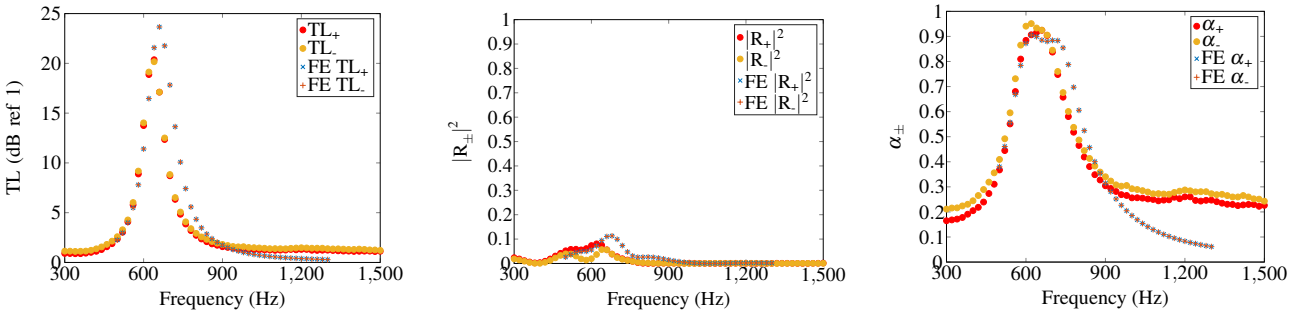

(a) (b) (c)

Fig. 6.7 Experimental and FE results obtained with 7 ERs (OC configuration): (a) Transmission Loss, (b) Power Reflection coefficient, (c) Power Absorption coefficient.

The previous protocol stands, single frequency sine excitations are used from 300 Hz to 1500 Hz, with a duration of 3 seconds. The TL, and Power Reflection and Absorption coefficients are presented in Fig. 6.7 for the OC configuration. The TL reaches 21 dB at the resonance of the ERs (Fig. 6.7a). Most of the acoustic energy is dissipated using the resonators, as the absorption coefficient is close to 1 at the ERs resonance (Fig. 6.7c). As expected, the numerical simulations (conducted with the same parameters for all resonators) are in strong agreement with the experimental results. This shows that the linear liner can be efficient, without implementing an optimal impedance.
Note that the reflection coefficients in OC configuration $|R_+|^2$ and $|R_-|^2$ are not identical (Fig. 6.7b). This is due to the asymmetry of the liner along the $Z-$axis, due to the slight natural differences between each ER

Similarly to the previous analysis featuring a single resonator, the parameters of the ERs are modified to target a specific frequency $f_d^{[j]} = 1100$ Hz with $j \in [\![1,7]\!]$, and $f_d^{[j]}$ being the targeted frequency. The $\eta_K^{[j]}$ parameters are chosen accordingly, while $\eta_M^{[j]} = \eta_R^{[j]} = 1$ for all $j \in [\![1,7]\!]$. The results are presented in Fig. 6.8, and are extremely similar to the single resonator results. Observe that the TL is significantly increased at 1100 Hz to 18 dB, while a TL increase can be noted at the loudspeaker's natural frequency (Fig. 6.8a). Observe that the OC configuration offers better performance at the natural frequency, as the loudspeaker is helped by its natural frequency. Moreover, the TL decrease at 600 Hz is confirmed with multiple resonators, along with a slightly negative absorption coefficient (Fig. 6.8c). The control strategy creates a slightly active resonator when deleting the natural resonance of the loudspeaker.

The same analysis can be realized with $j \in [\![1,7]\!]$, $\eta_R^{[j]} = 1/2$. The results are presented in Fig. 6.9. As for the single resonator, the TL has significantly increased at the ER's resonance frequency (un to 35 dB) compared to the OC configuration (Fig. 6.9a), along with an increase in the reflection coefficient (Fig. 6.9b). The absorption coefficient (Fig. 6.9c) follows the same evolution as the TL.

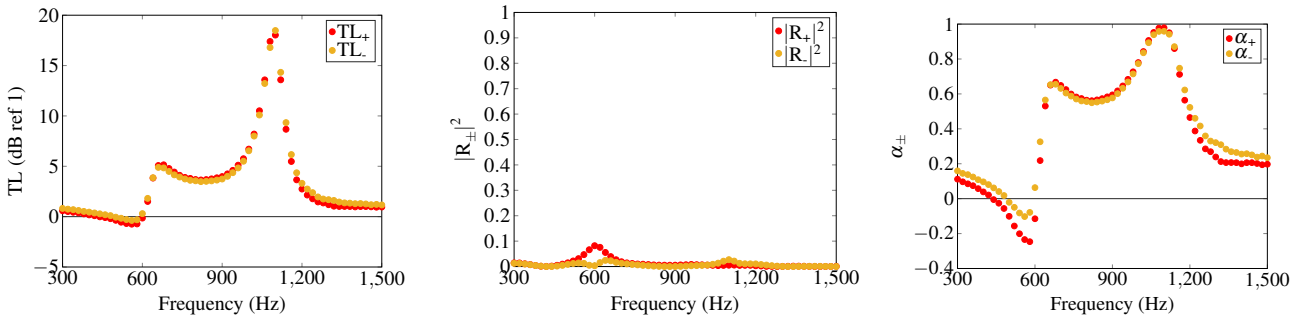

(a) (b) (c)

Fig. 6.8 Experimental results obtained with 7 ERs with $\forall j \in [\![1,7]\!]$, $f_d^{[j]} = 1100$ Hz: (a) Transmission Loss, (b) Power Reflection coefficient, (c) Power Absorption coefficient.

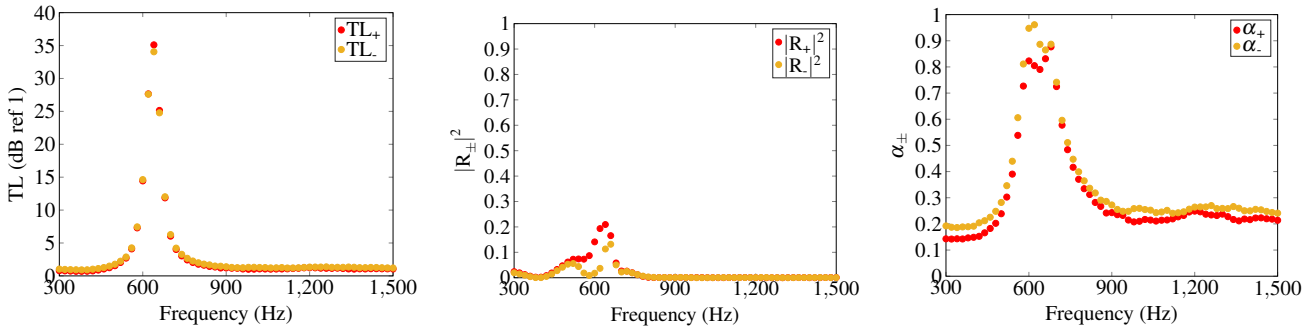

(a) (b) (c)

Fig. 6.9 Experimental results obtained with 7 ERs with $\forall j \in [\![1,7]\!]$, $\eta_R^{[j]} = 1/2$: (a) Transmission Loss, (b) Power Reflection coefficient, (c) Power Absorption coefficient.

Nonlinear behaviors can participate in broadening the frequency bandwidth of efficiency, while featuring nonlinear phenomena that can be interesting for noise control purposes.

6.6 The nonlinear metasurface

The study of the nonlinear metasurface is realized in this section, with the investigation of a single nonlinear resonator, and the study of the distributed network. As stability issues have been observed for a linear metasurface in the case of modifying the resonance frequency through the modification of η_K, the following study keeps the stiffness and mass coefficients at the natural resonance of the loudspeaker. As the analysis is complexified by the experimental bench, as well as the use of multiple resonators, and also because of time constraints, only hardening cubic restoring forces are implemented in this section.

6.6.1 A single nonlinear resonator

The investigation of the single nonlinear ER remains important despite the preceding studies, as the ER is strongly coupled to a tube that does not perfectly behave as a infinite one. As a result, modal interactions could happen, which could lead to beneficial or unfavorable phenomena in the distributed network.

The protocol is similar to the previous ones, single frequency sine excitation signals are produced by the acoustic sources, from 500 Hz to 1500 Hz, with a 14s duration, and the recording of an additional second. The

duration enables the establishment of the steady-state regime (as previously), but permits to implement the modified control strategy presented in Chapter 5. Measurements with either classical ($f_{ext}^{ES} = f_{ext}^{m}$) or modified control with added synthetic forces ($f_{ext}^{ES} = f_{ext}^{m} + f_{ext}^{a}$) are realized. The case of added synthetic vector states (such as displacement or velocity) is not considered in this Chapter. In the case of modified control, the procedure is close to the one seen in the previous Chapter:

- For $0 < t < 2$, the classical control is implemented: $f_{ext}^{ES} = f_{ext}^{m}$, (meaning that $f_{ext}^{a} = 0$), and a first steady-state regime is reached;
- For $2 \leq t < 10$, the modified control is activated: $f_{ext}^{ES} = f_{ext}^{m} + f_{ext}^{a}$ with $f_{ext}^{a} = \frac{a}{2}\tanh(t-2)$, and a steady-state induced by a ER higher energy equilibrium point can be reached;
- For $10 \leq t \leq 15$, the return to a classical control is realized with $f_{ext}^{a} = 0$.

As previously, the parameters are chosen such as : $\eta_K = \eta_M = \eta_R = 1$, while a hardening cubic nonlinearity is introduced: $\beta_{\text{NL}} = 1 \times 10^{13}$ m^{-2}.

First, let us study the ES displacement computed during experiments in Fig. 6.10. The results obtained with the classical control ($f_{ext}^{ES} = f_{ext}^{m}$), with the modified control ($f_{ext}^{ES} = f_{ext}^{m} + f_{ext}^{a}$) and with increasing and decreasing frequency sweeps are plotted. The solution of the ES equation obtained by the HBM method truncated to the first harmonic is also plotted, taking the excitation amplitude as the mean value of the experimental pressure. Observe that the mono-harmonic signals follow the frequency sweeps for both the classical and modified control strategy. As expected, the modified control strategy is able to follow the higher energy points featured by frequency sweeps. However, the modified control strategy attains equilibrium points that the frequency sweeps do not attain. The HBM solution, despite the strong approximation of the mean amplitude, predicts that the bifurcation frequency is higher than the one determined from frequency sweeps. It shows that the obtained behavior is a nonlinear hardening one, as expected.

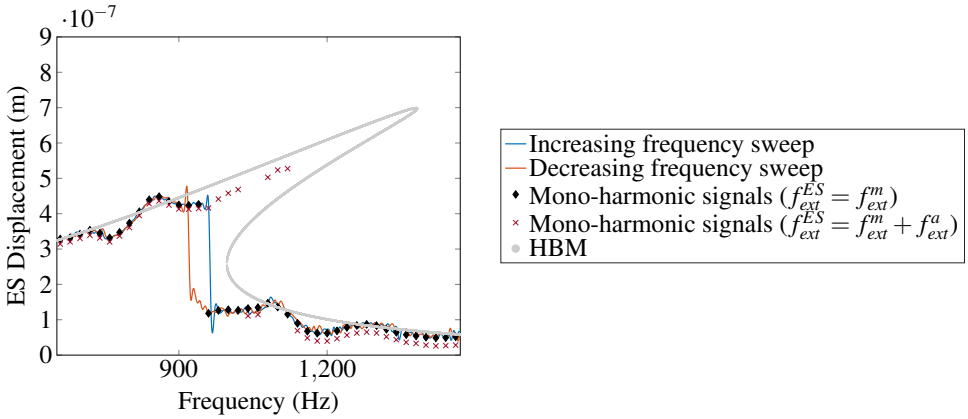

Fig. 6.10 Experimentally obtained ES Displacement with increasing and decreasing frequency sweeps and single frequency excitation signals with both $f_{ext}^{ES} = f_{ext}^{m}$ and $f_{ext}^{ES} = f_{ext}^{m} + f_{ext}^{a}$ with $a = 40$ Pa. The experimental results are compared with an HBM solution of the ES equation with one harmonic (with the value of the excitation assumed of constant amplitude equal to the mean pressure (≈ 1.70 Pa) measured during the experiment).

Moreover, the experimental TL, Power Absorption and Reflection coefficients are plotted in Fig. 6.11 for the classical control ($f_{ext}^{ES} = f_{ext}^{m}$), and in Fig. 6.12 for the modified control ($f_{ext}^{ES} = f_{ext}^{m} + f_{ext}^{a}$).
The results obtained with a classical control show a lower TL (Fig. 6.11a), reflection coefficient (Fig. 6.11b), and absorption coefficient (Fig. 6.11c) than the OC case (in gray). However, the nonlinear ER significantly broadens

the frequency bandwidth of efficiency. Moreover, the peaks of the absorption and reflection coefficients, and the TL are shifted towards higher frequencies.

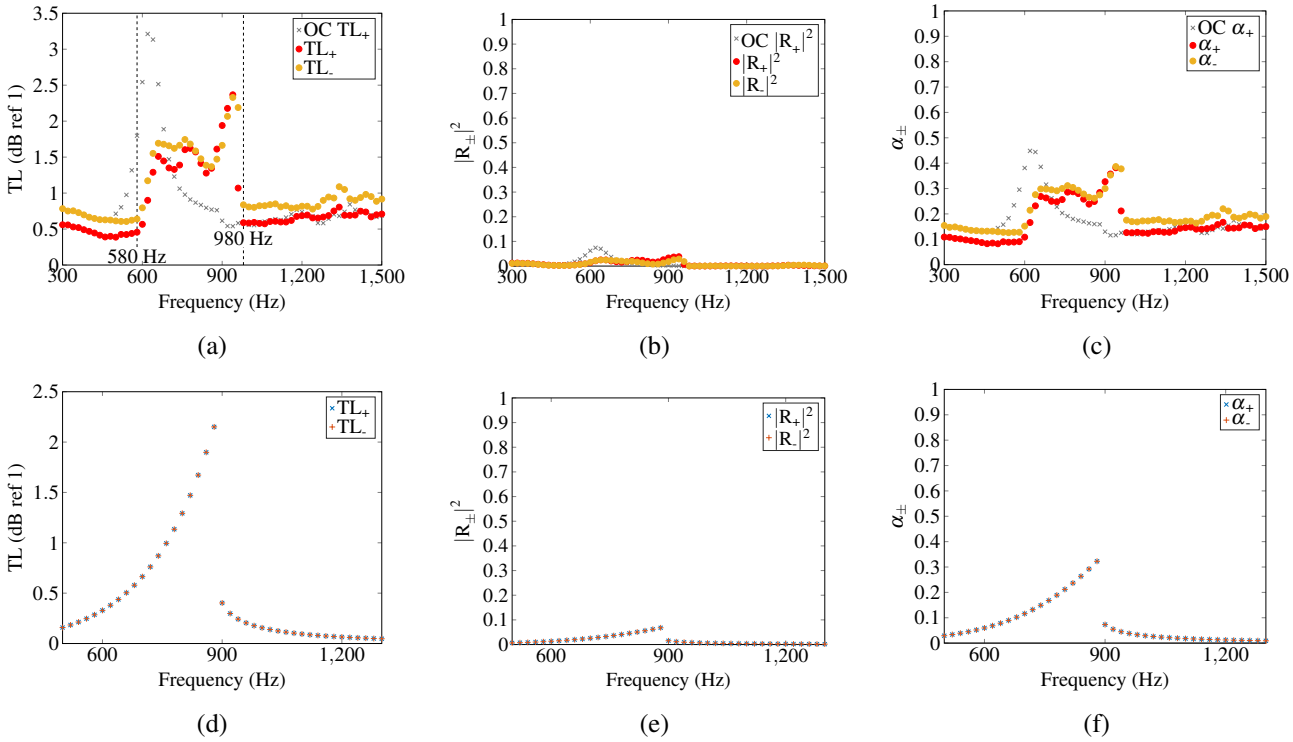

Fig. 6.11 Experimental (a,b,c) and FE (d,e,f) results obtained with 1 ER with the classical control strategy ($f_{ext}^{ES} = f_{ext}^{m}$): (a,d) Transmission Loss, (b,e) Power Reflection coefficient, (c,f) Power Absorption coefficient.

The TL, absorption and reflection coefficients obtained using the FE analysis are illustrated in Fig. 6.11. The FE predictions are in good agreement with the experimental results. Observe that the qualitative behavior is well captured by the FE simulations, as the order of magnitude of the TL, reflection coefficient and absorption, as well as the jump phenomenon are predicted. However, the frequency of the jump, the accurate values of TL magnitude, and the shape of the curve with respect to frequency can be improved.

Simulating the controller, and taking into account the delay (and eventual uncertainties in the model identification) in the FE model would enable to model the increased TL at the natural frequency of the loudspeaker. However, it could significantly increase the calculation time, as an additional ODE needs to be solved at each time step, for each ER.

Nevertheless, the modeling of the controller is not sufficient as the ER's response is amplitude-frequency dependent (due to its nonlinear nature), which results in an inaccurate response if the acoustic solicitation is not identical to the experimental one. As a result, the FE model could be significantly improved by:

- The acoustic characterization of the terminations (using the Two Microphones method for example). The Sommerfeld condition applied at each end of the FE tube could be modified to add the reflection and absorption of the termination. It would improve the accuracy of the acoustic level inside the waveguide, as well as exciting the modes of the tube that participate in the response. Indeed, the experimental tube can not be assumed to have perfect absorption conditions at both ends, therefore the acoustic longitudinal modes of the tube are excited (even if they might be largely damped).

- The characterization of the excitation loudspeakers (acoustic sources). The excitation amplitude is not constant across the frequency range of interest, despite the corrective gains that have been put in place. By measuring the acoustic source spectra, the same spectra could be applied in the FE model for reproducing the experimental acoustic excitation. Moreover, both acoustic sources do not deliver an identical sound spectra, and each of them should be characterized.

Applying these modifications to the FE model would leave minor uncertainties such as the junctions between the tubes, or between the ER and walls of the tube. Consequently, the model could be improved by adding several degrees of complexity, without creating 2D or 3D FE models.

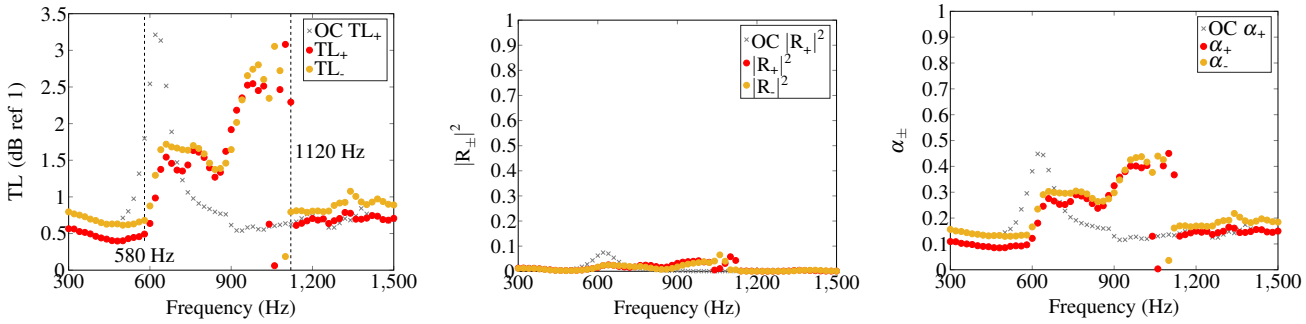

(a) (b) (c)

Fig. 6.12 Experimental results obtained with 1 ER with the modified control strategy ($f_{ext}^{ES} = f_{ext}^{m} + f_{ext}^{a}$): (a) Transmission Loss, (b) Power Reflection coefficient, (c) Power Absorption coefficient.

The results obtained with the modified control ($f_{ext}^{ES} = f_{ext}^{m} + f_{ext}^{a}$) are illustrated in Fig. 6.12. Observe that the efficiency bandwidth is extended towards higher frequencies (from 980 Hz to 1120 Hz), with higher TL amplitude (Fig. 6.12a) and absorption coefficient (Fig. 6.12c) before the jump. The maximum TL amplitude is similar to the OC one, indicating that eventual optimization of the nonlinear ER's parameters may enable better performance than the classical linear ER. The reflection coefficient (Fig. 6.12b) follows the same evolution as the TL and absorption coefficient.

Finally, Fig. 6.13 presents the time plots and corresponding spectrogram of the ES displacement for both classical and modified control for a 1020 Hz sine excitation. Observe that the ER's response is much larger with the modified control than with the classical one as the high energy equilibrium is reached (Figs. 6.13a and 6.13c). The spectrogram of the time histories of the classical control (Fig. 6.13b) shows that most of the energy is contained at the excitation frequency (1020 Hz), but a slight production of the third harmonics (3060 Hz) can be observed. The spectrogram of the modified control time plot (Fig. 6.13d) features the same result before the launch of the modified control. When the steady-state is reached (around 5 seconds), energy at higher frequencies are spotted at multiples of the excitation frequency. The odd frequencies (third and fifth) are clearly recognizable, while the first pair frequency (2040 Hz) can be observed. Consequently, energy is scattered at higher frequencies by the nonlinear ER.

Note that the method for determining the TL assumes mono-harmonic signals, and does not take into account the multiharmonic scattering of the ERs.

Moreover, note that the first cross-sectional mode of the tube is placed at 3118 Hz (for rigid walls). However, it has been seen that the nonlinear ER scatter energy towards harmonics, at close and higher frequencies than the cutoff one. It results in the excitation of cross-sectional propagative modes, which are evanescent below the cutoff frequency, preventing from doing a straightforward analysis.

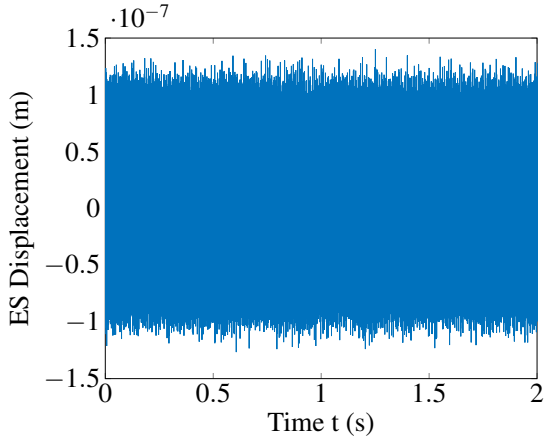

(a) $f_{ext}^{ES} = f_{ext}^{m}$

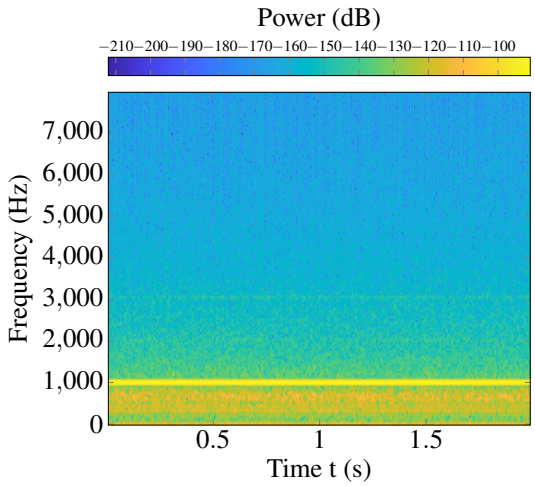

(b) $f_{ext}^{ES} = f_{ext}^{m}$

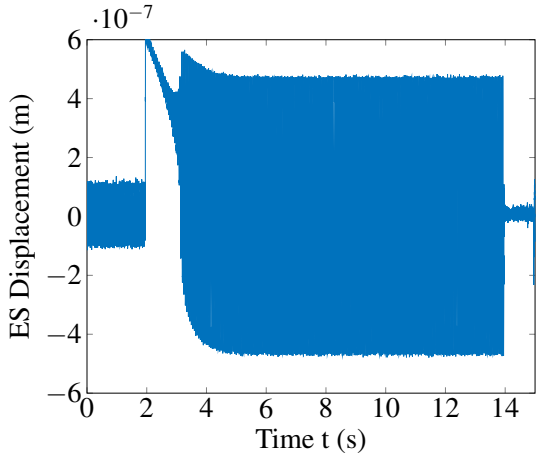

(c) $f_{ext}^{ES} = f_{ext}^{m} + f_{ext}^{a}$

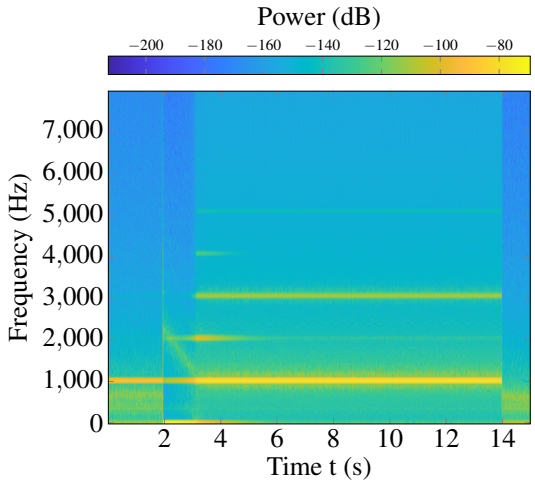

(d) $f_{ext}^{ES} = f_{ext}^{m} + f_{ext}^{a}$

Fig. 6.13 Time plots and corresponding spectrogram with 1 ER in the case of classical ($f_{ext}^{ES} = f_{ext}^{m}$) and modified control strategy ($f_{ext}^{ES} = f_{ext}^{m} + f_{ext}^{a}$) for a 1020 Hz sine excitation: (a) Transmission Loss, (b) Power Reflection coefficient, (c) Power Absorption coefficient.

6.6.2 The distributed network of nonlinear resonators

The following section presents the preliminary results of the nonlinear metasurface composed of multiple ERs at low excitation amplitudes. The following results correspond to the first approach of a nonlinear acoustic liner.

As previously, the parameters are chosen such as : $\forall j \in [\![1,7]\!], \quad \eta_K^{[j]} = \eta_M^{[j]} = \eta_R^{[j]} = 1$, to avoid instabilities, while a hardening cubic nonlinearity is introduced: $\forall j \in [\![1,7]\!], \quad \beta_{\text{NL}}^{[j]} = 1 \times 10^{13}$ m^{-2}.

The TL, power reflection and absorption coefficients are plotted in Fig. 6.14 for the classical control and in Fig. 6.15 for the modified control. Observe that the nonlinear liner created with the classical control offers a lower TL (10 dB) (Fig. 6.14a) than the OC liner (20 dB). However, similarly to the single resonator results, the efficiency bandwidth is largely broaden towards higher frequencies. The reflection coefficient (Fig. 6.14b) is not modified, indicating that the energy is either absorbed, or scattered at higher (or lower) frequencies. The absorption coefficient shows similar performance as the OC measurement (Fig. 6.14c). However, the TL is lower for the nonlinear

ER, with almost equivalent reflection coefficients. Indeed, the absorption coefficient is defined as the energy that is neither transmitted or reflected at the fundamental harmonics. As a result, the absorption coefficient accounts for the energy absorbed, but also for the energy scattered at higher or lower frequencies than the fundamental harmonics by the nonlinear liner. Consequently, this indicator should be used with caution with nonlinear liners.

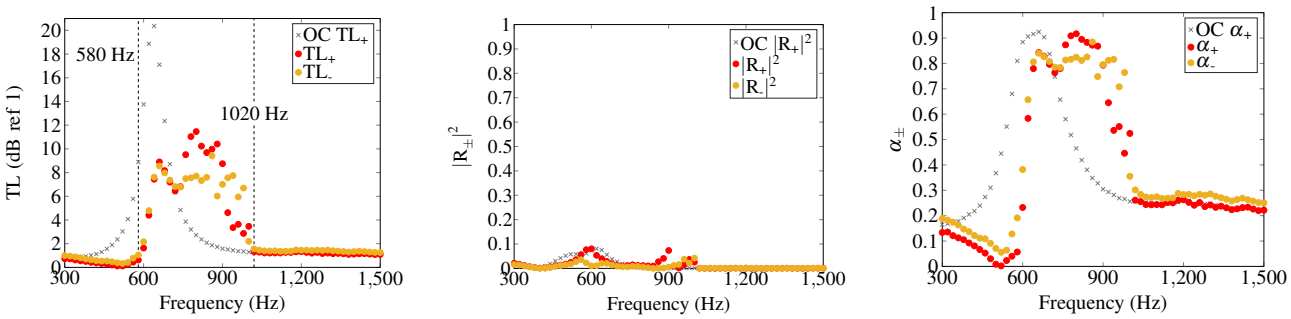

(a) (b) (c)

Fig. 6.14 Experimental results obtained with 7 ERs with the classical control strategy ($f_{ext}^{ES} = f_{ext}^{m}$): (a) Transmission Loss, (b) Power Reflection coefficient, (c) Power Absorption coefficient.

The modified control strategy shows an enlargement of the efficiency bandwidth (see the TL in Fig. 6.15a) compared to the classical control strategy. The results are similar for the reflection coefficient (Fig. 6.14b) and absorption coefficient (Fig. 6.14c). However, the TL and absorption coefficient below 600 Hz are reduced compared to the OC measurement, resulting from the absorption shift towards higher frequencies.

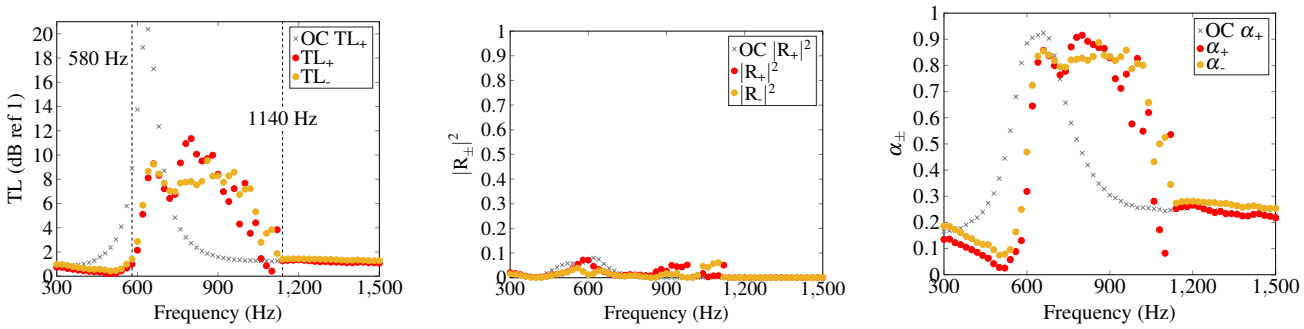

(a) (b) (c)

Fig. 6.15 Experimental and FE results obtained with 7 ERs with the modified control strategy ($f_{ext}^{ES} = f_{ext}^{m} + f_{ext}^{a}$): (a) Transmission Loss, (b) Power Reflection coefficient, (c) Power Absorption coefficient.

In addition, the minimum and maximum values of the envelopes of the ES Displacement are plotted for the first resonator as an example in Fig. 6.16. Plotting this data is used to spot obvious quasi-periodic behavior, common in nonlinear systems. However, the minimum and maximum amplitude of the envelope for all ERs shows that no quasi-periodic response can be spotted easily. Frequency sweeps can also provide interesting insight about these phenomena, but have not revealed quasi-periodic or chaotic phenomena. Other more sophisticated methods can be used for spotting quasi-periodic behavior, such as the observation of energy exchange between ERs after filtering. However, this method was not successful either. Another method using the transient behavior of ERs for spotting frequencies at which the system exhibit quasi-periodic behavior might be used in future investigations [38].

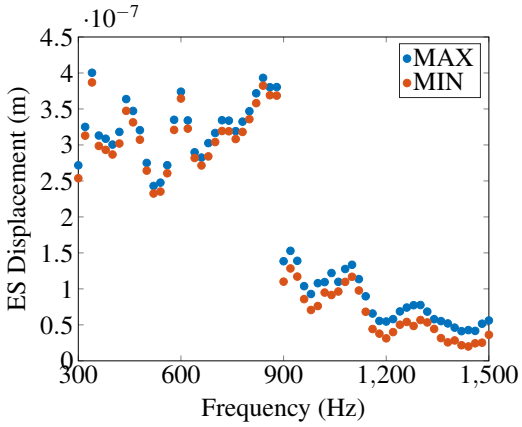

Fig. 6.16 ES Displacement obtained with Cell 1 for 7 ERs.

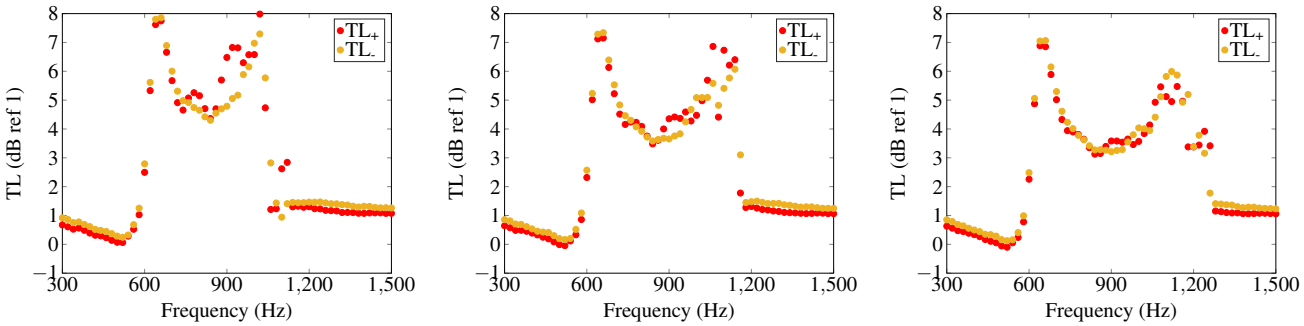

(a) (b) (c)

Fig. 6.17 Experimental TL obtained with 7 ERs with the classical control strategy ($f_{ext}^{ES} = f_{ext}^{m}$), with the excitation gain being: (a) 2, (b) 3, (c) 4.

The TL for the nonlinear liner with the classical control is plotted in Fig. 6.17 for multiple gains of the excitation signal (2, 3 and 4). Observe that the efficiency bandwidth is enlarged with the values of the excitation gain, while the TL magnitude slightly decreases. This phenomenon is expected as the ER's nonlinear response extends towards higher frequencies (hardening behavior), and the response amplitude decreases relatively to the excitation amplitude (see Chapter 3, Fig. 3.16a).

Nonlinear resonators in liners and metamaterials enable the creation of larger resonant bandgaps. The optimization of the parameters would probably permit nonlinear liners to be competitive compared to linear ones, but is yet to be proved. Additionally, the search for nonlinear phenomena, such as chaotic bands or quasi-periodic behavior would permit better performance of nonlinear liners. Moreover, the coupling of these liners to acoustic modes of a tube would be interesting to investigate for practical implementations.

6.7 Perspective: study of solitons inside the metasurface

This section presents the preliminary analytical calculations made for the study of solitons in the proposed nonlinear metasurface. A classical model extensively used in the literature is used, but is yet to be validated against experimental and numerical data.

To study the nonlinear metasurface, an analogous periodic electrical structure is considered. The analogy is widely spread in Acoustics to model waveguides and usually leads to the Transmission Line Approach (TLA).

In this approach, the applied pressure is analogous to a voltage p_n, and the electrical current u_n is analogous to the fluid particles velocity v for a cross-section with a constant area S_{cs} (the cross-section of the waveguide): $u_n = S_{cs}v$. Consequently, the particles displacement is analogous to the electric charge flowing through the circuit: $\frac{dq_n}{dt} = u_n = S_{cs}v$. Let us consider the long-wavelength limit and model the acoustic medium and an ER that interact with it by the TLA illustrated in Fig. 6.18. This model has been used extensively for modeling constant cross-sectional ducts interacting with Helmholtz resonators or cavities [2, 85]. In the long wavelength approximation (compared to the size of an ER), the acoustic medium of the length of an ER can be modeled with an acoustic mass L_w and a compliance C_w. The resonator is modeled by an electrical impedance $Z_R[u_{R_n}]$ that can be developed as a inductance L_R and nonlinear capacitance C_R.

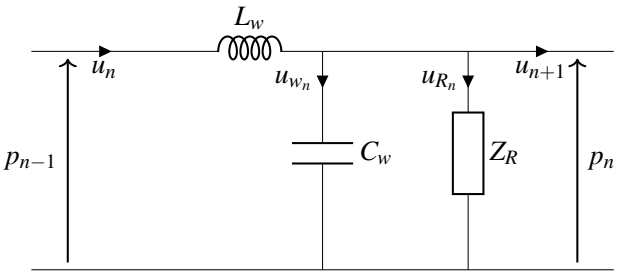

Fig. 6.18 The $n-$th cell modeled by an analogous electrical circuit (TLA).

6.7.1 Behavior of the liner

The analysis of such system can be realized through the study of the pressure p_n, fluid velocity u_n, or velocity of the air particles in contact with the ER's membrane u_{R_n}. The velocity u_{R_n} can be considered equal to the ER membrane's velocity by continuity conditions. The study of pressure p_n or fluid velocity u_n is the most natural choice, as it represents the acoustic medium, and is the choice made in the literature. However, this choice does not permit the full analytical solving of the system, as the operator Z_R has to be inverted. This operator being nonlinear in our case, the implicit function theorem (stated in Chapter 3) does not ensure the invertibility. Previous studies have assumed that the resonator is linear to go around this problem, such as Achilleos *et al.* in [2] that assumed a nonlinear behavior of the wave propagation ($C_w = C_w(p_n)$ being a function of the pressure p_n) and a linear behavior of the Helmholtz resonators (Z_R being a linear operator applied to u_{R_n}). This study considers the other way around, the acoustic medium is linear, and the resonator is nonlinear (implying Z_R nonlinear operator that applies to u_{R_n}). As a result, choosing to study the system through the variable u_{R_n} enables a fully analytical approach of the problem.

From Kirchhoff's laws, the velocity u_n writes:

$$u_n - u_{n+1} = u_{w_n} + u_{R_n} \tag{6.19}$$

where u_{w_n} is the fluid velocity flowing in the capacitance C_w. Considering the relation at the previous cell $n-1$, and differentiating the two relations, it yields:

$$2u_n - u_{n+1} - u_{n-1} = u_{w_n} - u_{w_{n-1}} + u_{R_n} - u_{R_{n-1}} \tag{6.20}$$

To study the system through the variable u_{R_n}, the other variables should be replaced as function of u_{R_n}. With this goal in mind, three relations can be found from Kirchhoff's laws:

1. The following condition is obtained by considering the right part of the circuit:

$$p_n = Z_R[u_{R_n}] \tag{6.21}$$

2. Similarly, by considering the center part of the circuit:

$$V_{C_{w_n}} = p_n = Z_R[u_{R_n}] \tag{6.22}$$

where $V_{C_{w_n}}$ is the voltage across the compliance. Defining $\frac{dq_{w_n}}{dt} = u_{w_n}$, the capacitance's law writes:

$$V_{C_{w_n}} C_w = q_{w_n} \tag{6.23}$$

which gives the following relation when substitued in Eq. (6.22):

$$q_{w_n} = C_w Z_R[u_{R_n}] \tag{6.24}$$

that also writes:

$$u_{w_n} = C_w \frac{dZ_R}{dt}[u_{R_n}] \tag{6.25}$$

3. Similarly, by considering the left part of the circuit:

$$Z_R[u_{R_{n-1}}] - V_{L_{w_n}} - Z_R[u_{R_n}] = 0 \tag{6.26}$$

where $V_{L_{w_n}}$ is the voltage across the inductance. By developing the voltage:

$$\frac{d^2 q_n}{dt^2} = \frac{du_n}{dt} = \frac{1}{L_w}(Z_R[u_{R_{n-1}}] - Z_R[u_{R_n}]) \tag{6.27}$$

Equation 6.20 can be derived with respect to time, and expressed as a function of displacements:

$$2\frac{d^2 q_n}{dt^2} - \frac{d^2 q_{n+1}}{dt^2} - \frac{d^2 q_{n-1}}{dt^2} = \frac{d^2 q_{w_n}}{dt^2} - \frac{d^2 q_{w_{n-1}}}{dt^2} + \frac{d^2 q_{R_n}}{dt^2} - \frac{d^2 q_{R_{n-1}}}{dt^2} \tag{6.28}$$

By substituting Eqs. (6.24) and (6.27) in Eq. (6.28), it yields:

$$\frac{1}{L_w}\left(3Z_R[u_{R_{n-1}}] - 3Z_R[u_{R_n}] + Z_R[u_{R_{n+1}}] - Z_R[u_{R_{n-2}}]\right) = C_w \frac{d^2}{dt^2}\left(Z_R[u_{R_n}] - Z_R[u_{R_{n-1}}]\right) + \frac{d^2}{dt^2}(q_{R_n} - q_{R_{n-1}}) \tag{6.29}$$

Equation (6.29) can be treated using the continuum limit ($n \to \infty$ and the size between two cells $\Delta z \to 0$) by considering that for a given function $f \in C^3$ function of a variable z:

$$3f(z) - 3f(z-\Delta z) + f(z-2\Delta z) - f(z+\Delta z) \approx -\Delta z^3 f^{(3)}(z) \tag{6.30a}$$

$$f(z) - f(z-\Delta z) \approx \Delta z f'(z) \tag{6.30b}$$

The continuum approximation makes $q_{R_n}(t) \to q_R(t,z)$ where $z = n\Delta z$:

$$\frac{\Delta z^3}{L_w}\frac{\partial^3 Z_R}{\partial z^3}[u_R] = C_w \Delta z \frac{\partial^3 Z_R}{\partial t^2 \partial z}[u_R] + \Delta z \frac{\partial^3 q_R}{\partial t^2 \partial z} \tag{6.31}$$

which can be reduced to the following equation after integrating with respect to z:

$$\frac{\Delta z^2}{L_w}\frac{\partial^2 Z_R}{\partial z^2}[u_R] = C_w\frac{\partial^2 Z_R}{\partial t^2}[u_R] + \frac{\partial^2 q_R}{\partial t^2} + C_1 \tag{6.32}$$

where C_1 is the constant from the integration. We aim at studying localized responses (solitons), which gives $C_1 = 0$ when $z \to \infty$. By developing Z_R as being an inductance L_R, and two capacitances: a linear one of capacitance C_{R_0} and a nonlinear one of capacitance $C_R(q_R) = C_{R_0}C_{R_{NL}}(q_R)$, it yields the following expression for Z_R:

$$Z_R[u_R] = Z_R\left[\frac{\partial q_R}{\partial t}\right] = L_R\frac{\partial^2 q_R}{\partial t^2} + \frac{q_R}{C_{R_0}} + \frac{q_R}{C_R(q_R)}, \tag{6.33}$$

and by defining the sound velocity c_0 and natural linear pulsation ω_0 of the resonator such as:

$$c_0^2 = \frac{\Delta z^2}{C_w L_w}, \tag{6.34a}$$

$$\omega_0^2 = \frac{1}{C_{R_0}L_R}, \tag{6.34b}$$

and by substituting in Eq. (6.32), it yields:

$$\frac{\partial^4 q_R}{\partial t^4} + \frac{\partial^2 q_R}{\partial t^2}\left(\omega_0^2 + \frac{1}{C_w L_R}\right) + \omega_0^2\frac{\partial^2}{\partial t^2}\left(\frac{q_R}{C_{R_{NL}}(q_R)}\right) - c_0^2\frac{\partial^4 q_R}{\partial t^2 \partial z^2} - c_0^2\omega_0^2\left(\frac{\partial^2 q_R}{\partial z^2} + \frac{\partial^2}{\partial z^2}\left(\frac{q_R}{C_{R_{NL}}(q_R)}\right)\right) = 0 \tag{6.35}$$

This equation shows dispersive behavior from the order 4 derivatives, and a nonlinear propagation from the wave equation of nonlinear contributions. The model is expressed in dimensionless form by the following change of variables (inspired from [2]):

$$\tau = \tilde{\omega}_0 t \tag{6.36a}$$

$$\zeta = \frac{\tilde{\omega}_0}{c_0\sqrt{\alpha}}z \tag{6.36b}$$

$$\frac{q_R}{q_{R_0}} = \sqrt{\varepsilon}Q_R \tag{6.36c}$$

where $\alpha = \dfrac{1}{1 + \dfrac{C_{R0}}{C_w}}$, $q_{R_0} = \sqrt{\beta_{NL}}$ with β_{NL} being the coefficient of the nonlinearity (hidden in $C_{R_{NL}}$). Moreover, ε is defined as a small parameter: $0 < \varepsilon << 1$. The parameter $\tilde{\omega}_0$ is a characteristic spectral width set by initial conditions [2]. From Eq. (6.35), it yields:

$$\Omega^2\left(\alpha\frac{\partial^4 Q_R}{\partial\tau^4} - \frac{\partial^4 Q_R}{\partial\tau^2\partial\zeta^2}\right) + \left(\alpha\frac{\partial^2}{\partial\tau^2}\left(\frac{Q_R}{C_{R_{NL}}(q_{R_0}\sqrt{\varepsilon}Q_R)}\right) - \frac{\partial^2}{\partial\zeta^2}\left(\frac{Q_R}{C_{R_{NL}}(q_{R_0}\sqrt{\varepsilon}Q_R)}\right)\right) + \frac{\partial^2 Q_R}{\partial\tau^2} - \frac{\partial^2 Q_R}{\partial\zeta^2} = 0 \tag{6.37}$$

where $\Omega = \dfrac{\tilde{\omega}_0}{\omega_0}$. For example, by choosing the nonlinear ER is to be a Duffing oscillator $C_{R_{NL}}(q_R) = 1/(\beta_{NL}q_R^2)$, it gives the following equation:

$$\Omega^2\left(\alpha\frac{\partial^4 Q_R}{\partial\tau^4} - \frac{\partial^4 Q_R}{\partial\tau^2\partial\zeta^2}\right) + \varepsilon\left(\alpha\frac{\partial^2}{\partial\tau^2}\left(Q_R^3\right) - \frac{\partial^2}{\partial\zeta^2}\left(Q_R^3\right)\right) + \frac{\partial^2 Q_R}{\partial\tau^2} - \frac{\partial^2 Q_R}{\partial\zeta^2} = 0 \tag{6.38}$$

The linear limit of these equations enable to grasp the dispersive behavior of the metamaterial, and to compare to FE and experimental results to validate the model.

6.7.2 Search for localized solitons

To search for the existence of localized solitons, let us set the variable $\xi = \zeta - c\tau$, where c is the dimensionless group velocity of waves, Eq. (6.37) can be reduced to the following:

$$\Omega^2 \frac{d^4 Q_R}{d\xi^4}(\alpha c^4 - c^2) + (\alpha c^2 - 1)\frac{d^2}{d\xi^2}\left(\frac{Q_R}{C_{R_{NL}}(q_{R_0}\sqrt{\varepsilon}Q_R)}\right) + (c^2 - 1)\frac{d^2 Q_R}{d\xi^2} = 0 \tag{6.39}$$

Assuming boundary conditions such that $Q_R \to 0$ as $\xi \to \pm\infty$, and integrating 2 times, multiplying by $\frac{dQ_R}{d\xi}$, and integrating again with respect to ξ yields:

$$\frac{1}{2}\left(\frac{dQ_R}{d\xi}\right)^2 + \frac{1}{2}Q_R^2 \frac{c^2 - 1}{\Omega^2 c^2(\alpha c^2 - 1)} + \frac{1}{\Omega^2 c^2}\int \frac{dQ_R}{dt}\frac{Q_R}{C_{R_{NL}}(q_{R_0}\sqrt{\varepsilon}Q_R)}d\xi = 0 \tag{6.40}$$

Equation (6.40) can be seen as a particle in motion under the potential V_{eff}:

$$V_{eff}(Q_R) = \frac{1}{2}Q_R^2 \frac{c^2 - 1}{\Omega^2 c^2(\alpha c^2 - 1)} + \frac{1}{\Omega^2 c^2}\int \frac{dQ_R}{dt}\frac{Q_R}{C_{R_{NL}}(q_{R_0}\sqrt{\varepsilon}Q_R)}d\xi \tag{6.41}$$

In case of a Duffing oscillator, the potential is reduced to:

$$V_{eff,1}(Q_R) = \frac{1}{2}Q_R^2 \frac{c^2 - 1}{\Omega^2 c^2(\alpha c^2 - 1)} + \varepsilon \frac{1}{\Omega^2 c^2}\frac{1}{4}Q_R^4 \tag{6.42}$$

It should be noted that this form of potential does not enable the creation of localized solitons, as no motion is allowed for a particle starting at the origin (see Fig. 6.19a). However, the nature of the loudspeakers and of the developed liners enable to program targeted behaviors. As a result, these calculations are essential to the design of the nonlinear metamaterial. For example, targeting a softening behavior would necessitate $\beta_{NL} > 0$. Setting that $\beta_{NL} \to -\beta_{NL}$ with $\beta_{NL} > 0$, it gives the following potential $V_{eff,2}$:

$$V_{eff,2}(Q_R) = \frac{1}{2}Q_R^2 \frac{c^2 - 1}{\Omega^2 c^2(\alpha c^2 - 1)} - \varepsilon \frac{1}{\Omega^2 c^2}\frac{1}{4}Q_R^4 \tag{6.43}$$

However, observe in Fig. 6.19b that this behavior does not enable the creation of localized solitons either. The opposite potential enables the creation of localized solitons. As a result, choosing a negative linear capacitance and a positive nonlinear cubic restoring force: $C_{R_0} < 0$ and $\beta_{NL} < 0$ (as $C_R(q_R) = C_{R_0}C_{R_{NL}}(q_R)$), it yields the following potential:

$$V_{eff,3}(Q_R) = -\frac{1}{2}Q_R^2 \frac{c^2 - 1}{\Omega^2(\alpha c^4 - c^2)} + \varepsilon \frac{1}{\Omega^2 c^2}\frac{1}{4}Q_R^4 \tag{6.44}$$

This potential is plotted in Fig. 6.19c and clearly shows that localized solitons can arise from this potential. Future works will benefit from the study of the effective potential to design the nonlinear liners. The propagation of the soliton would be realized on the boundary domain, therefore creating so-called edge solitons.

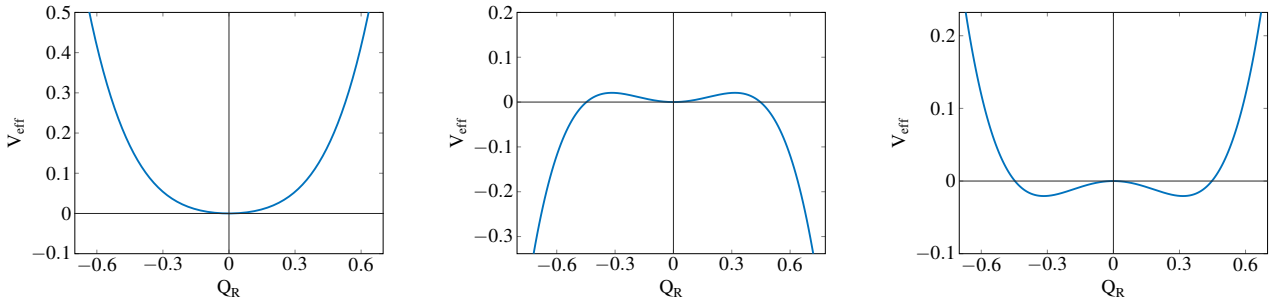

(a) $V_{eff,1}$ (b) $V_{eff,2}$ (c) $V_{eff,3}$

Fig. 6.19 Effective potentials V_{eff} for different restoring forces of the resonator.

6.8 Conclusion of the chapter

This chapter develops a nonlinear metasurface in the form of an acoustic liner of nonlinear resonators at low excitation amplitudes. Analytical and numerical tools are developed to support the experimental investigation of such challenging materials. The main contributions are:

- The experimental development of a nonlinear metasurface at low excitation amplitudes,
- The demonstration of the enlargement of the frequency bandwidth of efficiency of the nonlinear liner against the linear one.
- The analytical study of eventual solitons in such nonlinear liners.

This chapter is a preliminary step towards nonlinear metamaterials at low amplitudes and the study of their behaviors. Many perspectives can be seen, but the main ones deriving from this work are the following:

- The optimization of the liners' parameters for maximizing Transmission Loss.
- The investigation of other nonlinear behaviors to target lower frequencies (via softening nonlinear restoring forces for example).
- The investigation of a strongly coupled nonlinear liner to an acoustic mode of a tube, which should lead to extreme nonlinear phenomena.
- The study of nonlinear behaviors that can arise in these conditions. Phenomena such as chaotic passbands and quasi-periodic behaviors could improve the performance of nonlinear liners as well as improving our understanding of nonlinear metamaterials and physical phenomena (such as the cochlea's behavior [124]).
- The development of metamaterials in which solitons can travel would permit to manage energy localization for noise mitigation and eventual energy harvesting.

Finally, this chapter paves the way for future investigations about acoustic nonlinear liners, which are promising for noise mitigation if optimized.

Chapter 7

Conclusion and Perspectives

This last section aims at summarizing the main advances presented in the dissertation, and to sum up the perspectives of the present work.

Results

Chapter 2 is a detail literature review of the evolution of the field of active noise control, from the start of noise cancellation to the modern electroacoustic absorber. Innovative techniques, laws and transducers are discussed with the presentation of their benefits and downsides, and the position of the dissertation in the literature is clarified. Moreover, nonlinear dynamics are introduced and a brief overview of nonlinear shunts for piezoelectric materials is realized.

Chapter 3 presents the developed method for enforcing nonlinear behaviors in actuators in their linear regime. The mathematical formalization of the control strategy is highlighted and conditions for enforcing the desired behaviors are derived. The application of the control strategy for an electroacoustic resonator is conducted, and convergence is demonstrated. Numerical simulations are achieved to investigate the implementation of the control strategy, and numerical proof of the realization of nonlinear behavior is showed. Finally, the enforcement of a nonlinear electroacoustic resonator using the control strategy is conducted in a open-field environment, experimentally validating the control strategy by the achievement of the desired nonlinear behavior at low excitation amplitudes. Classical nonlinear behavior are highlighted.

Chapter 4 considers the coupling of the developed nonlinear electroacoustic resonator to an acoustic mode of a tube, an experiment is created and its model is validated. The analytical (Method of Multiple Scales) and numerical investigations of the model are achieved and compared against experimental results for various different nonlinear restoring forces at low excitation amplitudes. Results show that the control strategy enforces precisely the desired behavior. In addition, experimental results proved that the nonlinear electroacoustic resonator is able to absorb energy with better performances than an optimized linear Tuned Mass Damper.

Previous Chapters highlighted the dependence of the performances of nonlinear resonators to initial conditions. Chapter 5 extended the control strategy to enable the choice of the equilibrium points regardless of initial conditions. The mathematical formalization of the control strategy is updated, and numerical investigations validated its extension. Experimental validations are conducted with both the open-field and the coupled

experiment of the two previous Chapters.

Finally, Chapter 6 develops a liner of nonlinear electroacoustic resonators at low excitation amplitude. An experimental bench is designed to receive 7 electroacoustic resonators. Experiments are conducted with linear and nonlinear liners, showing the enlargement of the efficiency bandwidth with nonlinear resonators. A finite element model of the experiment is built with a good agreement with the experimental results. However, improvements of the finite element model are needed due to the nonlinear nature of the liner. In addition, an analytical model is built to investigate the study of solitons inside the metamaterials at low excitation amplitudes, showing the needed behaviors from the liners to achieve the creation of such nonlinear phenomena.

Perspectives

This Ph.D. work leaves many research-related perspectives to investigate. Indeed, the perspectives can be sorted by main themes being the improvement of the control strategy and its extension, the investigation of more complex and promising behaviors of the individual electroacoustic resonator, and of the nonlinear liners of electroacoustic resonators.

Perspectives for the control strategy

The main perspectives of the control strategy are the following:

- Proving the asymptotic convergence of the control strategy in the general case (here only proven in the case of the electroacoustic resonator).
- The application of the control strategy to other goals and transducers, such as the artificial creation of nonlinear sensors at low excitation amplitudes for adaptive sensibilities. Moreover, the application of such control strategy to the plasmacoustic transducers from [140], or to piezoelectric materials would open interesting behaviors to investigate.
- The adaptation of the control strategy to enable the realization of linear actuators from nonlinear ones.
- The augmentation of the control strategy to delete the remaining resonance of the loudspeaker, that is difficult to completely suppress.
- The improvement of the extension of the control strategy to target higher energy equilibrium points regardless of initial conditions. A method for targeting 1 specific equilibrium point when more than 2 stable ones co-exist would lead to the full controllability of the electroacoustic resonator. Moreover, the determination of a critical parameter a that ensures that the additional external force leads inevitably to the targeted equilibrium point is needed to make the method operational. An online adaptive law with a stopping criterion could be imagined also.

Perspectives for the behaviors

Natural perspectives about the investigation of particular behaviors have emerged from the creation of digitally programmable nonlinear resonators. The main ones are the following:

- The investigation of nonlinear damping for noise mitigation. Nonlinear damping has recently became the focus of numerous studies in mechanics for vibration mitigation, and its study for noise mitigation and in nonlinear metamaterials would enable the improvements of the liners.

- The optimization of the liners' parameters for maximizing Transmission Loss and absorption. Possible introduction of spacings between resonators and acoustic foams to stabilize and absorb the energy scattered at higher frequencies by the nonlinear liner could develop an extremely efficient liner for noise mitigation.
- The investigation of other nonlinear behaviors to target lower frequencies (via softening nonlinear restoring forces for example).
- The study of strongly coupled nonlinear resonators to an acoustic mode, with an individual resonator or full liners, which would lead to nonlinear phenomena useful for improving our understanding and for possible acoustic control.
- The study of non-local, nonlinear behaviors in liners and the research of nonlinear-based phenomena in acoustic liners such as chaotic bands and quasi-periodic behaviors could significantly improve the performances of nonlinear liners. Moreover, the understanding of nonlinear metamaterials could be improved by the study of these liners. In addition, the understanding of physical phenomena could be improved (such as the cochlea's behavior [124]) by the investigation of such liners.
- The development of metamaterials in which solitons can travel would enable energy localization for acoustic dissipation, noise mitigation or energy harvesting.

References

[1] Abeloos, G., Müller, F., Ferhatoglu, E., Scheel, M., Collette, C., Kerschen, G., Brake, M., Tiso, P., Renson, L., and Krack, M. (2022). A consistency analysis of phase-locked-loop testing and control-based continuation for a geometrically nonlinear frictional system. *Mechanical Systems and Signal Processing*, 170:108820.

[2] Achilleos, V., Richoux, O., Theocharis, G., and Frantzeskakis, D. J. (2015). Acoustic solitons in waveguides with Helmholtz resonators: Transmission line approach. *Physical Review E*, 91(2):023204.

[3] Alamo Vargas, V., Gourdon, E., and Ture Savadkoohi, A. (2018). Nonlinear softening and hardening behavior in Helmholtz resonators for nonlinear regimes. *Nonlinear Dynamics*, 91(1):217–231.

[4] Alfahmi, O. and Erturk, A. (2024). Programmable hardening and softening cubic inductive shunts for piezoelectric structures: Harmonic balance analysis and experiments. *Journal of Sound and Vibration*, 571:118029.

[5] Alfahmi, O., Sugino, C., and Erturk, A. (2022). Duffing-type digitally programmable nonlinear synthetic inductance for piezoelectric structures. *Smart Materials and Structures*, 31(9):095044.

[6] Allard, J. and Atalla, N. (2009). *Propagation of Sound in Porous Media: Modelling Sound Absorbing Materials*.

[7] Asami, T. and Nishihara, O. (2003). Closed-form exact solution to h optimization of dynamic vibration absorbers (application to different transfer functions and damping systems). *Journal of Vibration and Acoustics*, 125:398–405.

[8] Awrejcewicz, J. and Lamarque, C.-H. (2003). *Bifurcation and Chaos in Nonsmooth Mechanical Systems*, volume 45. WORLD SCIENTIFIC.

[9] Babisch, W. (2008). Road traffic noise and cardiovascular risk. *Noise and Health*, 10:27.

[10] Bai, L., Yao, H., Han, C., Jing, X., Chen, L.-Q., Vakakis, A. F., and Yang, T. (2025). Recent advances in nonlinear vibration metamaterials. *Mechanical Systems and Signal Processing*, 236:113046.

[11] Banks, S. and Dinges, D. F. (2007). Behavioral and physiological consequences of sleep restriction. *Journal of Clinical Sleep Medicine*, 03:519–528.

[12] Bardos, C., Lebeau, G., and Rauch, J. (1987). Contrôle et stabilisation pour l'équation des ondes. *Journées Equations aux dérivées partielles*, pages 1–15.

[13] Bastien, J., Bernardin, F., Lamarque, C.-H., and Noël, C. (2013). *Nonsmooth Deterministic or Stochastic Discrete Dynamical Systems*. Wiley.

[14] Beck, B. S., Schiller, N. H., and Jones, M. G. (2015). Impedance assessment of a dual-resonance acoustic liner. *Applied Acoustics*, 93:15–22.

[15] Bellet, R. (2010). *Vers une nouvelle technique de contrôle passif du bruit : absorbeur dynamique non linéaire et pompage énergétique*. PhD thesis, Université de Provence, Aix-Marseille.

[16] Bellet, R., Cochelin, B., Herzog, P., and Mattei, P. O. (2010). Experimental study of targeted energy transfer from an acoustic system to a nonlinear membrane absorber. *Journal of Sound and Vibration*, 329(14):2768–2791.

[17] Beranek, L. L. and Mellow, T. J. (2012). *Acoustics: Sound Fields and Transducers*. Academic Press.

[18] Billon, K., Bono, E. D., Perez, M., Salze, E., Matten, G., Gillet, M., Ouisse, M., Volery, M., Lissek, H., Mardjono, J., and Collet, M. (2022). In flow acoustic characterisation of a 2D active liner with local and non local strategies. *Applied Acoustics*, 191:108655.

[19] Bitar, D., Gourdon, E., Lamarque, C. H., and Collet, M. (2019). Shunt loudspeaker using nonlinear energy sink. *Journal of Sound and Vibration*, 456:254–271.

[20] Bitar, D., Ture Savadkoohi, A., Lamarque, C.-H., Gourdon, E., and Collet, M. (2018). Targeted nonlinear energy transfer for electroacoustic absorbers. In *IUTAM Symposium on Exploiting Nonlinear Dynamics for Engineering Systems*, pages 71–80.

[21] Bitar, D., Ture Savadkoohi, A., Lamarque, C. H., Gourdon, E., and Collet, M. (2020). Extended complexification method to study nonlinear passive control. *Nonlinear Dynamics*, 99(2):1433–1450.

[22] Blevins, R. D. (1979). *Formulas for natural frequency and mode shape*. Van Nostrand Reinhold Ltd.

[23] Bodén, H. (2012). One-sided multi-port techniques for characterisation of in-duct samples with nonlinear acoustic properties. *Journal of Sound and Vibration*, 331:3050–3067.

[24] Bodén, H. (2013). Two-sided multi-port techniques for characterisation of in-duct samples with non-linear acoustic properties. *Acta Acustica united with Acustica*, 99:359–378.

[25] Bongard, F., Lissek, H., and Mosig, J. R. (2010). Acoustic transmission line metamaterial with negative/zero/positive refractive index. *Physical Review B*, 82:094306.

[26] Bono, E. D., Collet, M., and Ouisse, M. (2024). The advection boundary law in absence of mean flow: Passivity, nonreciprocity and enhanced noise transmission attenuation. *Journal of Sound and Vibration*, 590:118603.

[27] Bono, E. D., Collet, M., Ouisse, M., Salze, E., Volery, M., Lissek, H., and Mardjono, J. (2025a). The advection boundary law in presence of mean flow and plane wave excitation: Passivity, nonreciprocity and enhanced noise transmission attenuation. *Journal of Sound and Vibration*, 618:119293.

[28] Bono, E. D., Salze, E., Collet, M., Gillet, M., Ouisse, M., Volery, M., Lissek, H., and Mardjono, J. (2025b). Experimental assessment of a programmable electroacoustic liner in a representative turbofan facility. *Applied Acoustics*, 240:110896.

[29] Boulandet, R., Lissek, H., Karkar, S., Collet, M., Matten, G., Ouisse, M., and Versaevel, M. (2018). Duct modes damping through an adjustable electroacoustic liner under grazing incidence. *Journal of Sound and Vibration*, 426:19–33.

[30] Boulandet, R., Rivet, E., and Lissek, H. (2016). Sensorless electroacoustic absorbers through synthesized impedance control for damping low-frequency modes in cavities. *Acta Acustica united with Acustica*, 102:696–704.

[31] Brillouin, L. (1946). *Wave Propagation in Periodic Structures: Electric Filters and Crystal Lattices*. Dover Publications, Inc.

[32] Bukhari, M. A., Barry, O. R., and Vakakis, A. F. (2023). Breather propagation and arrest in a strongly nonlinear locally resonant lattice. *Mechanical Systems and Signal Processing*, 183:109623.

[33] Champoux, Y. and Allard, J.-F. (1991). Dynamic tortuosity and bulk modulus in air-saturated porous media. *Journal of Applied Physics*, 70:1975–1979.

[34] Coanda, H. (1931). Procédé de protection contre les bruits. FR Patent 722 274.

[35] Cochelin, B., Herzog, P., and Mattei, P. O. (2006). Experimental evidence of energy pumping in acoustics. *Comptes Rendus Mécanique*, 334(11):639–644.

[36] Collet, M., David, P., and Berthillier, M. (2009). Active acoustical impedance using distributed electrodynamical transducers. *The Journal of the Acoustical Society of America*, 125(2):882–894.

[37] Cremer, L. (1953). Theory regarding the attenuation of sound transmitted by air in a rectangular duct with an absorbing wall, and the maximum attenuation constant produced during this process. (in german). *Acustica*, pages 249–263.

[38] da Silveira Zanin, C., Ture Savadkoohi, A., Baguet, S., Dufour, R., and Hurel, G. (2022). Nonlinear vibratory energy exchanges in a meta-cell. *International Journal of Non-Linear Mechanics*, 146:104148.

[39] David, P., Collet, M., and Cote, J. M. (2010). Experimental implementation of acoustic impedance control by a 2D network of distributed smart cells. *Smart Materials and Structures*, 19(3).

[40] de Bedout, J., Franchek, M., Bernhard, R., and Mongeau, L. (1997). Adaptive-passive noise control with self-tuning helmholtz resonators. *Journal of Sound and Vibration*, 202(1):109–123.

[41] De Bono, E. (2021). *Electro-active boundary control for noise mitigation: Local and Advective strategies*. PhD thesis, Ecole Centrale Lyon, Ecully.

[42] De Bono, E., Collet, M., Matten, G., Karkar, S., Lissek, H., Ouisse, M., Billon, K., Laurence, T., and Volery, M. (2022). Effect of time delay on the impedance control of a pressure-based, current-driven Electroacoustic Absorber. *Journal of Sound and Vibration*, 537:117201.

[43] De Bono, E., Morell, M., Collet, M., Gourdon, E., Ture Savadkoohi, A., Ouisse, M., and Lamarque, C. (2024). Model-inversion control to enforce tunable duffing-like acoustical response on an electroacoustic resonator at low excitation levels. *Journal of Sound and Vibration*, 570:118070.

[44] Dekemele, K., Giraud-Audine, C., and Thomas, O. (2024). A piezoelectric nonlinear energy sink shunt for vibration damping. *Mechanical Systems and Signal Processing*, 220:111615.

[45] Delany, M. E. and Bazley, E. N. (1970). Acoustical properties of fibrous absorbent materials. *Applied Acoustics*, 3(2):105–116.

[46] Demiquel, A., Achilleos, V., Theocharis, G., and Tournat, V. (2024). Envelope vector solitons in nonlinear flexible mechanical metamaterials. *Wave Motion*, 131:103394.

[47] Den Hartog, J. (1934). *Mechanical Vibrations*. McGraw-Hill, New York.

[48] Deng, B., Wang, P., He, Q., Tournat, V., and Bertoldi, K. (2018). Metamaterials with amplitude gaps for elastic solitons. *Nature Communications*, 9:3410.

[49] Detroux, T., Habib, G., Masset, L., and Kerschen, G. (2015). Performance, robustness and sensitivity analysis of the nonlinear tuned vibration absorber. *Mechanical Systems and Signal Processing*, 60:799–809.

[50] Duran, H., Cuevas-Maraver, J., Kevrekidis, P. G., and Vainchtein, A. (2023). Discrete breathers in a mechanical metamaterial. *Physical Review E*, 107:014220.

[51] Elliott, S. J., Tehrani, M. G., and Langley, R. S. (2015). Nonlinear damping and quasi-linear modelling. *Philosophical Transactions of the Royal Society A: Mathematical, Physical and Engineering Sciences*, 373:20140402.

[52] Ewins, D. J. (2000). *Modal Testing: Theory, Practice and Application*. John Wiley & Sons, Ltd.

[53] Fang, N., Xi, D., Xu, J., Ambati, M., Srituravanich, W., Sun, C., and Zhang, X. (2006). Ultrasonic metamaterials with negative modulus. *Nature Materials*, 5:452–456.

[54] Fang, X., Wen, J., Bonello, B., Yin, J., and Yu, D. (2017). Ultra-low and ultra-broad-band nonlinear acoustic metamaterials. *Nature Communications*, 8:1288.

[55] Fayolle, H., Giraud-Audine, C., and Thomas, O. (2025). Optimisation and performance comparison of direct and parametric piezoelectric energy harvester with geometrical nonlinearities. *Journal of Sound and Vibration*, page 119343.

[56] Field, C. and Fricke, F. (1998). Theory and applications of quarter-wave resonators: A prelude to their use for attenuating noise entering buildings through ventilation openings. *Applied Acoustics*, 53:117–132.

[57] Fleming, A., Moheimani, S., and Behrens, S. (2005). Synthesis and implementation of sensor-less active shunt controllers for electromagnetically actuated systems. *IEEE Transactions on Control Systems Technology*, 13:246–261.

[58] Fleming, A. J., Niederberger, D., Moheimani, S. O. R., and Morari, M. (2007). Control of resonant acoustic sound fields by electrical shunting of a loudspeaker. *IEEE Transactions on Control Systems Technology*, 15:689–703.

[59] Frahm, H. (1911). Device for damping vibrations of bodies.

[60] Furstoss, M., Thenail, D., and Galland, M. A. (1997). Surface impedance control for sound absorption: Direct and hybrid passive/ active strategies. *Journal of Sound and Vibration*, 203(2):219–236.

[61] Galland, M.-A., Mazeaud, B., and Sellen, N. (2005). Hybrid passive/active absorbers for flow ducts. *Applied Acoustics*, 66(6):691–708.

[62] Gatti, G., Brennan, M., and Tang, B. (2019). Some diverse examples of exploiting the beneficial effects of geometric stiffness nonlinearity. *Mechanical Systems and Signal Processing*, 125:4–20.

[63] Gatti, G. and Tehrani, M. G. (2019). Some features of geometric nonlinear damping on isolation performance. *Journal of Physics: Conference Series*, 1264:012060.

[64] Gendelman, O. (2012). Analytic treatment of a system with a vibro-impact nonlinear energy sink. *Journal of Sound and Vibration*, 331(21):4599–4608.

[65] Gendelman, O., Manevitch, L. I., Vakakis, A. F., and M'closkey, R. (2001). Energy pumping in nonlinear mechanical oscillators: Part Idynamics of the underlying hamiltonian systems. *Journal of Applied Mechanics, Transactions ASME*, 68(1):34–41.

[66] Gendelman, O. V. (2008). Targeted energy transfer in systems with non-polynomial nonlinearity. *Journal of Sound and Vibration*, 315(3):732–745.

[67] Georgiadis, F., Vakakis, A. F., Mcfarland, D. M., and Bergman, L. (2005). Shock isolation through passive energy pumping caused by nonsmooth nonlinearities. *International Journal of Bifurcation and Chaos*, 15(06):1989–2001.

[68] Glé, P., Gourdon, E., and Arnaud, L. (2011). Acoustical properties of materials made of vegetable particles with several scales of porosity. *Applied Acoustics*, 72:249–259.

[69] Goodwin, G. C., Graebe, S. F., and Salgado, M. E. (2000). *Control System Design*, volume 27. Prentice Hall, New Jersey.

[70] Gourc, E., Mattei, P.-O., Côte, R., and Capaldo, M. (2025). Increasing dynamic range of ness by using geometric nonlinear damping.

[71] Gourc, E., Michon, G., Seguy, S., and Berlioz, A. (2015). Targeted Energy Transfer Under Harmonic Forcing With a Vibro-Impact Nonlinear Energy Sink: Analytical and Experimental Developments. *Journal of Vibration and Acoustics*, 137(3).

[72] Gourdon, E., Alexander, N., Taylor, C., Lamarque, C., and Pernot, S. (2007). Nonlinear energy pumping under transient forcing with strongly nonlinear coupling: Theoretical and experimental results. *Journal of Sound and Vibration*, 300(3-5):522–551.

[73] Gourdon, E. and Seppi, M. (2010). On the use of porous inclusions to improve the acoustical response of porous materials: Analytical model and experimental verification. *Applied Acoustics*, 71:283–298.

[74] Gourdon, E., Ture Savadkoohi, A., and Alamo Vargas, V. (2018). Targeted energy transfer from one acoustical mode to an helmholtz resonator with nonlinear behavior. *Journal of Vibration and Acoustics*, 140(6).

[75] Guicking, D. (2009). Patents on Active Control of Sound and Vibration-an Overview. Technical report, Universitat Gottingen.

[76] Guicking, D. and Karcher, K. (1984). Active impedance control for one-dimensional sound. *Journal of Vibration and Acoustics*, 106(3):393–396.

[77] Guicking, D. and Lorenz, E. (1984). An active sound absorber with porous plate. *Journal of Vibration and Acoustics*, 106(3):389–392.

[78] Guo, X., Lissek, H., and Fleury, R. (2020). Improving Sound Absorption Through Nonlinear Active Electroacoustic Resonators. *Physical Review Applied*, 13(1).

[79] Habib, G., Detroux, T., Viguié, R., and Kerschen, G. (2015). Nonlinear generalization of den hartogs equal-peak method. *Mechanical Systems and Signal Processing*, 52-53:17–28.

[80] Hermiller, J. and Maddux, M. (2013). Morphing resonators for adaptive noise reduction. US Patent 8915329 B1.

[81] Hu, B., Fang, X., Cheng, L., Wen, J., and Yu, D. (2023). Attenuation of impact waves in a nonlinear acoustic metamaterial beam. *Nonlinear Dynamics*, 111:15801–15816.

[82] Hurel, G., Ture Savadkoohi, A., and Lamarque, C. H. (2019). Passive control of a two degrees-of-freedom pendulum by a non-smooth absorber. *Nonlinear Dynamics*, 98(4):3025–3036.

[83] Hurel, G., Ture Savadkoohi, A., and Lamarque, C. H. (2021). Design of a nonlinear absorber for a 2 degrees of freedom pendulum and experimental validation. *Structural Control and Health Monitoring*, 28(11).

[84] Hussein, M. I., Leamy, M. J., and Ruzzene, M. (2014). Dynamics of phononic materials and structures: Historical origins, recent progress, and future outlook. *Applied Mechanics Reviews*, 66.

[85] Ioannou Sougleridis, I., Richoux, O., Achilleos, V., Theocharis, G., Desjouy, C., and Frantzeskakis, D. (2023). Acoustic solitons in a periodic waveguide: Theory and experiments. *Journal of Sound and Vibration*, 546:117433.

[86] Johnson, D. L., Koplik, J., and Dashen, R. (1987). Theory of dynamic permeability and tortuosity in fluid-saturated porous media. *Journal of Fluid Mechanics*, 176:379–402.

[87] Karkar, S., De Bono, E., Collet, M., Matten, G., Ouisse, M., and Rivet, E. (2019). Broadband Nonreciprocal Acoustic Propagation Using Programmable Boundary Conditions: From Analytical Modeling to Experimental Implementation. *Physical Review Applied*, 12(5).

[88] Kerschen, G., McFarland, D. M., Kowtko, J. J., Lee, Y. S., Bergman, L. A., and Vakakis, A. F. (2007). Experimental demonstration of transient resonance capture in a system of two coupled oscillators with essential stiffness nonlinearity. *Journal of Sound and Vibration*, 299(4-5):822–838.

[89] Kovacic, I. and Brennan, M. J. M. J. (2011). *The Duffing equation : nonlinear oscillators and their phenomena*. John Wiley & Sons, Ltd.

[90] Kuznetsov, Y. A. (2023). *Elements of Applied Bifurcation Theory*, volume 112. Springer International Publishing.

[91] Labetoulle, A., Missoum, S., Gourdon, E., and Ture Savadkoohi, A. (2024). Stochastic optimization of targeted energy transfer with time-dependent cubic nonlinearity. *Communications in Nonlinear Science and Numerical Simulation*, 139:108314.

[92] Labetoulle, A., Ture Savadkoohi, A., and Gourdon, E. (2022). Detection of different dynamics of two coupled oscillators including a time-dependent cubic nonlinearity. *Acta Mechanica*, 233(1):259–290.

[93] Lagarrigue, C., Groby, J. P., Tournat, V., Dazel, O., and Umnova, O. (2013). Absorption of sound by porous layers with embedded periodic arrays of resonant inclusions. *The Journal of the Acoustical Society of America*, 134:4670–4680.

[94] Lamarque, C.-H., Gendelman, O. V., Ture Savadkoohi, A., and Etcheverria, E. (2011). Targeted energy transfer in mechanical systems by means of non-smooth nonlinear energy sink. *Acta Mechanica*, 221(1-2):175–200.

[95] Lee, C.-L., Chen, Y.-T., Chung, L.-L., and Wang, Y.-P. (2006). Optimal design theories and applications of tuned mass dampers. *Engineering Structures*, 28:43–53.

[96] Lee, Y. S., Kerschen, G., McFarland, D. M., Hill, W. J., Nichkawde, C., Strganac, T. W., Bergman, L. A., and Vakakis, A. F. (2007a). Suppressing aeroelastic instability using broadband passive targeted energy transfers, part 2: Experiments. *AIAA Journal*, 45:2391–2400.

[97] Lee, Y. S., Vakakis, A. F., Bergman, L. A., McFarland, D. M., and Kerschen, G. (2007b). Suppression aeroelastic instability using broadband passive targeted energy transfers, part 1: Theory. *AIAA Journal*, 45:693–711.

[98] Leroux, M., Langlois, S., and Savadkoohi, A. T. (2023). Investigation of nonlinear control of galloping with a linear beam with elastic boundary conditions. *International Journal of Non-Linear Mechanics*, 156:104484.

[99] Li, J. and Chan, C. T. (2004). Double-negative acoustic metamaterial. *Physical Review E*, 70:055602.

[100] Lissek, H., Boulandet, R., and Fleury, R. (2011). Electroacoustic absorbers: Bridging the gap between shunt loudspeakers and active sound absorption. *The Journal of the Acoustical Society of America*, 129(5):2968–2978.

[101] Liu, Z., Zhang, X., Mao, Y., Zhu, Y. Y., Yang, Z., Chan, C. T., and Sheng, P. (2000). Locally resonant sonic materials. *Science*, 289:1734–1736.

[102] Long, M. (2014). *Architectural Acoustics (Second Edition)*. Academic Press, Boston, second edition edition.

[103] Lueg, P. (1934). Process of silencing sound oscillations. US Patent 2043416.

[104] Malher, A., Touzé, C., Doaré, O., Habib, G., and Kerschen, G. (2017). Flutter control of a two-degrees-of-freedom airfoil using a nonlinear tuned vibration absorber. *Journal of Computational and Nonlinear Dynamics*, 12.

[105] Malléjac, M., Volery, M., Lissek, H., and Fleury, R. (2025). Active control of electroacoustic resonators in the audible regime: control strategies and airborne applications. *npj Acoustics*, 1:4.

[106] Manevitch, L., Gourdon, E., and Lamarque, C. (2007). Parameters optimization for energy pumping in strongly nonhomogeneous 2 dof system. *Chaos, Solitons & Fractals*, 31(4):900–911.

[107] Manevitch, L. I. (2001). The description of localized normal modes in a chain of nonlinear coupled oscillators using complex variables. *Nonlinear Dynamics*, 25(1-3):95–109.

[108] Matsuhisa, H., Ren, B., and Sato, S. (1992). Semiactive control of duct noise by a volume-variable resonator. *Jsme International Journal Series III-Vibration Control Engineering Engineering for Industry*, 35(2):223–228.

[109] McFarland, D. M., Bergman, L. A., and Vakakis, A. F. (2005). Experimental study of non-linear energy pumping occurring at a single fast frequency. *International Journal of Non-Linear Mechanics*, 40:891–899.

[110] Miljkovic, D. (2016). Active noise control: From analog to digital - Last 80 years. *2016 39th International Convention on Information and Communication Technology, Electronics and Microelectronics. MIPRO 2016 - Proceedings*, pages 1151–1156.

[111] Morandi, F., Miniaci, M., Marzani, A., Barbaresi, L., and Garai, M. (2016). Standardised acoustic characterisation of sonic crystals noise barriers: Sound insulation and reflection properties. *Applied Acoustics*, 114:294–306.

[112] Morell, M., Collet, M., Gourdon, E., Savadkoohi, A. T., and De Bono, E. (2025a). Experimental validation of the analytical modelling of a digitally created duffing acoustic nonlinear oscillator at low amplitudes. *Mechanics & Industry*, 26:2.

[113] Morell, M., Gourdon, E., Collet, M., Savadkoohi, A. T., and De Bono, E. (2023). Nonlinear digitally created electroacoustic absorber designed for acoustic energy pumping. *Proceedings of Forum Acusticum*, pages 4807–4810.

[114] Morell, M., Gourdon, E., Collet, M., Ture Savadkoohi, A., De Bono, E., and Lamarque, C.-H. (2024). Towards digitally programmed nonlinear electroacoustic resonators for low amplitude sound pressure levels: Modeling and experiments. *Journal of Sound and Vibration*, 584:118437.

[115] Morell, M., Labetoulle, A., Gourdon, E., Bono, E. D., Collet, M., and Savadkoohi, A. T. (2025b). On the programming of cubic acoustic resonator with periodic time-dependent coefficient. *Communications in Nonlinear Science and Numerical Simulation*, 150:108972.

[116] Morse, P. (1939). Some Aspects of the Theory of Room Acoustics. *The Journal of the Acoustical Society of America*, 11:56–66.

[117] Nagaya, K., Hano, Y., and Suda, A. (2001). Silencer consisting of two-stage helmholtz resonator with auto-tuning control. *The Journal of the Acoustical Society of America*, 110:289–295.

[118] Nayfeh, A. H. and Mook, D. T. (1995). *Nonlinear Oscillations*. John Wiley & Sons, Ltd.

[119] Nucera, F., Lo Iacono, F., McFarland, D., Bergman, L., and Vakakis, A. (2008). Application of broadband nonlinear targeted energy transfers for seismic mitigation of a shear frame: Experimental results. *Journal of Sound and Vibration*, 313(1-2):57–76.

[120] Nucera, F., McFarland, D., Bergman, L., and Vakakis, A. (2010). Application of broadband nonlinear targeted energy transfers for seismic mitigation of a shear frame: Computational results. *Journal of Sound and Vibration*, 329(15):2973–2994.

[121] Olson, H. F. (1961). Electronic sound absorber. US Patent 2983790.

[122] Olson, H. F. and May, E. G. (1953). Electronic Sound Absorber. *The Journal of the Acoustical Society of America*, 25(6):1130–1136.

[123] Orduña-Bustamante, F. and Nelson, P. A. (1992). An adaptive controller for the active absorption of sound. *The Journal of the Acoustical Society of America*, 91:2740–2747.

[124] Padlewski, M. (2025). *Active Acoustic Metamaterials: A New Way to Understand Nonlinear and Topological Phenomena*. PhD thesis, EPFL, Lausanne.

[125] Padlewski, M., Volery, M., Fleury, R., Lissek, H., and Guo, X. (2023). Active acoustic su-schrieffer-heeger-like metamaterial. *Physical Review Applied*, 20:014022.

[126] Pease, R. A. (2008). A Comprehensive Study of the Howland Current Pump A Comprehensive Study of the Howland Current Pump Applications for the Howland Current Pump AN-1515. *Most*, 29:12.

[127] Piégay, C., Glé, P., Gourdon, E., Gourlay, E., and Marceau, S. (2018). Acoustical model of vegetal wools including two types of fibers. *Applied Acoustics*, 129:36–46.

[128] Popa, B.-I. and Cummer, S. A. (2014). Non-reciprocal and highly nonlinear active acoustic metamaterials. *Nature Communications*, 5:3398.

[129] Pérez, J. G., Ghadami, A., Sanches, L., Michon, G., and Epureanu, B. I. (2022). Data-driven optimization for flutter suppression by using an aeroelastic nonlinear energy sink. *Journal of Fluids and Structures*, 114:103715.

[130] Rayleigh, J. (1877). *The Theory of Sound*. Macmillan and Co.

[131] Raze, G., Abeloos, G., and Kerschen, G. (2025). Experimental continuation in nonlinear dynamics: recent advances and future challenges. *Nonlinear Dynamics*, 113:4949–4997.

[132] Raze, G., Jadoul, A., Guichaux, S., Broun, V., and Kerschen, G. (2020). A digital nonlinear piezoelectric tuned vibration absorber. *Smart Materials and Structures*, 29:015007.

[133] Rivet, E. (2016). *Room Modal Equalisation with Electroacoustic Absorbers*. PhD thesis, EPFL, Lausanne.

[134] Rivet, E., Karkar, S., and Lissek, H. (2017a). Broadband Low-Frequency Electroacoustic Absorbers Through Hybrid Sensor-/Shunt-Based Impedance Control. *IEEE Transactions on Control Systems Technology*, 25(1):63–72.

[135] Rivet, E., Karkar, S., and Lissek, H. (2017b). On the optimisation of multi-degree-of-freedom acoustic impedances of low-frequency electroacoustic absorbers for room modal equalisation. *Acta Acustica united with Acustica*, 103(6):1025–1036.

[136] Roberson, R. E. (1952). Synthesis of a nonlinear dynamic vibration absorber. *Journal of the Franklin Institute*, 254(3):205–220.

[137] Rossing, T. D., editor (2014). *Springer Handbook of Acoustics*. Springer New York.

[138] Sakagami, K., Matsutani, K., and Morimoto, M. (2010). Sound absorption of a double-leaf micro-perforated panel with an air-back cavity and a rigid-back wall: Detailed analysis with a helmholtzkirchhoff integral formulation. *Applied Acoustics*, 71:411–417.

[139] Sakagami, K., Nakamori, T., Morimoto, M., and Yairi, M. (2009). Double-leaf microperforated panel space absorbers: A revised theory and detailed analysis. *Applied Acoustics*, 70:703–709.

[140] Sergeev, S., Fleury, R., and Lissek, H. (2023). Ultrabroadband sound control with deep-subwavelength plasmacoustic metalayers. *Nature Communications*, 14(1):2874.

[141] Shami, Z. A., Giraud-Audine, C., and Thomas, O. (2022a). A nonlinear piezoelectric shunt absorber with 2:1 internal resonance: experimental proof of concept. *Smart Materials and Structures*, 31:035006.

[142] Shami, Z. A., Giraud-Audine, C., and Thomas, O. (2022b). A nonlinear piezoelectric shunt absorber with a 2:1 internal resonance: Theory. *Mechanical Systems and Signal Processing*, 170:108768.

[143] Shami, Z. A., Giraud-Audine, C., and Thomas, O. (2023). Saturation correction for a piezoelectric shunt absorber based on 2:1 internal resonance using a cubic nonlinearity. *Smart Materials and Structures*, 32:055024.

[144] Sieber, J. and Krauskopf, B. (2008). Control based bifurcation analysis for experiments. *Nonlinear Dynamics*, 51:365–377.

[145] Simeone, L. (2017). *Nonlinear damping in energy harvesters*. PhD thesis, University of Southampton, Southampton.

[146] Soltani, P., Kerschen, G., Tondreau, G., and Deraemaeker, A. (2017). Tuning of a piezoelectric vibration absorber attached to a damped structure. *Journal of Intelligent Material Systems and Structures*, 28:1115–1129.

[147] Standard, A. (2009). E2611-09 : Standard Test Method for Measurement of Normal Incidence Sound Transmission of Acoustical Materials Based on the Transfer Matrix Method. *ASTM International*.

[148] Stansfeld, S., Berglund, B., Clark, C., Lopez-Barrio, I., Fischer, P., Öhrström, E., Haines, M., Head, J., Hygge, S., van Kamp, I., and Berry, B. (2005). Aircraft and road traffic noise and children's cognition and health: a cross-national study. *The Lancet*, 365:1942–1949.

[149] Tang, S., Ng, C., and Lam, E. (2012). Experimental investigation of the sound absorption performance of compartmented helmholtz resonators. *Applied Acoustics*, 73:969–976.

[150] Tehrani, M. G. and Gattulli, V. (2016). Vibration control using nonlinear damped coupling. *Journal of Physics: Conference Series*, 744:012132.

[151] Tester, B. J. (1973a). Ray models for sound propagation and attenuation in ducts, in the absence of mean flow. *Journal of Sound and Vibration*, 27(4):515–531.

[152] Tester, B. J. (1973b). The optimization of modal sound attenuation in ducts, in the absence of mean flow. *Journal of Sound and Vibration*, 27(4):477–513.

[153] Thenail, D., Lacour, O., Galland, M. A., and Furstoss, M. (1997). The Active Control of Wall Impedance. *Acta Acust.*, 83:1039–1044.

[154] Ture Savadkoohi, A., Lamarque, C. H., Weiss, M., Vaurigaud, B., and Charlemagne, S. (2016). Analysis of the 1:1 resonant energy exchanges between coupled oscillators with rheologies. *Nonlinear Dynamics*, 86(4):2145–2159.

[155] Ture Savadkoohi, A., Manevitch, L. I., and Lamarque, C.-H. (2011). Analysis of the transient behavior in a two dof nonlinear system. *Chaos, Solitons & Fractals*, 44(6):450–463.

[156] Vakakis, A. F. and Gendelman, O. (2001). Energy pumping in nonlinear mechanical oscillators: Part IIresonance capture. *Journal of Applied Mechanics, Transactions ASME*, 68(1):42–48.

[157] Vakakis, A. F., Gendelman, O. V., Bergman, L. A., McFarland, D. M., Kerschen, G., and Lee, Y. S. (2009). *Nonlinear Targeted Energy Transfer in Mechanical and Structural Systems I & II*. Springer.

[158] Vargas, V. A., Gourdon, E., and Savadkoohi, A. T. (2017). Nonlinear behaviors of an acoustical resonator: theoretical and experimental evidences. *Procedia Engineering*, 199:643–648.

[159] Volery, M., Guo, X., and Lissek, H. (2023). Robust direct acoustic impedance control using two microphones for mixed feedforward-feedback controller. *Acta Acustica*, 7:2.

[160] Volpe, M., Bellizzi, S., and Côte, R. (2021). Polyharmonic distortion approach for nonlinear acoustic load characterization. *Journal of Sound and Vibration*, 514:116426.

[161] Volvert, M. (2024). *Resonant phase lags of nonlinear mechanical systems*. PhD thesis, University of Liège, Liège, Belgium.

[162] Weiss, M., Ture Savadkoohi, A., Gendelman, O., and Lamarque, C. (2014). Dynamical behavior of a mechanical system including Saint-Venant component coupled to a non-linear energy sink. *International Journal of Non-Linear Mechanics*, 63:10–18.

[163] Weiss, M., Vaurigaud, B., Ture Savadkoohi, A., and Lamarque, C.-H. (2018). Control of vertical oscillations of a cable by a piecewise linear absorber. *Journal of Sound and Vibration*, 435:281–300.

[164] World Health Organization (2011). Burden of disease from environmental noise, quantification of healthy life years lost in europe. Technical report.

[165] World Health Organization (2018). Environmental noise guidelines for the european region. Technical report.

[166] Yang, M. and Sheng, P. (2017). Sound absorption structures: From porous media to acoustic metamaterials. *Annual Review of Materials Research*, 47:83–114.

[167] Zeidler, E. (1990). *Nonlinear Functional Analysis and Its Applications*. Springer New York, New York, NY.

[168] Zhang, J., Romero-García, V., Theocharis, G., Richoux, O., Achilleos, V., and Frantzeskakis, D. J. (2017). Bright and gap solitons in membrane-type acoustic metamaterials. *Physical Review E*, 96:022214.

Appendix A

ER's parameters estimation

A.1 The Thiele-Small parameters

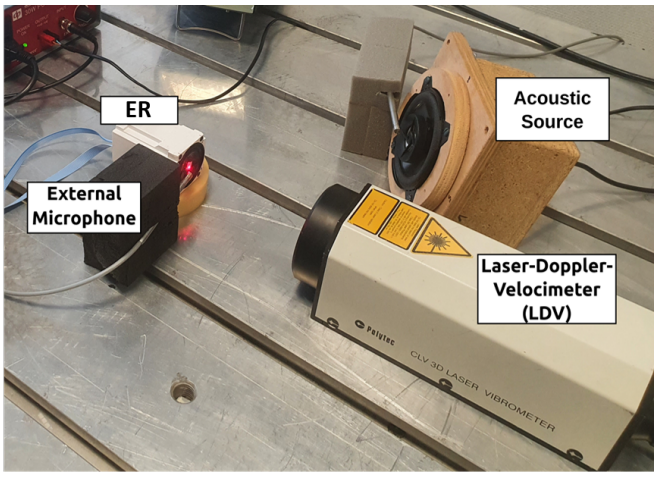

Fig. A.1 Experimental setup

This appendix aims at briefly describing the method of identification of the modal parameters of the first mode of the loudspeaker. The needed assumptions are:

1. Low excitation amplitudes: we consider the loudspeaker in its linear regime.
2. Low frequency amplitudes: we consider that the wavelength is large enough compared to the diameter of the loudspeaker's membrane.
3. The loudspeaker is excited on its first mode: the operating frequencies are situated near its first mode.

The loudspeaker's first mode can be described by equation (A.1):

$$M_0\ddot{x}(t) + R_0\dot{x}(t) + K_0x(t) = p(t)S_d - Bli(t) \tag{A.1}$$

where x denotes the modal coordinate of the ER's membrane, and M_0, R_0, and K_0 correspond to the modal mass, damping and stiffness respectively of the loudspeaker's first mode. The variable S_d is the effective area of the loudspeaker's membrane, and Bl is the force factor of the Lorentz force, where B denotes the magnetic field created by the magnet of the loudspeaker, and l the length of the solenoid. The operator $\dot{\bullet}$ corresponds to the time

derivative. Let us apply a Laplace transform with the Laplace variable $s \in \mathbb{C}$ to Eq. A.1:

$$M_0 s v(s) + R_0 v(s) + K_0 \frac{v(s)}{s} = p(s) S_d - Bli(s) \tag{A.2}$$

where $v = \dot{x}$ stands for the velocity of the membrane of the loudspeaker. When no current is applied into the loudspeaker's coil, the acoustic impedance Z_{a0} of the loudspeaker is:

$$Z_{a0}(s) = \frac{p(s)}{v(s)} = \frac{M_0}{S_d} s + \frac{R_0}{S_d} + \frac{K_0}{S_d} \frac{1}{s} \tag{A.3}$$

To retrieve the acoustic modal parameters M_0/S_d, R_0/S_d and K_0/S_d, the curve-fitting of the experimental transfer function between p and v can be realized. The choice is here to realize an optimization of the root mean square of the difference between the measured and the analytical impedance on the bandwidth $500-600$ Hz. To measure these quantities, a microphone is placed close to the loudspeaker's membrane to retrieve the pressure, and a Laser Doppler Velocimeter (LDV) measures the velocity of the membrane. An acoustic source excites the loudspeaker with a frequency sweep. The experimental setup is presented in Figure A.1. The transfer function is plotted in Figure A.2a.

Once the first measurement is done, the coefficient Bl/S_d is still unknown. To measure this coefficient, an additional measurement with a non-zero electrical current has to be realized. Let us set the current i as being proportional to the measured pressure p:

$$i(s) = -gp(s) \tag{A.4}$$

with g a constant coefficient. It gives the following acoustic impedance:

$$Z_a = \frac{Z_{a0}}{1 + g\dfrac{Bl}{S_d}} \tag{A.5}$$

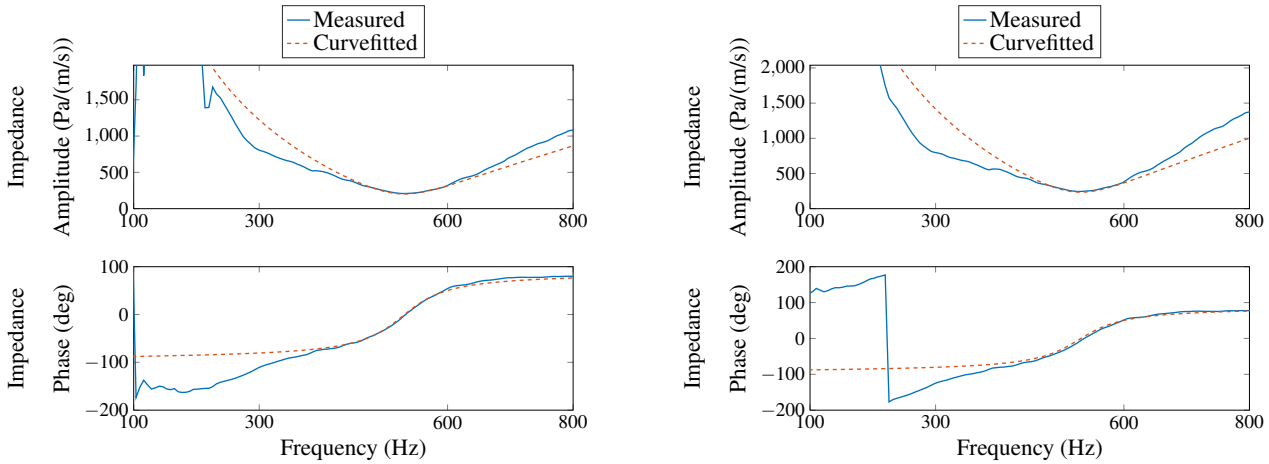

(a) Modulus and phase of the transfer function without electrical current

(b) Modulus and phase of the transfer function with electrical current $i = 0.001p$

Fig. A.2 Experimental setup and results for the estimation of the parameters of the loudspeaker's first mode, for the cell used in Chapters 3, 4 and 5.

The expression of equation (A.5) is then curve-fitted to the transfer function obtained through experimental measurements to obtain Bl/S_d with the same method as for the estimation of the modal parameters. The acoustic

impedance and its curve-fitting are depicted in Figure A.2b with a gain $g = 0.001$. This experiment is repeated 3 times, and the average values are taken as the modal parameters of the loudspeaker.

A.2 The sensitivity of microphones

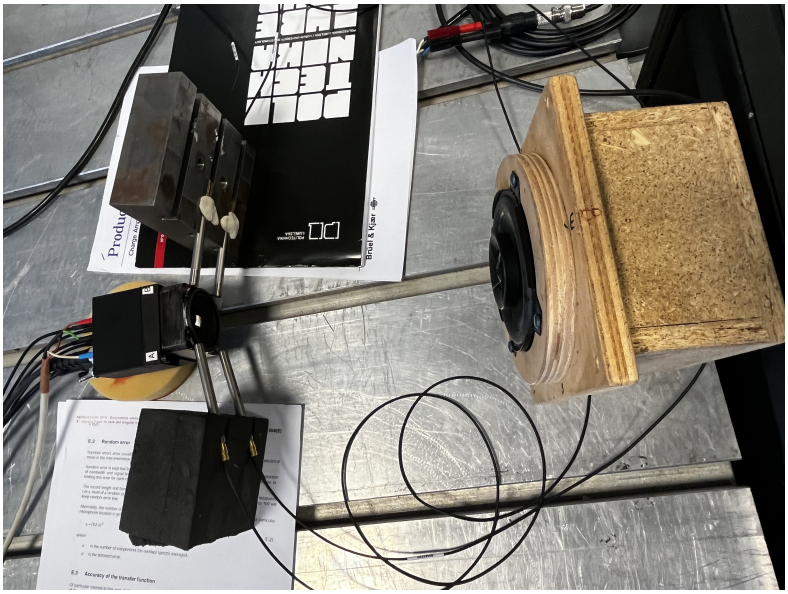

Fig. A.3 Experimental setup for estimating the built-in microphones sensitivity of the cell used in Chapter 6.

The method for determining the sensitivity of built-in microphones are well-known, and are here briefly described. It lies on the use of external microphones which have already known sensitivities (e.g. Bruel&Kjaer© microphones with their calibration system). By placing the reference microphone (the external one) close to the built-in one, both microphones are under the same external load. The comparison of both signals enables to estimate the sensitivity of the built-in microphone using the following relation:

$$S_{\text{built-in}} = \frac{V_{RMS,\text{built-in}}}{V_{RMS,\text{ref}}} S_{\text{ref}} \tag{A.6}$$

where $S_{\text{built-in}}$ and S_{ref} stand for the microphone sensitivities of the built-in and reference microphones respectively, and $V_{RMS,\text{built-in}}$ and $V_{RMS,\text{ref}}$ corresponds to the Root Mean Square (RMS) value of the measured voltage coming from the built-in and reference microphone respectively.

This method is used simultaneously for the 4 built-in microphones used for the control strategy in Chapter 6. The estimation is realized through the measurement of 3 different sound pressures at 4 different frequencies over the frequency range of interest. A frequency chirp is then realized to obtain the sensitivity spectra at one sound pressure.

A.3 Data for the cells used in Chapter 5 (metamaterial)

The experiments for the full estimation of the ERs parameters for Chapter 6 are pictured here. The method for estimating the Thiele-Small parameters is presented previously (Section A.1), and for estimating the microphones' sensitivities also (Section. A.2). Consequently, the figures used for the parameters estimation are displayed here without further presentation. Only one set of experiment (out of 3 for the Thiele-Small parameters for example) are displayed, but the estimated parameters are given for all experiments.

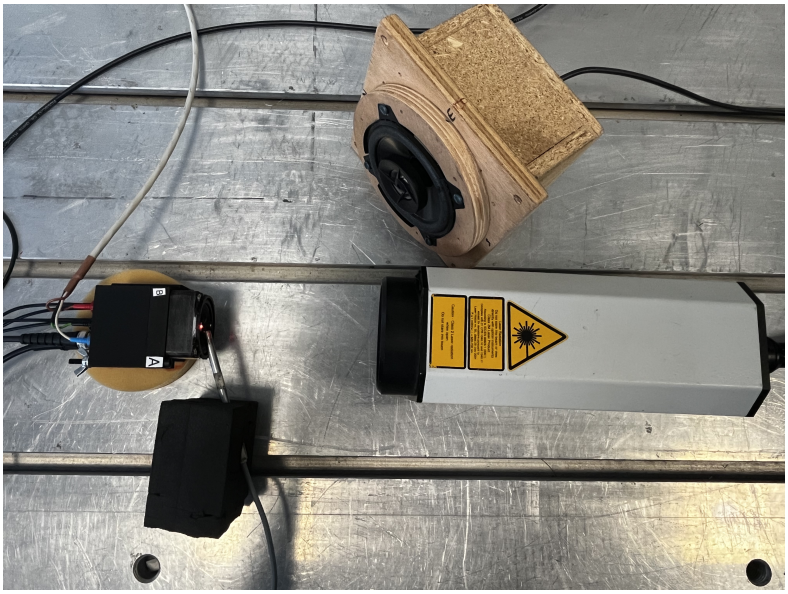

Fig. A.4 Experimental setup for estimating the Thiele-Small parameters of the loudspeaker used in the Chapter 6.

A.3.1 Thiele-Small parameters

The parameters used for the programming of the control are given in Table A.1:

Table A.1 Mean value and standard deviation of the estimated Thiele-Small parameters for each cell.

Cell	M_0/S_d	R_0/S_d	K_0/S_d	Bl/S_d
Cell 1	0.4223 ± 0.0015	279.8 ± 0.29	$6.827 \times 10^6 \pm 3.3 \times 10^4$	125.9 ± 0.24
Cell 2	0.4425 ± 0.0001	308.7 ± 0.3	$7.362 \times 10^6 \pm 1.9 \times 10^3$	150.5 ± 1.4
Cell 3	0.4414 ± 0.00057	257.8 ± 0.58	$6.967 \times 10^6 \pm 1 \times 10^4$	147 ± 0.72
Cell 4	0.4263 ± 0.00022	221.8 ± 0.34	$7.019 \times 10^6 \pm 1.4 \times 10^4$	183.1 ± 0.35
Cell 5	$0.4315 \pm 9.3 \times 10^{-5}$	283.2 ± 0.22	$6.72 \times 10^6 \pm 4.7 \times 10^2$	146.6 ± 0.85
Cell 6	0.4538 ± 0.00019	350.7 ± 0.63	$6.831 \times 10^6 \pm 5 \times 10^2$	188.7 ± 0.15
Cell 7	0.4399 ± 0.00091	274.2 ± 0.15	$6.966 \times 10^6 \pm 9.6 \times 10^3$	140.2 ± 3.4
Unit	$\mathrm{kg\,m^{-2}}$	$\mathrm{kg\,s^{-1}\,m^{-2}}$	$\mathrm{kg\,s^{-2}\,m^{-2}}$	$\mathrm{kg\,m^{-1}\,A^{-1}\,s^{-2}}$

The first set of measurements for estimating the Thiele-Small parameters are presented in Fig. A.5, and the parameters estimated from each set of measurement is given in Table A.2.

Table A.2 Estimation of the Thiele-Small parameters for each measurement

Cell	Measurement	M_0/S_d	R_0/S_d	K_0/S_d	Bl/S_d
Cell 1	A	0.424	280.1	6.866×10^6	125.6
	B	0.4214	279.6	6.807×10^6	126
	C	0.4214	279.8	6.808×10^6	126.1
Cell 2	A	0.4426	309.1	7.364×10^6	149.5
	B	0.4424	308.6	7.36×10^6	149.8
	C	0.4425	308.5	7.363×10^6	152.1
Cell 3	A	0.4408	257.4	6.955×10^6	147.8
	B	0.4418	257.6	6.971×10^6	146.4
	C	0.4418	258.5	6.974×10^6	146.8
Cell 4	A	0.4261	222.2	7.003×10^6	182.9
	B	0.4265	221.7	7.027×10^6	183
	C	0.4263	221.6	7.027×10^6	183.5
Cell 5	A	0.4316	283	6.72×10^6	145.7
	B	0.4314	283.2	6.72×10^6	147.3
	C	0.4314	283.5	6.719×10^6	147
Cell 6	A	0.454	351.3	6.831×10^6	188.6
	B	0.4536	350.7	6.831×10^6	188.8
	C	0.4538	350.1	6.831×10^6	188.8
Cell 7	A	0.441	274.3	6.977×10^6	136.3
	B	0.4395	274	6.962×10^6	142.5
	C	0.4392	274.2	6.959×10^6	141.8
Unit		$\mathrm{kg\,m^{-2}}$	$\mathrm{kg\,s^{-1}\,m^{-2}}$	$\mathrm{kg\,s^{-2}\,m^{-2}}$	$\mathrm{kg\,m^{-1}\,A^{-1}\,s^{-2}}$

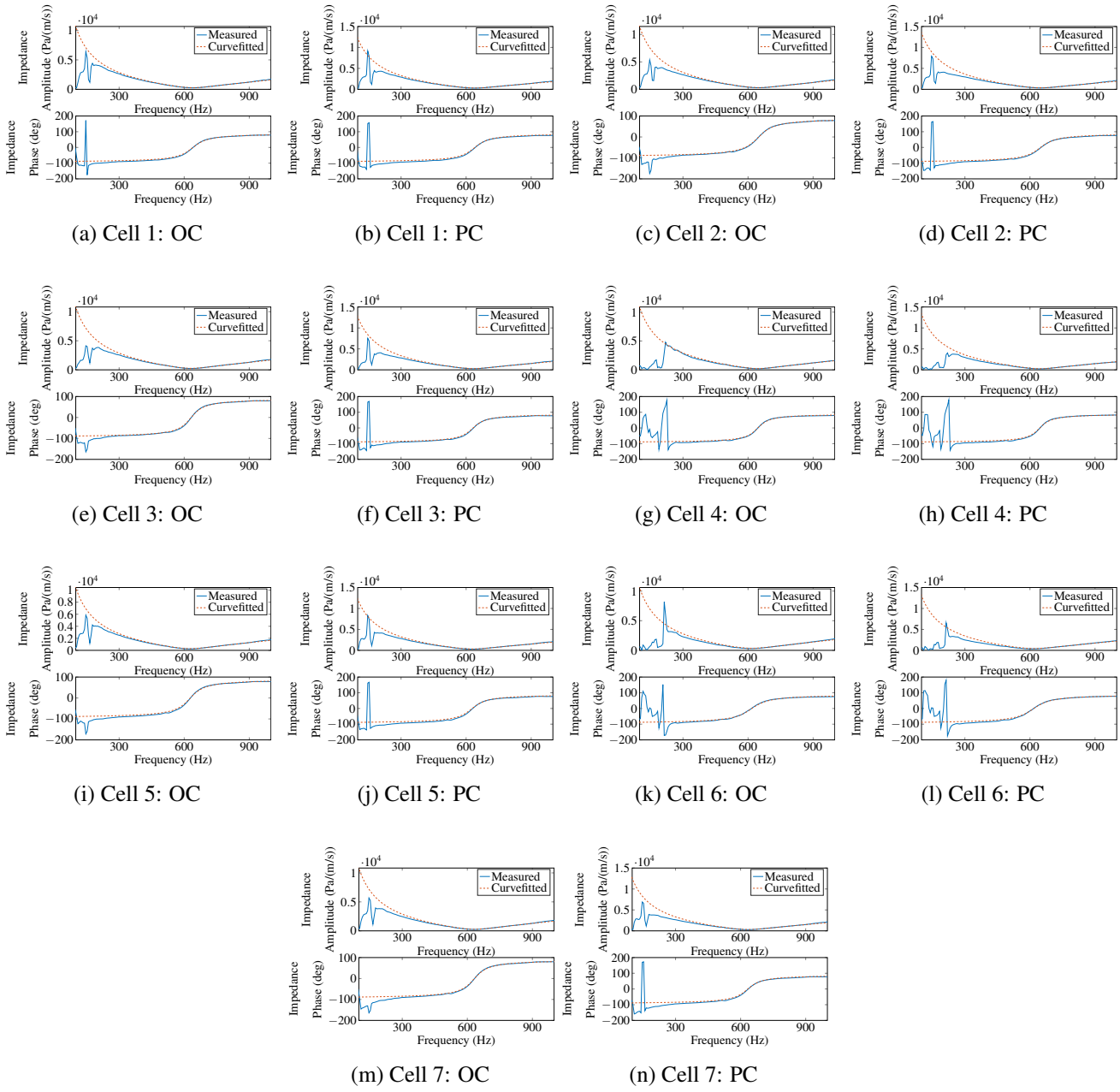

(a) Cell 1: OC (b) Cell 1: PC (c) Cell 2: OC (d) Cell 2: PC

(e) Cell 3: OC (f) Cell 3: PC (g) Cell 4: OC (h) Cell 4: PC

(i) Cell 5: OC (j) Cell 5: PC (k) Cell 6: OC (l) Cell 6: PC

(m) Cell 7: OC (n) Cell 7: PC

Fig. A.5 First set of Open Current (OC) and Proportional Current (PC) measurements for the ERs.

A.3.2 Microphones

The sensitivities obtained by calculating the mean value of the estimated sensitivities at the 4 defined frequencies 400 Hz, 600 Hz, 800 Hz, and 1000 Hz are detailed in Table A.3, with their offset in Table A.4. Measurements of the sensitivity of the microphones for all microphones and ERs are plotted in Fig. A.6. Note that the microphone B from Cell 4 is not working.

Table A.3 Sensitivity parameters of the microphones of the Cells.

	Sensitivity			
Cell	A	B	C	D
Cell1	$6.8261 \times 10^{-3} \pm 1.58 \times 10^{-4}$	$5.8414 \times 10^{-3} \pm 3.73 \times 10^{-5}$	$6.4630 \times 10^{-3} \pm 3.20 \times 10^{-5}$	$7.9707 \times 10^{-3} \pm 1.05 \times 10^{-4}$
Cell2	$4.6091 \times 10^{-3} \pm 4.71 \times 10^{-5}$	$5.2198 \times 10^{-3} \pm 7.08 \times 10^{-5}$	$3.8086 \times 10^{-3} \pm 3.34 \times 10^{-5}$	$5.5993 \times 10^{-3} \pm 5.74 \times 10^{-5}$
Cell3	$6.7821 \times 10^{-3} \pm 8.81 \times 10^{-5}$	$6.9088 \times 10^{-3} \pm 9.52 \times 10^{-5}$	$6.2375 \times 10^{-3} \pm 4.22 \times 10^{-5}$	$6.3159 \times 10^{-3} \pm 9.23 \times 10^{-5}$
Cell4	$5.0406 \times 10^{-3} \pm 9.17 \times 10^{-5}$	$4.3376 \times 10^{-3} \pm 1.43 \times 10^{-3}$	$6.3276 \times 10^{-3} \pm 1.14 \times 10^{-4}$	$6.4611 \times 10^{-3} \pm 1.23 \times 10^{-4}$
Cell5	$4.1419 \times 10^{-3} \pm 4.59 \times 10^{-5}$	$4.0566 \times 10^{-3} \pm 5.12 \times 10^{-5}$	$6.6140 \times 10^{-3} \pm 3.87 \times 10^{-5}$	$5.9721 \times 10^{-3} \pm 8.33 \times 10^{-5}$
Cell6	$8.1871 \times 10^{-3} \pm 6.97 \times 10^{-4}$	$6.4184 \times 10^{-3} \pm 3.71 \times 10^{-4}$	$6.0341 \times 10^{-3} \pm 5.63 \times 10^{-4}$	$5.6050 \times 10^{-3} \pm 4.91 \times 10^{-4}$
Cell8	$3.1586 \times 10^{-3} \pm 1.28 \times 10^{-5}$	$4.6898 \times 10^{-3} \pm 3.67 \times 10^{-5}$	$5.9542 \times 10^{-3} \pm 3.50 \times 10^{-5}$	$6.3005 \times 10^{-3} \pm 9.27 \times 10^{-5}$

Table A.4 Offset parameters of the microphones of the Cells.

	Offset			
Cell	A	B	C	D
Cell1	3.8173×10^{-3}	5.1113×10^{-3}	4.5648×10^{-3}	5.2452×10^{-3}
Cell2	3.1549×10^{-3}	4.4134×10^{-3}	3.8362×10^{-3}	4.5684×10^{-3}
Cell3	3.7217×10^{-3}	4.7450×10^{-3}	4.2331×10^{-3}	4.9652×10^{-3}
Cell5	2.9041×10^{-3}	4.4826×10^{-3}	3.5098×10^{-3}	4.1897×10^{-3}
Cell6	2.6600×10^{-4}	2.3318×10^{-4}	$3.6947e-05$	4.8037×10^{-4}
Cell4	3.8332×10^{-3}	-1.3650×10^{-2}	3.6019×10^{-3}	4.0135×10^{-3}
Cell8	3.7641×10^{-3}	4.9503×10^{-3}	4.4269×10^{-3}	5.0980×10^{-3}

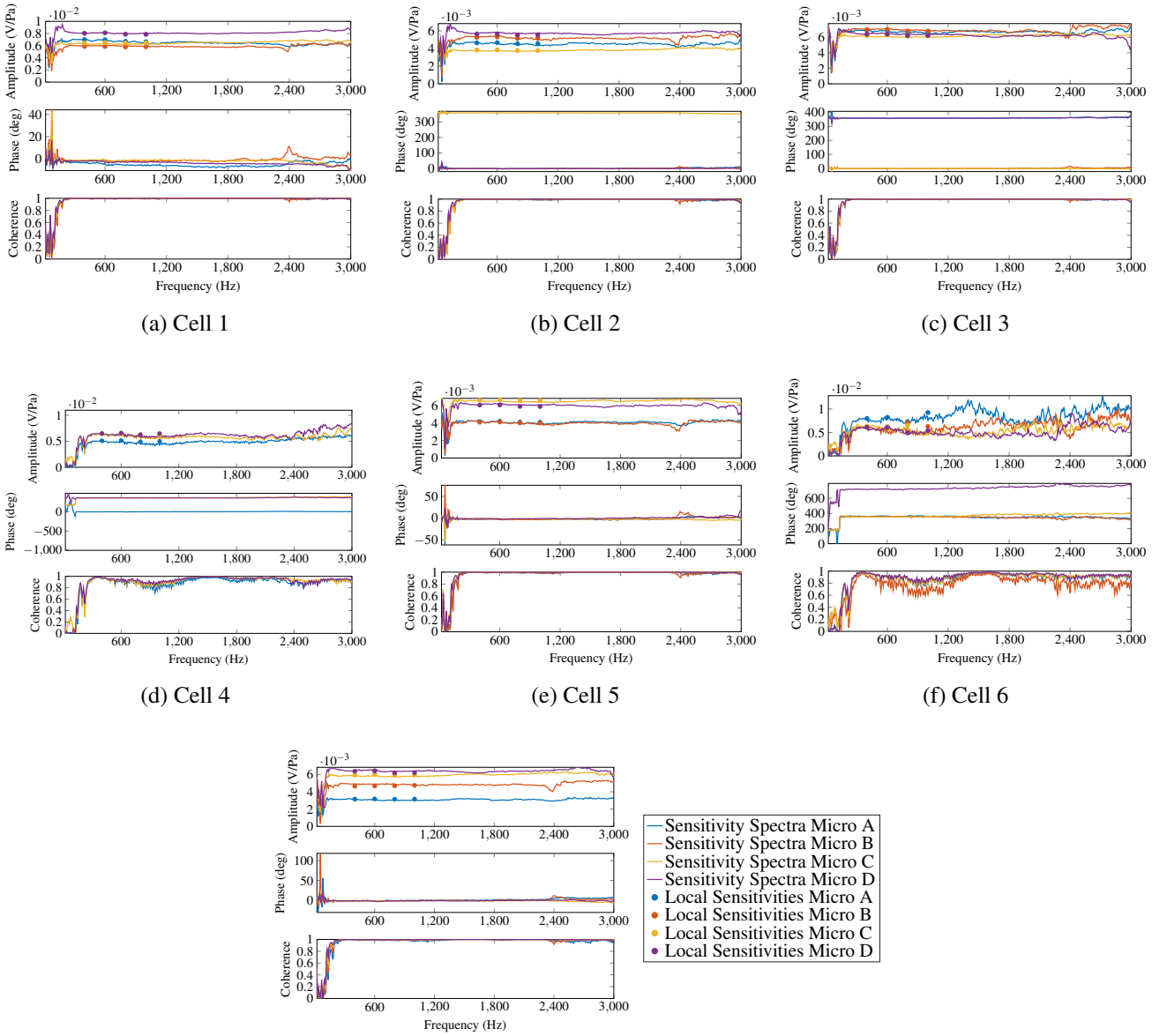

(a) Cell 1 (b) Cell 2 (c) Cell 3

(d) Cell 4 (e) Cell 5 (f) Cell 6

(g) Cell 7

Fig. A.6 Figures of the sensitivity of the 4 microphones for the 7 ERs with respect to the frequency.

Appendix B

Estimation of parameters of the acoustic mode of the tube's cavity

B.1 Method

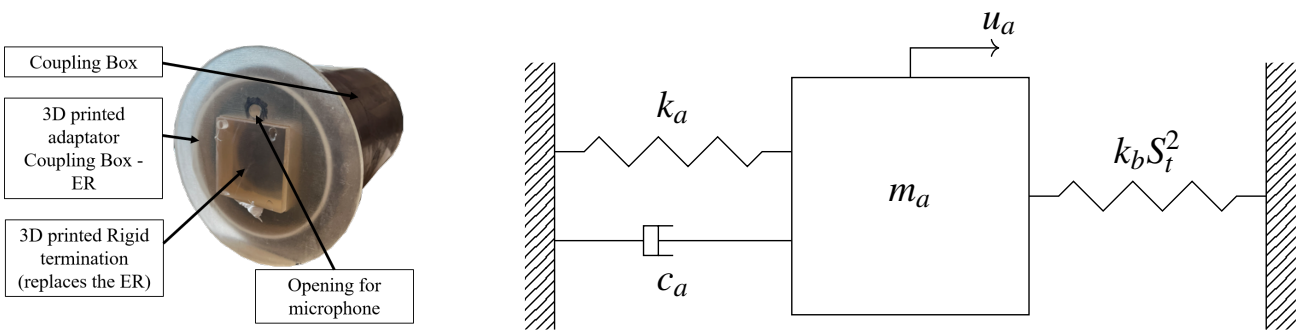

Fig. B.1 Picture (a) and Scheme (b) of the model for the rigid termination set-up.

To obtain the parameters of the tube 's acoustic first mode, we could also proceed with curve-fitting, in stationary or transient regime. However, the retained solution consists in calculating the parameters m_a, k_b and γ based on the model, and deducing the remaining parameters through simple modal analysis. We consider the experimental setup presented in Fig. 4.2, with a rigid termination instead of the ER, and the opening for the microphone closed by the microphone, pictured in Fig. B.1a. In this case, the first mode of the tube is no longer coupled to the ER, and the rigid termination model can be derived:

$$m_a \ddot{u}_a(t) + c_a \dot{u}_a(t) + (k_a + k_b S_t^2) u_a(t) = 0 \tag{B.1}$$

where u_a, m_a, k_a, and c_a denote the modal coordinate, modal mass, modal stiffness and modal damping of the first acoustic mode of the tube respectively. The parameter k_b is obtained through the calculations of Section 4.4 and S_t stands for the area of the reduced section of the tube. The operator $\dot{\bullet}$ corresponds to the time derivative. We denote the equivalent stiffness $K = k_a + k_b S_t^2$. The mechanical representation of the system is illustrated in Fig. B.1b. A frequency sweep excitation signal is sent by the acoustic source on a large frequency bandwidth. The pressure inside the tube is measured by a microphone, and we obtain the relation:

$$p = \varphi(f) \tag{B.2}$$

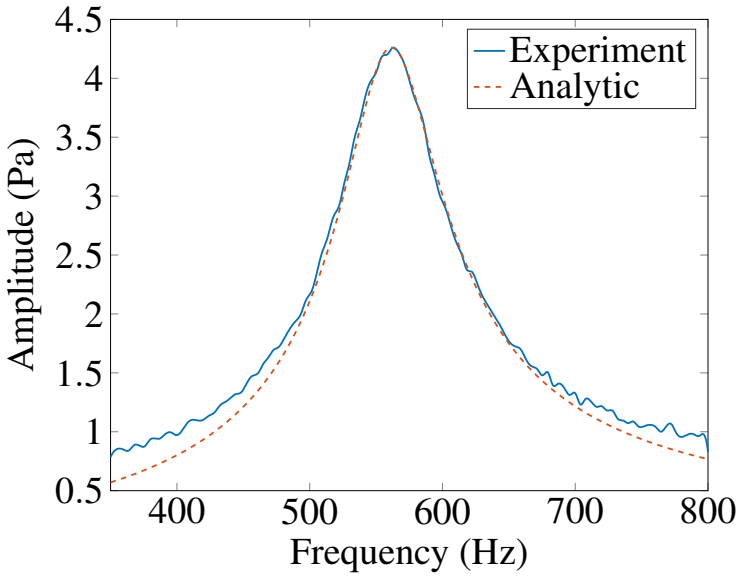

Fig. B.2 Envelop of the pressure inside the tube with a reduced section with a rigid termination.

with φ the function which maps the envelop of the pressure amplitude with respect to the frequency. The frequency of the first mode f_0 is then identified by selecting the frequency with the highest signal amplitude. Then, we find the frequencies f_1 and f_2 (with $f_2 > f_1$) which satisfy the condition:

$$\frac{\varphi(f_0)}{\sqrt{2}} = \varphi(f) \tag{B.3}$$

Let us denote $\Delta_f = f_2 - f_1$. The parameters k_a and c_a can be deduced:

$$\begin{cases} K = (2\pi f_0)^2 m_a \\ k_a = K - k_b S_t^2 \\ c_a = 2\pi \Delta_f m_a \end{cases} \tag{B.4}$$

This process is repeated 5 times, and the average values are retained. The pressure level sent into the tube is then obtained by curve-fitting of an analytical expression of φ onto the measured quantity. The model and the experiment are compared in Figure B.2. The parameters identification and the model are in excellent agreement with the experimental measurements, despite the numerous calculation-based parameters (that are not determined using measurements) such as k_b, or m_a. However, the analytical prediction is not extremely accurate far from resonance. The bandwidth $500 - 700$ Hz is satisfying for further numerical predictions and design.

Another method could be the simple curve-fitting of the model (the solution can be found easily) with the experimental results. However, the curve-fitting is here used as a verification of the determined parameters.

B.2 Influence of the anti-resonance

This section aims at explaining the differences between the model and the experiment. Taking into account the inevitable model uncertainties (in both ER and tube cavity models) of the simplified numerical model, the shift of the experimental bifurcation with respect to the numerical one is understandable. However, the low-frequency

inaccuracy of the numerical results is due to an antiresonance of the tube cavity at lower frequencies than the acoustic mode of the tube, as depicted in Fig B.3. The model does not take into account the antiresonance at 115 Hz, which could impact the coupling with the ER, and consequently, it could contribute to the discrepancy between measurements and simulations. The influence of the antiresonance can not be ignored. Nevertheless, notice that slight pressure variations in the experimental set-up may trigger the bifurcation earlier or later than simulated with numerical means. Moreover, considering both the complexity of the actual system and the simplicity of the numerical model (reduced to one mode), the agreement between measurements and simulations is reasonable.

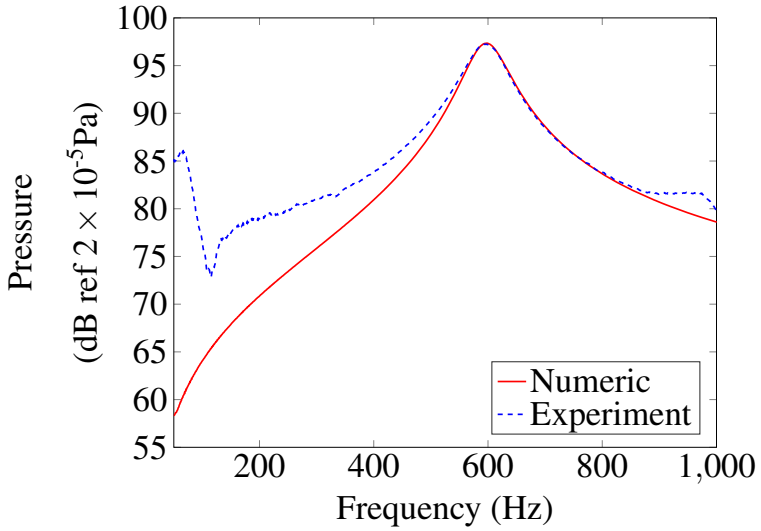

Fig. B.3 Variation of the pressure amplitude inside the reduced-section tube with a rigid termination

B.3 Sensitivity analysis of the damping parameter

The form of the damping parameter of the primary system c_a has been chosen arbitrarily to model multiple physical damping phenomena. As a result, a preliminary study regarding its influence on the results is needed. The damping parameter is obtained using the rigid termination measurement. The determination of its value has been done using three measurements at different excitation amplitudes. The value of the damping parameter is taken as the mean value of the multiple measurement, where the uncertainty is taken as the standard deviation of the estimated damping values:

$$c_a = 0.0386 \pm 1.1 \times 10^{-4} \text{ kg.s}^{-1} \tag{B.5}$$

Let us consider the parameter $c_{a,p}$ such as $c_{a,p} \in [0.8c_a; 1.2c_a]$. Its definition takes into account a variation of 20% of c_a, which is larger than the calculated uncertainty. Let us plot the experimental data along with simulations realized with different values of $c_{a,p}$ in the case of a cubic hardening restoring force with $\mu_K = \mu_M = 1$, $\mu_R = 1/8$ and $\beta_{textNL} = 2 \times 10^{11}$ m^{-2}. The variation of the pressure amplitude inside the reduced-section tube is presented for increasing frequency sweep in Fig. B.4a, and decreasing frequency sweep in Fig. B.4b. One can observe that the bifurcation frequency changes depending on the damping parameter of the acoustic mode of the tube. The lower value of the parameter gives the lower frequency of bifurcation, and the higher value of the parameter gives the higher frequency of bifurcation.

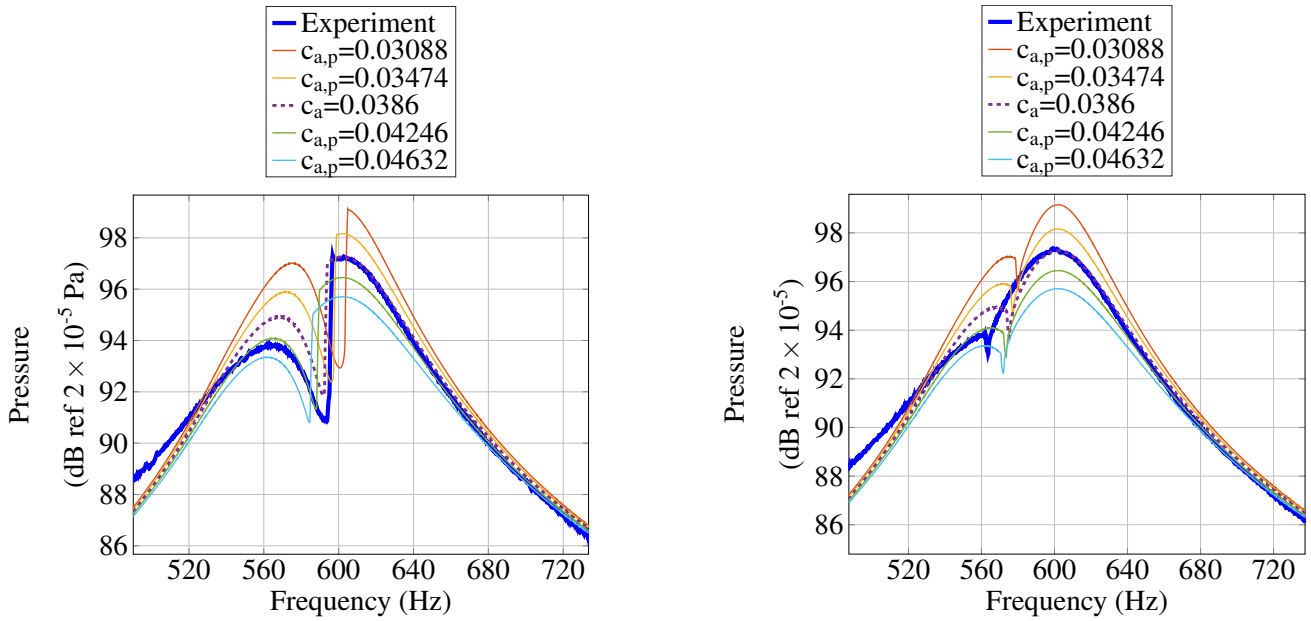

Fig. B.4 Variation of the pressure amplitude inside the reduced-section tube as a function of frequency for multiple values of damping c_a with (a) increasing frequency sweep (b) decreasing frequency sweep.

Moreover, let us plot the quality of the prediction of the simulations with each c_a using the indicator:

$$\text{Indicator} = \sum_i (x^i_{c_a} - y^i)^2 \tag{B.6}$$

where $x^i_{c_a}$ stands for the values of the pressure spectra predicted by simulations for each value of the damping parameter c_a. The variable y^i denotes the values of the pressure spectra from experimental data. One can see in Fig. B.5 that the best value given by this indicator is the measured value $c_a = 0.0386$ kg.s^{-1}.

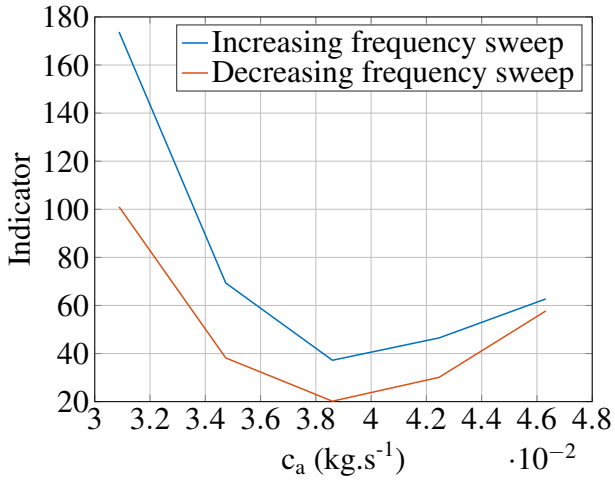

Fig. B.5 Least mean square indicator of the difference of simulations done with multiple values of c_a

Appendix C

Analytical study

C.1 General study

This appendix aims at describing the method used for the analytical studies. The analytical method chosen to study such a system is the Multiple Scale Method (MSM) [118], coupled to the complex variables of Manevitch [107]. This method has been extensively employed for the study of nonlinear dynamical systems [94, 82, 154, 92, 38, 21]. We present the analytical study of the two degree of freedom for a general nonlinear stiffness fonction F_{NL}.

C.1.1 The standard form system

The system under consideration is governed by system of Eqs. (4.23). This is a two-degree of freedom system. Here, a epsilon is set for book-keeping, and its value will be discussed using the estimated and measured parameters of the experiment.
Defining the excitation as $p_{ls}(t) = P\sin(\Omega t)$ with Ω its pulsation, system of equation (4.23) becomes:

$$\begin{cases} m_a\ddot{u}_a(t) + c_a\dot{u}_a(t) + k_a u_a(t) + \dfrac{\gamma}{\alpha}\big(u_a(t) - \alpha x(t)\big) = -S_t P\sin(\Omega t) \\ M_d\ddot{x}(t) + R_d\dot{x}(t) + F_{\mathrm{NL}}(t,x) + \gamma\big(\alpha x(t) - u_a(t)\big) = 0 \end{cases} \tag{C.1}$$

If we set the eigen pulsation of the acoustic first mode of the tube:

$$\omega_0 = \sqrt{\frac{k_a}{m_a}} \tag{C.2}$$

We set that $\bullet' = \dfrac{\mathrm{d}}{\mathrm{d}\tau}$ is a time differential operator regarding to the time $\tau \in \mathbb{R}_+$ defined as:

$$\tau = \omega_0 t = \sqrt{\frac{k_a}{m_a}}t \tag{C.3}$$

To re-scale the variables u_a and x, let us introduce the constant $\chi \in \mathbb{R}$ and the following change of variables:

$$\begin{cases} u_a \to \chi u_a \\ x \to \chi x \end{cases} \tag{C.4}$$

such that:

$$\begin{cases} u_a(t) = O(1) \\ x(t) = O(1) \end{cases} \tag{C.5}$$

It yields the system of equations with the normalized pulsation regarding the primary system (the acoustic mode):

$$\begin{cases} u_a''(\tau) + \dfrac{c_a}{\sqrt{k_a m_a}} u_a'(\tau) + u_a(\tau) + \dfrac{\gamma}{\alpha k_a}\big(u_a(\tau) - \alpha x(\tau)\big) = -\dfrac{S_t P}{k_a \chi} \sin\left(\dfrac{\Omega}{\omega_0}\tau\right) \\ x''(\tau) + \dfrac{R_d}{M_d}\sqrt{\dfrac{m_a}{k_a}} x'(\tau) + \dfrac{m_a}{M_d k_a \chi} F_{\mathrm{NL}}(\tau, \chi x) + \dfrac{\gamma}{\alpha k_a}\dfrac{m_a \alpha}{M_d}\big(\alpha x(\tau) - u_a(\tau)\big) = 0 \end{cases} \tag{C.6}$$

In mechanics, the parameter ε is defined as the ratio between the mass of the nonlinear oscillator and the mass of the primary system. In this case, the mass of the ER is higher than the mass of the air volume. As a result, the parameter $\varepsilon << 1$ is defined here for book-keeping. Let us consider the system rearranged from Eq. (4.23) as in [154]:

$$\begin{cases} u_a'' + \varepsilon \xi_a u_a' + u_a + \varepsilon \gamma_0 (u_a - \alpha x) = -\varepsilon f \sin(\nu \tau) \\ \varepsilon\Big(x'' + \xi_m x' + \zeta \tilde{F}_{\mathrm{NL}}(t, x) + \gamma_0 \mu (\alpha x - u_a)\Big) = 0 \end{cases} \tag{C.7}$$

where $\varepsilon << 1$ and $\tilde{F}_{\mathrm{NL}}$ is the nonlinear restoring force after re-scaling equations. The parameters are defined as:

$$\begin{cases} \dfrac{c_a}{\sqrt{k_a m_a}} = \varepsilon \xi_a \\ \dfrac{\gamma}{\alpha k_a} = \varepsilon \gamma_0 \\ \dfrac{S_t P}{k_a \chi} = \varepsilon f \\ \dfrac{R_t}{M_t}\sqrt{\dfrac{m_a}{k_a}} = \xi_m \\ \dfrac{\gamma}{\alpha k_a}\dfrac{m_a \alpha}{M_t} = \gamma_0 \mu \\ \dfrac{m_a}{M_d k_a \xi} F_{\mathrm{NL}}(\tau, \xi x) = \zeta \tilde{F}_{\mathrm{NL}} \end{cases} \tag{C.8}$$

Where the parameters ξ_a, γ_0, f, ξ_m, K_L, K_{NL} and $\gamma_0 \mu$ should be order $O(1)$. The parameter ν is the normalized pulsation of the excitation pulsation Ω defined as depending on σ the detuning parameter, meaning that the solution is studied around the resonance of the system:

$$\nu = \frac{\Omega}{\omega_0} = 1 + \sigma\varepsilon \tag{C.9}$$

The MSM approach is introduced here by the decomposition of the time τ in new time scales as:

$$T_k = \varepsilon^k \tau \ \in \mathbb{R}_+ \qquad ; \qquad k \in [\![0\ ;\ N]\!] \tag{C.10}$$

Let us introduce the complex variables of Manevitch which are functions of new time scales T_k [107]:

$$\begin{array}{rccc} \varphi_a : & (\mathbb{R}_+)^N & \longrightarrow & \mathbb{C} \\ & (T_0, ..., T_N) & \longmapsto & \varphi_a(T_1, ...T_N) \end{array} \tag{C.11}$$

$$\begin{array}{rccc} \varphi_m : & (\mathbb{R}_+)^N & \longrightarrow & \mathbb{C} \\ & (T_0,...,T_N) & \longmapsto & \varphi_m(T_1,...T_N) \end{array} \tag{C.12}$$

Such that (with $i^2=-1$):

$$\begin{cases} u_a' + i\nu u_a = \varphi_a(T_0,...,T_N)\,\mathrm{e}^{i\nu\tau} \\ x' + i\nu x = \varphi_m(T_0,...,T_N)\,\mathrm{e}^{i\nu\tau} \end{cases} \tag{C.13}$$

The complex variables of Manevitch enable to facilitate the calculations by considering complex variables that contain information about the velocity and the displacement, meaning that no information is lost with the use of these variables. Here, the complex variables of Manevitch are considered without their extension to additional harmonics [21]: only the first harmonic stays. Additionally, a Galerkin procedure is used to reduce the order of the problem to the first harmonic of the solution, assuming that the solution may be decomposed as a Fourier series, *i.e.* a sum of mono-harmonic waves. The considered Galerkin method consists to project the variables on the orthonormal Fourier basis vectors. Let us consider the modified hermitian inner product $<.,.>$ of $L_2(\mathbb{R}_+,\mathbb{C})$ space over a period of oscillation of $\frac{\nu}{2\pi}$ periodic functions:

$$\forall (f,g)\in L_2(\mathbb{R}_+,\mathbb{C}), \qquad < f,g >= \frac{\nu}{2\pi}\int_0^{\frac{2\pi}{\nu}} f g^* \mathrm{d}t \tag{C.14}$$

where $\bullet^*$ denotes the complex conjugate. The considered inner product stays sesquilinear, hermitian symmetric, and positive-definite. Let us consider a general function $\Theta : \mathbb{R}_+ \longrightarrow \mathbb{C}$ with $n\in\mathbb{N}$. The function Θ writes as the linear combination of its projection on each vector of the Fourier basis:

$$\Theta(t) = \sum_k < \Theta(t), \mathrm{e}^{ik\nu t} > \mathrm{e}^{ik\nu t} = \sum_k \theta_k(t)\,\mathrm{e}^{ik\nu t} \tag{C.15}$$

where θ_k is the projection of Θ on the k-th Fourier vector:

$$\theta_k(t) =< \Theta(t), \mathrm{e}^{ik\nu t} >= \frac{\nu}{2\pi}\int_0^{\frac{2\pi}{\nu}} \Theta(t)\,\mathrm{e}^{-ik\nu t}\,\mathrm{d}t \tag{C.16}$$

By introducing the complex variables of Manevitch, and applying the Galerkin procedure supposing that φ_a, φ_m and their complex conjugate φ_a^*, φ_m^* are independent of $T_0=\tau$ (this assumption is verified after the fact), the system of equations (4.30) reads:

$$\begin{cases} \dfrac{\mathrm{d}\varphi_a}{\mathrm{d}\tau} + i\nu\dfrac{\varphi_a}{2} + \varepsilon\xi_a\dfrac{\varphi_a}{2} + \dfrac{\varphi_a}{2i\nu} + \varepsilon\dfrac{\gamma_0}{2i\nu}(\varphi_a - \alpha\varphi_m) = \varepsilon\dfrac{-f}{2i} \\ \varepsilon\left(\dfrac{\mathrm{d}\varphi_m}{\mathrm{d}\tau} + i\nu\dfrac{\varphi_m}{2} + \xi_m\dfrac{\varphi_m}{2} + \zeta R_\nu(\varphi_m,\varphi_m^*) + \dfrac{\gamma_0\mu}{2i\nu}(\alpha\varphi_m - \varphi_a)\right) = 0 \end{cases} \tag{C.17}$$

where:

$$R_\nu(\varphi_m,\varphi_m^*) = \frac{\nu}{2\pi}\int_0^{\frac{2\pi}{\nu}} \tilde{F}_{\mathrm{NL}}(\tau,\varphi_m,\varphi_m^*)\,\mathrm{e}^{-i\nu\tau}\,d\tau \tag{C.18}$$

Eq. (C.10) yields the definition of the time derivative regarding τ:

$$\frac{\mathrm{d}}{\mathrm{d}\tau} = \sum_{k=0}^{N} \varepsilon^k \frac{\partial}{\partial T_k} \tag{C.19}$$

System of Eqs. (C.17) yields equations at each order of ε. In our study, the equations corresponding to the different orders $O(\varepsilon^k)$ with $k\in[\![0\ ;\ N]\!]$ are considered. The orders correspond to the time scale considered and as a result to the fast and slow system dynamics.

C.1.2 Fast system dynamics

The system at $O(\varepsilon^0)$ is written with the consideration that $\nu = 1+\varepsilon\sigma = 1+o(\varepsilon^0)$:

$$O(\varepsilon^0): \begin{cases} \dfrac{\partial \varphi_a}{\partial T_0} + i\dfrac{\varphi_a}{2} + \dfrac{\varphi_a}{2i} = 0 \\ \dfrac{\partial \varphi_m}{\partial T_0} + i\dfrac{\varphi_m}{2} + \xi_m \dfrac{\varphi_m}{2} + \zeta R_1(\varphi_m, \varphi_m^*) + \dfrac{\gamma_0\mu}{2i}(\alpha\varphi_m - \varphi_a) = 0 \end{cases} \tag{C.20}$$

The first equation of the system yields that:

$$\frac{\partial \varphi_a}{\partial T_0} = 0 \tag{C.21}$$

which confirms the previously assumed hypothesis "φ_a independent of T_0". The second equation of the system can be studied in the case of an asymptotic state, when $T_0 \longrightarrow \infty$. It gives that:

$$\frac{\partial \varphi_m}{\partial T_0} \xrightarrow[T_0 \longrightarrow \infty]{} 0 \tag{C.22}$$

As a result, the system of equations reads:

$$i\frac{\varphi_m}{2}\Big(1 - \alpha\gamma_0\mu - i\xi_m\Big) + \zeta R_1(\varphi_m, \varphi_m^*) + i\gamma_0\mu\frac{\varphi_a}{2} = 0 \tag{C.23}$$

We define the map $\mathscr{H}$ as it follows:

$$\mathscr{H}(\varphi_a, \varphi_a^*, \varphi_m, \varphi_m^*) = i\frac{\varphi_m}{2}\Big(1 - \alpha\gamma_0\mu - i\xi_m\Big) + \zeta R_1(\varphi_m, \varphi_m^*) + i\gamma_0\mu\frac{\varphi_a}{2} \tag{C.24}$$

The set $W = \{(\varphi_a, \varphi_m) \in \mathbb{C}^2 \quad / \quad \mathscr{H}(\varphi_a, \varphi_a^*, \varphi_m, \varphi_m^*) = 0\}$ defines the slow invariant manifold (SIM). This manifold stands for the fixed points of the dynamical system thanks to Eq. (C.22). As a result, it is the topological space representing the asymptotic fixed points of the system.
The SIM can be expressed as:

$$\forall(\varphi_a, \varphi_m) \in W \quad ; \quad \varphi_a = -\frac{\varphi_m}{\gamma_0\mu}\Big(1 - \alpha\gamma_0\mu - i\xi_m\Big) + \frac{2i}{\gamma_0\mu}\zeta R_1(\varphi_m, \varphi_m^*) \tag{C.25}$$

The complex variables of Manevitch can be expressed in the polar domain with the amplitudes $(N_a, N_m) \in {\mathbb{R}_+}^2$ and $(\delta_a, \delta_m) \in [-\pi; \pi]^2$:

$$\begin{cases} \varphi_a(T_1, ..., T_N) = N_a(T_1, ..., T_N)\, e^{i\delta_a(T_1, ..., T_N)} \\ \varphi_m(T_0, ..., T_N) = N_m(T_0, ..., T_N)\, e^{i\delta_m(T_0, ..., T_N)} \end{cases} \tag{C.26}$$

Replacing the polar domain form of the complex variables of Manevitch in Eq. (C.25), and taking the real and imaginary parts of the equation reads:

$$\forall(\varphi_a, \varphi_m) \in W \quad ; \quad \begin{cases} N_a\cos(\delta_a - \delta_m) = \dfrac{N_m}{\gamma_0\mu}(\alpha\gamma_0\mu - 1) + \Re\Big(\dfrac{2i}{\gamma_0\mu}\, e^{-i\delta_m}\, \zeta R_1(N_m e^{i\delta_m}, N_m e^{-i\delta_m})\Big) \\ N_a\sin(\delta_a - \delta_m) = -\dfrac{N_m}{\gamma_0\mu}\xi_m + \Im\Big(\dfrac{2i}{\gamma_0\mu}\, e^{-i\delta_m}\, \zeta R_1(N_m e^{i\delta_m}, N_m e^{-i\delta_m})\Big) \end{cases} \tag{C.27}$$

Which writes also as a developed form:

$$\forall(\varphi_a,\varphi_m)\in W\ ;\ \begin{cases} N_a\cos(\delta_a-\delta_m)=\dfrac{N_m}{\gamma_0\mu}\left(\alpha\gamma_0\mu-1\right)+\dfrac{2}{\gamma_0\mu}\zeta\Big(\sin(\delta_m)\Re\big(R_1(\varphi_m,\varphi_m^*)\big)-\cos(\delta_m)\Im\big(R_1(\varphi_m,\varphi_m^*)\big)\Big) \\ N_a\sin(\delta_a-\delta_m)=-\dfrac{N_m}{\gamma_0\mu}\xi_m+\dfrac{2}{\gamma_0\mu}\zeta\Big(\cos(\delta_m)\Re\big(R_1(\varphi_m,\varphi_m^*)\big)+\sin(\delta_m)\Im\big(R_1(\varphi_m,\varphi_m^*)\big)\Big) \end{cases} \tag{C.28}$$

Using the real and imaginary parts, the magnitude of the SIM can be easily retrieved, as well as the phase between φ_a and φ_m. In the later considered cases, the SIM is not a function of phases δ_a and δ_m, as the considered nonlinearities are not time-dependent. The amplitude of the SIM writes:

$$\begin{aligned} N_a^2=&\left(\frac{N_m}{\gamma_0\mu}\left(\alpha\gamma_0\mu-1\right)+\frac{2}{\gamma_0\mu}\zeta\Big(\sin(\delta_m)\Re\big(R_1(\varphi_m,\varphi_m^*)\big)-\cos(\delta_m)\Im\big(R_1(\varphi_m,\varphi_m^*)\big)\Big)\right)^2 \\ &+\left(-\frac{N_m}{\gamma_0\mu}\xi_m+\frac{2}{\gamma_0\mu}\zeta\Big(\cos(\delta_m)\Re\big(R_1(\varphi_m,\varphi_m^*)\big)+\sin(\delta_m)\Im\big(R_1(\varphi_m,\varphi_m^*)\big)\Big)\right)^2 \end{aligned} \tag{C.29}$$

The phase of the SIM writes:

$$\delta_a-\delta_m=\arctan\left(\frac{-\dfrac{N_m}{\gamma_0\mu}\xi_m+\dfrac{2}{\gamma_0\mu}\zeta\Big(\cos(\delta_m)\Re\big(R_1(\varphi_m,\varphi_m^*)\big)+\sin(\delta_m)\Im\big(R_1(\varphi_m,\varphi_m^*)\big)\Big)}{\dfrac{N_m}{\gamma_0\mu}\left(\alpha\gamma_0\mu-1\right)+\dfrac{2}{\gamma_0\mu}\zeta\Big(\sin(\delta_m)\Re\big(R_1(\varphi_m,\varphi_m^*)\big)-\cos(\delta_m)\Im\big(R_1(\varphi_m,\varphi_m^*)\big)\Big)}\right) \tag{C.30}$$

C.1.3 Unstable zones of the SIM

Let us consider the second equation of system (C.20) and its complex conjugate:

$$\frac{\partial\varphi_m}{\partial T_0}+i\frac{\varphi_m}{2}\Big(1-\alpha\gamma_0\mu-i\xi_m\Big)+\zeta R_1(\varphi_m,\varphi_m^*)+i\gamma_0\mu\frac{\varphi_a}{2}=0 \tag{C.31}$$

Knowing that φ_a is independent of T_0, one can search the boundary of unstable zones only perturbing φ_m:

$$\begin{cases} \varphi_m\longrightarrow\varphi_m+\Delta\varphi_m \\ \varphi_m^*\longrightarrow\varphi_m^*+\Delta\varphi_m^* \end{cases} \tag{C.32}$$

It gives the following system:

$$\begin{cases} \dfrac{\partial\Delta\varphi_m}{\partial T_0}=-\dfrac{i}{2}\Delta\varphi_m\Big(1-\alpha\gamma_0\mu-i\xi_m\Big)-\zeta\Big(R_1(\varphi_m+\Delta\varphi_m,\varphi_m^*+\Delta\varphi_m^*)-R_1(\varphi_m,\varphi_m^*)\Big) \\ \dfrac{\partial\Delta\varphi_m^*}{\partial T_0}=\dfrac{i}{2}\Delta\varphi_m^*\Big(1-\alpha\gamma_0\mu+i\xi_m\Big)-\zeta\Big(R_1(\varphi_m+\Delta\varphi_m,\varphi_m^*+\Delta\varphi_m^*)-R_1(\varphi_m,\varphi_m^*)\Big)^* \end{cases} \tag{C.33}$$

By developing the Taylor series of the function R_1 (that we suppose holomorphic on a subset $U\subset\mathbb{C}^2$) at the point $(\varphi_m,\varphi_m^*)\in U$:

$$R_1(\varphi_m+\Delta\varphi_m,\varphi_m^*+\Delta\varphi_m^*)=R_1(\varphi_m,\varphi_m^*)+\Delta\varphi_m\frac{\partial R_1}{\partial\varphi_m}(\varphi_m,\varphi_m^*)+\Delta\varphi_m^*\frac{\partial R_1}{\partial\varphi_m^*}(\varphi_m,\varphi_m^*)+o\Big(||(\Delta\varphi_m,\Delta\varphi_m^*)||_{\mathbb{C}^2}\Big) \tag{C.34}$$

By substituting:

$$\begin{cases} \dfrac{\partial \Delta\varphi_m}{\partial T_0} \approx -\dfrac{\Delta\varphi_m}{2}\left(i(1-\alpha\gamma_0\mu-i\xi_m)+2\zeta\dfrac{\partial R_1}{\partial\varphi_m}(\varphi_m,\varphi_m^*)\right)-\dfrac{\Delta\varphi_m^*}{2}\left(2\zeta\dfrac{\partial R_1}{\partial\varphi_m^*}(\varphi_m,\varphi_m^*)\right) \\ \dfrac{\partial \Delta\varphi_m^*}{\partial T_0} \approx -\dfrac{\Delta\varphi_m^*}{2}\left(-i(1-\alpha\gamma_0\mu+i\xi_m)+2\zeta\dfrac{\partial R_1^*}{\partial\varphi_m^*}(\varphi_m,\varphi_m^*)\right)-\dfrac{\Delta\varphi_m}{2}\left(2\zeta\dfrac{\partial R_1^*}{\partial\varphi_m}(\varphi_m,\varphi_m^*)\right) \end{cases} \tag{C.35}$$

The conjugated term of each equation creates coupling between the two ordinary differential equations. Indeed, supposing that $\tilde{F}_{\mathrm{NL}}$ is linear, it can be seen that coupling between the two complex conjugate equations does not appear.

It is easily seen that both equations are ODEs in $\Delta\varphi_m$ and $\Delta\varphi_m^*$. A general matrix form can be presented in Eq. (C.36), as we do a linearization of the equation in $\Delta\varphi_m$: we decide to neglect the terms of order $O(\Delta\varphi_m^2)$ and superior orders:

$$\begin{pmatrix} \dfrac{\partial \Delta\varphi_m}{\partial T_0} \\ \dfrac{\partial \Delta\varphi_m^*}{\partial T_0} \end{pmatrix} = \mathbf{M}\begin{pmatrix} \Delta\varphi_m \\ \Delta\varphi_m^* \end{pmatrix} \tag{C.36}$$

where the matrix $\mathbf{M}\in\mathbb{M}_{2,2}$ reads:

$$\mathbf{M} = -\frac{1}{2}\begin{pmatrix} i(1-\alpha\gamma_0\mu-i\xi_m)+2\zeta\dfrac{\partial R_1}{\partial\varphi_m}(\varphi_m,\varphi_m^*) & 2\zeta\dfrac{\partial R_1}{\partial\varphi_m^*}(\varphi_m,\varphi_m^*) \\ 2\zeta\dfrac{\partial R_1^*}{\partial\varphi_m}(\varphi_m,\varphi_m^*) & -i(1-\alpha\gamma_0\mu+i\xi_m)+2\zeta\dfrac{\partial R_1^*}{\partial\varphi_m^*}(\varphi_m,\varphi_m^*) \end{pmatrix} \tag{C.37}$$

The non-diagonal elements of the matrix are created by the nonlinear last term of Eqs. (C.33). The solution of the ODE Eq. (C.36) with initial conditions $\Delta\varphi_m(0)=\Delta\varphi_{m,0}$ is:

$$\Delta\varphi_m(T_0) = \mathrm{e}^{\mathbf{M}T_0}\Delta\varphi_{m,0} \tag{C.38}$$

Information regarding the stability of the solution is provided by the spectrum of $\mathbf{M}$. We are interested in the real part of the eigenvalues, as they are responsible for stability. Let Ξ be the spectrum of $\mathbf{M}$. We decompose $\Xi\subset\mathbb{C}$ as:

$$\begin{aligned} \Xi_- &= \{\lambda\in\Xi \quad / \quad \Re(\lambda)<0\} \\ \Xi_0 &= \{\lambda\in\Xi \quad / \quad \Re(\lambda)=0\} \\ \Xi_+ &= \{\lambda\in\Xi \quad / \quad \Re(\lambda)>0\} \end{aligned} \tag{C.39}$$

with $\Xi=\Xi_-\cup\Xi_0\cup\Xi_+$. A fixed point $(\varphi_a,\varphi_m)\in W$ is asymptotically stable if $\Delta\varphi_m \xrightarrow[T_0\longrightarrow\infty]{} 0$. If $\Delta\varphi_m$ diverges, the fixed point is asymptotically unstable. We can decompose the SIM W in the same manner:

$$\begin{aligned} W_- &= \{(\varphi_a,\varphi_m)\in W \quad / \quad \lambda\in\Xi_-\} \\ W_0 &= \{(\varphi_a,\varphi_m)\in W \quad / \quad \lambda\in\Xi_0\} \\ W_+ &= \{(\varphi_a,\varphi_m)\in W \quad / \quad \lambda\in\Xi_+\} \end{aligned} \tag{C.40}$$

As a result, if the eigenvalues $\lambda\in\Xi_+$, the fixed point is unstable: : $(\varphi_a,\varphi_m)\in W_+$. If $\lambda\in\Xi_-$, the fixed point is stable: $(\varphi_a,\varphi_m)\in W_-$. The stability bounds are defined by the subset W_0.

We determine the eigenvalues of the application $\mathbf{M}$. Let us denote the terms of the matrix $\mathbf{M}_{kl}$ with the indices $(k,l)\in\{1,2\}$, where k is the indice of lines and l of columns. The characteristic polynomial χ of the matrix can

be calculated in order to get the eigenvalues:

$$\chi(\lambda) = (\mathbf{M}_{11} - \lambda)(\mathbf{M}_{22} - \lambda) - \mathbf{M}_{12}\mathbf{M}_{21} \tag{C.41}$$

which yields:

$$\chi(\lambda) = \lambda^2 + b\lambda + c \tag{C.42}$$

with $b = -\operatorname{tr}(\mathbf{M}) = -(\mathbf{M}_{11} + \mathbf{M}_{22})$ and $c = \det(\mathbf{M}) = \mathbf{M}_{11}\mathbf{M}_{22} - \mathbf{M}_{12}\mathbf{M}_{21}$.

For all cases, we notice that $(b,c) \in \mathbb{R}^2$. Being a quadratic equation, up to two eigenvalues of the matrix can be obtained, named λ_1 and λ_2:

$$\begin{cases} \lambda_1 = \dfrac{-b - \sqrt{b^2 - 4c}}{2} \\ \lambda_2 = \dfrac{-b + \sqrt{b^2 - 4c}}{2} \end{cases} \tag{C.43}$$

Multiple cases arise, depending on the value of the discriminant of the quadratic equation.

If $b^2 - 4c < 0$

In this case, $(\lambda_1, \lambda_2) \in \mathbb{C}^2$:

$$\begin{cases} \lambda_1 = \dfrac{-b - i\sqrt{4c - b^2}}{2} \\ \lambda_2 = \dfrac{-b + i\sqrt{4c - b^2}}{2} \end{cases} \tag{C.44}$$

It gives that $\Re(\lambda_1) = \Re(\lambda_2) = -\frac{b}{2}$. The sign of b gives the stability: if b is negative, the real part of the eigenvalues is positive, $\lambda_1, \lambda_2 \in \Xi_+$. The positivity of b implies a negative real part of the eigenvalues, $\lambda_1, \lambda_2 \in \Xi_-$.

If $b^2 - 4c = 0$

In this case, $(\lambda_1, \lambda_2) \in \mathbb{R}^2$ as:

$$\lambda_1 = \lambda_2 = \frac{-b}{2} \tag{C.45}$$

This case defines a manifold with the same conditions as the preceding case: the sign of b determines the stability of the fixed points.

If $b^2 - 4c > 0$

In this case, $(\lambda_1, \lambda_2) \in \mathbb{R}^2$:

$$\begin{cases} \lambda_1 = \dfrac{-b - \sqrt{b^2 - 4c}}{2} \\ \lambda_2 = \dfrac{-b + \sqrt{b^2 - 4c}}{2} \end{cases} \tag{C.46}$$

If $b < 0$, the condition $\lambda_1 > 0 \iff c > 0 \iff \lambda_1 \in \Xi_+$. If $c > 0$, it defines the unstable manifold, and $c < 0$ defines the stable manifold. The condition $c = 0$ gives the manifold W_0 defining the boundary between the stable W_- and unstable manifolds W_+.

In the same manner, if $b > 0$, the condition $\lambda_2 > 0 \iff c < 0 \iff \lambda_2 \in \Xi_+$. If $c < 0$, it defines the unstable manifold, and $c > 0$ defines the stable manifold.

It can be summed up with the condition: $\operatorname{sgn}(b).c < 0 \Longrightarrow \lambda_1, \lambda_2 \in \Xi_+$.

C.1.4 Slow system dynamics

The slow time scale corresponds to the equations at $O(\varepsilon)$. The first equation of (C.17) at order $O(\varepsilon)$ gives:

$$\frac{\partial \varphi_a}{\partial T_1} + \frac{i\varphi_a}{2}(2\sigma - \gamma_0 - i\xi_a) + \frac{i\alpha\gamma_0}{2}\varphi_m = \frac{if}{2} \tag{C.47}$$

We can set a manifold defined as $E = \{(\varphi_a, \varphi_m) \in \mathbb{C}^2 \quad / \quad \mathscr{E}(\varphi_a, \varphi_a^*, \varphi_m, \varphi_m^*) = 0\}$, with:

$$\mathscr{E}(\varphi_a, \varphi_a^*, \varphi_m, \varphi_m^*) = \frac{i\varphi_a}{2}(2\sigma - \gamma_0 - i\xi_a) + \frac{i\alpha\gamma_0}{2}\varphi_m - \frac{if}{2} \tag{C.48}$$

Additionally, the evolution of the SIM $\mathscr{H}$ at time scale T_1 can be calculated using the chain rule:

$$\begin{cases} \dfrac{\mathrm{d}\mathscr{H}}{\mathrm{d}T_1} = \dfrac{\partial \mathscr{H}}{\partial \varphi_a}\dfrac{\partial \varphi_a}{\partial T_1} + \dfrac{\partial \mathscr{H}}{\partial \varphi_m}\dfrac{\partial \varphi_m}{\partial T_1} + \dfrac{\partial \mathscr{H}}{\partial \varphi_a^*}\dfrac{\partial \varphi_a^*}{\partial T_1} + \dfrac{\partial \mathscr{H}}{\partial \varphi_m^*}\dfrac{\partial \varphi_m^*}{\partial T_1} \\ \dfrac{\mathrm{d}\mathscr{H}^*}{\mathrm{d}T_1} = \dfrac{\partial \mathscr{H}^*}{\partial \varphi_a}\dfrac{\partial \varphi_a}{\partial T_1} + \dfrac{\partial \mathscr{H}^*}{\partial \varphi_m}\dfrac{\partial \varphi_m}{\partial T_1} + \dfrac{\partial \mathscr{H}^*}{\partial \varphi_a^*}\dfrac{\partial \varphi_a^*}{\partial T_1} + \dfrac{\partial \mathscr{H}^*}{\partial \varphi_m^*}\dfrac{\partial \varphi_m^*}{\partial T_1} \end{cases} \tag{C.49}$$

which can be rearranged as:

$$\begin{pmatrix} \dfrac{\partial \mathscr{H}}{\partial \varphi_m} & \dfrac{\partial \mathscr{H}}{\partial \varphi_m^*} \\ \dfrac{\partial \mathscr{H}^*}{\partial \varphi_m} & \dfrac{\partial \mathscr{H}^*}{\partial \varphi_m^*} \end{pmatrix} \begin{pmatrix} \dfrac{\partial \varphi_m}{\partial T_1} \\ \dfrac{\partial \varphi_m^*}{\partial T_1} \end{pmatrix} = - \begin{pmatrix} \dfrac{\partial \mathscr{H}}{\partial \varphi_a} & \dfrac{\partial \mathscr{H}}{\partial \varphi_a^*} \\ \dfrac{\partial \mathscr{H}^*}{\partial \varphi_a} & \dfrac{\partial \mathscr{H}^*}{\partial \varphi_a^*} \end{pmatrix} \begin{pmatrix} \dfrac{\partial \varphi_a}{\partial T_1} \\ \dfrac{\partial \varphi_a^*}{\partial T_1} \end{pmatrix} \tag{C.50}$$

Let $\mathbf{A}$ stand for the jacobian matrix of $(\mathscr{H}, \mathscr{H}^*)$ regarding the variables φ_m and φ_m^*:

$$\mathbf{A} = \begin{pmatrix} \dfrac{\partial \mathscr{H}}{\partial \varphi_m} & \dfrac{\partial \mathscr{H}}{\partial \varphi_m^*} \\ \dfrac{\partial \mathscr{H}^*}{\partial \varphi_m} & \dfrac{\partial \mathscr{H}^*}{\partial \varphi_m^*} \end{pmatrix} \tag{C.51}$$

The method defines the equilibrium and singular points as being the intersection of the manifolds W and E, combined with a condition about the invertibility of $\mathbf{A}$. The non-invertibility of $\mathbf{A}$ gives the extremums of the SIM regarding φ_m and φ_m^* in the time scale T_1. As a result, the singular points are defined as:

$$W \cap E \cap \{(\varphi_a, \varphi_m) \in \mathbb{C}^2 / \det(\mathbf{A}) = 0\} \Longleftrightarrow \begin{cases} \mathscr{E}(\varphi_a, \varphi_m, \varphi_a^*, \varphi_m^*) = 0 \\ \mathscr{H}(\varphi_a, \varphi_m, \varphi_a^*, \varphi_m^*) = 0 \\ \det(\mathbf{A}) = 0 \end{cases} \tag{C.52}$$

And equilibrium points are defined as:

$$W \cap E \cap \{(\varphi_a, \varphi_m) \in \mathbb{C}^2 / \det(\mathbf{A}) \neq 0\} \Longleftrightarrow \begin{cases} \mathscr{E}(\varphi_a, \varphi_m, \varphi_a^*, \varphi_m^*) = 0 \\ \mathscr{H}(\varphi_a, \varphi_m, \varphi_a^*, \varphi_m^*) = 0 \\ \det(\mathbf{A}) \neq 0 \end{cases} \tag{C.53}$$

Equilibrium points

The equilibrium points are defined by the intersection of the manifolds defined by $\varepsilon = 0$ and $\mathscr{H} = 0$. Let us solve the system defined by equations (C.53):

$$\begin{cases} \dfrac{i\varphi_a}{2}(2\sigma - \gamma_0 - i\xi_a) + \dfrac{i\alpha\gamma_0}{2}\varphi_m - \dfrac{if}{2} = 0 \\ i\dfrac{\varphi_m}{2}\Big(1 - \alpha\gamma_0\mu - i\xi_m\Big) + \zeta R_1(\varphi_m, \varphi_m^*) + i\gamma_0\mu\dfrac{\varphi_a}{2} = 0 \\ \det(\mathbf{A}) \neq 0 \end{cases} \tag{C.54}$$

As previously done in equation (C.25), the second equation of system (C.54) can be organized to express φ_a as a function of φ_m. To find the intersection between the manifolds W and E, this equation can be replaced in the first equation of (C.54):

$$f = \alpha\gamma_0\varphi_m - \frac{\varphi_m}{\gamma_0\mu}(1 - \alpha\gamma_0\mu - i\xi_m)(2\sigma - \gamma_0 - i\xi_a) + \frac{2i}{\gamma_0\mu}(2\sigma - \gamma_0 - i\xi_a)\zeta R_1(\varphi_m, \varphi_m^*) \tag{C.55}$$

Taking the real and imaginary part of the equation:

$$\begin{cases} f = \left(\dfrac{N_m}{\gamma_0\mu}\right)\Bigg(\cos\delta_m\Big(\alpha\gamma_0^2\mu - (1 - \alpha\gamma_0\mu)(2\sigma - \gamma_0) + \xi_a\xi_m\Big) - \sin\delta_m\Big(\xi_m(2\sigma - \gamma_0) + \xi_a(1 - \alpha\gamma_0\mu)\Big) \\ \qquad\qquad + \dfrac{2\zeta}{N_m}\Big(\xi_a\Re(R_1) - (2\sigma - \gamma_0)\Im(R_1)\Big)\Bigg) \\ 0 = \left(\dfrac{N_m}{\gamma_0\mu}\right)\Bigg(\cos\delta_m\Big(\xi_m(2\sigma - \gamma_0) + \xi_a(1 - \alpha\gamma_0\mu)\Big) + \sin\delta_m\Big(\alpha\gamma_0^2\mu - (1 - \alpha\gamma_0\mu)(2\sigma - \gamma_0) + \xi_a\xi_m\Big) \\ \qquad\qquad + \dfrac{2\zeta}{N_m}\Big(\xi_a\Im(R_1) + (2\sigma - \gamma_0)\Re(R_1)\Big)\Bigg) \end{cases} \tag{C.56}$$

Calculating the modulus, the square of the sum of both equations is provided in Eq. (C.57). It is noticeable that the expression Eq. (C.57) can be considered as a polynomial with variable σ. If R_1 is function of σ, further calculations should be realized in order to reduce following equation in higher order polynomial.

$$f^2 = \left(\frac{Nm}{\gamma_0\mu}\right)^2\Big(A\sigma^2 + B\sigma + C\Big) \tag{C.57}$$

where:

$$\begin{cases} A = 4(1-\alpha\gamma_0\mu)^2 + 4\xi_m^2 + \dfrac{16\zeta^2}{N_m^2}|R_1(\varphi_m,\varphi_m^*)|^2 \\ \qquad + \dfrac{16\zeta}{N_m}\left(\xi_m\Big(\Re(R_1)\cos\delta_m + \Im(R_1)\sin\delta_m\Big) + (1-\alpha\gamma_0\mu)\Big(\Im(R_1)\cos\delta_m - \Re(R_1)\sin\delta_m\Big)\right) \\ B = -4\gamma_0\xi_m^2 - 4(1-\alpha\gamma_0\mu)\big(\gamma_0(1-\alpha\gamma_0\mu) + \alpha\gamma_0^2\mu\big) - \dfrac{16\zeta^2\gamma_0}{N_m^2}|R_1(\varphi_m,\varphi_m^*)|^2 \\ \qquad + \dfrac{16\zeta\gamma_0}{N_m}\left((1-\alpha\gamma_0\mu)\Big(\Re(R_1)\sin\delta_m - \Im(R_1)\cos\delta_m\Big) - \xi_m\Big(\Re(R_1)\cos\delta_m + \Im(R_1)\sin\delta_m\Big)\right) \\ \qquad + \dfrac{8\zeta\alpha\gamma_0^2\mu}{N_m}\left(\Re(R_1)\sin\delta_m - \Im(R_1)\cos\delta_m\right) \\ C = (1-\alpha\gamma_0\mu)^2(\xi_a^2+\gamma_0^2) + \gamma_0^2\xi_m^2 + (\alpha\gamma_0^2\mu + \xi_a\xi_m)^2 + 2\alpha\gamma_0^3\mu(1-\alpha\gamma_0\mu) \\ \qquad + \dfrac{4\zeta^2}{N_m^2}(\xi_a^2+\gamma_0^2)|R_1(\varphi_m,\varphi_m^*)|^2 \\ \qquad + \dfrac{4\zeta\gamma_0^2}{N_m}\left(\xi_m\Big(\Re(R_1)\cos\delta_m + \Im(R_1)\sin\delta_m\Big) + (1-\alpha\gamma_0\mu)\Big(\Im(R_1)\cos\delta_m - \Re(R_1)\sin\delta_m\Big)\right) \\ \qquad + \dfrac{4\zeta\xi_a}{N_m}\Big((1-\alpha\gamma_0\mu)\xi_a - \gamma_0\xi_m\Big)\left(\Im(R_1)\cos\delta_m - \Re(R_1)\sin\delta_m\right) \\ \qquad + \dfrac{4\zeta}{N_m}\Big(\alpha\gamma_0^2\mu + \xi_a\xi_m\Big)\left(\xi_a\Big(\Re(R_1)\cos\delta_m + \Im(R_1)\sin\delta_m\Big) + \gamma_0\Big(\Im(R_1)\cos\delta_m - \Re(R_1)\sin\delta_m\Big)\right) \end{cases} \tag{C.58}$$

Solving this equation for roots gives the points $(\varphi_a, \varphi_m, \sigma) \in W \cap E$.

Singular points

The matrix **A** is:

$$\mathbf{A} = \begin{pmatrix} \dfrac{i}{2}(1-\alpha\gamma_0\mu - i\xi_m) + \zeta\dfrac{\partial R_1}{\partial\varphi_m}(\varphi_m,\varphi_m^*) & \zeta\dfrac{\partial R_1}{\partial\varphi_m^*}(\varphi_m,\varphi_m^*) \\ \zeta\dfrac{\partial R_1^*}{\partial\varphi_m}(\varphi_m,\varphi_m^*) & -\dfrac{i}{2}(1-\alpha\gamma_0\mu + i\xi_m) + \zeta\dfrac{\partial R_1^*}{\partial\varphi_m^*}(\varphi_m,\varphi_m^*) \end{pmatrix} \tag{C.59}$$

And its determinant is:

$$\det(\mathbf{A}) = \frac{1}{4}\Big((1-\alpha\gamma_0\mu)^2 + \xi_m^2\Big) + \frac{i}{2}\zeta\left((1-\alpha\gamma_0\mu - i\xi_m)\frac{\partial R_1^*}{\partial\varphi_m^*} - (1-\alpha\gamma_0\mu + i\xi_m)\frac{\partial R_1}{\partial\varphi_m}\right) + \zeta^2\left(\frac{\partial R_1^*}{\partial\varphi_m^*}\frac{\partial R_1}{\partial\varphi_m} - \frac{\partial R_1}{\partial\varphi_m^*}\frac{\partial R_1^*}{\partial\varphi_m}\right) \tag{C.60}$$

The equation $\det(\mathbf{A}) = 0$ provides the singular points.

C.2 The cubic restoring force function

The cubic hardening and softening restoring force functions are given Eq. (4.42) in a unique function F_{NL}. The preliminary work of Section C.1 permits us to calculate:

$$\frac{m_a}{M_d k_a \chi}F_{\mathrm{NL}}(t,\chi x) = \frac{m_a}{M_d k_a \chi}K_d(\chi x(t) + \beta_{\mathrm{NL}}(\chi x)^3(t)) \tag{C.61}$$

After the change in variables Eq. (C.4), it reads:

$$\frac{m_a}{M_d k_a \chi} F_{\mathrm{NL}}(\tau, \chi x) = \zeta \tilde{F}_{\mathrm{NL}}(\tau, x) \tag{C.62}$$

with the re-scaled parameters:

$$\begin{cases} \zeta = \dfrac{m_a K_d}{M_d k_a} \\ \tilde{\beta}_{\mathrm{NL}} = \chi^2 \beta_{\mathrm{NL}} \\ \tilde{F}_{\mathrm{NL}}(\tau, x) = (x(\tau) + \tilde{\beta}_{\mathrm{NL}} x^3(\tau)) \end{cases} \tag{C.63}$$

The function used for the calculations of the analytical results is estimated:

$$\forall (\varphi_m, \varphi_m^*) \in \mathbb{C}^2, \quad R_1(\varphi_m, \varphi_m^*) = < \tilde{F}_{\mathrm{NL}}(\tau, \varphi_m), \mathrm{e}^{iT_0} > = -i\left(\frac{\varphi_m}{2} + \frac{3}{8}\tilde{\beta}_{\mathrm{NL}} \varphi_m^2 \varphi_m^*\right) \tag{C.64}$$

Which gives the following real and imaginary parts:

$$\forall (\varphi_m, \varphi_m^*) \in \mathbb{C}^2 \qquad \begin{cases} \Re(R_1(\varphi_m, \varphi_m^*)) = \left(\dfrac{N_m}{2} + \dfrac{3}{8}\tilde{\beta}_{\mathrm{NL}} N_m^3\right) \sin \delta_m \\ \Im(R_1(\varphi_m, \varphi_m^*)) = -\left(\dfrac{N_m}{2} + \dfrac{3}{8}\tilde{\beta}_{\mathrm{NL}} N_m^3\right) \cos \delta_m \end{cases} \tag{C.65}$$

Fast system dynamics

To estimate the fast system dynamics, we use Eqs. (C.64) and (C.65) to retrieve the SIM defined in Eq. (C.25):

$$\varphi_a = -\frac{\varphi_m}{\gamma_0 \mu}\left(1 - \zeta - \alpha\gamma_0\mu - \frac{3}{4}\zeta\tilde{\beta}_{\mathrm{NL}}|\varphi_m|^2 - i\xi_m\right) \tag{C.66}$$

Which gives the magnitude of the SIM:

$$N_a = \frac{N_m}{\gamma_0 \mu}\sqrt{\left(1 - \zeta - \alpha\gamma_0\mu - \frac{3}{4}\zeta\tilde{\beta}_{\mathrm{NL}} N_m^2\right)^2 + \xi_m^2} \tag{C.67}$$

As it is well known, the SIM for a cubic restoring force is not dependent of δ_m.

Unstable zones of the SIM

The matrix $\mathbf{M}$ defined in Eq. (C.36) yields:

$$\mathbf{M} = -\frac{i}{2}\begin{pmatrix} 1 - \zeta - \alpha\gamma_0\mu - \frac{3}{2}\zeta\tilde{\beta}_{\mathrm{NL}}|\varphi_m|^2 - i\xi_m & -\frac{3}{4}\zeta\tilde{\beta}_{\mathrm{NL}}\varphi_m^2 \\ \frac{3}{4}\zeta\tilde{\beta}_{\mathrm{NL}}\varphi_m^{*^2} & -\left(1 - \zeta - \alpha\gamma_0\mu - \frac{3}{2}\zeta\tilde{\beta}_{\mathrm{NL}}|\varphi_m|^2 + i\xi_m\right) \end{pmatrix} \tag{C.68}$$

Let us consider the value of the multiple possible cases:

If $b^2 - 4c < 0$

In this case, we have $b = -\mathrm{tr}(\mathbf{M}) = \xi_m$. As the aim of the study is not to inject energy into the system, the damping ξ_m of the ER is taken positive. As a result, the real part of the eigenvalue is negative $\Re(\lambda_1) = \Re(\lambda_2) \leq 0$. This case defines a manifold where the fixed points are stable: $\lambda_1, \lambda_2 \in \Xi_-$.

If $b^2-4c=0$

This case is identical as the previous one. So, $\lambda_1,\lambda_2 \in \Xi_-$.

If $b^2-4c>0$

The following stands: $\text{sgn}(b).c<0 \Longrightarrow \lambda_1,\lambda_2 \in \Xi_+$. In our study, $\text{sgn}(b)=1$, which leads to:

$$c<0 \Longrightarrow \lambda_1,\lambda_2 \in \Xi_+ \tag{C.69}$$

The points $(\varphi_a,\varphi_m) \in W$ such that $c<0$ are within the unstable zones of the SIM. We can solve the equation:

$$\frac{1}{4}\left(\xi_m^2+\left(1-\zeta-\alpha\gamma_0\mu-\frac{3}{2}\zeta\tilde{\beta}_{\text{NL}}|\varphi_m|^2\right)^2\right)-\left(\frac{3}{8}\zeta\tilde{\beta}_{\text{NL}}\right)^2|\varphi_m|^4<0 \tag{C.70}$$

which can be organized as:

$$\left(\frac{27}{16}\zeta\tilde{\beta}_{\text{NL}}{}^2\right)X^2-3\zeta\tilde{\beta}_{\text{NL}}\left(1-\zeta-\alpha\gamma_0\mu\right)X+\left(\xi_m^2+(1-\zeta-\alpha\gamma_0\mu)^2\right)<0 \tag{C.71}$$

where $X=|\varphi_m|^2=N_m^2$. It is a quadratic equation, which solutions X_1 and X_2 are:

$$\begin{cases} X_1=\dfrac{(1-\zeta-\alpha\gamma_0\mu)+\frac{1}{2}\sqrt{(1-\zeta-\alpha\gamma_0\mu)^2-3\xi_m^2}}{\frac{9}{8}\zeta\tilde{\beta}_{\text{NL}}} \\ X_2=\dfrac{(1-\zeta-\alpha\gamma_0\mu)-\frac{1}{2}\sqrt{(1-\zeta-\alpha\gamma_0\mu)^2-3\xi_m^2}}{\frac{9}{8}\zeta\tilde{\beta}_{\text{NL}}} \end{cases} \tag{C.72}$$

This equation results in the instability of the set of points $\{(\varphi_a,\varphi_m)\in W \quad / \quad |\varphi_m|^2 \in [X_1,X_2]\}$. Each solution X_k, $k=\{1,2\}$ gives two solutions for the equation $X_k=N_m^2$. However, only the positive solutions are chosen, as $N_m \in \mathbb{R}_+$. We can observe that in order to get an unstable manifold, the condition $b^2-4c>0$ is needed, which means that X_1 and X_2 would be two dissociated real solutions. It gives the following condition on the parameters ζ and ξ_m:

$$(1-\zeta-\alpha\gamma_0\mu)^2-3\xi_m^2>0 \tag{C.73}$$

This condition in the literature is well known and usually defines a critical value of the damping $\xi_{2,c}$ value. In our study, a critical value of the linear stiffness ζ_c can be defined as well. However, the possible range of the value of the linear stiffness is limited by the hypothesis of the loudspeaker being solicited on its linear first mode.

Slow system dynamics

To estimate the equilibrium points of the system, we use Eqs. (C.64) and (C.65) to retrieve the equilibrium points defined in Eqs. (C.57) and (C.58):

$$f^2=\left(\frac{Nm}{\gamma_0\mu}\right)^2\left(A\sigma^2+B\sigma+C\right) \tag{C.74}$$

where:

$$\begin{cases} A = 4 - 8\zeta - 6\beta_{NL}\zeta Nm^2 + 4\zeta^2 + 6\beta_{NL}\zeta^2 Nm^2 + \frac{9}{4}\beta_{NL}^2\zeta^2 Nm^4 - 8\alpha\gamma_0\mu + 8\alpha\gamma_0\mu\zeta \\ \qquad + 6\alpha\gamma_0\mu\zeta\beta_{NL}Nm^2 + 4\alpha^2\gamma_0^2\mu^2 + 4\xi_m^2 \\ B = -4\gamma_0 + 8\gamma_0\zeta + 6\beta_{NL}\gamma_0\zeta Nm^2 - 4\gamma_0\zeta^2 - 6\beta_{NL}\gamma_0\zeta^2 Nm^2 - \frac{9}{4}\gamma_0\beta_{NL}^2\zeta^2 Nm^4 + 4\alpha\gamma_0^2\mu - 4\alpha\gamma_0^2\mu\zeta \\ \qquad - 3\alpha\gamma_0^2\mu\zeta\beta_{NL}Nm^2 - 4\gamma_0\xi_m^2 \\ C = \gamma_0^2 - 2\gamma_0^2\zeta - \frac{3}{2}\gamma_0^2\zeta\beta_{NL}Nm^2 + \gamma_0^2\zeta^2 + \frac{3}{2}\gamma_0^2\zeta^2\beta_{NL}Nm^2 + \frac{9}{16}\gamma_0^2\zeta^2\beta_{NL}^2Nm^4 + \xi_a^2 - 2\zeta\xi_a^2 \\ \qquad - \frac{3}{2}\zeta\xi_a^2\beta_{NL}Nm^2 + \zeta^2\xi_a^2 + \frac{3}{2}\zeta^2\xi_a^2\beta_{NL}Nm^2 + \frac{9}{16}\zeta^2\xi_a^2\beta_{NL}^2Nm^4 - 2\alpha\gamma_0\mu\xi_a^2 + 2\alpha\gamma_0\mu\zeta\xi_a^2 \\ \qquad + \frac{3}{2}\alpha\gamma_0\zeta\mu\beta_{NL}\xi_a^2Nm^2 + \alpha^2\gamma_0^2\mu^2\xi_a^2 + 2\alpha\gamma_0^2\mu\xi_a\xi_m + \gamma_0^2\xi_m^2 + \xi_a^2\xi_m^2 \end{cases} \tag{C.75}$$

This equation can be solved analytically. However, as the coefficients are composed of many terms, a numerical resolution is realized by searching for the roots of this expression.

Furthermore, the singular points can be found by considering the condition defined in Eq. (C.60):

$$\frac{1}{4}((\alpha\gamma_0\mu + \zeta - 1)^2 + \xi_m^2) + \frac{3}{64}\beta_{NL}\zeta(9\beta_{NL}\zeta N_m^4 + 16N_m^2(\alpha\gamma_0\mu + \zeta - 1)) = 0 \tag{C.76}$$

C.3 The non polynomial restoring force function

The logarithmic potential restoring force functions are given Eq. (4.46) in a unique function F_{NL}. The preliminary work of Section C.1 permits us to calculate:

$$\frac{m_a}{M_d k_a \chi} F_{\mathrm{NL}}(t, \chi x) = \frac{K_d \chi x}{1 + \beta_{\mathrm{NL}} \chi^2 x^2} \tag{C.77}$$

After the change in variables Eq. (C.4), it reads:

$$\frac{m_a}{M_d k_a \chi} F_{\mathrm{NL}}(\tau, \chi x) = \zeta \tilde{F}_{\mathrm{NL}}(\tau, x) \tag{C.78}$$

with the re-scaled parameters:

$$\begin{cases} \zeta = \dfrac{m_a K_d}{M_d k_a} \\ \tilde{\beta}_{\mathrm{NL}} = \chi^2 \beta_{\mathrm{NL}} \\ \tilde{F}_{\mathrm{NL}}(\tau, x) = \dfrac{x}{1 + \tilde{\beta}_{\mathrm{NL}} x^2} \end{cases} \tag{C.79}$$

The function used for the calculations of the analytical results is estimated:

$$\forall (\varphi_m, \varphi_m^*) \in \mathbb{C}^2, \quad R_1(\varphi_m, \varphi_m^*) = \frac{-i\varphi_m}{|\varphi_m|^2 \tilde{\beta}_{\mathrm{NL}}} \left(1 - \frac{1}{\sqrt{1 + |\varphi_m|^2 \tilde{\beta}_{\mathrm{NL}}}} \right) \tag{C.80}$$

Similarly to the literature [], the R_1 function can reads as:

$$R_1(\varphi_m, \varphi_m^*) = -\frac{i\varphi_m}{2} G(|\varphi_m|^2) \tag{C.81}$$

where the function $G : \mathbb{R}^* \longrightarrow \mathbb{R}$ is set as:

$$G(|\varphi_m|^2) = \frac{2}{|\varphi_m|^2 \tilde{\beta}_{\mathrm{NL}}} \left(1 - \frac{1}{\sqrt{1 + |\varphi_m|^2 \tilde{\beta}_{\mathrm{NL}}}} \right) \tag{C.82}$$

As a result, it gives the following real and imaginary parts:

$$\forall (\varphi_m, \varphi_m^*) \in \mathbb{C}^2 \qquad \begin{cases} \Re(R_1(\varphi_m, \varphi_m^*)) = \dfrac{1}{2} N_m \sin(\delta_m) G(|\varphi_m|^2) \\ \Im(R_1(\varphi_m, \varphi_m^*)) = -\dfrac{1}{2} N_m \cos(\delta_m) G(|\varphi_m|^2) \end{cases} \tag{C.83}$$

Fast system dynamics

To estimate the fast system dynamics, we use Eqs. (C.80) and (C.83) to retrieve the SIM defined in Eq. (C.25):

$$\varphi_a = -\frac{\varphi_m}{\gamma_0 \mu} \left(1 - \zeta G(|\varphi_m|^2) - \alpha \gamma_0 \mu - i \xi_m \right) \tag{C.84}$$

Which gives the magnitude of the SIM:

$$N_a = \frac{N_m}{\gamma_0 \mu} \sqrt{\left(1 - \alpha \gamma_0 \mu - \zeta G(|\varphi_m|^2) \right)^2 + \xi_m^2} \tag{C.85}$$

Unstable zones of the SIM

The matrix $\mathbf{M}$ defined in Eq. (C.36) is set with

$$\mathbf{M} = -\frac{1}{2} \begin{pmatrix} i(1 - \alpha\gamma_0\mu - i\xi_m - \zeta G(|\varphi_m|^2) - \zeta |\varphi_m|^2 G'(|\varphi_m|^2)) & -i\zeta \varphi_m^2 G'(|\varphi_m|^2) \\ i\zeta \varphi_m^{*2} G'(|\varphi_m|^2) & -i(1 - \alpha\gamma_0\mu + i\xi_m - \zeta G(|\varphi_m|^2) - \zeta |\varphi_m|^2 G'(|\varphi_m|^2)) \end{pmatrix} \tag{C.86}$$

Notice that the variable of the function G is $\varphi_m \varphi_m^* = |\varphi_m|^2 = Nm^2$. Let us consider the value of the multiple possible cases:

If $b^2 - 4c < 0$

In this case, we have $b = -\mathrm{tr}(\mathbf{M}) = \xi_m$. As the aim of the study is not to inject energy into the system, the damping ξ_m of the ER is taken positive. As a result, the real part of the eigenvalue is negative $\Re(\lambda_1) = \Re(\lambda_2) \leq 0$. This case defines a manifold where the fixed points are stable: $\lambda_1, \lambda_2 \in \Xi_-$.

If $b^2 - 4c = 0$

This case is identical as the previous one. So, $\lambda_1, \lambda_2 \in \Xi_-$.

If $b^2 - 4c > 0$

The following stands: $\mathrm{sgn}(b).c < 0 \Longrightarrow \lambda_1, \lambda_2 \in \Xi_+$. In our study, $\mathrm{sgn}(b) = 1$, which leads to:

$$c < 0 \Longrightarrow \lambda_1, \lambda_2 \in \Xi_+ \tag{C.87}$$

The points $(\varphi_a, \varphi_m) \in W$ such that $c < 0$ are within the unstable zones of the SIM. We can solve the equation:

$$-\frac{1}{4}\Big((\alpha\gamma_0\mu-1)^2+2\zeta|\varphi_m|^2G'(|\varphi_m|^2)(\alpha\gamma_0\mu+\zeta G(|\varphi_m|^2)-1)+\zeta G(|\varphi_m|^2)(2\alpha\gamma_0\mu+\zeta G(|\varphi_m|^2)-2)+\xi_m^2\Big)<0 \tag{C.88}$$

This equation results in the instability of the set of points defined by the previous equation.

Slow system dynamics

To estimate the equilibrium points of the system, we use Eqs. (C.95) and (C.98) to retrieve the equilibrium points defined in Eqs. (C.57) and (C.58):

$$f^2 = \left(\frac{Nm}{\gamma_0\mu}\right)^2\Big(A\sigma^2+B\sigma+C\Big) \tag{C.89}$$

where:

$$\begin{cases} A = 4-8\zeta G(|\varphi_m|^2)+4\zeta^2G(|\varphi_m|^2)^2-8\alpha\gamma_0\mu+8\alpha\gamma_0\mu\zeta G(|\varphi_m|^2)+4\alpha^2\gamma_0^2\mu^2+4\xi_m^2 \\ B = -4\gamma_0+8\gamma_0\zeta G(|\varphi_m|^2)-4\gamma_0\zeta^2G(|\varphi_m|^2)^2+4\alpha\gamma_0^2\mu-4\alpha\gamma_0^2\zeta\mu G(|\varphi_m|^2)-4\gamma_0\xi_m^2 \\ C = \gamma_0^2-2\zeta\gamma_0^2G(|\varphi_m|^2)+\gamma_0^2\zeta^2G(|\varphi_m|^2)^2+\xi_a^2-2\zeta\xi_a^2G(|\varphi_m|^2)+\zeta^2\xi_a^2G(|\varphi_m|^2)^2 \\ \qquad -2\alpha\gamma_0\mu\xi_a^2+2\alpha\gamma_0\mu\zeta\xi_a^2G(|\varphi_m|^2)+\alpha^2\gamma_0^2\mu^2\xi_a^2+2\alpha\gamma_0^2\mu\xi_a\xi_m+\gamma_0^2\xi_m^2+\xi_a^2\xi_m^2 \end{cases} \tag{C.90}$$

This equation is probably difficult to solve analytically. As a result, a numerical resolution is realized by searching for the roots of this expression.

Furthermore, the singular points can be found by adding the condition defined in Eq. (C.60):

$$-\frac{1}{2}\Big((\alpha\gamma_0\mu-1)^2+2\zeta|\varphi_m|^2G'(|\varphi_m|^2)(\alpha\gamma_0\mu+\zeta G(|\varphi_m|^2)-1)+\zeta G(|\varphi_m|^2)(2\alpha\gamma_0\mu+\zeta G(|\varphi_m|^2)-2)+\xi_m^2\Big)=0 \tag{C.91}$$

C.4 The Piecewise linear restoring force function

The linear piecewise restoring force functions are given Eq. (C.92) in a unique function F_{NL}. The preliminary work of Section C.1 permits us to calculate:

$$\frac{m_a}{M_d k_a \chi}F_{\mathrm{NL}}(t,\chi x) = \begin{cases} K_2\chi x-(K_1-K_2)\delta & \text{if } \chi x<-\delta \\ K_1\chi x & \text{if } -\delta<\chi x<\delta \\ K_2\chi x+(K_1-K_2)\delta & \text{if } \delta<\chi x \end{cases} \tag{C.92}$$

After the change in variables Eq. (C.4), it reads:

$$\frac{m_a}{M_d k_a \chi}F_{\mathrm{NL}}(\tau,\chi x) = \zeta\tilde{F}_{\mathrm{NL}}(\tau,x) \tag{C.93}$$

with the re-scaled parameters:

$$\begin{cases} \zeta = \dfrac{m_a K_d}{M_d k_a} \\ \tilde{F}_{\mathrm{NL}}(\tau,x) = \begin{cases} \Upsilon x - (1-\Upsilon)\delta/\chi & \text{if } x < -\delta/\chi \\ x & \text{if } -\delta/\chi < x < \delta/\chi \\ \Upsilon x + (1-\Upsilon)\delta/\chi & \text{if } \delta/\chi < x \end{cases} \end{cases} \tag{C.94}$$

where $\Upsilon \in \mathbb{R}^*$ stands for the ratio between the slopes K_2 and K_1: $\Upsilon = K_2/K_1$. The fonction used for the calculations of the analytical results is estimated:

$$\begin{aligned} \forall(\varphi_m,\varphi_m^*) \in \mathbb{C}^2, \quad R_1(\varphi_m,\varphi_m^*) &= < \tilde{F}_{\mathrm{NL}}(\tau,\varphi_m), \mathrm{e}^{iT_0} > \\ &= \frac{i\varphi_m}{\pi\nu}\left((\Upsilon-1)\frac{\delta\nu}{\chi|\varphi_m|}\sqrt{1-\left(\frac{\delta\nu}{\chi|\varphi_m|}\right)^2} - \Upsilon\arccos\left(\frac{\delta\nu}{\chi|\varphi_m|}\right) - \arcsin\left(\frac{\delta\nu}{\chi|\varphi_m|}\right)\right) \end{aligned} \tag{C.95}$$

Similarly to the literature [], the R_1 function can reads as:

$$R_1(\varphi_m,\varphi_m^*) = -\frac{i\varphi_m}{2}G(|\varphi_m|^2) \tag{C.96}$$

where the function $G : \mathbb{R}^* \longrightarrow \mathbb{R}$ is set as:

$$G(|\varphi_m|^2) = -\frac{2}{\pi\nu}\left((\Upsilon-1)\frac{\delta\nu}{\chi|\varphi_m|}\sqrt{1-\left(\frac{\delta\nu}{\chi|\varphi_m|}\right)^2} - \Upsilon\arccos\left(\frac{\delta\nu}{\chi|\varphi_m|}\right) - \arcsin\left(\frac{\delta\nu}{\chi|\varphi_m|}\right)\right) \tag{C.97}$$

As a result, it gives the following real and imaginary parts:

$$\forall(\varphi_m,\varphi_m^*) \in \mathbb{C}^2 \qquad \begin{cases} \Re(R_1(\varphi_m,\varphi_m^*)) = \dfrac{1}{2}N_m \sin(\delta_m) G(|\varphi_m|^2) \\ \Im(R_1(\varphi_m,\varphi_m^*)) = -\dfrac{1}{2}N_m \cos(\delta_m) G(|\varphi_m|^2) \end{cases} \tag{C.98}$$

The results previously obtained for a non-polynomial restoring force function in Section C.3 stand for this case, and are not rewritten here.

Appendix D

The cubic restoring force with a periodic time-dependent coefficient

This appendix presents a journal article whose results are not included in the main body of the manuscript. This journal article has been realized in the context of a collaboration with Aurélie Labetoulle whose Ph.D. topic relates to nonlinear restoring forces with time-dependent coefficients. In this context, this journal article is the result of the experiments, numerical simulations and optimization that have been done in the framework of the work presented in Chapter 4. As a result, the nonlinear behavior featured in Aurélie's Ph.D thesis is enforced to the ER by using the control strategy presented in Chapter 3. The experimental tests are realized in the coupled environment of Chapter 4 and compared to the model. The following contributions of the articles are:

- A nonlinear restoring force featuring a time-dependent coefficient can be enforced by using the developed control strategy of Chapter 3.
- The nonlinear resonator with a restoring force featuring a time-dependent coefficient is capable of acoustic absorption, and with better performance than a nonlinear resonator with constant coefficients by extending the frequency bandwidth of absorption, and by increasing the energy absorption thanks to parametric resonance.

To achieve these contributions, the article features experimental results obtained in the coupled environment of the tube with a numerical study of the two-degrees of freedom system (both presented in Chapter 4). Moreover, numerical and experimental optimizations are realized with increasing frequency sweeps (in case of a hardening behavior).

This collaboration specifically features possible applications of the control strategy such as a new experimental method for testing nonlinear behaviors at low costs.

Commun Nonlinear Sci Numer Simulat 150 (2025) 108972

Contents lists available at ScienceDirect

Communications in Nonlinear Science and Numerical Simulation

journal homepage: www.elsevier.com/locate/cnsns

Research paper

On the programming of cubic acoustic resonator with periodic time-dependent coefficient

Maxime Morell [a,*], Aurélie Labetoulle [a], Emmanuel Gourdon [a], Emanuele De Bono [b], Manuel Collet [c], Alireza Ture Savadkoohi [a]

[a] ENTPE, Ecole Centrale de Lyon, CNRS, LTDS, UMR5513, 3 rue Maurice Audin, Vaulx-en-Velin, 69518, France
[b] Ecole Centrale de Lyon, CNRS, ENTPE, LTDS, UMR5513, 36 av. Guy de Collongue, Ecully, 69130, France
[c] CNRS, Ecole Centrale de Lyon, ENTPE, LTDS, UMR5513, 36 av. Guy de Collongue, Ecully, 69130, France

ARTICLE INFO

Keywords:
Time-dependent coefficient
Programmable
Low amplitude
Electroacoustic resonator

ABSTRACT

In this article, we investigate an electroacoustic resonator with a programmed cubic nonlinearity with constant and time-dependent coefficients. We design an experiment coupling an acoustic mode of a tube with a digitally programmable nonlinear resonator. Both simulations and experiments are carried out to compare optimized points for the resonator with programmed cubic nonlinearity with constant and time-dependent coefficients. We show that the frequency bandwidth of efficiency and the noise reduction are greater with varying nonlinearity than with constant nonlinearity.

1. Introduction

The propagation of waves through a medium is an issue tackled across many fields of physics [1] and engineering [2,3]. Acoustic waves over a wide range of frequencies and amplitudes may create dangerous situations in the short or long term. Efficient vibration control requires a broad frequency response, achievable by passive systems like acoustic foams [1,4] or active noise reduction devices [5–7] that produce waves in phase opposition. However, these systems are either poorly performing at low frequencies, or across the entire considered space. A hybrid solution consists of using electrical current to adapt the acoustic impedance of a surface using controlled electroactive loudspeakers [8–10]. This approach does not produce phase-opposition waves, and may be efficient at low frequencies [11]. Although nonlinearities offer benefits for reducing vibrations, impedance control methods have largely remained linear until recent developments [12,13]. However, in other fields such as mechanics, nonlinear phenomena have been extensively studied to broaden the frequency range of efficiency of passive systems [14]. A key advantage is the ability of a nonlinear resonator to tune its resonance frequency to align with a primary oscillator's resonance frequency [15]. A further benefit is the targeted energy transfer from the primary oscillator to the auxiliary nonlinear oscillator once the nonlinear activation threshold is reached [16,17]. Furthermore, many types of nonlinear resonators aiming to mitigate vibrations have been studied such as vibroimpact resonators [18,19], the Duffing-type resonator [20–22] or piecewise oscillators [23–27]. Until recently, in acoustics, nonlinear absorption has only been achieved by high activation thresholds, limiting its application to extremely noisy environments [28–30]. Nevertheless, the active impedance control approach by electroacoustic resonators [31–34] has recently been extended to achieve nonlinear behaviors at low excitation levels [12,13,35,36]. Moreover, the control strategy proposed in [12,13,35] is also suitable for achieve parametric resonators, so far largely overlooked as a means to reduce noise and vibrations.

* Corresponding author.
E-mail address: maxime.morell@entpe.fr (M. Morell).

https://doi.org/10.1016/j.cnsns.2025.108972
Received 25 November 2024; Received in revised form 16 May 2025; Accepted 17 May 2025
Available online 5 June 2025
1007-5704/© 2025 The Authors. Published by Elsevier B.V. This is an open access article under the CC BY license (http://creativecommons.org/licenses/by/4.0/).

The combination of nonlinear and parametric characteristics could lead to effective absorption across a wide frequency range. However, its potential is yet to be demonstrated.

In this article, a digitally programmed cubic resonator with time-dependent coefficient to control a tube acoustic mode at low excitation levels is used. By combining numerical and experimental approaches, it is shown that nonlinear auto-parametric acoustic resonators are more efficient than classical Duffing oscillators in controlling a mode. To properly demonstrate this result, an optimization of both programmed cubic nonlinearities with constant and time-dependent coefficients is conducted through both simulations and experiments.

2. The control strategy

The impedance control strategy used in this paper is detailed in De Bono et al. [13,35], which is able to enforce the desired acoustic response of an electroacoustic resonator (ER). The flexibility of such control algorithm allows to implement nonlinear behaviors with time-varying parameters, without requiring high excitation levels. An ER is composed of a 5-cm wide loudspeaker collocated with a microphone, and linked to a controller: a dSPACE MicroLabBox DS1202 device working at 50 kHz. The microphone retrieves the pressure close to the membrane of the loudspeaker. Based upon real-time integration [13], the controller computes the electrical current to be sent into the loudspeaker's coil using the measured pressure, and a prediction of the displacement, velocity, and acceleration of the loudspeaker's membrane. At low excitation frequencies and amplitudes, the loudspeaker can be described as a single-degree-of-freedom system as in Eq. (1a). The control equations needed to synthesize the control algorithm are provided:

$$M_0\ddot{x}(t) + R_0\dot{x}(t) + K_0x(t) = S_d p(t) - Bli(t) \tag{1a}$$

$$i(t) = \frac{1}{Bl}(-M_0\ddot{x}_d(t) - R_0\dot{x}_d(t) - K_0x_d(t) + S_d p(t)) \tag{1b}$$

$$M_d\ddot{x}_d(t) + R_d\dot{x}_d(t) + K_dx_d(t) + F_{NL}(x_d,t) = Sp(t) \tag{1c}$$

where x and x_d stand for the displacement and desired displacement of the loudspeaker membrane, and S_d denotes its effective area. The parameters M_0, R_0, K_0 represent the modal characteristics of the loudspeaker, when no electrical current is sent into the coil. The damping parameter R_0 includes all types of damping means. The parameters M_d, R_d, K_d correspond to the desired modal parameters of the first mode of the loudspeaker, and F_{NL} is a nonlinear stiffness force function, which can be chosen digitally in the programming of the control [13,35]. The variable p denotes the measured pressure at the surface of the loudspeaker's membrane. Bl is the Laplace force factor corresponding to the magnet's magnetic field B and to the length of the solenoid l. The electrical current sent into the solenoid is represented by i [Eq. (1b)] and is obtained by computing Eq. (1b) based on the estimation of the targeted state given by Eq. (1c). The controller employs a numerical scheme to integrate the differential equation of the desired behavior [Eq. (1c)] using the measured pressure, which yields the prediction of the displacement x_d, velocity $\dot{x}_d$ and acceleration $\ddot{x}_d$ of the loudspeaker's membrane. The Eq. (1c) is solved using a specific numerical scheme taking into account its impact on the experimental implementation complexity that could induce numerical latency. In this study, the chosen numerical scheme is a fourth order Runge–Kutta like algorithm. While the displacement x_d is computed at each increment of the scheme t, $t+h/2$ and $t+h$ with h the time step, the pressure is not measured at each increment, which would necessitate to dissociate the acquisition rate from the calculation rate. The pressure is considered constant during the time step, which is reasonable considering the high sampling rate of 50 kHz compared to the excitation frequencies (800 Hz maximum). The predictions obtained through the numerical resolution of Eq. (1c) are introduced in the control parameter equation [Eq. (1b)] to compute the electrical current i at each time step [13]. This method permits to digitally program a linear or nonlinear behavior of a transducer at low excitation amplitudes, where the transducer is within its linear regime.

The presented control presents some limitations that are defined by the needed assumptions. The control strategy uses a model of the loudspeaker in order to make a feedforward controller. The model of the loudspeaker assumes that the ER response is dominated by its first mode, with low excitation frequencies and amplitudes. In a case where these assumptions are no longer fulfilled, the controller might lead to instabilities. As a result, the loudspeaker should remain in its linear domain, and should work at frequencies close to its linear first mode. Moreover, a loss in the acoustical passivity of the ER can be observed at high frequencies (more than 3 kHz) due to the time delay in the digital implementation of the controller [33].

3. The cubic nonlinearity with time-dependent coefficient

The desired behavior Eq. (1c) displays the function F_{NL} containing the time-varying nonlinear stiffness. A general periodic form as a Fourier series for the nonlinear time-varying stiffness is assumed [37,38]:

$$F_{NL}(x_d,t) = K_dK(t)x_d^3(t) = K_d\left(\sum_{n=-\infty}^{n=\infty}\tilde{K}_n\,\mathrm{e}^{j\omega nt}\right)x_d^3(t) \tag{2}$$

where ω is the excitation frequency, and $\tilde{K}_n \in \mathbb{C}$. To consider only the first harmonic, a Galerkin procedure is applied to the nonlinear function. Supposing that x_d is as follows:

$$x_d(t) = A_{-1}\,\mathrm{e}^{-j\omega t} + A_1\,\mathrm{e}^{j\omega t} \tag{3}$$

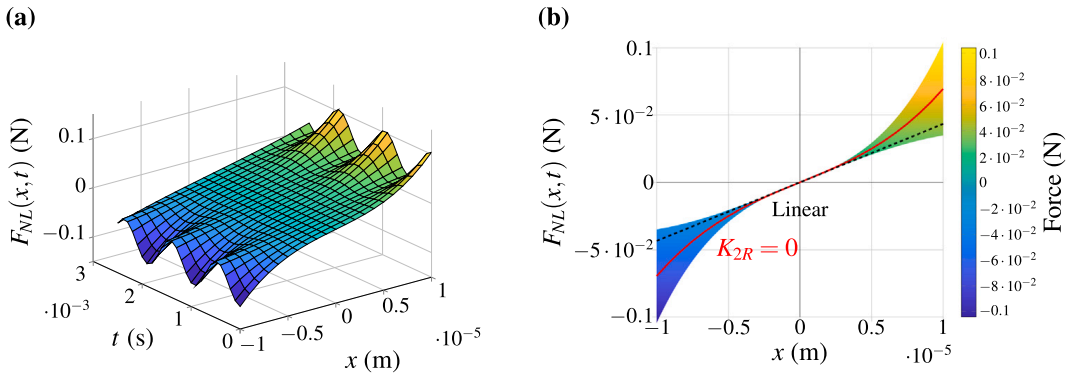

Fig. 1. (a)–(b) Plots of the nonlinear time-varying restoring force with respect to the time and to the displacement of the ER's membrane with $\tilde{K}_0 = 6 \times 10^9$ m^{-2} and $\tilde{K}_{2R} = 4 \times 10^8$ m^{-2} and $\omega = 2\pi \times 530$ rad.s^{-1}.

The Galerkin procedure writes:

$$F_{NL,k} = \frac{\omega}{2\pi} \int_0^{\frac{2\pi}{\omega}} F_{NL}(t)\, \mathrm{e}^{-jk\omega t}\, \mathrm{d}t = \frac{\omega}{2\pi} \int_0^{\frac{2\pi}{\omega}} K_d \Big(\sum_{n=-\infty}^{n=+\infty} \tilde{K}_n\, \mathrm{e}^{jn\omega t} \Big) \Big(A_{-1}\, \mathrm{e}^{-j\omega t} + A_1\, \mathrm{e}^{j\omega t} \Big)^3 \mathrm{e}^{-jk\omega t}\, \mathrm{d}t \tag{4}$$

with $F_{NL,k}$ the kth Fourier harmonic of F_{NL}. In the case of $k = 1$, it yields non-zero terms corresponding to the following terms of $K(t)$:

$$K(t) = \tilde{K}_4\, \mathrm{e}^{4j\omega t} + \tilde{K}_2\, \mathrm{e}^{2j\omega t} + \tilde{K}_{-2}\, \mathrm{e}^{-2j\omega t} + \tilde{K}_0 \tag{5}$$

By developing the complex coefficients $\tilde{K}_n = \tilde{K}_{nR} + j\tilde{K}_{nI}$, it gives:

$$K(t) = \tilde{K}_0 + 2\tilde{K}_{2R} \cos(2\omega t) - 2\tilde{K}_{2I} \sin(2\omega t) + f(\tilde{K}_{4R}, \tilde{K}_{4I}, 4\omega t) \tag{6}$$

with f a function of $\tilde{K}_{4R}$, $\tilde{K}_{4I}$, and t. To simplify the programming of the control, the coefficients $\tilde{K}_{2I}$, $\tilde{K}_{4I}$ and $\tilde{K}_{4R}$ are set to zero. Setting $\tilde{K}_{2I}$ to 0 imposes the phase of the time modulation. In the following, the phase of the excitation signal is chosen to ensure that the resonator stays acoustically passive. However, the choice of setting $\tilde{K}_{2I} = 0$ has been made to facilitate the experimental implementation of the control, and to allow the realization of an experimental optimization. The optimization is needed to be able to compare the cubic nonlinearity using constant coefficient with the cubic nonlinearity including time-dependent coefficient. The nonlinear varying stiffness is shown in Fig. 1(a) and its varying coefficient becomes:

$$K(t) = \tilde{K}_0 + 2\tilde{K}_{2R} \cos(2\omega t) \tag{7}$$

By setting $\tilde{K}_{2R} = 0$, the varying nonlinearity becomes the classic Duffing equation. As an example, $\tilde{K}_0$ and $\tilde{K}_{2R}$ are chosen in a manner that F_{NL} is always positive with a positive displacement, for having a hardening behavior. The Fig. 1(b) pictures the restoring force in the (x, F_{NL}) plan of Fig. 1(a), with respect to the displacement x. It reveals that the time modulation of the nonlinearity contributes to create a hybrid behavior in which the nonlinearity exhibits softening behavior at specific times, while maintaining an overall hardening characteristic due to the constant term. However, it is essential to select carefully the pair of parameters $(\tilde{K}_0, \tilde{K}_{2R})$ to prevent numerical instabilities during programming. The condition $\forall t \in \mathbb{R}_+ \quad K(t) > 0$ effectively excludes cases of negative stiffness. Considering the extreme possible values for the cosine function, the following condition is identified:

$$-\frac{\tilde{K}_0}{2} < \tilde{K}_{2R} < \frac{\tilde{K}_0}{2} \tag{8}$$

When the condition is fulfilled, the global restoring force is odd, and $\forall t \in \mathbb{R}_+,\ \forall x \in \mathbb{R}_+,\ K_d x_d(t) + F_{NL}(x,t) < 0$. The oddity of the function and the preceding condition ensures that the created force is in the opposite direction of the mass displacement [Fig. 1(b)].

4. Method

4.1. The experimental bench

An experimental bench that couples the nonlinear resonator to a cavity mode of a tube is used [28,29,35]. The experiment is composed of a tube with a reduced section area S_t and a length L_t connected at one end to an acoustic source (AS) and at the other end to a coupling box of length L_{cb} and radius r_{cb}. The coupling box is terminated by the nonlinear resonator. The waveguide is pictured in Fig. 2(b). The experimental set-up includes a fixed microphone placed inside the tube with a reduced section for data analysis of the cavity acoustic mode of the tube. A second microphone is positioned in the coupling box to measure the pressure on the membrane of the ER. The experimental set-up is pictured in Fig. 2(a). Assuming that the programmed control works perfectly:

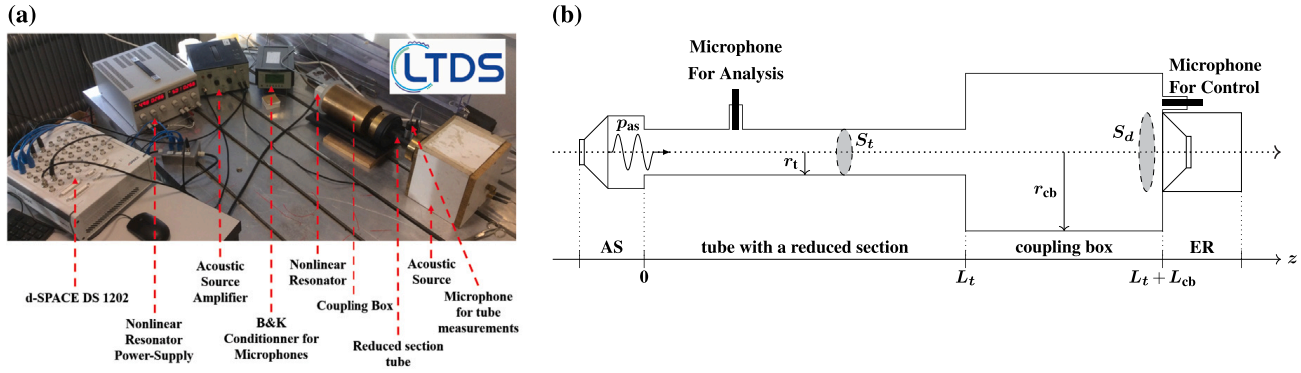

Fig. 2. (a) Experimental set-up. (b) Scheme of the tube experiment.

Table 1
Dimensions and parameters of the experiment and simulation.

	Dimension	Value	Unit
Tube	r_t	1.45×10^{-2}	m
	S_t	6.61×10^{-4}	m^2
	L_t	0.204	m
Coupling box	r_{cb}	0.05	m
	L_{cb}	0.125	m
	γ	125.54	kg s^{-2}
ER	S_d	1.3×10^{-3}	m^2
	M_d	3.89×10^{-4}	kg
	R_d	3.29×10^{-2}	kg s^{-1}
	K_d	4.34×10^{3}	kg s^{-2}
Acoustic mode	m	8.22×10^{-5}	kg
	c	3.96×10^{-2}	kg s^{-1}
	k	1.38×10^{3}	kg s^{-2}

$\forall t \in \mathbb{R}_+$, $x(t) = x_d(t)$, and with the assumptions of plane waves and linear acoustics without flow, the model of the experiment writes [28,35]:

$$\begin{cases} m\ddot{u}(t) + c\dot{u}(t) + ku(t) + \dfrac{\gamma}{\alpha}\big(u(t) - \alpha x(t)\big) = -S_t p_{\text{as}}(t) \\ M_d\ddot{x}(t) + R_d\dot{x}(t) + K_d x(t) + K_d K(t) x(t)^3 + \gamma\big(\alpha x(t) - u(t)\big) = 0 \end{cases} \tag{9}$$

where the variables u stand for the modal coordinates of the first acoustic mode of the tube. The parameters m, c, and k are the modal parameters of the tube's acoustic first mode, and α is the ratio between the areas of the loudspeaker membrane and of the reduced section tube $\alpha = S_d/S_t$. The γ parameter represents an equivalent stiffness of the coupling box, and p_{as} the pressure induced by the acoustic source. The system is excited with 60 s long increasing and decreasing frequency sweeps between 350 Hz and 800 Hz. The frequency ω of the time-dependent coefficient of the cubic stiffness is chosen equal to the frequency of the excitation.

The model of the experiment is solved using a 4-th order Runge–Kutta numerical scheme in the different cases encountered in the following. The simulation parameters from the model and from the experiment are detailed in Table 1.

The modal parameters of the ER are chosen identical to the eigen modal parameters of the loudspeaker for the modal mass and stiffness such as:

$$\begin{cases} M_d = M_0 \\ K_d = K_0 \\ R_d = R_0/8 \end{cases} \tag{10}$$

The modal damping is lowered to permit the existence of the bifurcation. Indeed, analytical results have provided a condition of the existence of the bifurcations on the damping of a nonlinear resonator coupled to a linear oscillator [39]. This condition states that there exists a critical value of damping and linear stiffness beyond which there are no bifurcations. The choice of $R_d = R_0/8$ ensures that the bifurcation exists in this system for the linear stiffness $K_d = K_0$.

The choice of keeping $K_d = K_0$ and $M_d = M_0$ is due to the tuning of the nonlinear resonance of the ER to the tube acoustic mode. In this case, the ER's linear resonance is slightly below the tube acoustic mode, which allows the programmed nonlinear hardening resonance to oscillate at the same frequencies as the tube acoustic resonance.

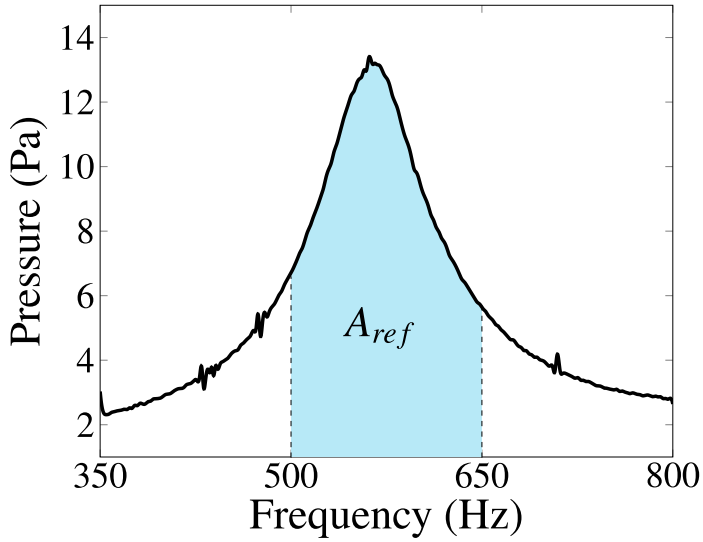

Fig. 3. Envelope of the pressure inside the reduced section tube with a rigid termination.

4.1.1. The reference measure

To understand resonators' efficiency with the cubic nonlinearity both using a constant and time-varying coefficient, a reference measure is realized by introducing a rigid termination instead of the resonator. The replacement of the resonator with a rigid termination permits to identify the modal parameters of the acoustic mode of the tube with a single measure by curvefitting the calculated response to the envelope of the time signal obtained using a frequency sine sweep. Fig. 3 shows the envelope of the pressure time signal. The envelope is obtained by computing the modulus of the Hilbert transform of the time signal. The obtained parameters are detailed in Table 1. The method for identifying the parameters is extensively described in [39].

4.2. The metric for realizing an optimization

For the purpose of comparing the classical cubic nonlinearity with the cubic nonlinearity with a time-varying coefficient, a metric is set:

$$\mathbb{A}_k^l = \frac{\int_{t_1}^{t_2} |H(p_k^l)(t)|dt}{\int_{t_1}^{t_2} |H(p_{ref})(t)|dt} = \frac{A_k^l}{A_{ref}} \tag{11}$$

where H stands for the Hilbert transform of the pressure p inside the reduced section tube. The bounds t_1 and t_2 represent the instants corresponding to the frequencies 500 Hz and 650 Hz during the frequency sweeps. The indices $k = \{\text{num}, \text{exp}\}$ denote numeric and experiment, and $l = \{c, v\}$ constant and varying. The variable p_{ref} corresponds to the pressure inside the tube when the ER is replaced with a rigid termination. This metric is the ratio between the areas of the time signal envelops of a considered measure A_k^l and the reference measure A_{ref} [Fig 3] done with a rigid termination. The rigid termination measure and its surface area A_{ref} is described in Fig 3. Lower metric values correspond to better absorption cases.

5. Results

5.1. The cubic nonlinearity with a constant coefficient

Fig. 4(a) displays the experimental pressure within the reduced section tube and the predicted desired displacement x_d of the loudspeaker's membrane for a cubic nonlinearity with a constant coefficient . A nonlinear hardening behavior is observed in the displacement of the ER. At the frequencies of the nonlinear resonance, which coincide within the frequencies of the bifurcations A and B , a significant decrease in the pressure appears. Indeed, the nonlinear ER oscillates with higher amplitudes resulting in better energy pumping. Broadening the frequency range of the nonlinear resonance, along with raising its amplitude is of great interest to improve the absorption capabilities of the nonlinear ER. Simulations are realized with the parameters of Table 1 and are plotted in Figs. 4(b) and 4(c). Figures 4(b) and 4(c) compare the numerical simulations with the experimental results. The pressure inside the reduced section tube is plotted in Fig. 4(b) for an increasing frequency sweep and in Fig 4(c) for a decreasing frequency sweep. One can see a good agreement between experimental data and simulations, despite minor shifts in the frequencies of the bifurcations. This inaccuracy of the model is attributed to parameter uncertainties [35].

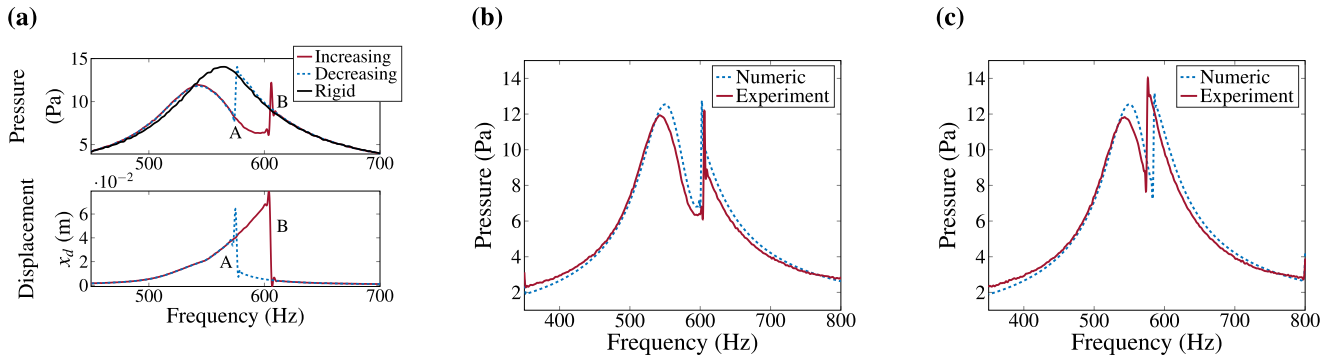

Fig. 4. (a) Envelopes of the pressure inside the reduced section tube and computed displacement of the ER's membrane for increasing and decreasing frequency sweeps with $\tilde{K}_0 = 6 \times 10^9$ m^{-2} and $\tilde{K}_{2R} = 0$ m^{-2} (nonlinearity with a constant coefficient). (b)–(c) Comparison of the envelopes of the pressure inside the reduced section tube for experiment and simulation in the case of increasing (b) and decreasing (c) frequency sweeps in the case of a constant coefficient. .

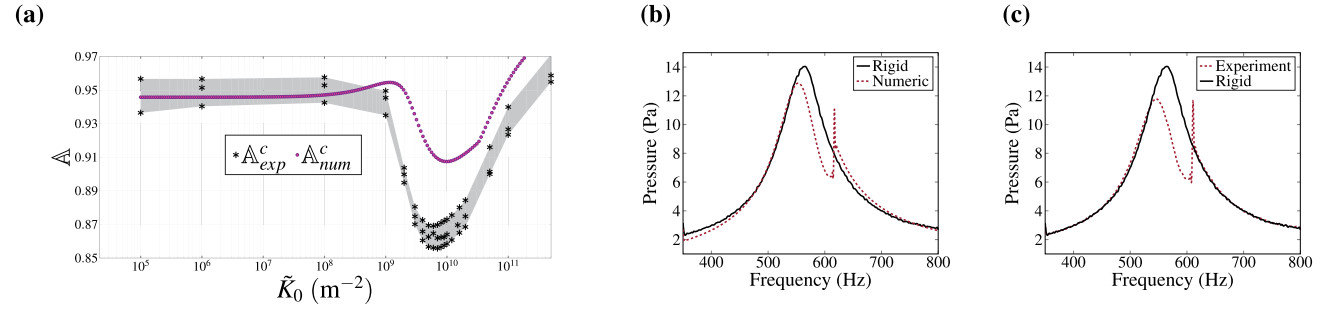

Fig. 5. (a) Value of the optimization metric with respect to the optimization parameter for both simulations and experiments in the case of the cubic nonlinearity with a constant coefficient. (b)–(c) Envelopes of the pressure inside the reduced section tube for the numerical optimal point (b) and experimental optimal point (c) in the case of the cubic nonlinearity with a constant coefficient.

It is worth noticing that the main difference between the ER including a constant coefficient cubic nonlinearity and a Nonlinear Energy Sink (NES) is that a NES is purely nonlinear. The considered system looks like a grounded NES. However, classical NES systems are pure nonlinear without any linear part, e.g. pure cubic nonlinearity. In our considered system, a linear part exists due to the linear mode of the ER [35], looking like more Roberson-type oscillator [22] than a NES. As the control is feedforward, the linear mode of the ER cannot be deleted and it is not possible to create a purely nonlinear system [40]. However, the use of a feedback controller may allow the suppression of the linear mode, which could be eventually coupled to the presented feedforward controller [40]. Another main dissimilarity with the NES lies in the non-reciprocity of the coupling between the ER and the acoustic mode of the tube seen in Eqs. (9). Nonetheless, the acoustic formulation realized in [35] demonstrates that the coupling can be considered reciprocal. Finally, theoretical studies carried out by authors [37,39] show that if the system faces fold singularities or if its equilibrium point is placed in the unstable zone of the slow invariant manifold, then it will present quasi-periodic responses. This response has been experimentally spotted by the authors as well where they looked in detail at time responses of the system for fixed frequencies of the excitation [41]. However, the authors have demonstrated that the particular system studied here rarely induces quasi-periodic oscillations for a cubic nonlinearity with a constant coefficient [39].

The previously presented metric is considered to assess the efficiency of a given nonlinear ER. The optimized values of $\tilde{K}_0$ and $\tilde{K}_{2R}$ are searched for the case of cubic nonlinearities with both constant coefficient and time-dependent coefficients. The case of increasing frequency sweeps of the AS is arbitrarily chosen for the optimization, which is the most favorable case for a hardening behavior. Indeed, the ER equilibrium point depends on the initial conditions.

Regarding the cubic nonlinearity with constant coefficient, the parameter $\tilde{K}_{2R}$ is set to 0, and simulations and experiments are realized with $\tilde{K}_0 \in [10^5, 10^{12}]$ m^{-2} to find a global optimum. As such experimental campaign is spread over multiple weeks, the experimental results might present slight discrepancies due to changes in temperature, humidity, or other physical parameter that can change the modal parameters of the tube acoustic mode. In this context, multiple measures with the same parameters spread over multiple days have been realized. The shaded gray area in Fig. 5(a) contains the experimental results and is bounded by the maximum and minimum results obtained through the experimental campaign.

In Fig. 5(a), the metric $\mathbb{A}$ is represented with respect to the optimization parameter $\tilde{K}_0$ for both experimental and numerical results. A numerical optimal point $\mathbb{A}^c_{num} = 0.907$ is observed for the parameter $\tilde{K}_0 = 9.88 \times 10^9$ m^{-2} which is dissociated from the lowest experimental optimal point $\mathbb{A}^c_{exp} = 0.856$ at $\tilde{K}_0 = 7 \times 10^9$ m^{-2}. This difference can be attributed to the previously noted discrepancies between the experimental results and model simulations. Moreover, the numerical metric values are higher than for the experiment. Fig. 5(b) represents the pressure envelope for the simulations optimal point. The pressure level is higher than the experimental optimal point presented in Fig. 5(c), confirming that the simulation metric values are higher than the experimental

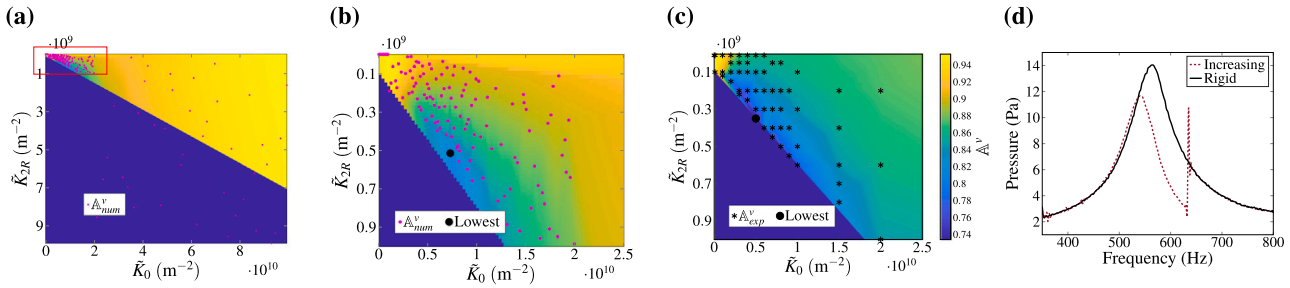

Fig. 6. (a)–(b) Value of the optimization metric with respect to the optimization parameter for both simulations (a) with its zoom (b) and experiments (c) in the case of the cubic nonlinearity with a time-varying coefficient. (d) Envelopes of the pressure inside the reduced section tube for the experimental optimal point in the case of the cubic nonlinearity with a time-varying coefficient.

ones. However, the model reveals the existence of a global optimum and provides insight into the parameter regions where the experimental optimum is likely to be found.

5.2. The cubic nonlinearity with a time-dependent coefficient

A similar process is applied to the cubic nonlinearity with time-varying coefficient with $\tilde{K}_0 \in [10^5, 10^{12}]$ m^{-2} and $\tilde{K}_{2R} \in [0, 10^9]$ m^{-2}. A search for optimums with the simulations is done through random shooting in the optimization parameters $\tilde{K}_0$ and $\tilde{K}_{2R}$ [Fig. 6(a)]. A hyperplane is then extrapolated from the simulation points to map the metric values in the plan $(\tilde{K}_0, \tilde{K}_{2R})$. This hyperplane is the surface fitting the simulation points. The plan is not computed in the zones where the model poorly fits the experiment, even if the stability condition is fulfilled [Eq. (8)]. This first sampling permits to identify the zone where the optimum might be, which is situated in the red rectangle. A new simulation study with random shooting in the red rectangle is done to improve the precision of the numerical optimization [Fig. 6(b)]. The lower metric point $\mathbb{A}^{\upsilon}_{num} = 0.805$ is obtained for $\tilde{K}_0 = 7.29 \times 10^9$ m^{-2} and $\tilde{K}_{2R} = 5.14 \times 10^8$ m^{-2}. As the experimental map of the metric value is realized using a random shooting, one cannot ensure that this point is the optimum. Moreover, the zone where the model poorly fits the experiment has not been investigated, which does not ensure that the point is the optimal value.

An experimental optimization is realized in the previously defined reduced zone investigated through the numerical simulations [Fig. 6(c)]. The measurements were mainly conducted in the zones identified with the better metric values during the numerical simulations. One can see that the optimization plan extrapolated from the measures is similar to the numerical optimization plan. The represented plane is the surface fitting the experimental points. However, the metric values are lower for the experimental results than for the numerical one, in the same manner as the cubic nonlinearity with constant coefficient. This phenomenon can be explained by the simulation assumption that the control works perfectly, which leads to neglect the remaining influence of the linear mode of the loudspeaker. The lower metric points are situated close to the defined frontier in both numerical and experimental optimizations. The lower metric point $\mathbb{A}^{\upsilon}_{exp} = 0.733$ is obtained for $\tilde{K}_0 = 5 \times 10^9$ m^{-2} and $\tilde{K}_{2R} = 3.5 \times 10^8$ m^{-2}. Fig. 6(d) presents the measurement, highlighting a substantial reduction in pressure levels within the reduced section tube over a broad frequency range.

The comparison between cubic nonlinearities with constant and time-varying coefficients reveals that the classical cubic nonlinearity optimal point has a higher metric value than many of the non-optimal points of the cubic nonlinearity time-varying coefficient. As a result, the cubic nonlinearity with a time-dependent coefficient is generally more efficient than the classical duffing nonlinearity. The optimization of the other parameters, and the higher harmonics of the periodic stiffness may also improve the performances of the ER. Moreover, the zone closer to the stability condition, where the model does not fit the experimental results, may reveal lower metric values. The phenomena involved in this zone have to be investigated.

As previously described, if the nonlinear resonance can be broadened while increasing the amplitudes of the oscillations, the acoustic absorption capabilities should be improved. In Fig. 7(a), the experimental results of the cubic nonlinearity with a constant coefficient and with a time-dependent coefficient are compared for increasing frequency sweeps. The time-dependent coefficient case provides a broadened resonance with higher amplitude oscillations seen in the displacement curves, leading to better absorption capabilities for a larger frequency bandwidth, which can be seen in the pressure curves. However, one may notice that the maximal pressure is unchanged, while the minimum pressure is improved for both signals. This phenomenon is due to the linear part of the stiffness of the ER. The ER linear resonance facilitates the apparition of the nonlinear resonance at low excitation amplitudes, which builds upon the ER linear resonance. This linear resonance also limitates the absorption capabilities of the ER at its resonance frequency.

6. Conclusion

To summarize, the cubic nonlinearity with a time-varying coefficient has demonstrated greater potential than the classical cubic nonlinearity in mitigating noise and vibrations. The control method to program a cubic nonlinearity with a time-varying coefficient

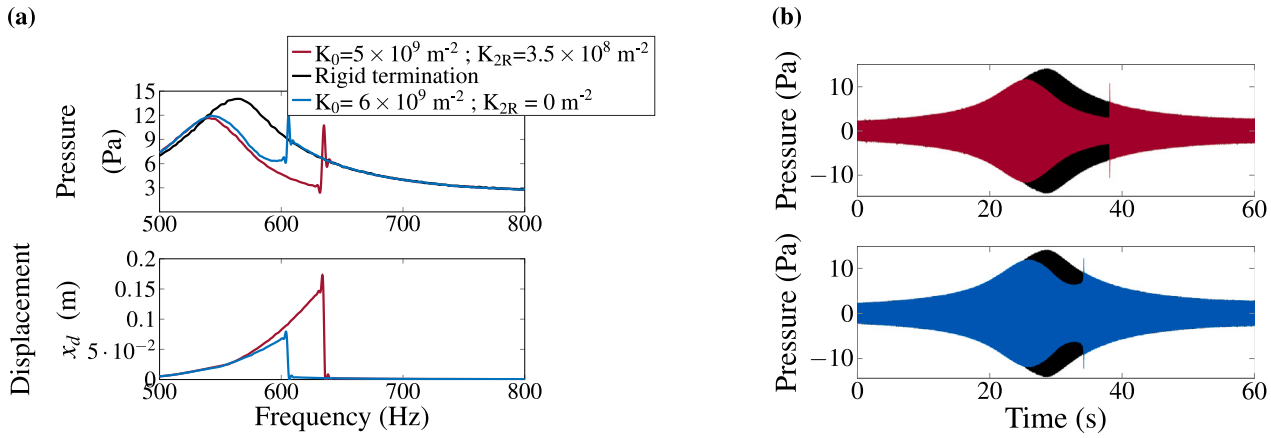

Fig. 7. Comparison of the experimental envelopes of the pressure inside the reduced section tube and computed displacement of the ER's membrane for increasing frequency sweeps between the cubic nonlinearity with a constant coefficient $\tilde{K}_0 = 6 \times 10^9$ m^{-2}, $\tilde{K}_{2R} = 0$ m^{-2} and the cubic nonlinearity with a time-dependent coefficient $\tilde{K}_0 = 5 \times 10^9$ m^{-2}, $\tilde{K}_{2R} = 3.5 \times 10^8$ m^{-2}.

within a loudspeaker is presented and adapted from the control method to create a constant coefficient. The programmed resonator with a time-dependent nonlinear coefficient efficiently controlled the acoustic cavity mode of a tube. The obtained results indicate that a large set of parameters $\{\tilde{K}_0, \tilde{K}_{2R}\}$ provides more efficient varying nonlinearity than the optimized cubic nonlinearity with a constant coefficient. However, further research is needed to investigate the unknown zone, and the phenomena at stake. Moreover, many parameters have not been optimized such as the stiffness of the sine part of the periodic stiffness $\tilde{K}_{2I}$ or its modulating frequency ω. The optimization of a large number of parameters in complex nonlinear problems on a large frequency bandwidth would require advanced optimization techniques, and should be investigated in future studies. Such nonlinearity has a significant potential by its ability to mitigate vibrations on a large frequency bandwidth thanks to its nonlinear parametric nature. Furthermore, the use of this nonlinearity is not limited to acoustics, and should be investigated in other fields.

CRediT authorship contribution statement

Maxime Morell: Writing – review & editing, Writing – original draft, Visualization, Validation, Software, Methodology, Investigation, Formal analysis, Data curation, Conceptualization. **Aurélie Labetoulle:** Writing – review & editing, Validation, Methodology, Investigation, Formal analysis, Data curation, Conceptualization. **Emmanuel Gourdon:** Writing – review & editing, Validation, Supervision, Resources, Project administration, Funding acquisition, Conceptualization. **Emanuele De Bono:** Writing – review & editing, Supervision, Software, Conceptualization. **Manuel Collet:** Writing – review & editing, Validation, Supervision, Resources, Project administration, Funding acquisition. **Alireza Ture Savadkoohi:** Writing – review & editing, Validation, Supervision, Resources, Project administration, Funding acquisition, Conceptualization.

Declaration of competing interest

The authors declare that they have no known competing financial interests or personal relationships that could have appeared to influence the work reported in this paper.

Acknowledgments

The authors thank Abdelhakim Ezzerouki for providing helpful assistance in the electronic realization of the experiment. The authors would like to gratefully thank the following organizations for supporting this research: (i) The "Ministère de la transition écologique" and (ii) LABEX CELYA (ANR-10-LABX-0060) of the "Université de Lyon" within the program "Investissement d'Avenir" (ANR-11-IDEX-0007) operated by the French National Research Agency (ANR).

Data availability

No data was used for the research described in the article.

References

[1] Delany ME, Bazley EN. Acoustical properties of fibrous absorbent materials. Appl Acoust 1970;3:105–16. http://dx.doi.org/10.1016/0003-682X(70)90031-9.

[2] Nucera F, Iacono FL, McFarland D, Bergman L, Vakakis A. Application of broadband nonlinear targeted energy transfers for seismic mitigation of a shear frame: Experimental results. J Sound Vib 2008;313:57–76. http://dx.doi.org/10.1016/j.jsv.2007.11.018.

[3] Nucera F, McFarland D, Bergman L, Vakakis A. Application of broadband nonlinear targeted energy transfers for seismic mitigation of a shear frame: Computational results. J Sound Vib 2010;329:2973–94. http://dx.doi.org/10.1016/j.jsv.2010.01.020.

[4] Piégay C, Glé P, Gourdon E, Gourlay E, Marceau S. Acoustical model of vegetal wools including two types of fibers. Appl Acoust 2018;129:36–46. http://dx.doi.org/10.1016/j.apacoust.2017.06.021, URL https://linkinghub.elsevier.com/retrieve/pii/S0003682X17303274.

[5] Rayleigh J. The theory of sound. Macmillan; 1896.

[6] Miljkovic D. Active noise control: From analog to digital - last 80 years. In: 2016 39th international convention on information and communication technology, electronics and microelectronics, MIPRO 2016 - proceedings. Institute of Electrical and Electronics Engineers Inc; 2016, p. 1151–6. http://dx.doi.org/10.1109/MIPRO.2016.7522313.

[7] Guicking D. Patents on active control of sound and vibration-an overview. 2009, URL http://www.guicking.de/dieter.

[8] Olson HF, May EG. Electronic sound absorber. J Acoust Soc Am 1953;25:1130–6. http://dx.doi.org/10.1121/1.1907249.

[9] Guicking D, Karcher K. Active impedance control for one-dimensional sound. J Vib Acoust Trans ASME 1984;106:393–6. http://dx.doi.org/10.1115/1.3269207.

[10] Thenail D, Lacour O, Galland MA, Furstoss M. The active control of wall impedance. Acustica 1997;83:1039–44.

[11] Collet M, David P, Berthillier M. Active acoustical impedance using distributed electrodynamical transducers. J Acoust Soc Am 2009;125:882–94. http://dx.doi.org/10.1121/1.3026329, URL https://pubs.aip.org/jasa/article/125/2/882/794389/Active-acoustical-impedance-using-distributed.

[12] Guo X, Lissek H, Fleury R. Improving sound absorption through nonlinear active electroacoustic resonators. Phys Rev Appl 2020;13. http://dx.doi.org/10.1103/PhysRevApplied.13.014018.

[13] De Bono E, Morell M, Collet M, Gourdon E, Ture Savadkoohi A, Ouisse M, et al. Model-inversion control to enforce tunable Duffing-like acoustical response on an electroacoustic resonator at low excitation levels. J Sound Vib 2024;570:118070. http://dx.doi.org/10.1016/j.jsv.2023.118070.

[14] Vakakis AF, Gendelman OV, Bergman LA, McFarland DM, Kerschen G, Lee YS. Nonlinear targeted energy transfer in mechanical and structural systems I & II. 2009.

[15] Gatti G, Brennan M, Tang B. Some diverse examples of exploiting the beneficial effects of geometric stiffness nonlinearity. Mech Syst Signal Process 2019;125:4–20. http://dx.doi.org/10.1016/j.ymssp.2018.08.024.

[16] Gendelman O, Manevitch LI, Vakakis AF, M'closkey R. Energy pumping in nonlinear mechanical oscillators: Part I—dynamics of the underlying Hamiltonian systems. J Appl Mech Trans ASME 2001;68:34–41. http://dx.doi.org/10.1115/1.1345524.

[17] Vakakis AF, Gendelman O. Energy pumping in nonlinear mechanical oscillators: Part II—resonance capture. J Appl Mech Trans ASME 2001;68:42–8. http://dx.doi.org/10.1115/1.1345525.

[18] Gendelman O. Analytic treatment of a system with a vibro-impact nonlinear energy sink. J Sound Vib 2012;331:4599–608. http://dx.doi.org/10.1016/j.jsv.2012.05.021, URL https://linkinghub.elsevier.com/retrieve/pii/S0022460X12003884.

[19] Gourc E, Michon G, Seguy S, Berlioz A. Targeted energy transfer under harmonic forcing with a vibro-impact nonlinear energy sink: Analytical and experimental developments. J Vib Acoust 2015;137. http://dx.doi.org/10.1115/1.4029285.

[20] Nayfeh AH, Mook DT. Nonlinear oscillations. 1995.

[21] Kovacic I, Brennan MJ. The duffing equation : nonlinear oscillators and their phenomena. Wiley; 2011, p. 369.

[22] Roberson RE. Synthesis of a nonlinear dynamic vibration absorber. J Franklin Inst 1952;254:205–20. http://dx.doi.org/10.1016/0016-0032(52)90457-2.

[23] Georgiadis F, Vakakis AF, McFarland DM, Bergman L. Shock isolation through passive energy pumping in a system with piecewise linear stiffnesses. ASMEDC; 2003, p. 1569–74. http://dx.doi.org/10.1115/DETC2003/VIB-48490.

[24] Lamarque C-H, Gendelman OV, Savadkoohi AT, Etcheverria E. Targeted energy transfer in mechanical systems by means of non-smooth nonlinear energy sink. Acta Mech 2011;221:175–200. http://dx.doi.org/10.1007/s00707-011-0492-0.

[25] Hurel G, Savadkoohi AT, Lamarque CH. Passive control of a two degrees-of-freedom pendulum by a non-smooth absorber. Nonlinear Dynam 2019;98:3025–36. http://dx.doi.org/10.1007/S11071-019-04891-0.

[26] Hurel G, Savadkoohi AT, Lamarque CH. Design of a nonlinear absorber for a 2 degrees of freedom pendulum and experimental validation. Struct Control Heal Monit 2021;28. http://dx.doi.org/10.1002/STC.2814.

[27] da Silveira Zanin C, Savadkoohi AT, Baguet S, Dufour R, Hurel G. Nonlinear vibratory energy exchanges in a meta-cell. Int J Non-Linear Mech 2022;146:104148. http://dx.doi.org/10.1016/j.ijnonlinmec.2022.104148.

[28] Bellet R, Cochelin B, Herzog P, Mattei PO. Experimental study of targeted energy transfer from an acoustic system to a nonlinear membrane absorber. J Sound Vib 2010;329:2768–91. http://dx.doi.org/10.1016/j.jsv.2010.01.029.

[29] Gourdon E, Savadkoohi AT, Vargas VA. Targeted energy transfer from one acoustical mode to an Helmholtz resonator with nonlinear behavior. J Vib Acoust Trans ASME 2018;140. http://dx.doi.org/10.1115/1.4039960.

[30] Bouzid I, Côte R, Mattei P-O. Towards a bistable vibroacoustic nonlinear absorber: optimum efficiency of a bistable nonlinear energy sink. Nonlinear Dynam 2025;113:8019–38. http://dx.doi.org/10.1007/s11071-024-10572-4.

[31] Karkar S, De Bono E, Collet M, Matten G, Ouisse M, Rivet E. Broadband nonreciprocal acoustic propagation using programmable boundary conditions: From analytical modeling to experimental implementation. Phys Rev Appl 2019;12. http://dx.doi.org/10.1103/PhysRevApplied.12.054033.

[32] Billon K, De Bono E, Perez M, Salze E, Matten G, Gillet M, et al. In flow acoustic characterisation of a 2D active liner with local and non local strategies. Appl Acoust 2022;191:108655. http://dx.doi.org/10.1016/j.apacoust.2022.108655, URL https://linkinghub.elsevier.com/retrieve/pii/S0003682X22000299.

[33] De Bono E, Collet M, Matten G, Karkar S, Lissek H, Ouisse M, et al. Effect of time delay on the impedance control of a pressure-based, current-driven electroacoustic absorber. J Sound Vib 2022;537:117201. http://dx.doi.org/10.1016/J.JSV.2022.117201, URL https://linkinghub.elsevier.com/retrieve/pii/S0022460X22003959.

[34] De Bono E, Collet M, Ouisse M. The advection boundary law in absence of mean flow: Passivity, nonreciprocity and enhanced noise transmission attenuation. J Sound Vib 2024;590:118603. http://dx.doi.org/10.1016/j.jsv.2024.118603, URL https://www.sciencedirect.com/science/article/pii/S0022460X24003663.

[35] Morell M, Gourdon E, Collet M, Ture Savadkoohi A, De Bono E, Lamarque C-H. Towards digitally programmed nonlinear electroacoustic resonators for low amplitude sound pressure levels: Modeling and experiments. J Sound Vib 2024;584:118437. http://dx.doi.org/10.1016/j.jsv.2024.118437, URL https://www.sciencedirect.com/science/article/pii/S0022460X24002001.

[36] Morell M, Gourdon E, Collet M, Savadkoohi AT, De Bono E. Nonlinear digitally created electroacoustic absorber designed for acoustic energy pumping. Proc Forum Acusticum 2023;4807–10. http://dx.doi.org/10.61782/fa.2023.0862.

[37] Labetoulle A, Savadkoohi AT, Gourdon E. Detection of different dynamics of two coupled oscillators including a time-dependent cubic nonlinearity. Acta Mech 2022;233:259–90. http://dx.doi.org/10.1007/s00707-021-03119-w, URL https://link.springer.com/10.1007/s00707-021-03119-w.

[38] Labetoulle A, Missoum S, Gourdon E, Savadkoohi AT. Stochastic optimization of targeted energy transfer with time-dependent cubic nonlinearity. Commun Nonlinear Sci Numer Simul 2024;139:108314. http://dx.doi.org/10.1016/j.cnsns.2024.108314.

[39] Morell M, Collet M, Gourdon E, Savadkoohi AT, De Bono E. Experimental validation of the analytical modelling of a digitally created duffing acoustic nonlinear oscillator at low amplitudes. Mech Ind 2025;26:2. http://dx.doi.org/10.1051/meca/2024036.
[40] Volery M, Guo X, Lissek H. Robust direct acoustic impedance control using two microphones for mixed feedforward-feedback controller. Acta Acust 2023;7:2. http://dx.doi.org/10.1051/aacus/2022058.
[41] da Silveira Zanin CE, Labetoulle A, De Bono E, Gourdon E, Collet M, Savadkoohi AT. Experimental evidences of nonlinear programmable electroacoustic loudspeaker. Build Acoust 2023;30:249–63. http://dx.doi.org/10.1177/1351010X231184040.

Appendix E

The Metasurface experiment

This appendix presents the basic calibrations of the experimental bench of the distributed network experiment, described in Chapter 6. The experimental bench is placed in its rigid configuration. The measurements are realized with the same protocol as the ones in Chapter 6, i.e. with single frequency sine wave from both loudspeakers at side A (LS A) and side B (LS B) for 2 seconds for frequencies from 300 Hz to 1500 Hz with a 1 Hz step.

E.1 The acoustic sources calibration

The calibration of the sources have to be made for the resonators do deliver similar acoustic levels in the tube for the treatment of nonlinear liners. A method based on the control of the excitation sources has been proposed in [24]. However, in this work, a more straightforward approach is proposed. The calibration of the excitation gains have to be made beforehand, based on the acoustic levels in the tube with a rigid configuration. The proposed protocol lies in the measurement of the acoustic pressure at the loudspeaker's nearest microphone $p_f(t)^{[k]}$ at the frequency f, with $k \in \{A,B\}$ being the superscript denoting the loudspeaker of interest. The mean value of the envelope of the steady-state signal is estimated:

$$\overline{p_f}^{[k]} = \frac{1}{t_2 - t_1} \int_{t_1}^{t_2} |H(p_f^{[k]})(t)| dt, \quad k \in \{A,B\} \tag{E.1}$$

where $H(p_f)$ stands for the Hilbert transform of p_f. A gain $g_f^{[k]}$, $k \in \{A,B\}$ is then applied at each frequency f being:

$$g_f^{[k]} = \frac{1}{\overline{p_f}}, \quad k \in \{A,B\} \tag{E.2}$$

The implementation for frequency sweeps is to apply the gain $g_f^{[k]}$ being the nearest of the instantaneous frequency. The results of the pressure at the nearest microphone for LS A and LS B with and without the frequency adaptive gain $g_f^{[k]}$ are plotted in Fig. E.1. Observe that the amplitude of the pressure is high at lower frequencies, and present strong variations. The frequency adaptive gains enable to effectively modify the frequency response of the acoustic pressure to minor variations, and is used throughout the measurement campaign.

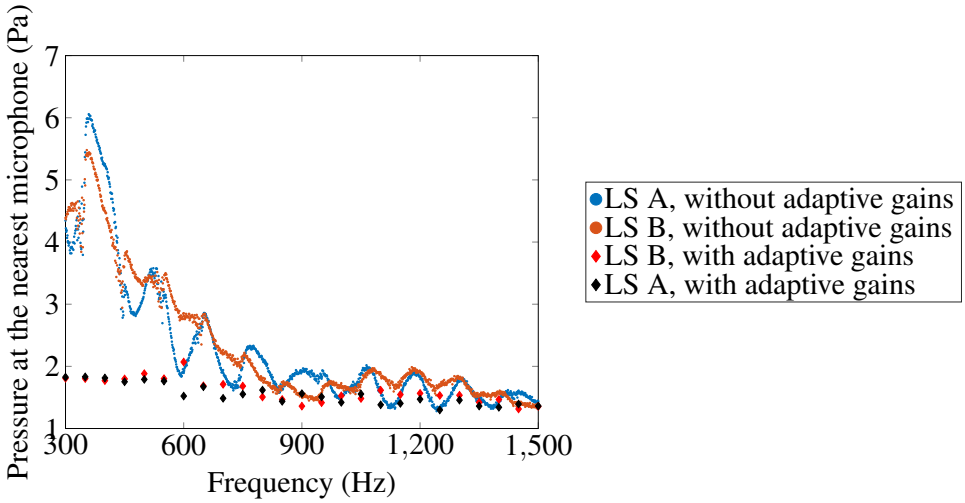

Fig. E.1 Mean value of the envelope of the pressure measured by the nearest microphone of the loudspeaker.

E.2 The rigid liner configuration

The TL, power reflection and absorption coefficients are plotted in Fig. E.2. Observe that the TL is below 1 dB across the frequency range of interest (Fig. E.2a). Moreover, the reflection coefficient is extremely low (Fig. E.2b). The absorption coefficient translates the energy lost by acoustic leaks or vibrating structures (Fig. E.2c). Note that the absorption coefficient is quite high for a rigid configuration. Finally, observe that the measurements from both sides are not identical, signifying that the tube is not symmetrical.

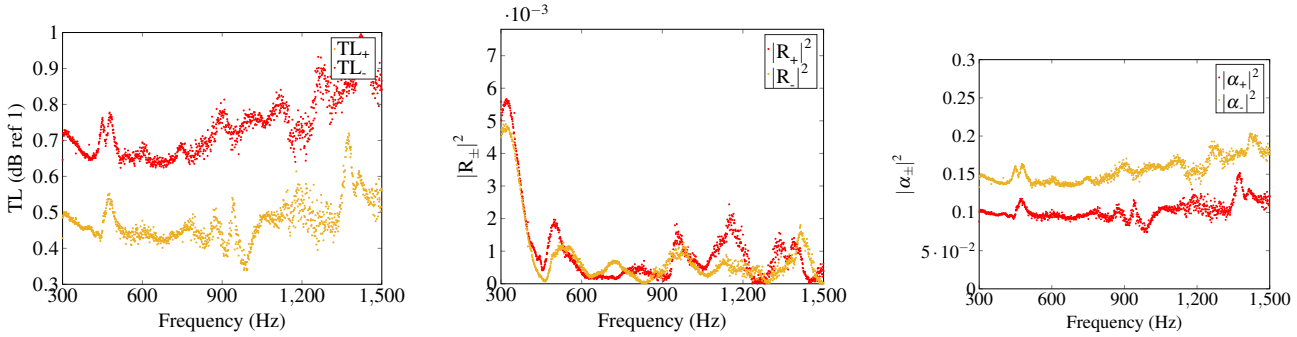

(a) (b) (c)

Fig. E.2 Experimental results obtained with the fully rigid configuration: (a) Transmission Loss, (b) Power Reflection coefficient, (c) Power Absorption coefficient.